DEC 15 1961

UCRL-6625

MASTER

UNCLASSIFIED

UNIVERSITY OF CALIFORNIA

CLASSIFICATION CANCELLED
Date 11-26-73
R. B. Martin, USAEC ORO
Research & Technical Support Div.

Exempt from CCRP Re-review Requirements
(per 7/22/82 Duff/Caddle memorandum)
NK 7-3-14

Ernest O. Lawrence Radiation Laboratory

AEC RESEARCH AND DEVELOPMENT REPORT

PLUTO QUARTERLY REPORT No. 9

RESTRICTED DATA
This document contains restricted data as defined in the Atomic Energy Act of 1954. Its transmittal or disclosure of its contents in any manner to an unauthorized person is prohibited.

LIVERMORE SITE

UNCLASSIFIED

DISTRIBUTION OF THIS DOCUMENT IS UNLIMITED

1 7958

DISCLAIMER

This report was prepared as an account of work sponsored by an agency of the United States Government. Neither the United States Government nor any agency Thereof, nor any of their employees, makes any warranty, express or implied, or assumes any legal liability or responsibility for the accuracy, completeness, or usefulness of any information, apparatus, product, or process disclosed, or represents that its use would not infringe privately owned rights. Reference herein to any specific commercial product, process, or service by trade name, trademark, manufacturer, or otherwise does not necessarily constitute or imply its endorsement, recommendation, or favoring by the United States Government or any agency thereof. The views and opinions of authors expressed herein do not necessarily state or reflect those of the United States Government or any agency thereof.

DISCLAIMER

Portions of this document may be illegible in electronic image products. Images are produced from the best available original document.

UNCLASSIFIED

UCRL-6625
Nuclear Ramjet
Engines, C-90
M-3679 (25th Ed.)

This document contains 223 pages,
including pp. i-vi.
This is copy 142 of 186 Series A.

CLASSIFICATION CANCELLED
Date 11-26-73
R. B. Martin, USAEC ORO
Research & Technical Support Div.

UNIVERSITY OF CALIFORNIA
Lawrence Radiation Laboratory
Livermore, California

Contract No. W-7405-eng-48

NOTICE
This report was prepared as an account of work sponsored by the United States Government. Neither the United States nor the United States Atomic Energy Commission, nor any of their employees, nor any of their contractors, subcontractors, or their employees, makes any warranty, express or implied, or assumes any legal liability or responsibility for the accuracy, completeness or usefulness of any information, apparatus, product or process disclosed, or represents that its use would not infringe privately owned rights.

PLUTO QUARTERLY REPORT NO. 9*

(July-September 1961)
(Title: Unclassified)

by

The Nuclear Propulsion Division Staff

October 10, 1961

*Previous Quarterly Reports

No. 1, UCRL-5699
No. 2, UCRL-5829
No. 3, UCRL-5925
No. 4, UCRL-6101
No. 5, UCRL-6143
No. 6, UCRL-6258
No. 7, UCRL-6376
No. 8, UCRL-6516

UNCLASSIFIED

RESTRICTED DATA
This document contains restricted data as defined in the Atomic Energy Act of 1954. Transmittal or the disclosure of its contents in any manner to an unauthorized person is prohibited.

DISTRIBUTION OF THIS DOCUMENT IS UNLIMITED

SECRET

DISTRIBUTION

Series A

	Copy No.
LRL Livermore,	
Information Division	1 - 15
John S. Foster	16
Forrest Fairbrother	17
C. M. Van Atta	18
Roger E. Batzel	19 - 20
Theodore C. Merkle	21 - 25
Harry L. Reynolds	26
Richard P. Connell	27
James W. Bell	28
Robert W. Westbrook	29
Albert J. Kirschbaum	30
Henry C. McDonald	31
W. Blake Myers	32 - 36
Albert J. Rothman	37
Monte P. Hickenlooper	38
James S. Kane	39
W. E. Humphrey	40
William C. Grayson, Jr.	41
DASA Livermore Liaison Office,	
Norman G. Hunt	42
LRL Berkeley,	
R. K. Wakerling	43
Hayden S. Gordon	44
LRL Mercury, Nevada,	
James L. Olsen	45
Division of Military Application, Washington,	
Brig. Gen. A. W. Betts	46
U. S. Atomic Energy Commission, Washington,	
Irving Hoffman	47 - 48
Advanced Research Projects Agency	49
Air Force Special Weapons Center	50

SECRET

DISTRIBUTICN (Continued)

Series A

	Copy No.
Air Technical Intelligence Center	51
Air University Library	52
Albuquerque Cperations Cffice	53
Allegany Ballistics Laboratory	54
Argonne National Laboratory	55
Army Ballistic Missile Agency	56 - 57
Atomic Energy Commission, Washington	58 - 61
Atomics International	62
Battelle Memorial Institute	63
Brookhaven National Laboratory	64
Bureau of Naval Weapons	65 - 68
Bureau of Naval Weapons (SPO)	69
Bureau of Ships	70
Canoga Park Area Office	71
Chance-Vought Aircraft, Inc., Dallas (BUWEPS)	72
Chicago Cperations Cffice	73
Chicago Patent Group	74
Convair Division, San Diego	75
Convair Division, San Diego (BUWEPS)	76
Defense Atomic Support Agency, Sandia	77
Defense Atomic Support Agency, Washington	78
Director of Defense Research and Engineering (OSD)	79
duPont Company, Aiken	80
General Electric Company (ANPD)	81 - 86
General Electric Company, Richland	87 - 88
Jet Propulsion Laboratory	89
Lockheed Aircraft Corporation, Burbank	90
Los Alamos Scientific Laboratory	91 - 92
Marquardt Corporation	93 - 96
NASA Ames Research Center	97
NASA Flight Research Center	98
NASA George C. Marshall Space Flight Center	99

DISTRIBUTION (Continued)

Series A

	Copy No.
NASA Langley Research Center	100
NASA Lewis Research Center	101 - 105
National Aeronautics and Space Administration, Washington	106 - 107
Naval Air Development Center	108
Naval Ordnance Test Station	109
North American Aviation, Inc., Downey	110
Nuclear Development Corporation of America	111 - 112
Oak Ridge Operations Office	113
Office of the Chief of Naval Operations	114
Patent Branch, Washington	115
Phillips Petroleum Company (NRTS)	116
Pratt and Whitney Aircraft Division	117
RAND Corporation	118 - 119
San Francisco Operations Office	120
Sandia Corporation	121
School of Aviation Medicine	122
Strategic Air Command	123
Union Carbide Nuclear Company (ORNL)	124 - 133
USAF Headquarters	134
USAF Headquarters (OVCS)	135
Wright Air Development Division	136 - 141
Office of Technical Information Extension	142 - 186

PLUTO QUARTERLY REPORT NO. 9

Table of Contents

	Page No.
CHAPTER I – TORY II-A	1
Section I – Preliminary Statement Tory II-A-1 High-Power Runs	1
Section II – Neutronics	2
Section III – Aerothermodynamics, Tory II-A-1 Operation May 14, 1961 (Final)	12
Section IV – Controls	12
Section V – Engineering – Tory II-A Fuel Element Behavior	12
CHAPTER II – MATERIALS DEVELOPMENT AND PILOT PLANT ACTIVITIES	25
Section I – Process and Materials Development	25
Section II – General Chemistry	75
CHAPTER III – HOT BOX	93
CHAPTER IV – TORY II-C	102
Section I – Neutronics	102
Section II – Engineering	136
CHAPTER V – TORY III	201
Section I – Introduction	201
Section II – Engineering	201

TABLE OF CONVERSIONS

°C	°F	°C	°F	°C	°F
0	32	650	1202	1250	2282
50	122	700	1292	1300	2372
100	212	750	1382	1350	2402
150	302	800	1472	1400	2552
200	392	850	1562	1450	2642
250	482	900	1652	1500	2732
300	572	950	1742	1550	2822
350	662	1000	1832	1600	2912
400	752	1050	1922	1650	3002
450	842	1100	2012	1700	3092
500	932	1150	2102	1750	3182
550	1022	1200	2192	1800	3272
600	1112				

Btu/second-in^3	= 1.82 megawatts/foot^3
Btu/second	= 1.0548 kilowatts
Btu/hour-ft^2-°F	= 5.676×10^{-4} watt/cm^2-°C
Btu/lb-°F	= 1.0 calorie/g-°C
calorie	= 4.186 joules or watt-seconds
pound	= 454 grams
inch	= 2.54 centimeters
cubic foot	= 1728 cubic inches
cubic inch	= 16.387 cubic centimeters
megawatt-day	= 1.05 gram U^{235} fissioned (200 Mev per fission)
pound/ft^2	= 0.4882 gram/centimeter^2
pound/in^2	= 70.30 grams/centimeter^2
barn	= 10^{-24} centimeter^2
gravity (g)	= 980.7 cm/sec^2 = 32.17 ft/sec^2

MUL-14122

UCRL-6625

PLUTO QUARTERLY REPORT NO. 9

(July - September 1961)

Lawrence Radiation Laboratory, University of California
Livermore, California

CHAPTER I. TORY II-A

SECTION I. PRELIMINARY RESULTS TORY II-A-1

HIGH-POWER RUNS

The Tory II-A test program was brought to a successful conclusion with three test runs during late September and early October.

Operation of the reactor was graded in these three tests to reach three successively more rigorous sets of operation conditions: First, achievement of design core temperature and stress conditions with enhanced cooling of metal structure through lowered inlet air temperature; second, achievement of full design point conditions; and third, achievement of conditions substantially more severe than design point.

All objectives were reached without difficulty. In the final test the core was operated at the design temperature, and roughly twice the thermal stress levels of the successor reactor (Tory II-C) for a period of 90 seconds.

No evidence of damage to the reactor was observed in any of the tests, either from behavior during the tests or in effluent radioactivity levels, which were in agreement with the predicted emission of about 0.1% of all fission products.

Values of the principle operating parameters for the three final tests are listed below. These values are preliminary, and will undoubtedly shift to some extent as more data are reduced.

Date	Sept. 28	Oct. 5	Oct. 6
Power	150 Mw	185 Mw	175 Mw
Max core temp*	2280°F	2350°F	2500°F
Airflow rate	435 lb/sec	635 lb/sec	435 lb/sec
Inlet air temp	400°F	935°F	400°F

* "Maximum" here refers to the average temperature at the hottest axial station of the core.

SECRET RESTRICTED DATA

SECTION II. NEUTRONICS

FISSION FRAGMENT ESCAPE IN TORY II-A-1

Prediction of the hazard associated with the radioactive effluent of Tory II-A-1 presupposes some knowledge of the fractional fission fragment loss to the air stream. The mechanics whereby fission fragments may escape in the effluent include erosion, diffusion, and recoil. From past experiments on erosion of BeO at elevated temperatures by air containing water vapor(NAA-SR-4446), it was evident that erosion loss of fragments is negligible compared to recoil loss. Experiments conducted at LRL (UCRL-6148) indicate that diffusion losses may also be ignored in Tory II-A-1 in comparison with recoil loss. The recoil ranges in BeO of representative fission fragments as determined by the latter experiments are plotted versus mass number in Fig. I-1. The possibility of fuel depletion in and near the surface of the fuel tubes used for these experiments has been suggested. If this condition did exist, the actual recoil ranges in BeO would be greater than observed in the experiments, and the hazard, under certain conditions, could be greater than predicted. That any such fuel depletion was negligible may be shown qualitatively as follows: The ranges of representative light and heavy fission fragments (Mass Nos. 97 and 138) are 2.5 air-cm and 1.9 air-cm,respectively (The Science and Engineering of Nuclear Power – C. Goodman, Ed.). To a very good approximation, the air range varies linearly with mass number. [S. Katcoff et al: Phys. Rev. 74, 631 (1948)]. Further, the mass stopping power of various materials has been shown to be about the same for 4.66-Mev α rays as for the averaged fission products of U^{235}. [E. Segre and C. Wiegand: Phys. Rev. 70, 808 (1946)]. This suggests the use of the Bragg-Kleeman rule to get the approximate ranges in BeO of the U^{235} fission products from their known air ranges. From the Bragg-Kleeman rule:

$$R_1' = R_1 \rho_1 = 3.2 \times 10^{-4} \sqrt{A_1}\, R_{air} ,$$

where R_1 is the linear range of the particle in the stopping material of density ρ_1 (g/cm^3) and effective atomic weight A_1.

R_{air} is the linear range of the particle in air (15°C and 760 mm Hg) and R_1' is the range of the particle in grams per cm^2 of the material.

The ranges expected in BeO from this application of the Bragg-Kleeman rule are shown in Fig. I-1. Usually this rule gives ranges which are accurate

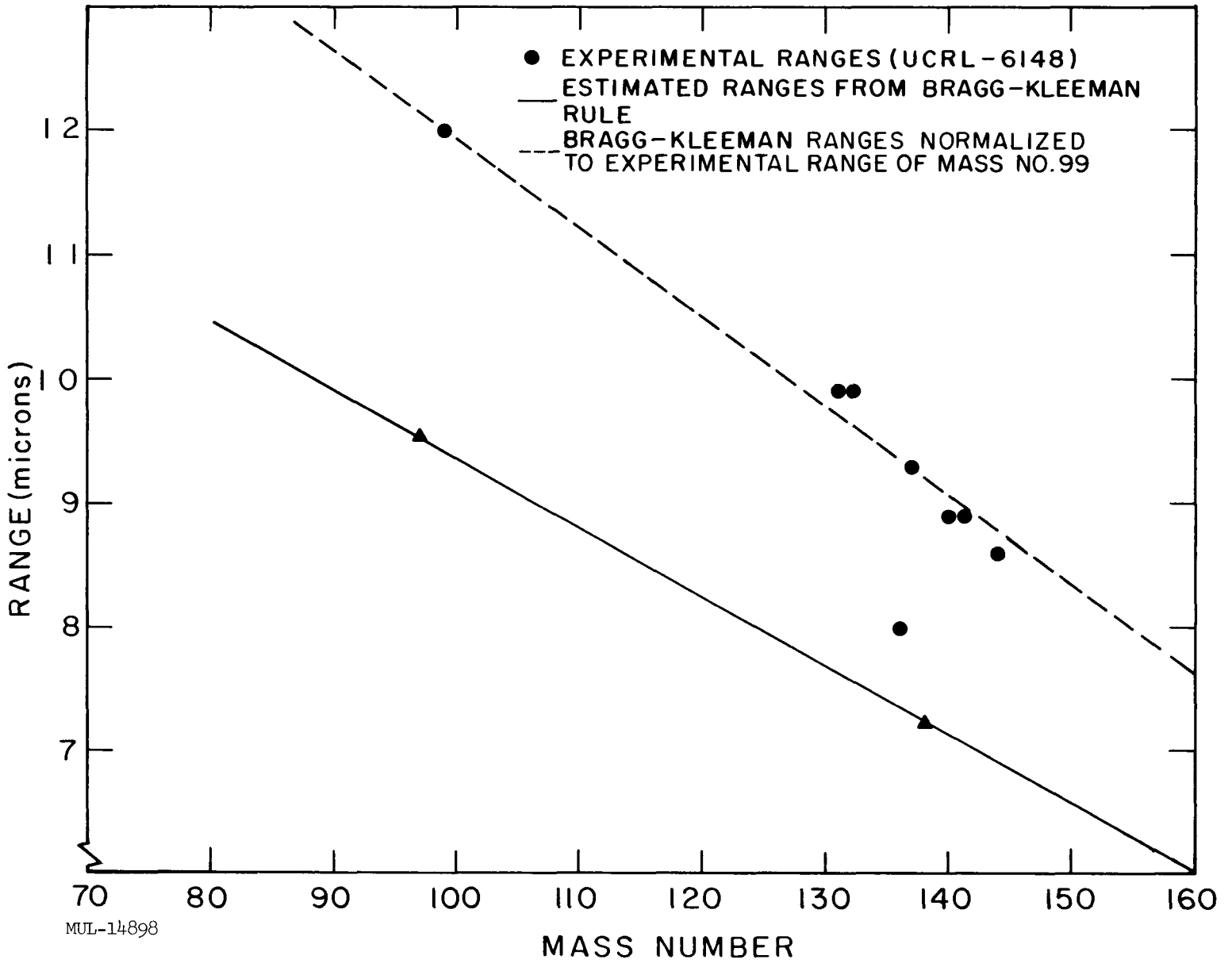

Fig. I-1. Range in BeO (99.6% theoretical density) of fission fragments from U^{235} thermal fission.

within ± 15%. However, it will be noted that the experimentally determined ranges exceed the predicted ranges by more than + 15%. From the nature of the experiments, fuel depletion would have evidenced itself in fewer recoils through the BeO surface, which would have been interpreted as shorter ranges. Thus, we conclude that fuel depletion was negligible. Perhaps stronger evidence of this fact is obtained by normalizing the Bragg-Kleeman ranges to the experimentally determined range for Mo^{99}. The excellent agreement (Fig. I-1) with the experimental ranges is significant. Had fuel depletion been present, one would expect the experimental range curve to have a greater slope than the Bragg-Kleeman range curve because of the shorter ranges of the heavier fragments.

Knowing the fission fragment ranges in BeO, the fraction of fragments which recoil into the air stream may be determined at once for any given fuel tube. For Tory II-A-1 fuel tubes this fraction is 0.0015. However, not all of the fragments entering the air stream will escape in the effluent. Those which have a favorable energy and direction will cross the intervening air gap to become imbedded in other parts of the fuel-tube inner wall. The probability of stopping in the air, once a fragment has entered it, has been calculated for different geometries. The results of that study, for the case in which we are interested (i.e., cyclindrical geometry), are presented in Fig. I-2. The product of the fraction escaping the inner BeO surface and the probability of being stopped in the air gives the fraction of fragments created by fission which stop in the air stream. This fraction has been used to do an integration over the length of the fuel-bearing region of Tory II-A-1, taking into account the axial variation of power density and air density. The axial power distribution, as deduced from the May 14, 1961, run (UCRL-6516, p. 11), was found to be 15 to 20% higher relative to the peak than had been predicted by Angie calculations. This refinement has been used in performing the present integration which gives the fission-fragment escape fraction for the entire reactor as 0.04% for the May 14 run, and 0.11% for the full power run.

Recognizing that the escape fraction varied with mass number of the fragments, an investigation was made to determine the effect of this variation. It was found that if one takes mass number 120 as being representative of the fractional gross fission product escape, the error in so doing is of the order of 5% at full power and diminishes with decreasing power. Hence, the range of mass number 120 in BeO (10.45 microns) leads to 0.15% as the fraction of

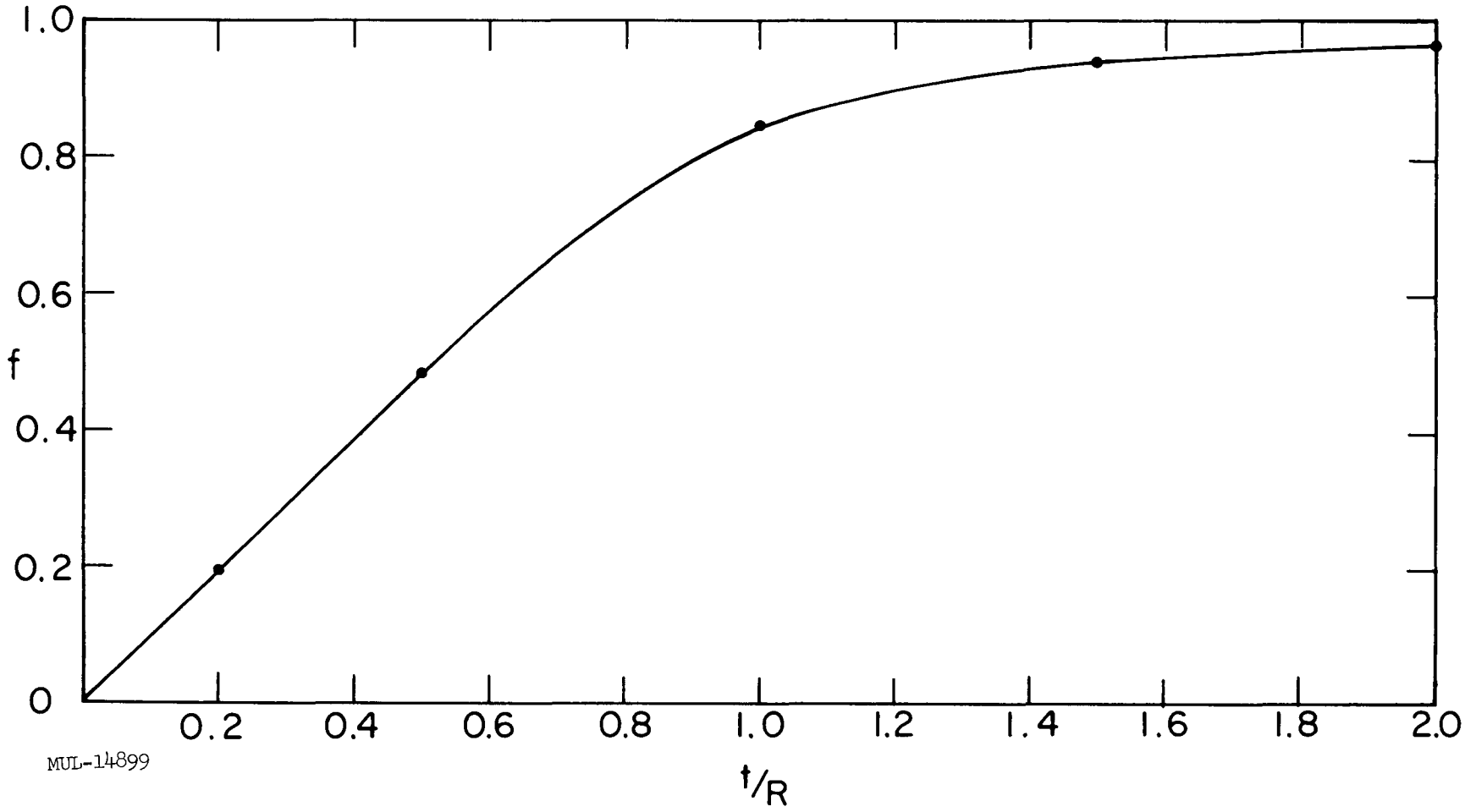

Fig. I-2. Fission fragment stoppage in air stream. f = the probability that a fission fragment which enters the air stream will be stopped in the air stream. t = inner diameter of fuel element. R = range of fission fragments in air stream.

fragments which penetrate the inner BeO surface of a Tory II-A-1 fuel tube, and dictates the fractional escape values given above. These values (0.04% at 50 Mw and 0.11% at 143 Mw) are considered to be accurate to within ±30% when one assigns reasonable uncertainties to the various factors which enter into the calculation (i.e., diffusion, erosion, range in air and BeO of fragments, power densities and air densities, etc.). At the present time, however, verification of the foregoing values cannot be expected from field measurements alone because of the many uncertainties involved in the field measurements themselves, not to mention those which relate to the interim history of the gross fission products which escaped. Field measurements may be expected to be uncertain by as much as a factor of ten. The inferred values listed above are submitted, therefore, as reliable estimates of the fission-fragment escape fraction from Tory II-A-1.

VOID STUDIES

In the application of neutronic diffusion codes to reactor design problems, it is often necessary to treat voids or gaps in the reactor. Diffusion codes are not directly applicable to such regions and it is necessary to use a scheme for transforming the problem into an equivalent one with no voids present. The Tory II-A reactor required a gap between core and reflector to allow the passage of a cooling air-stream. Other reactor voids are left by the removal of control rods, and are occasionally built into a reactor to permit experimental access to high neutron flux areas.

Experiments have been done with the LRL Spade facility involving simple critical assemblies with voids of various sizes and shapes in several reactor locations in order to test the accuracy of the calculational treatment. Experiments with reflected assemblies having gaps between core and reflector have been reported previously in UCRL-6036 and compared with various calculational treatments. These experiments have been extended to unreflected assemblies and include both one- and two-dimensional cases (Fig. I-3).

Three methods of treatment have been used and are briefly described in the following sections.

Method 1: Sufficient material from regions adjacent to the void is "smeared" into the void region to give a uniform relative density of 0.5 over the smeared and void regions.

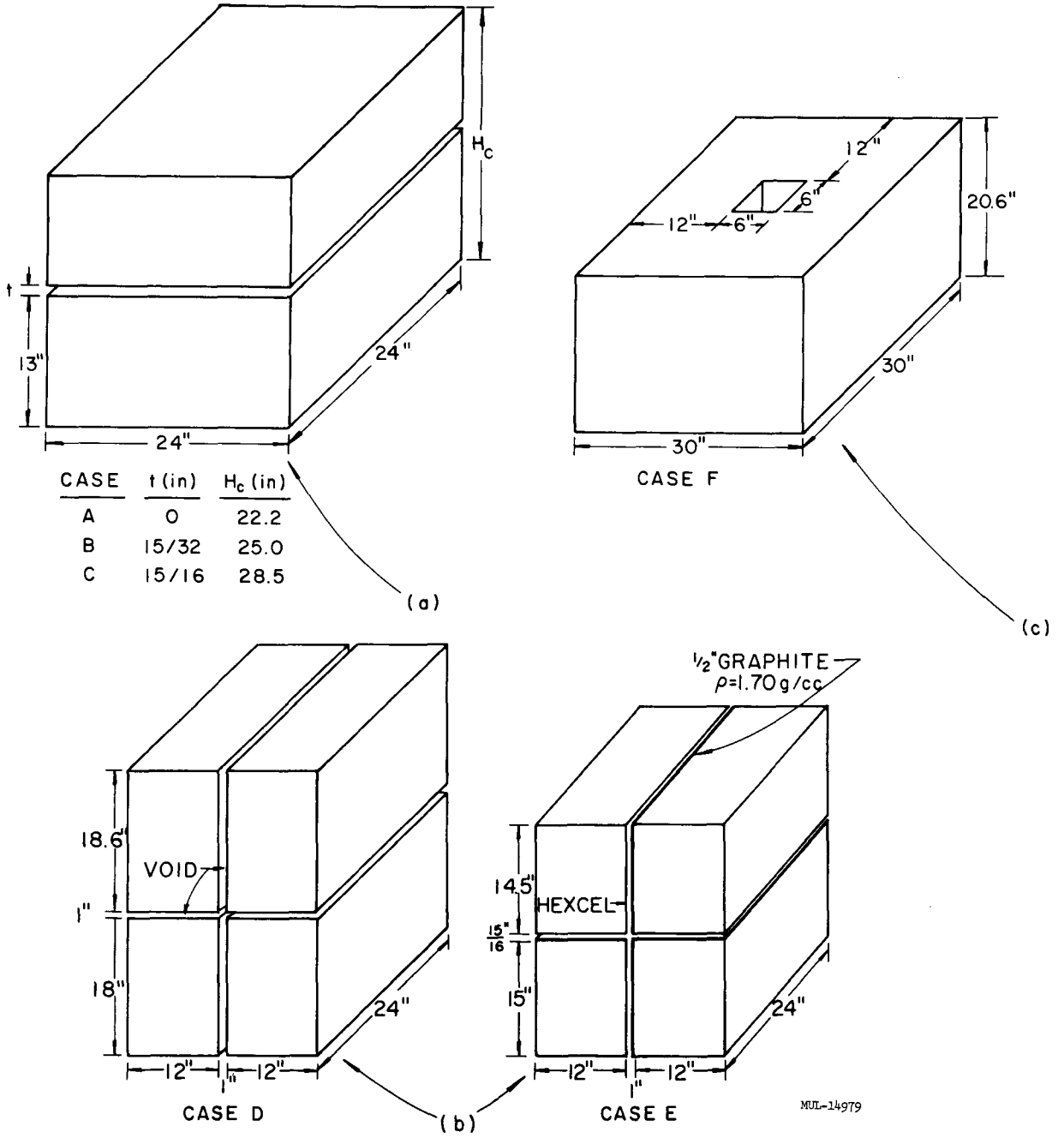

Fig. I-3. (a) Cases A, B, and C; one-dimensional Spade assembly; $BeO/U^{235} = 493$; 4-mil oralloy foil planes spaced 1 inch; $\rho_{BeO} = 2.86$ g/cc. (b) Cases D and E; two-dimensional assemblies, cruciform voids; $BeO/U^{235} = 493$; 4-mil oralloy planes spaced 1 inch; $\rho_{BeO} = 2.86$ g/cc. (c) Case F; two-dimensional assembly, square-well void; $BeO/U^{235} = 247$; 8-mil oralloy foil planes spaced 1 inch; $\rho_{BeO} = 2.86$ g/cc.

Method 2: The void region is filled with a "filler material" whose density is reduced in a series of problems over the range of densities allowable for diffusion calculations. A tangent is drawn to the curve at some relative density of filler material and extrapolated to zero relative density (see UCRL-6036 for details).

Method 3: A weighting curve has been developed from a series of Zoom calculations on a simple bare critical assembly where the density of all materials was reduced by 1% in each uniform zone in turn (Fig. I-4). This curve is then used to weight the void region according to its position in the assembly, and the density of the entire assembly is then reduced corresponding to a uniform smearing of materials into the weighted void region.

In the comparison of calculations with experiments, it is necessary to have a measure of the magnitude of the experimental effect as a standard. Diffusion calculations give k_{eff} as the answer, and it is, therefore, convenient to measure the experimental effect in reactivity units. Experimental critical assemblies have been constructed having the same details of assembly as the void assemblies, but without the void being present (Case A, Fig. I-3). These experiments serve as base problems from which to measure perturbation effects. A calculation of k_{eff} for the void assembly with the entire assembly represented as having uniformly full density minus k_{eff} for the base problem gives the effect of the void in terms of reactivity units. The void-worth calculated in this way for each assembly is listed in column 1 of Table I-1. Also listed in Table I-1 are the values of k_{eff} calculated by each of the three methods, and what percent of the reactivity effect is predicted by each.

Method 2 clearly provides the best results of the three treatments. Cases D and E, with a cruciform void and half-density graphite, are experiments relating to the Hot Box configuration.

The basis for the treatment of method 2 is that k_{eff} varies linearly with relative density of void filler over low densities (i.e., below $\rho/\rho_0 = 0.5$ with fueled BeO filler), and that deviation of the calculated k_{eff} from linearity at low densities is due to failure of the diffusion codes.

Referring to Fig. I-3, note the assembly labeled Case E. This experiment has the cruciform void of Case D, half-filled with graphite blocks, and simulates the presence of half-density graphite filling the void. k_{eff} was determined as a function of graphite filler density for both cases. The curves developed for both D and E are plotted in Fig. I-5. Also plotted is the k_{eff} for

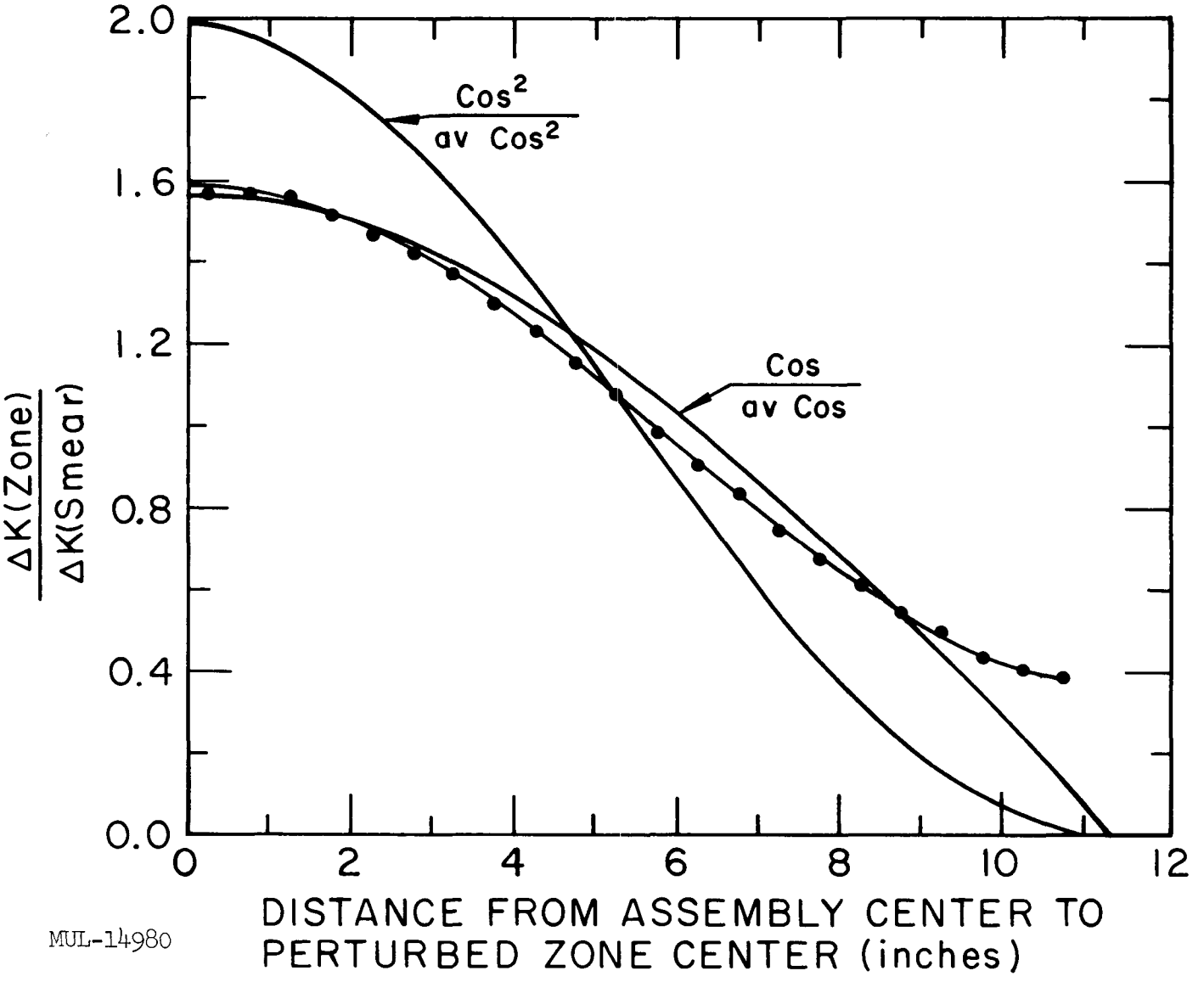

Fig. I-4. Spatial density variations; $BeO/U^{235} = 494$.

Table I-1. Results of Void Calculational Treatments.

Fig. I-3 case	k_{eff} Base problem	Void worth in reactivity units	Method 1		Method 2 (Extrapolated from $\rho/\rho_0 = 0.5$)		Method 3	
			k_{eff}	% predicted	k_{eff}	% predicted	k_{eff}	% predicted
	Z	Z	Z		Z		Z	
B	1.0026	0.0532	1.0070	91.7	0.9959	112.6	1.0170	72.9
	Z	Z	Z		Z		Z	
C	1.0026	0.1024	1.0226	80.5	1.0003	102.2	1.0376	65.8
	A	A	A				Z	
D	0.9976	0.1991	1.0426	77.4	--	--	1.0695	78.1
	A	A	A		A		Z	
F	1.0040	0.1546	1.0377	78.2	1.0163	92.0	1.0085	97.1

Z designates Zoom calculations.

A designates Angie calculations.

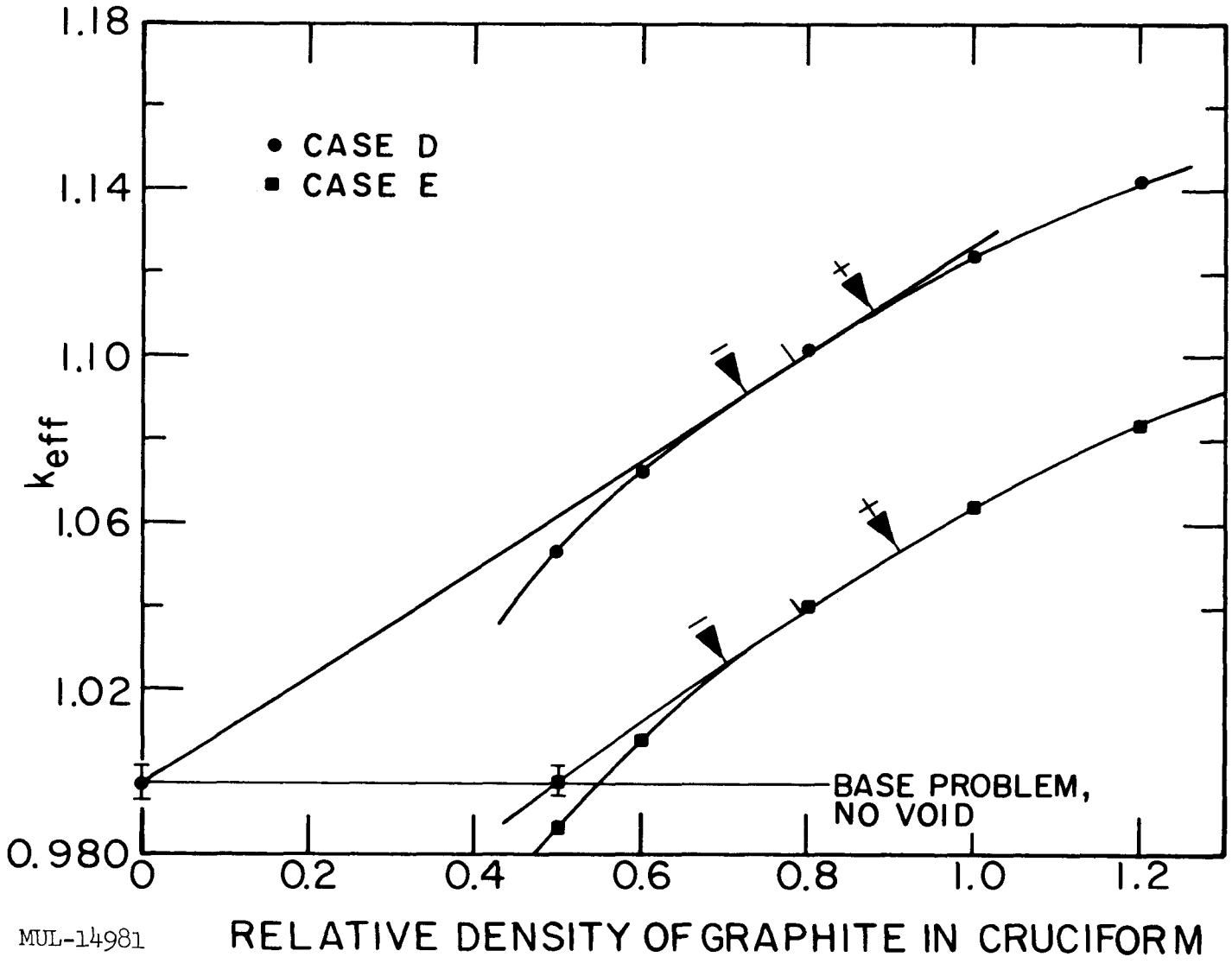

Fig. I-5. Angie calculations of cruciform void experiments (Cases D and E). Void filled with varying density graphite. BeO/U^{235} = 494. Case D – cruciform void, H = 37.6 in. Case E – cruciform of half-density graphite, H = 30-7/16 in.

the base problem with no void present and the experimental accuracy in critical height of ±0.1 inch is indicated. The tangents to the curves are drawn which extrapolated to the base problem k_{eff}, and the triangles indicate the range of relative densities whose tangent extrapolation would lie within the limits of experimental accuracy. The lower curve, developed for Case E, has the base problem k_{eff} plotted at $(\rho/\rho_0)_{graphite} = 0.5$ as the assembly was experimentally critical with half density graphite present.

The extrapolation point, determined for Case E, (i.e., $(\rho/\rho_0)_g = 0.78$) is then applied to Case D, and extrapolation yields a value of k_{eff} which is, within experimental accuracy, the k_{eff} of the base problem. Therefore, the assumption of linear variation of k_{eff} with fractional density of filler material at low filler density is verified.

SECTION III. AEROTHERMODYNAMICS, TORY II-A-1 OPERATION MAY 14, 1961 (FINAL)

The Aerothermodynamic aspects of this operation presented as preliminary data in Progress Report No. 8 can now be accepted as being final. During detailed data reduction, no significant discrepancies with regard to the preliminary results were noted.

SECTION IV. CONTROLS

During this period, the airflow control system has operated satisfactorily during several blowdown runs. Minor modifications and continuing preventive maintenance has been completed.

The power control system, in conjunction with the analog simulation of the reactor, has been used for additional operator training. Necessary minor modifications and preventive maintenance were performed. All control systems were in readiness for further high-power testing.

SECTION V. ENGINEERING – TORY II-A FUEL ELEMENT BEHAVIOR

TESTS TO DETERMINE FLEXURE STIFFNESS AND STRENGTH OF BeO TUBES

The specimens for this study were extruded, unfueled, BeO tubes having a hexagonal cross section containing a central circular hole. They were fabricated at LRL. The distance across flats of the hex was nominally 0.3 inch,

and the diameter of the central hole was nominally 0.2 inch. Densities were generally between 98 and 99 percent of theoretical.

The room-temperature dynamic modulus of each specimen was determined at a contractor's laboratory. Bend tests were conducted at room temperature, 1800, 2000, 2250, 2500, and 2700°F. Strain rate varied from specimen to specimen, but each bend test was conducted at a constant surface strain rate. In general, the strain rates used differed for different temperatures. In addition to these tests, curves of dynamic modulus versus temperature were obtained.

The bend tests had the following geometry:

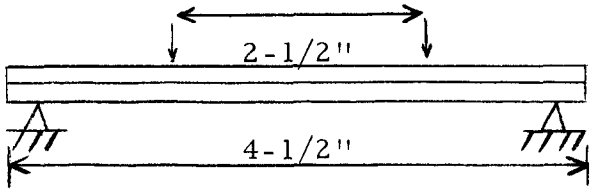

Deflection of the midpoint was measured with respect to points 1-1/4 inches on either side of the midpoint. These deflection measurements were converted to surface-strain values by assuming that the material behaves the same in tension as in compression.

The applied moment versus surface-strain curves obtained are shown in Fig. I-6.

The slopes of the stress-strain curves were determined from the slopes of the moment-surface strain curves assuming elastic behavior. Thus,

$$E = \frac{H}{2I}\left(\frac{\Delta M}{\Delta \epsilon_0}\right) ,$$

where E = apparent modulus of elasticity

H = height of cross section (distance across flats of hex)

I = moment of inertia of cross section about the neutral axis

$\left(\frac{\Delta M}{\Delta \epsilon_0}\right)$ = slope of moment-surface strain curve.

Similarly, the modulus of rupture was computed from the usual

$$\sigma = \frac{M_f H}{2I}$$

where M_f is the moment at fracture. The results obtained are given in Table I-2.

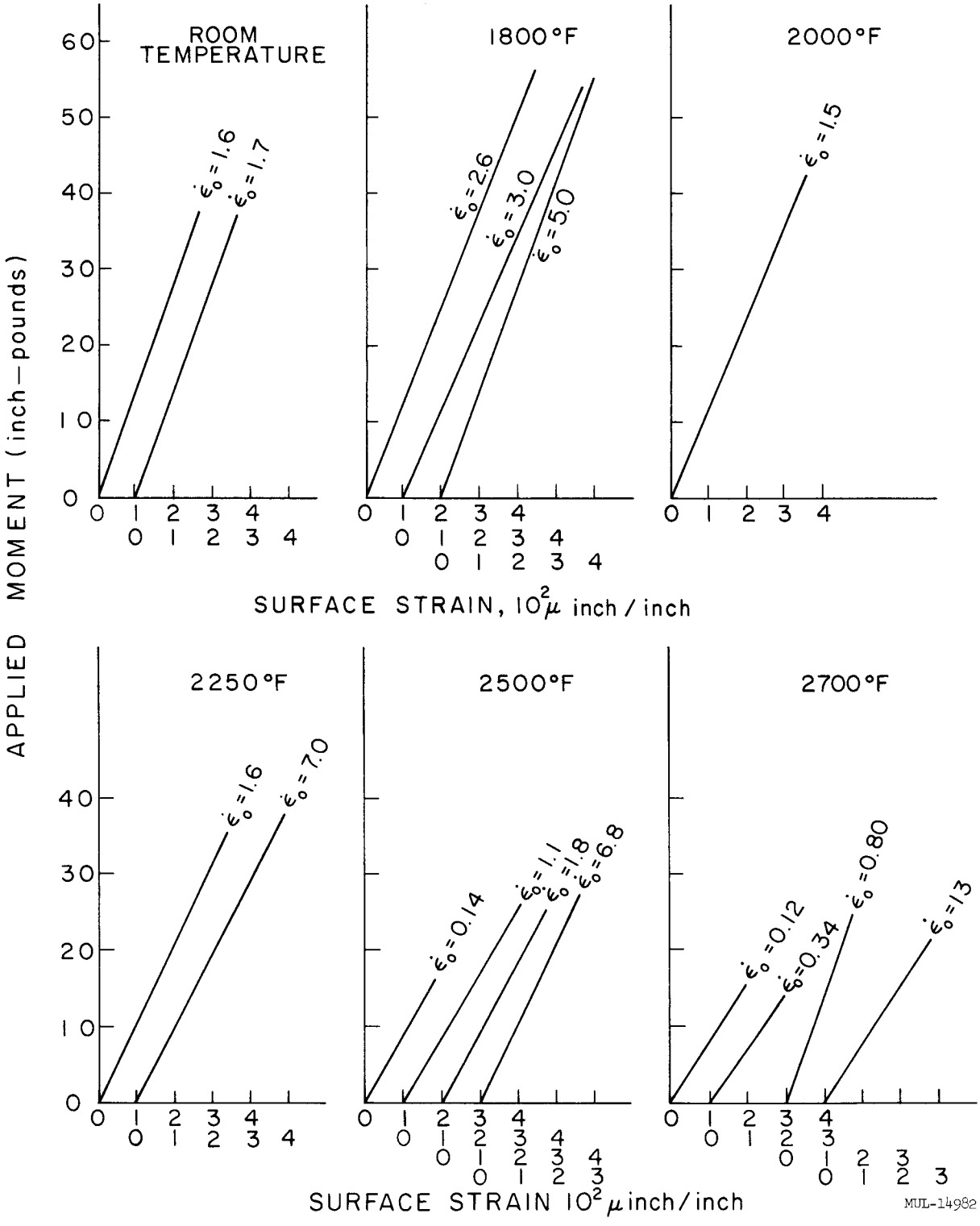

Fig. I-6. Moment — surface strain data from bend tests.

Table I-2. Bend Test Results.

Test temp °F	Surface strain rate (in./in./sec)	Room temp dynamic modulus (10^6 psi)	Apparent elastic modulus at test temp (10^6 psi)[a]	Modulus of rupture, psi	Specimen density (percent theoretical)	Moment of inertia of cross section about neutral axis (10^{-4} in^4)
R. T.	1.6	58.5	--	14,600	98.59	3.70
	1.7	57.5	--	14,900	98.54	3.72
1800	2.6	57.9	50.3	22,300	98.79	3.74
	3.0	55.0	43.3	21,200	98.57	3.80
	5.0	57.5	54.7	19,700	98.77	3.79
2000	1.5	58.6	50.3	17,000	98.77	3.70
2250	1.6	59.0	43.9	14,200	98.51	3.62
	7.0	59.0	39.6	15,400	98.92	3.62
2500	0.14	57.4	32.8	6,450	98.67	3.77
	1.1	60.0	34.3	10,500	98.47	3.61
	1.8	58.6	39.5	10,300	98.56	3.65
	6.8	55.3	39.7	10,700	98.65	3.82
2700	0.12	58.8	32.7	6,100	98.86	3.65
	0.34	56.5	26.4	5,550	98.82	3.77
	0.80	59.3	56.0[b]	9,300	98.87	3.70
	13	56.5	30.1	8,350	98.93	3.72

(a) Obtained from bend test.

(b) This result is questionable, see Fig. I-6.

Figure I-7 shows temperature dependence of the elastic modulus. The dynamic modulus curve shown is the average of results obtained from three specimens which were in excellent agreement with each other (the width of the scatter band was less than 0.03 units). This curve is also in reasonably good agreement with the results of other studies (UCRL-6457). Also shown are the apparent elastic moduli obtained from the bend tests in this study. The fact that the latter are lower than the dynamic moduli supports the idea that the behavior is not strictly elastic during the bend tests, in which the strain rates were considerably lower than the average strain rates in the dynamic tests.

The bend test results show no consistent relationship between modulus and strain rate. The fracture strengths tended to increase with strain rate, except at 1800°F where a decrease in strength with strain rate is observed.

Work was undertaken to examine the effect of high oxygen pressure and elevated temperature on class 10 (7.16 wt % UO_2) Tory II-A fuel tubes which contained residual thermally induced stresses.

Five tubes were prepared by placing them in an Argon atmosphere with a graphite rod inside the tube. The graphite rod was heated electrically, radiating power to the fuel tube, which in turn re-radiated to the cold vessel walls. Since heat is flowing radially out through the tube, a thermal stress pattern is set up. The magnitude of the stresses depends only on the quantity of heat radiated, which in turn depends only on tube temperature to the 4th power.

After heating the tubes to the temperature required to set up the desired stress level (about 3000°F), the tubes were held at temperature for about one hour in order to allow the stresses to relax by creep. When the power was turned off and the tubes returned to room temperature, reverse stresses of course appeared in the tubes. The magnitude of these reverse stresses was measured by x-ray diffraction methods.

Magnitudes were as follows:

Tube No. 3 - 7	KSI	Single crack - longitudinal	These cracks are believed to have appeared in handling after prestressing.
Tube No. 4 - 15	"	Single crack - longitudinal	
Tube No. 5 - 7	"		
Tube No. 6 - 8	"		
Tube No. 7 - 13	"	Two cracks - longitudinal	

Natural frequencies of the tubes were measured both before and after prestressing. There was no significant change in frequency.

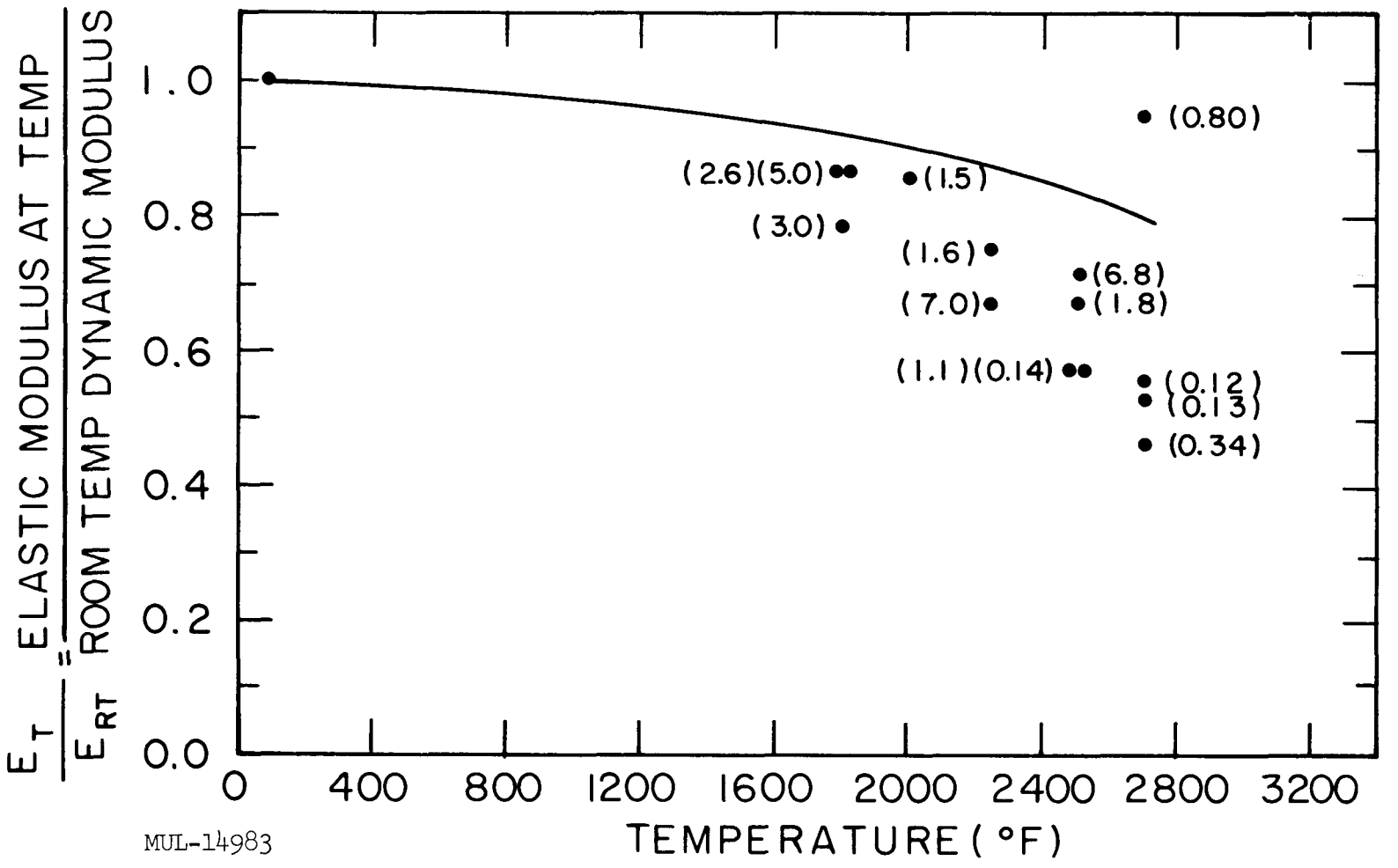

Fig. I-7. Temperature dependence of elastic modulus. The curve shows the dynamic modulus average of three specimens. The points show the bend test results; the numbers in parentheses are the surface strain rates in microinches/in./sec.

Figures I-8 and I-9 are photographic close-ups of tube 7 to show the cracks in detail.

Next the tubes were placed in a 65 psig oxygen and 2200°F environment. Numbers 4 and 5 were kept at temperature for 45 seconds. Numbers 6 and 7 were kept at temperature for 10 minutes.

Natural frequency was again measured. This time, tubes 4 and 5 again showed negligible frequency shift, but tubes 6 and 7 showed a decrease of about 400 cps in 9000 cps, or about 4-1/2%. Since modulus of elasticity varies as frequency squared, this implies about a 9% decrease in that quantity.

After the oxygen-furnace run, crazing was seen on the tubes. Tubes 6 and 7 (10-minute exposure) show much more crazing than tubes 4 and 5 which received 45 seconds at temperature. These are shown in Figs. I-10 through I-13.

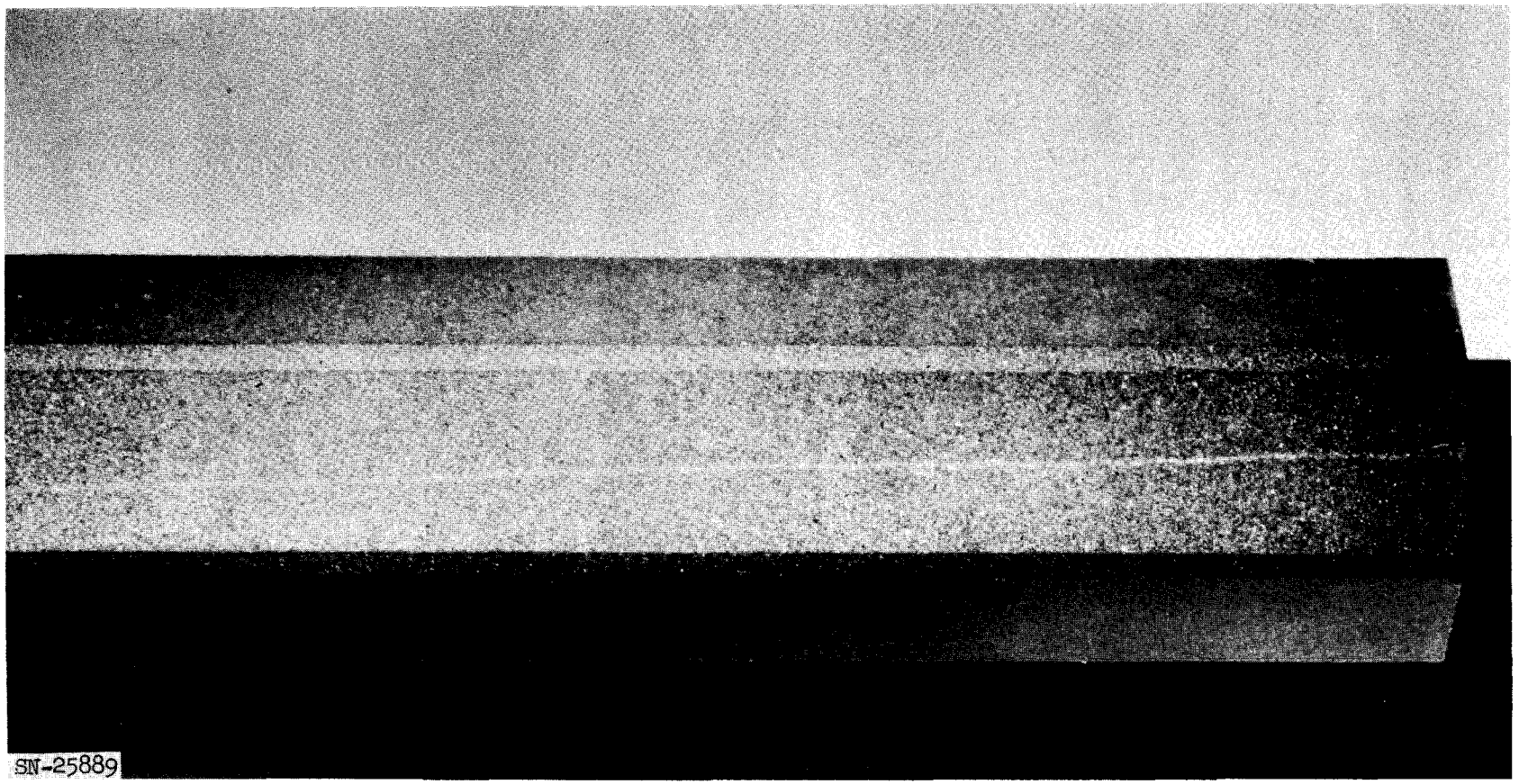

Fig. I-8. Closeup of tube 7 showing crack.

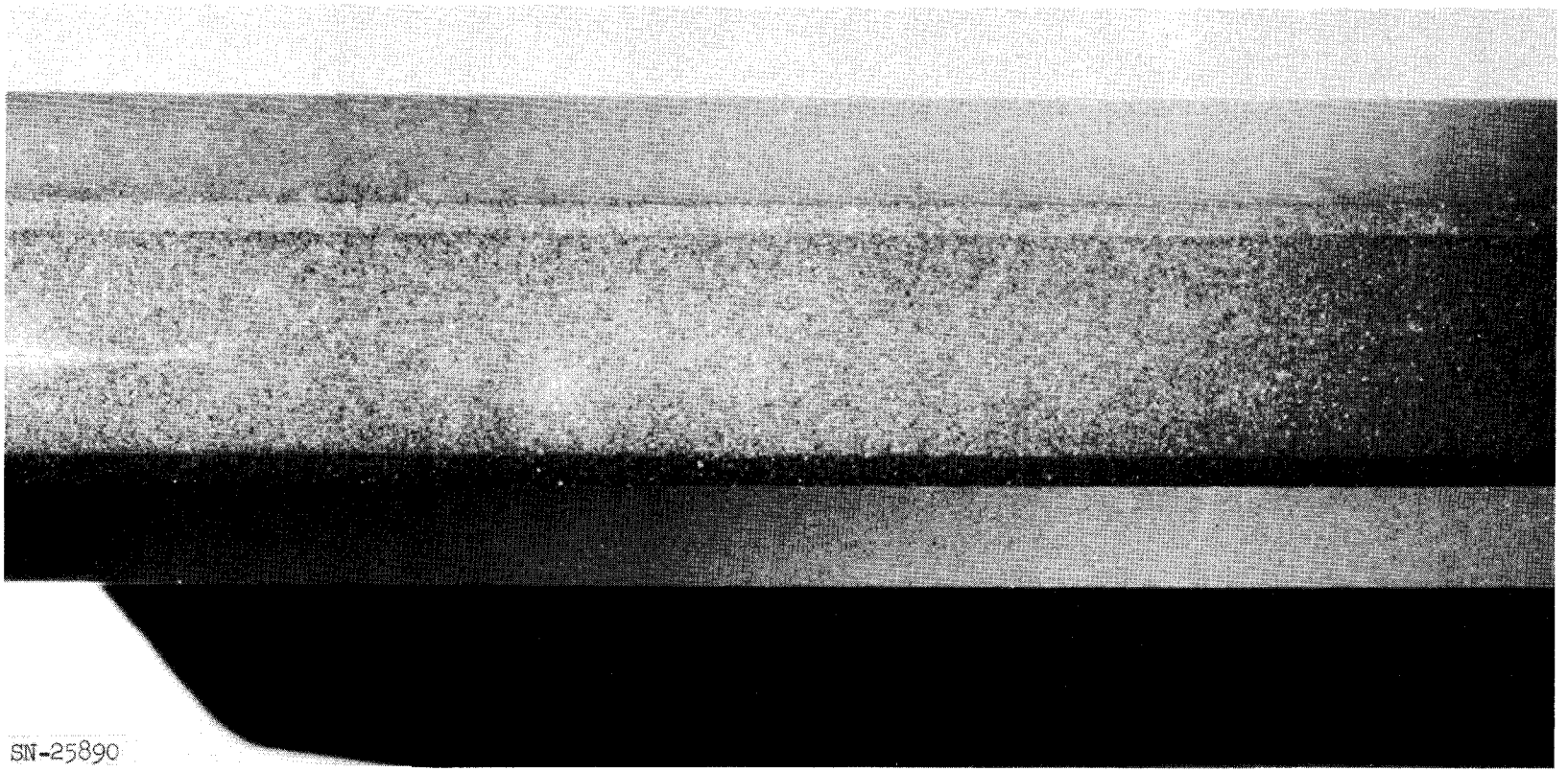

Fig. I-9. Closeup of tube 7 showing crack.

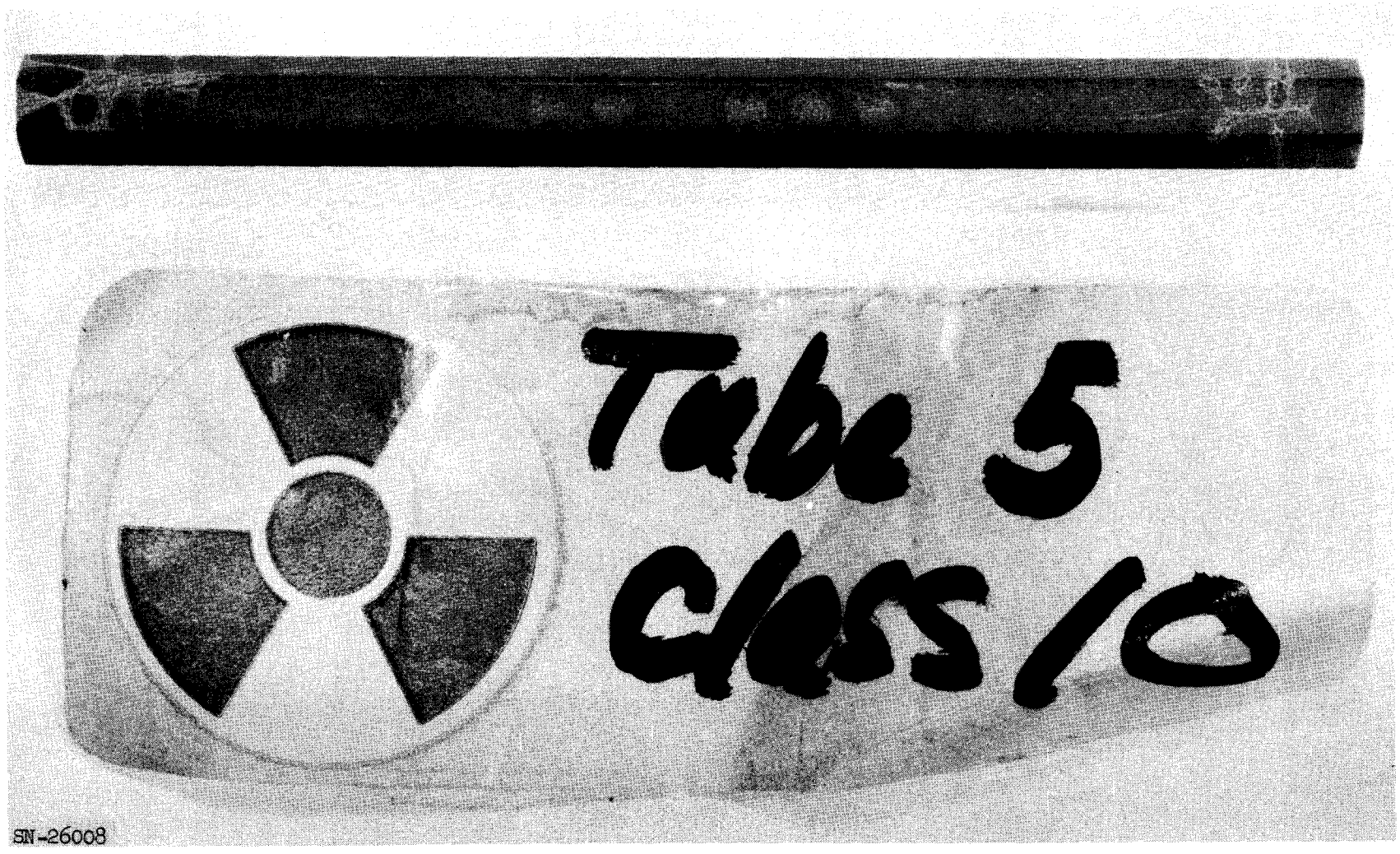

Fig. I-10. Crazing after oxygen-furnace run.

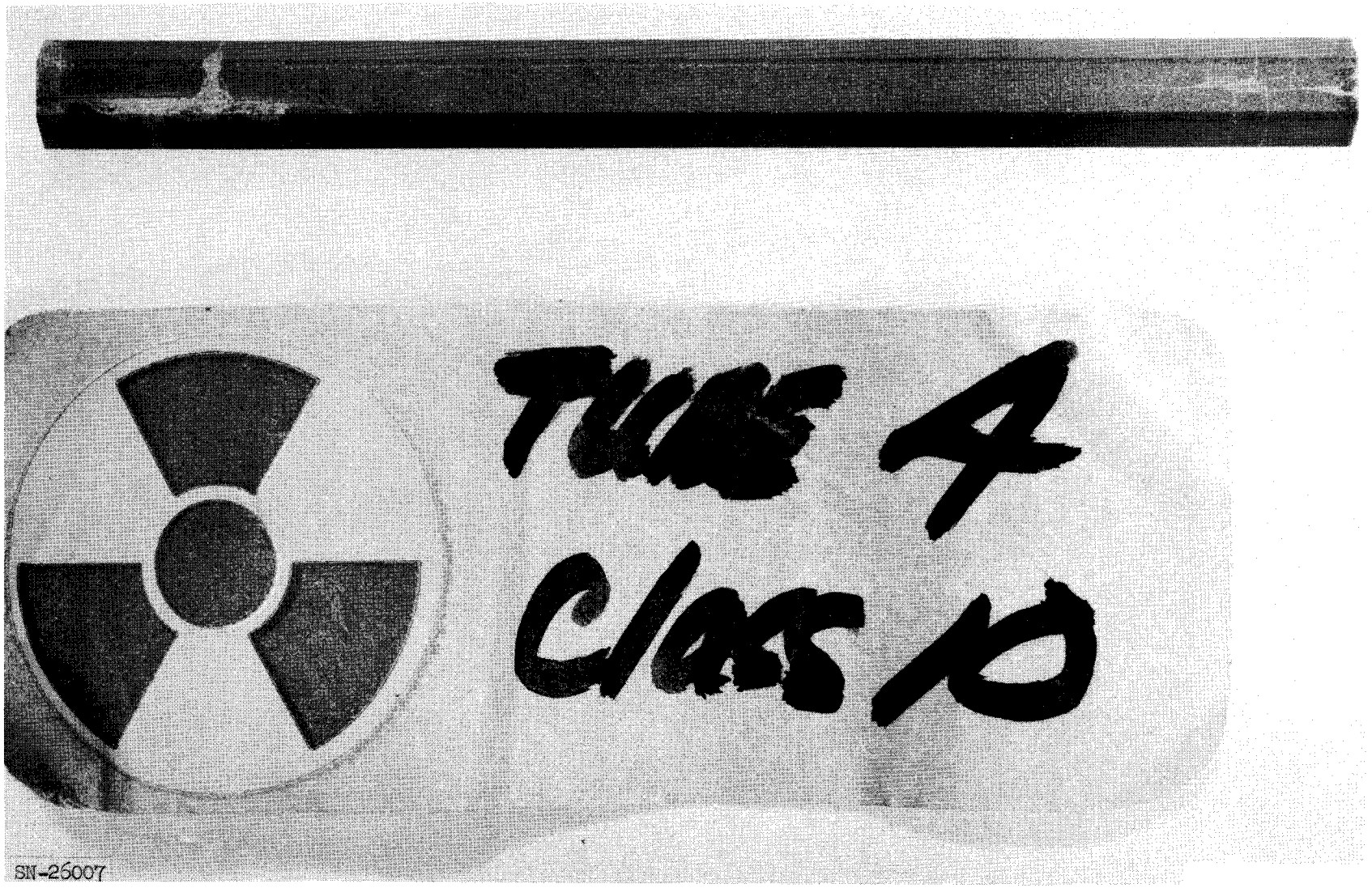

Fig. I-11. Crazing after oxygen-furnace run.

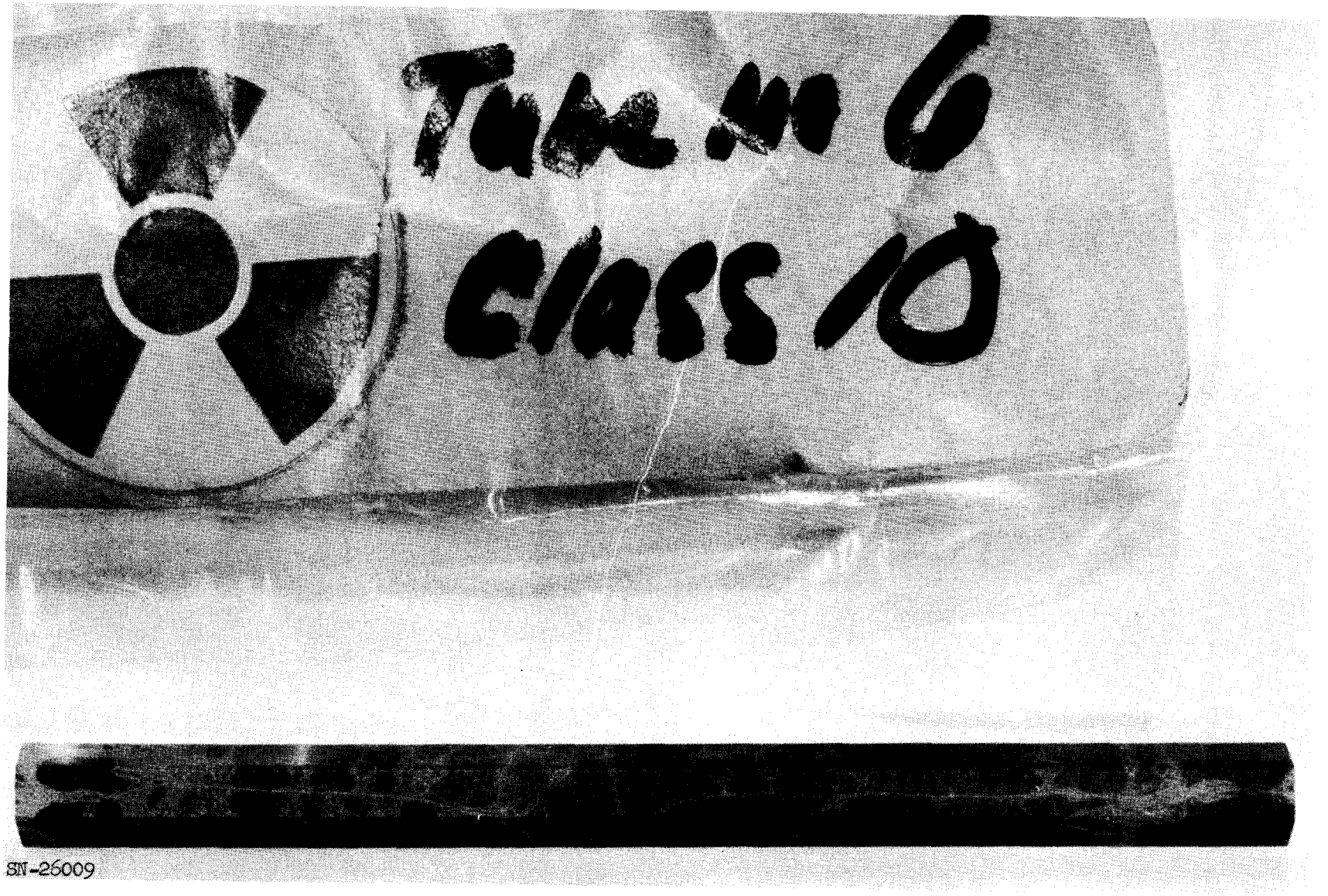

Fig. I-12. Crazing after oxygen-furnace run.

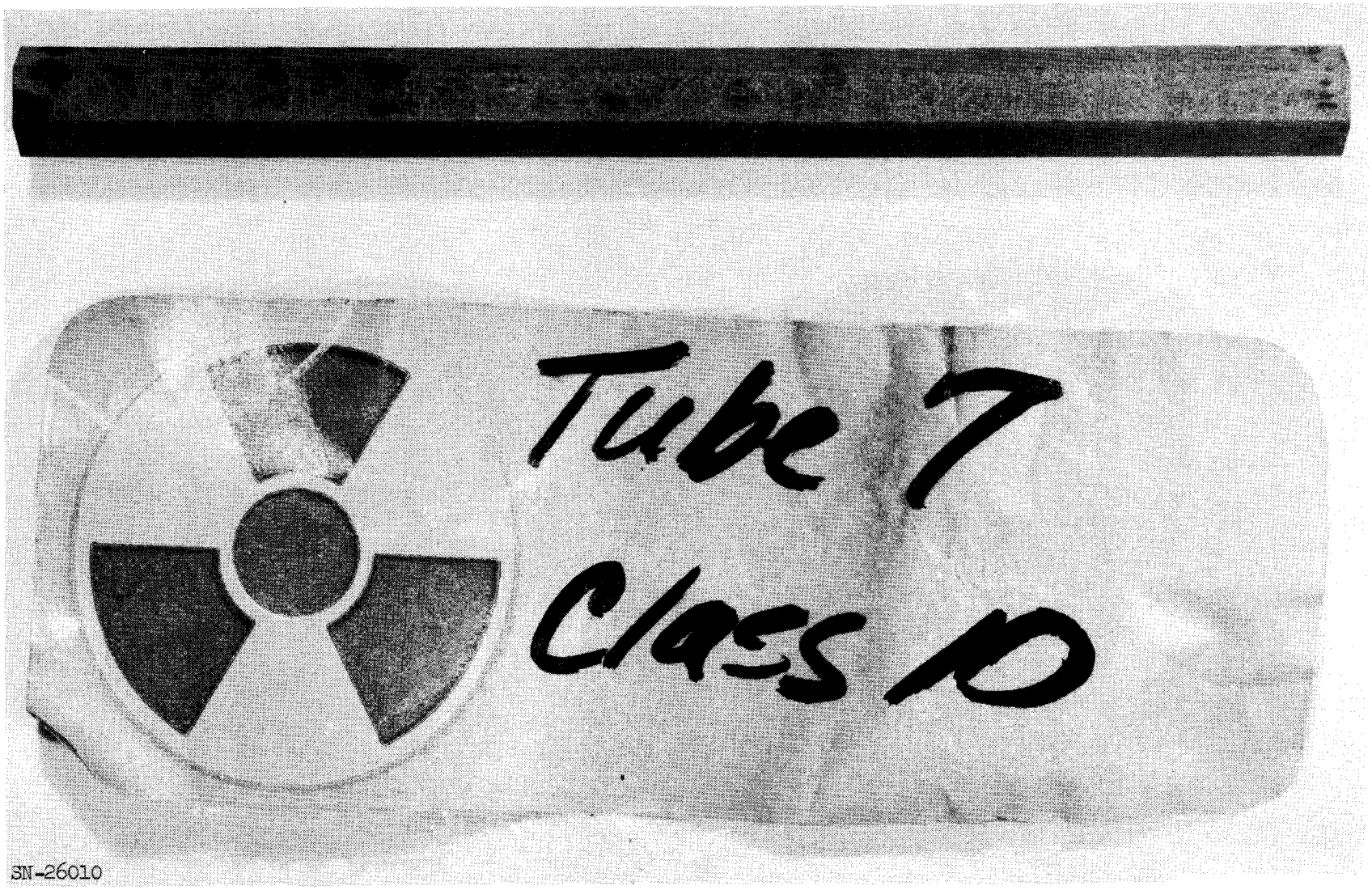

Fig. I-13. Crazing after oxygen-furnace run.

CHAPTER II. MATERIALS DEVELOPMENT AND PILOT PLANT ACTIVITIES

SECTION I. PROCESS AND MATERIALS DEVELOPMENT

I. MATERIAL STUDIES

A. Basic Studies

1. Growth of BeO Single Crystals

Beryllium oxide single crystals are being grown for a variety of high temperature physical and chemical property measurements. Crystals, 0.5 mm × 3.0 mm long, grown from molten lead monoxide and molten lead fluoride, were submitted to the x-ray laboratory for reactor irradiation and thermal expansion studies. In addition, 7 crystals were weighed, measured, and installed in high-pressure vessels for enlargement by hydrothermal techniques.

The choice of a suitable solvent for growing beryllium oxide crystals was made by trial and error with the help of previous experience. Mixtures of the appropriate salt with 20 m/o and 30 m/o beryllium oxide powder were contained in 50 cc platinum crucibles, heated 350°C above the melting point of the salt, soaked for two hours, then cooled at the rate of 4°C per hour. The following salts were tried: lithium chloride, beryllium fluoride, sodium tungstate, sodium and ammonium molybdate, potassium hydroxide, sodium fluoride, vanadium pentoxide, cuprous oxide, bismuth oxide, and sodium tetraborate. Crystals were obtained only from molten lead monoxide and lead fluoride. The crystal habit was acicular in which the long axis and the crystallographic c-axis coincided. The crystals are bounded by the principal $(10\bar{1}0)$ faces, capped by $(10\bar{1}1)$ faces and terminated by a (0001) face.

2. Electrical Properties of BeO

The electrical properties of BeO are being investigated as part of a general program to obtain transport data on this material at high temperatures. Measurements of the electrical conductivity to 1400°C on extruded samples, 97% of theoretical density, have shown BeO to be one of the best oxide insulators. The material possesses semiconducting properties above this temperature. Experiments have demonstrated that at 1400°C, 25% of the current is carried by ion migration, and suggest that all the conductivity will be ionic near the melting point.

Conductivity measurements were made on two samples using a two-probe dc voltmeter-ammeter method, and a two-probe ac bridge method. When log σ is plotted against 1/T, the curve shows a kink separating two straight lines. The critical temperature is determined to be 1022°C at 4.6×10^{-9} $(\text{ohm-cm})^{-1}$. Values of conductivity range from 10^{-15} $(\text{ohm-cm})^{-1}$ at 200°C to 10^{-5} $(\text{ohm-cm})^{-1}$ at 1600°C. The activation energy for the low temperature or extrinsic conduction region is calculated to be 20 Kcal/mole (0.87 ev). The activation energy for the high temperature or intrinsic conduction region is 58 Kcal/mole (2.5 ev).

The nature of the conduction process was studied using galvanic cells involving solid electrolytes. For example, if BeO were a pure electronic conductor, the emf of the cell,

Pt/Fe, FeO/BeO/Ni, NiO/Pt

would be zero. Actually the emf varied from 3 millivolts at 1100°C to 83 millivolts at 1400°C. An emf of 0.332 volts was measured using a pure ionic conductor such as ZrO_2 (with 15 mole percent CaO) in place of the BeO sample.

3. Oxidation of Uranium Monocarbide

The kinetics of oxidation of UC in the range from about 300°C to 380°C fit a first-order rate equation. Since the particles completely disrupt on oxidation, the rate is evidently dependent on the amount of material unreacted.

The reaction product, however, has not been established with any certainty. At first UO_3 and free carbon were thought to be the products since a black material was noticed in the orange-brown residue. Chemical analysis discounted any formation of free carbon.

In a few preliminary runs the residue was identified as UO_3 by x ray. However, all subsequent runs have been amorphous to x rays. The black material was separated from the orange-brown residue and identified as hexagonal U_3O_8 by x ray.

Two immediate problems are then encountered. First, identification of the amorphous phase, and second, inquiry into the reason for the presence of two phases in the oxidation product.

The oxidation residue, both amorphous material and U_3O_8, was heated to over 800°C. The recorded weight loss was consistent with the amorphous phase being U_2O_7 rather than UO_3. Infrared spectra have shown an

absorption peak at 1360-1380 cm^{-1}, while a peak is reported for U_2O_7 at 1390-1410 cm^{-1}. UO_3 has no peak in this region. The weight gain on oxidation is also indicative of the formation of U_2O_7.

A possible explanation of the two-phase residue is that the amorphous material is unstable at the temperature of oxidation and it slowly decomposes to U_3O_8. This change should be governed by the partial pressure of oxygen.

4. Preferred Orientation in BeO Tubes

Introduction

The preferred orientation of extruded BeO has been observed in sintered specimens for some time. Questions arose as to when this preferred orientation developed and what role it plays in the properties of the sintered tube. The work described in this report is an attempt to answer the former question; subsequent studies will attempt to answer the latter. From the results of this work, it appears as if the BeO powder is preferentially oriented as it exits from the extruder and that this orientation becomes more marked as one increases the sintering temperature and time.

Definition of the Random State

If the BeO crystallographic orientation were such that discrete BeO particles were oriented equally in all possible directions, then this could be defined as a state of random orientation, or simply randomness. Such a state would serve adequately as a reference line from which departures from randomness could be measured. The achievement of such a state is always open to debate. The procedure used to approximate a state of randomness in material to be x-rayed is to prepare a powder of the material. In this manner the ratio of pairs of peak intensities of specific crystallographic directions could be used as standards of randomness. Similar material in various stages of departure from randomness could then be compared with the standard, a measure of this departure determined, and tests of the significance of the departure from randomness made.

In this study the intensity of the reflections from the (002) and (100) crystallographic directions was measured. The selection of these directions was based on prior knowledge that the BeO in sintered tubes has a preferred orientation with the optic axis of many grains essentially parallel to the extrusion axis of the tube. If the outer flat surface of a tube with such an assumed orientation were x-rayed, the ratio of the (002) reflection relative

to the (100) reflection would be lower than the same ratio in the random state (r_s). On the other hand, if the cross section of the same tube were x-rayed, one would expect the ratio of the intensity of the (002) reflection to the intensity of the (100) reflection to be greater than r_s. With this as a background the following experiments were run.

Experimental Procedure

A series of BeO hexagonal tubes varying in fuel concentration from 0.0 to 5.0 w/o UO_2, and subjected to different sintering temperatures and times at temperature was analyzed by x-ray diffraction. Samples were analyzed just after extrusion, after drying, after starch burning, and after sintering. The tubes were sintered at each of the following temperatures for 0.5, 1, 2, 4, and 8 hours: 1500°C, 1600°C, 1700°C, and 1800°C. Standards of reference for randomness were obtained from powdered samples of starch-burned fueled and unfueled tubes, and a pulverized BeO tube after sintering at 1800°C. The ratio of the intensities of the (002) and (100) crystallographic reflections from these powders are listed in Table II-1. These different estimates were averaged and the ratio of 0.71 used as the random state reference ratio r_s.

The sintering was done in a hydrogen atmosphere with the time to temperature programmed so that all sintering conditions could be duplicated if the need arose. The hexagonal tubes used in this work were approximately one-inch long, 3/8-inch across the flats, and about 1/16-inch wall thickness.

The x-ray diffraction was carried out on a diffractometer using a proportional counter detector. Copper K radiation was used with a tube potential of 35 kv and a filament current of 20 ma. The goniometer was operated at a scan rate of two degrees per minute in the range 35° to 45° 2θ, allowing a recording of the (100) and (002) reflections of BeO. Preliminary work determined that reproducibility of the measure was high from sample to sample, sides on the same sample, and sites on a face. Subsequently, each hexagonal tube studied was x-rayed on only one flat face and on a cross-sectional surface.

After x-raying the tubes, measures of the intensity of the (100) and (002) reflections were made and the ratio of the intensities computed. These (002)/(100) estimates were then compared to the standard reference of 0.71 to determine the degree of departure from randomness.

Table II-1. Comparison of Observed (002/100) Peak Heights of Presintered, Starch Burned, Extruded BeO, BeO-UO_2 Tubes with Random (002/100) Peak Heights of Powdered BeO, BeO-UO_2.

w/o UO_2	Random or expected ratio × 100	Observed data	
		Flat	X-section
0 (pure BeO)	67	59,61	93,80
0.5	67	61,56	85,75
1.0	68	57,61	71,65
1.5	75	64,57	81,74
2.0	67	60,62	78,80
2.5	74	58,58	83,91
3.0	77	No data	68,71
3.5	66	62,65	79,79
4.0	82	59,59	79,87
4.5	70	55,58	85,95
5.0	No data at present	61,59	75,90
	Average 71.	60[a]	80[b]
	Standard deviation ± 5.	±3	±8

[a, b] A comparison of the arithmetic averages of the ratios computed across the flat and across the cross section, assuming homogeneous variances, indicates a significant difference between the random or expected powder patterns and the observed means reported above.

Results

Starch Burned Tubes. The x-ray data for the starch-burned tubes are summarized in Table II-2. The starch-burned data indicate a significant departure from the random state. A ratio of 0.60 for a side surface and 0.75 for a cross section was obtained on a BeO tube which had just been extruded and not starch burned. These ratios are essentially the same as those of the starch-burned tubes.

Sintered Tubes. The data for the pure BeO, 0.5, 2.5, and 4.5 w/o UO_2 sintered tubes are summarized in Table II-3. Here it can be seen that, in general, as one increases the sintering temperature, the preferred orientation increases. That is, the (002) / (100) ratio from the face of the sintered tubes as well as on the cross section of the tube departs more and more from the random state. The ratio obtained from the side surface is less than r_s, that from the cross section is greater. Furthermore, as the time at any one sintering temperature is increased, the orientation becomes more preferred.

Table II-2. Intensity of (002/100) Reflections on Starch-Burned Tubes. (Average of two determinations each concentration.)

UO_2 Concentration	Side	Cross section
0.0	0.60	0.86
0.5	0.59	0.80
1.0	0.59	0.68
1.5	0.61	0.78
2.0	0.61	0.80
2.5	0.58	0.87
3.0	--	0.70
3.5	0.63	0.79
4.0	0.59	0.83
4.5	0.57	0.90
5.0	0.60	0.83

Conclusion

There is no question that the material leaving the extruder is preferentially oriented with the c or crystallographic axis of the BeO aligned parallel to the extrusion axis.

Sintering of these tubes does not cause the preferred orientation, but merely enhances it by encouraging the grain to grow parallel to the extrusion axis.

5. BeO "Inversion"

The observation that negative crystals (euhedral voids) in BeO that had been heated to 2200°C no longer were aligned with the observed optic axis of the matrix grain was interpreted as indicating that the matrix grain had undergone reorientation without grain boundary movement, possibly as a result of crystal inversion. Single crystals of BeO grown from lead fluoride melt were heated on tungsten and on molybdenum strips in the x-ray vacuum camera furnace and also in a BeO crucible enclosed in tungsten in a hydrogen atmosphere.

No valid change in the x-ray pattern has been noted for any sample up to this temperature. Diffraction peaks which show splitting at the high temperatures can usually be eliminated by adjusting the sample position.

Above 2100°C crystals tended to volatilize in the x-ray camera. All crystals began as water-clear, optically perfect crystals, but emerged with severely corroded surfaces, cracks, and many fine inclusions (presumably voids). All had become polycrystalline with at least three domains

Table II-3. Intensity of (002/100) Reflections in BeO, 0.5, 2.5, and 4.5 w/o UO_2 in BeO Extruded Hexagonal Tubes as a Function of Sintering Temperature (T) and Time at Temperature (t). (A) Side of Tubes. (B) X-Section of Tubes.

A

	t(hours)						t				
T=1500°C	1/2	1	2	4	8	T=1600°C	1/2	1	2	4	8
BeO	--	0.49	--	0.39	0.45		0.42	0.45	0.45	0.28	0.32
0.5	0.54	0.52	0.53	0.43	0.47		0.47	0.42	0.45	0.36	0.26
2.5	0.57	0.52	0.50	0.41	0.47		0.42	0.44	0.47	0.27	0.39
4.5	0.62	0.53	0.54	0.43	0.47		0.46	0.45	0.45	0.45	0.39
T=1700°C						T=1800°C		45 min			
BeO	0.29	0.33	0.32	0.14	0.02		0.24	0.17	0.15	0.31	0.03
0.5	0.36	0.27	0.22	0.18	0.12		0.14	0.13	0.13	0.07	0.04
2.5	0.49	0.29	0.32	0.22	0.12		0.25	0.24	0.14	0.11	0.11
4.5	0.44	0.38	0.31	0.21	0.17		0.24	0.18	0.12	0.18	0.19

B

T=1500°C	1/2	1	2	4	8	T=1600°C	1/2	1	2	4	8
BeO	--	1.21	--	1.41	1.39		1.70	1.69	1.38	3.68	3.00
0.5	1.09	0.58	1.03	1.43	1.18		1.67	1.09	1.43	3.91	2.67
2.5	0.92	0.82	1.00	0.94	1.38		1.26	1.20	0.94	0.75	2.78
4.5	1.12	0.91	0.86	1.57	1.11		1.32	1.06	0.96	1.35	1.75
T=1700°C						T=1800°C					
BeO	1.21	5.75	3.35	10.22	23.50		11.83	2.60	24.33	52.50	19.75
0.5	2.50	4.50	2.76	14.29	8.27		7.14	10.00	6.67	18.50	4.79
2.5	1.64	2.29	3.00	4.00	10.00		3.75	4.76	8.00	5.33	8.50
4.5	2.50	1.57	2.43	7.20	6.00		4.25	5.50	4.50	8.14	6.30

having different optic orientations. Exact orientation could not be determined because of the inclusions. Orientations did not appear to be systematic and no twinning law was immediately evident. Experiments will be continued on whiskers condensed from the vapor in the hope of overcoming the inclusion difficulty. The experiment should also resolve the question as to whether the inclusions are associated with impurities introduced by the lead fluoride melt.

A sample of BeO single crystals has been irradiated in the Livermore Pool Type Reactor (LPTR) to the level of 10^{19} n/cm^2. This level should cause significant changes in the BeO lattice and it is hoped that comparison of single-crystal data for both irradiated and unirradiated crystals will indicate the defects developed. An untreated BeO single crystal is now being used to collect a standard set of x-ray intensity data for comparison with treated crystals.

Three interesting observations have been made. First, as samples are being heated and before they reach incandescence, a distinct bluish-violet flash is observed. It has not yet been determined if this thermoluminescence is the release of energy absorbed from the x-ray beam during the running of a reference room temperature pattern before breakup. Second, around 1650°C to 1700°C the profiles of some of the diffraction lines develop many sharp spikes which are quite often attributable to growth of grains. This temperature does correspond to onset of grain growth during sintering of BeO.

Third, the BeO appears to react with the tungsten above 1800°C. Both in vacuum and in nitrogen, a white fluffy growth appears on the surface of the sample and continues growing until it falls off the narrow sample. Then the process repeats until the BeO is all reacted. Although it has been noted to occur as low as 1800°C, it usually begins above 2000°C. In nitrogen the onset of growth appears inhibited but not prevented. One sample was held around 2200°C for 30 minutes before the growth commenced, but after 5 more minutes no BeO remained. The room temperature x-ray pattern of the growth indicates that it is WO_3 and suggests that the tungsten is acting as a getter for the oxygen from the BeO.

6. X-Ray Diffraction: Cr_2O_3-$2UO_3$

The x-ray study of the phase Cr_2O_3-$2UO_3$ has been completed up to the actual determination of the crystal structure. The preliminary set of precession patterns show the following extinctions: hkO when $h + k = 2n + 1$, hOℓ when $\ell = 2n$, and Okℓ when $\ell = 2n + 1$. These extinctions indicate the

unique space group D_{2h}^{14} - Pbcn. The specific gravity of the crystals is greater than 3.3, which suggests either one molecule per unit cell, specific gravity 4.18, or two molecules, specific gravity 8.36. One molecule per unit cell would require that the ninth oxygen be divided statistically on 2-, 4-, or 8-fold lattice sites because no odd-fold sites are allowed in the space group. Two molecules per unit cell will not require a statistical distribution of any atoms. Also, calculating the expected volume of two molecules using $133A^3$ for each oxygen atom, $3.1A^3$ for each uranium, and $1.4A^3$ for each chromium atom, gives a value of $261.4A^3$ compared with the actual cell volume of $288.0A^3$. The comparison is good considering the effective atom volumes are based on the close packing of spheres, a feature which exists only in the simplest of crystal structures.

High-temperature x-ray diffraction studies failed to detect any phase inversion up to 1400°C. The single crystals used in the x-ray study came from one high-temperature run which was left at 1200°C for 3 days. Many crystals were twinned, giving a pseudo-hexagonal habit, but no hexagonal phase has yet been observed.

Table II-4 lists the x-ray and physical properties of the phase. Table II-5 gives the indexed x-ray powder pattern of the compound.

Table II-4. Physical Properties of $Cr_2O_3 \cdot 2UO_3$.

a_o =	4.857 ± 10A
b_o =	11.692 ± 10A
c_o =	5.074 ± 10A
1/ =	$288.0A^3$
z =	2
calc. =	8.36 g/cc
N_x >	1.79
N_y >	1.79
N_z >	1.79

Color: golden brown

B. Fuel Retention and Stability

LRL has been attempting to develop a mix more stable than existing BeO-UO_2 and BeO-UO_2-ZrO_2, yet with good high-temperature properties (low fuel loss, low creep). Various solid solutions with UO_2 such as zirconia, ceria, etc., are being studied. One approach used by others has been to replace some of the yttria in a standard Y_2O_3-UO_2 mix in the hopes of avoiding

Table II-5. X-Ray Powder Pattern for $Cr_2O_3 \cdot 2UO_3$.

hkℓ	$Sin^2\theta$ calc.	$Sin^2\theta$ obs.	I	hkℓ	$Sin^2\theta$ calc.	$Sin^2\theta$ obs.	I
020	0.0174	0.0174	vw	042	0.1620	0.1614	w
110	0.0295	0.0294	w	240	0.1700	0.1686	w
021	0.0405	0.0408	vw	202	0.1931	0.1930	s
111	0.0526	0.0532	vs	241	0.1932		
130	0.0642	0.0643	s	222	0.2105	0.2105	vw
040	0.0694	0.0687	w	023	0.2255	0.2259	m
131	0.0873	0.0874	vw	310	0.2307	0.2308	vw
041	0.0926	0.0925	m			0.2347	vw
002	0.0925			113	0.2377	0.2384	m
200	0.1006	0.1006	mw	170	0.2378		
022	0.1099	0.1108	w	062	0.2488	0.2474	w
220	0.1180	0.1179	w	311	0.2538	0.2535	m
112	0.1220	0.1225	w	260	0.2568	0.2579	m
150	0.1337	0.1323	m	330	0.2654	0.2640	m
221	0.1411	0.1412	ms	133	0.2724	0.2735	vw
060	0.1562	0.1567	s	043	0.2776	0.2778	m
132	0.1567			080	0.2778		
151	0.1568			081	0.3009	0.2974	mw

the low-temperature Y_2O_3-BeO eutectic. LRL has also made mixes of UO_2-ZrO_2-Y_2O_3 and has begun to test them. Preliminary results are interesting and are reported below.

Tests were performed as follows.

1. Stable Fuel Mixtures

a. UO_2-Y_2O_3-ZrO_2

A UO_2-Y_2O_3-ZrO_2 composition using another organization's recipe was made to study its stability and fuel loss characteristics. This material has the following composition with the raw materials being blended by wet mixing:

44.9 w/o UO_2
32.4 w/o Y_2O_3
22.7 w/o of a 14 w/o Y_2O_3, 86 w/o ZrO_2 solid solution.

The blended powders were isostatically pressed at 30,000 psi, reacted for one hour at 2500°F (1370°C) in air, crushed and screened

through 150 mesh, and again isostatically pressed at 30,000 psi. Samples of this material were then reacted under the following conditions:

1500°C/1 hour in air
1500°C/2 hours in air
1600°C/1 hour in air
1700°C/1 hour in air
1800°C/1 hour in air
1850°C/1 hour in air*
1850°C/2 hours in hydrogen

* Not tested because it reacted with boat and was therefore contaminated.

After crushing, x-ray analysis showed all samples to be single-phase, face-centered solid solutions. Solid pieces of these samples were tested for oxidation stability in oxygen at 1650°C for 7 hours.

It appears that the following conclusions can be drawn from the data:

1. The higher the reaction temperatures in air, the lower the loss.
2. This material has good fuel retention, apparently better than Y_2O_3-UO_2-BeO. However, this material must be tested in admixture with BeO before qualifying it as a good fuel mixture.

Refer to Table II-6.

b. CeO_2 - UO_2

Various ceria-urania compositions were powder blended and air-reacted at 1350°C and 1500°C. Samples of these powders submitted for x-ray determination of phases present led to the results listed in Table II-7.

X-ray diffraction patterns were obtained for CeO_2 - UO_2 reacted powders which were melted in the arc-image furnace. The results are listed in the following table:

CeO_2 - UO_2 Reacted Powders, Melted in the Arc-Image Furnace, X-Ray Identification of Phases Present.

Sample	w/o UO_2	w/o CeO_2	Phases identified	
F-6	80	20	fcc, A_o 5.44 A	vvw lines not identified
F-9	50	50	fcc, A_o 5.435A	weak lines not identified
F-10	40	60	fcc, A_o 5.439A	few vvw lines.

Table II-6. Fuel Loss (1 atm Oxygen).

Duration: 7 hours
Atmosphere: oxygen
Rate of flow: 0.0086 CFM
Sample No. BF204S
Composition: 44.9% UO_2
32.4% Y_2O_3
22.7% of 14 w/o Y_2O_3 86 w/o ZrO_2 solid solution

Reaction treatment	X-ray data	Loss in 1 atm Oxygen (1650°C) Total (%)	Fuel (%)
1370°C/ 1 hr in air	2 fcc solid solutions 1) Y_2O_3-UO_2 a = 5.338A 2) Y_2O_3-ZrO_2 a = 5.173A	--	--
1500°C/ 1 hr in air	single fcc solid solution a = 5.287A	0.74	1.65
1500°C/ 2 hr in air	single fcc solid solution a = 5.287A	0.94	2.09
1600°C/ 1 hr in air	single fcc solid solution a = 5.287A	0.84	1.87
1700°C/ 1 hr in air	single fcc solid solution a = 5.278A	1.05/1.02	2.3/2.3
1800°C/ 1 hr in air	single fcc solid solution a = 5.278A	0.31/0.31	0.69/0.69
1850°C/ 1 hr in air	single fcc solid solution a = 5.301A	--	--
1850°C/ 2 hr in H_2	single fcc solid solution a = 5.312A	+1.42 (gain)	--

Supplemental data

Sample	Composition (%)	Loss in Oxygen 1525°C Total (%)	1525°C Fuel (%)	1650°C Total (%)	1650°C Fuel (%)
10X210Y 1700	1.06UO_2 0.8 ZrO_2	0.12	3.43	0.47	29.8
		0.17	3.24	0.48	30.5
6BF116	6.12UO_2 7.81 Y_2O_3	+0.11		0.33	2.2
		+0.08 (gain)	+0.1	0.31	2.1

Table II-7. CeO_2 - UO_2 Reacted Powders - X-Ray Diffraction of Phases.

(All mixtures air-reacted for 3 hr periods)

Sample	w/o UO_2	w/o CeO_2	Reaction temp °C	Phases identified
F-6	80	20	1500	fcc, $a_o = 5.43_3$A
F-6	80	20	1500	fcc, $a_o = 5.43_7$
F-6	80	20	1350	fcc, $a_o = 5.43_7$
F-6	80	20	1350	fcc, $a_o = 5.43_6$
F-7	70	30	1500	fcc, $a_o = 5.43_7$
F-7	70	30	1500	fcc, $a_o = 5.43_8$
F-7	70	30	1500	fcc, $a_o = 5.43_1$
F-7	70	30	1350	fcc, $a_o = 5.43_3$
F-7	70	30	1350	fcc, $a_o = 5.43_3$
F-7	70	30	1350	fcc, $a_o = 5.43_4$
F-8	60	40	1500	fcc, $a_o = 5.43_9$
F-8	60	40	1500	fcc, $a_o = 5.42_7$
F-8	60	40	1500	fcc, $a_o = 5.43_0$
F-8	60	40	1350	fcc, $a_o = 5.43_0$
F-8	60	40	1350	fcc, $a_o = 5.42_9$
F-8	60	40	1350	fcc, $a_o = 5.43_0$
F-9	50	50	1500	fcc, $a_o = 5.42_4$
F-9	50	50	1350	fcc, $a_o = 5.42_2$
F-9	50	50	1350	fcc, $a_o = 5.43_3$
F-10	40	60	1500	fcc, $a_o = 5.41_9$
F-10	40	60	1350	fcc, $a_o = 5.41_2$
F-10	40	60	1350	fcc, $a_o = 5.41_5$

c. $BeO-CeO_2-UO_2$

Fuel powders were incorporated in BeO by powder blending -325 mesh fuel powders with UOX-BeO. Samples of these mixtures were cold pressed at 20,000 psi, presintered in air, and sintered under various conditions. The BeO bodies contained 8 w/o UO_2 added as the stabilized CeO_2-UO_2 reacted powders.

The following table (II-8) lists the sinterability results obtained for the fueled BeO bodies. All of these powders and bodies were prepared by powder blending techniques. The fuel loadings for all the BF bodies were nominally 8 w/o UO_2 added as the reacted CeO_2-UO_2 powders (-325 mesh).

X-ray diffraction patterns were obtained for samples of the BF bodies listed in the tables which had been oxygen-heat-treated. These results are listed in Table II-9.

A point to be noted is the stability of the fcc phase in the CeO_2-UO_2 system for all the sintering and heat-treating conditions studied.

2. Stability Tests

Previous experience has indicated that the ZrO_2-UO_2 tetragonal solid solutions prepared in H_2 are not thermodynamically stable when powdered and reheated in air above 1000°C. On the other hand, fueled BeO tubes with approximately 13 w/o solid solution (58/42 mole percent ZrO_2 to UO_2) have exhibited excellent strength retention after testing under 75 psia O_2 at 1150°C – 1400°C for periods in excess of 10 hours.

Calculations indicate that the total volume change incurred in oxidizing the tetragonal ZrO_2-UO_2 SS (58 m/o ZrO_2, 42 m/o UO_2) to orthorhombic U_3O_8 and monoclinic ZrO_2 is only about 17 percent. This is only about one-half that encountered by the UO_2 to U_3O_8 transition. The dense BeO matrix appears to be capable of withstanding this smaller volume change.

Table II-8. Sinterability of CeO-UO_2-BeO Bodies.

Sample No.	Sintering conditions: Temp °C	Time (hr)	Atm	% Theor. ρ
BF-6 Bodies: F-6 20 w/o CeO_2, 80 w/o UO_2				
73A	1650	3	Air	93.14
74A	1650	3	Air	91.75
84A	1750	3	Air	95.95
65A	1650	3	H_2	99.07
66A	1650	3	H_2	97.96
77A	1750	3	H_2	96.79
78AA	1750	3	H_2	97.03
78BA	1750	3	H_2	95.73
79A	1750	3	H_2	96.79
83A	1750	3	H_2	96.48
BF-7 Bodies: F-7 30 w/o CeO_2, 80 w/o UO_2				
67A	1650	3	H_2	98.62
68A	1650	3	H_2	98.71
69A	1650	3	H_2	98.65
70A	1650	3	H_2	98.59
80A	1750	3	H_2	97.27
80B	1750	3	H_2	97.00
75A	1650	3	Air	94.18
76A	1650	3	Air	94.43
85A	1750	3	Air	97.24
86A	1750	3	Air	97.40
BF-8 Bodies: F-8 40 w/o CeO_2, 60 w/o UO_2				
91A	1650	3	H_2	97.06
92A	1650	3	H_2	96.97
108A	1750	3	H_2	97.09
109A	1750	3	H_2	97.00
99A	1650	3	Air	96.30
100A	1650	3	Air	95.93
119A	1750	3	Air	95.36
120A	1750	3	Air	95.54
BF-9 Bodies: F-9 50 w/o CeO_2, 50 w/o UO_2				
93A	1650	3	H_2	96.18
94A	1650	3	H_2	96.50
110A	1750	3	H_2	96.38
111A	1750	3	H_2	96.47
101A	1650	3	Air	96.74
102A	1650	3	Air	96.30
121A	1750	3	Air	95.91
122A	1750	3	Air	95.79
BF-10 Bodies: F-10 60 w/o CeO_2, 40 w/o UO_2				
95A	1650	3	H_2	96.59
96A	1650	3	H_2	97.17
112A	1750	3	H_2	97.78
113A	1750	3	H_2	97.11
106A	1650	3	Air	95.68
107A	1650	3	Air	95.42
123A	1650	3	Air	97.11
124A	1650	3	Air	96.94

Table II-9. X-Ray Diffraction Analysis of $BeO-CeO_2-UO_2$ Bodies After Oxygen-Heat-Treatment.

Body type	Sintering conditions	Phases identified by X-ray diffraction after O_2-heating
BF-8	Air, 1650°C, 3 hr	BeO, fcc, 5.42_4 + Several lines
BF-8	Air, 1750°C, 3 hr	BeO, fcc, 5.44
BF-8	H_2, 1750°C, 3 hr	BeO, fcc, 5.53_2 + fcc, 5.43_6
BF-9	Air, 1650°C, 3 hr	BeO, fcc, 5.53_2 + fcc, 5.43_6
BF-9	Air, 1750°C, 3 hr	BeO, fcc, 5.44
BF-9	H_2, 1750°C, 3 hr	BeO, fcc, 5.44
BF-10	Air, 1650°C, 3 hr	BeO, fcc, 5.44
BF-10	Air, 1750°C, 3 hr	BeO, fcc, 5.44
BF-10	H_2, 1750°C, 3 hr	BeO, fcc, 5.44 + Several lines

a. Cycling ($BeO-UO_2-ZrO_2$)

Cycling tests were conducted to further insure the performance of this material under Tory II-C conditions. Rapid cycling tests are given in Table II-10. Specimens were cycled 10 times under 75 psia O_2 according to the following schedule:

RT to test temperature - 20 minutes
Hold at test temperature - 20 minutes
Test temperature to RT - 20 minutes.

Test temperatures were 1150°C, 1250°C, and 1400°C. A slow-cycle test designed to spend considerable time in a temperature region where solid-solution instability could occur is also listed in Table II-10. Specimens were cycled 9 times under 75 psia O_2 over a period of 3 days according to the following schedule:

(9 cycles)	RT - 1150°C	3 hours
	Hold 1150°C	10 minutes
	1150°C - 800°C	1 hour
	Hold 800°C	10 minutes
	800°C - 1150°C	1 hour
	Overnight at 800°C	16 hours
	Overnight at 1150°C	16 hours.

Table II-10. Fuel Stability Testing. BeO-ZrO_2-UO_2 Tubes Cycled at 75 psia O_2.

Sample No.	Tube description[a]	Nominal $\%UO_2/\%ZrO_2$[b] mole ratio	Test temperature (°C)	Bulk density before (g/cc)	% weight change	Flex resonance ratio (R_B/R_A)	Thermal diffusivity ratio (R/R_o)	Mod. rupt. after testing (psi)[c]	Mode of failure
	RAPID CYCLING								
8	80X204, Fired 1750°C	7.8/4.9	1150	3.27	Nil	0.99	1.00	10,200[d, e]	Bending
14	80X204, Fired 1750°C	7.8/4.9	1150	3.27	Nil	1.00	1.00	11,000[d, e]	Bending
16	80X204, Fired 1750°C	7.8/4.9	1150	3.27	Nil	1.00	1.00	9,600[d, e]	Bending
34	80X204, Fired 1750°C	7.8/4.9	1150	3.27	Nil	1.04	1.00	26,700	Bending
35	80X204, Fired 1750°C	7.8/4.9	1150	3.26	Nil	1.00	1.00	31,100	Bending
39	80X204, Fired 1750°C	7.8/4.9	1150	3.27	Nil	1.03	1.00	24,300	Shear
4	80X204, Fired 1750°C	7.8/4.9	1250	No test	Nil	1.00	1.00	25,400[d, e]	Shear
15	80X204, Fired 1750°C	7.8/4.9	1250	No test	Nil	1.00	1.00	15,500[d, e]	Shear
20	80X204, Fired 1750°C	7.8/4.9	1250	No test	Nil	1.00	1.00	17,200[d, e]	Shear
6	80X204, Fired 1750°C	7.8/4.9	1400	No test	-0.15[f]	1.00	1.00	23,700[d]	Bending
10	80X204, Fired 1750°C	7.8/4.9	1400	No test	-0.17	1.00	1.00	21,300	Bending
18	80X204, Fired 1750°C	7.8/4.9	1400	No test	-0.12	1.01	1.00	33,100	Bending
9	244-800-192-21 (Fired 1700°C)	7.8/8.7	1150	3.36	+0.05	1.00	No test	37,300	Bending
23	244-800-192-21 (Fired 1700°C)	7.8/8.7	1150	3.36	+0.05	1.00	No test	34,100	Bending
53	244-800-192-21 (Fired 1700°C)	7.8/8.7	1150	3.36	+0.05	1.00	No test	30,200	Bending
	SLOW CYCLING								
65-27	80X204, Fired 1750°C	7.8/4.9	800-1150	3.27	+0.01	0.99	No test	31,000	Bending
-24	80X204, Fired 1750°C	7.8/4.9	800-1150	3.26	+0.01	0.99	No test	33,500	Bending
65-2	80X205, Fired 1750°C	7.8/4.9	800-1150	3.23	+0.01	1.00	No test	31,800	Bending
-3	80X205, Fired 1750°C	7.8/4.9	800-1150	3.26	+0.01	0.92	No test	30,300	Bending
65-35	80X205, Fired 1700°C	7.8/4.9	800-1150	3.25	+0.02	1.00	No test	35,700	Bending
-41	80X205, Fired 1700°C	7.8/4.9	800-1150	3.25	+0.02	1.00	No test	32,300	Bending
-49	80X205, Fired 1700°C	7.8/4.9	800-1150	3.25	+0.02	1.00	No test	33,900	Bending
-59	80X205, Fired 1700°C	7.8/4.9	800-1150	3.25	+0.02	1.00	No test	37,100	Bending
-64	80X205, Fired 1700°C	7.8/4.9	800-1150	3.25	+0.02	1.00	No test	38,200	Bending
65-68	10X151 (Control Tube-No ZrO_2)	10% UO_2	800-1150	3.23	+0.26	No test	No test	9,600	Bending

(a) All specimens 60 m/o ZrO_2-40 m/o UO_2 except specimens 9, 23, 53 (rapid cycling) which were 70 m/o ZrO_2 - 30 m/o UO_2.

(b) Percentage based on chemistry form batch 80X182. All tubes contain nominally 60 m/o ZrO_2, 40 m/o UO_2.

(c) 3-1/2-in. specimens, 4-point loading, 3-in. support, 2-in. load span.

(d) 3-in. specimens, 4-point loading, 2-1/2-in. support, 2-in. load span.

(e) Samples broken again on 1-1/2-in. centers. Average strengths: samples 4, 15, & 20 = 38,000 psi. samples 8, 14, & 16 = 34,300 psi.

(f) One of ten cycling excursions went to 1500°C instead of 1400°C.

Flexural resonance ratios and thermal diffusivity ratios indicate little change in strength as a result of both slow and rapid cycling. Room temperature modulus of rupture values indicate some uncertainty as to the effect of rapid-cycling tests. The first samples tested at 1150°C showed low strength when broken in 4-point loading (average modulus of rupture 10,300 psi). Sample fragments broken on 1-1/2-in. centers, 3-point load, gave no indication of strength loss (average modulus of rupture 34,200 psi). A second test at 1150°C showed strengths ranging from 26,700 to 31,100 psi. Sample 39 failed in shear and so is not a valid test. The shear stress at failure, however, was 24,300 psi, which is thus a lower limit to the bending stress. All samples tested at 1250°C failed in shear and the strength values represent lower limits. Fragments from this test broken on 1-1/2-in. centers, 3-point loading, yielded an average strength of 38,000 psi.

Samples cycled to 1400°C (one cycle to 1500°C) yielded an average strength of 26,000 psi after testing. This, coupled with thermal diffusivity and resonance-ratio data, indicate no significant loss in strength has resulted. The slight loss in weight (0.15% or approximately 1% UO_2) may be due to the higher temperature (1500°C) reached in one cycle.

The 70-30 m/o ZrO_2-UO_2 in BeO tubes (containing 8 w/o UO_2) were unaffected by the 1150°C cycle test. The higher mean strength after testing (33,900 psi) relative to the 60-40 ZrO_2-UO_2 tubes (27,400 psi) is most likely due to a lower firing temperature (1700°C).

In summary, it is difficult to explain the single set of low strengths at 1150°C. Indications are that the results are in error. Rationalizing the shear strengths as lower limits, we would conclude that there is no significant loss in strength due to rapid cycling at 1150°C, 1250°C, and 1400°C for 60-40 m/o ZrO_2-UO_2 in BeO. There is likewise no cycling effect on the 70-30 m/o mixtures at 1150°C.

b. Hot Bend (BeO-UO_2-ZrO_2)

Every specimen listed in Table II-11 has deformed under hot-bend loading. All samples contain 8 w/o UO_2 in a 60-40 m/o ZrO_2-UO_2 mixture in BeO, except sample 76-14, which contains 70-30 m/o ZrO_2-UO_2 in BeO. These tubes deform rapidly at 1400°C to 1450°C under stresses ranging from 6000 to 15,000 psi regardless of the gaseous environment (oxygen or argon). The effect of oxygen is clearly indicated in tests 76 and 86. In the

Table II-11. Fuel Stability Testing, $BeO-UO_2-ZrO_2$ Tubes.

Sample No.	Tube description	Nominal $\%UO_2/\%ZrO_2$	Atm/ psia	Temp °C/time (hr)	Hot-bend load (psi)[a]	Hot-bend performance	Mod. rupt. after testing (psi)
76-14	244-800-192-21 (Fired 1700°C, 192C)	7.8/8.7	O_2/75	1400/10	6,000	Failure after 0.8% strain in 1 hr-56 min (See Fig. II-1)	No test
59-4	80X182, Fired 1700°C	8.0/5.0	O_2/40	1450/94-100	6,000	Failure after 3.4% strain in about 2-1/2 hr (See Fig. II-2)	No test
86-22	249-800-201, (Fired 1700°C, 192C)	8.0/5.0	Argon/75	1400/2	15,000	Failure after 1.5% strain in 2 hr	No test
87-125	80X218, Fired 1700°C	8.0/5.0	O_2/75	1250/10	13,500	No failure – 0.9% strain	No test
82-16	10X210Y, Fired 1725°C, surface ground	1.0/0.6	O_2/75	1250/10	No test	No test	23,600
-161	80X211-212Y, Fired 1650°C	7.8/4.9	O_2/75	1250/10	No test	No test	35,600
-125	80X211-212Y, Fired 1675°C, surface ground	7.8/4.9	O_2/75	1250/10	No test	No test	31,200
-134	80X211-212Y, Fired 1675°C, surface ground	7.8/4.9	O_2/75	1250/10	No test	No test	31,600

MUL-15049

(a) All hot-bend loading in 3-pt., 3-in. span except in 87-125, which was 4-pt., 1-in. downcomer and 3-in. span.

argon test there was some small partial pressure of O_2 remaining which could not be expelled from the test chamber. At this low partial pressure of O_2, the tube withstood a bending stress of 15,000 psi for 2 hours, as compared to 6000 psi for 2 hours at 75 psia O_2. Furthermore, the percent strain developed prior to failure (1.5%) was twice that developed at 75 psia O_2 in essentially the same time to failure (~2 hours). Two specimens (76-14 and 59-4) are shown in Figs. II-1 and II-2, respectively.

c. Surface Grinding

In Table II-11, test 82 indicates that surface grinding has no obviously detrimental effect on stability at 1250°C, 75 psia O_2.

d. $BeO-CeO_2-UO_2$ Tubes

Tubes in this category (Table II-12) were tested at 1250°C and 1525°C. Modulus of rupture strengths before testing were around 25,000 psi. Air annealing seemed to cause some loss in strength, but more data are needed to confirm this. Strengths after testing averaged 16,400 psi for 17 tubes. This loss in strength was independent of firing temperature (1550°C and 1700°C), of test temperature (1250°C and 1525°C), and of annealing conditions (both air anneal at 1370°C and no anneal).

Fuel losses at 1525°C ranged from 9% to 20% UO_2 loss in 10 hours. There is some indication that the lower firing temperature (1550°C) causes higher fuel loss.

3. Fuel-Loss Testing

All fuel-loss data for this period have been listed in Tables II-13 and II-14. The results have been arranged according to composition (1.0%, 5.1%, 6.7%, 7.8% UO_2) and test temperature (1400°C, 1450°C, 1525°C, and 1550°C). Other testing variables are:

1. Atmosphere: argon or oxygen
2. Oxygen pressure: 1 or 5 atm
3. Effect of surface grinding
4. Effect of minor amounts of water vapor
5. Effect of firing temperature
6. UO_2-ZrO_2 ratio: 60 m/o ZrO_2-40 m/o UO_2
   70 m/o ZrO_2-30 m/o UO_2

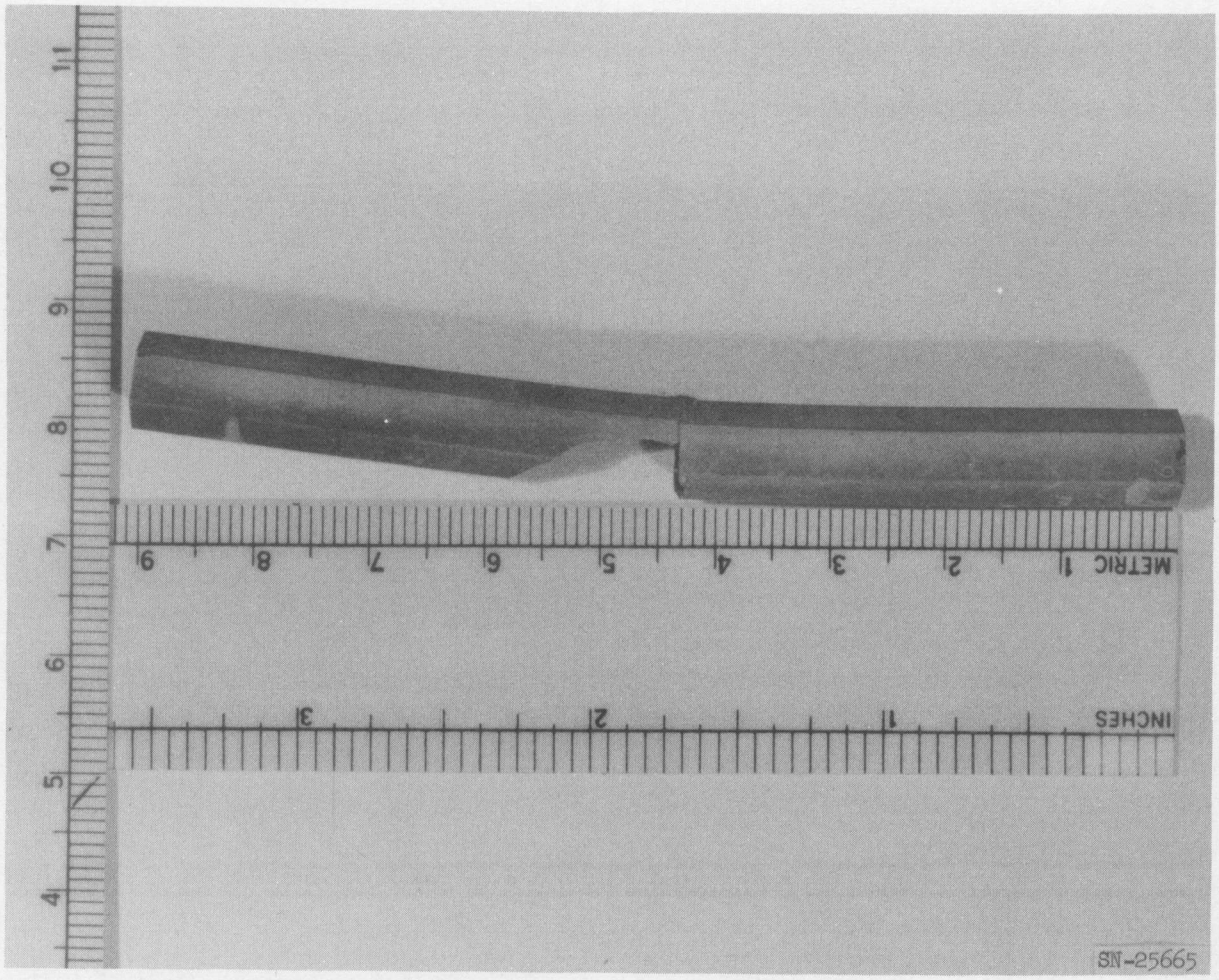

Fig. II-1. Sample No. 76-14, BeO-UO_2-ZrO_2 (7.8% UO_2); 6000 psi hot-bend load, 75 psia O_2, 1400°C; failure: 1 hr 56 min.

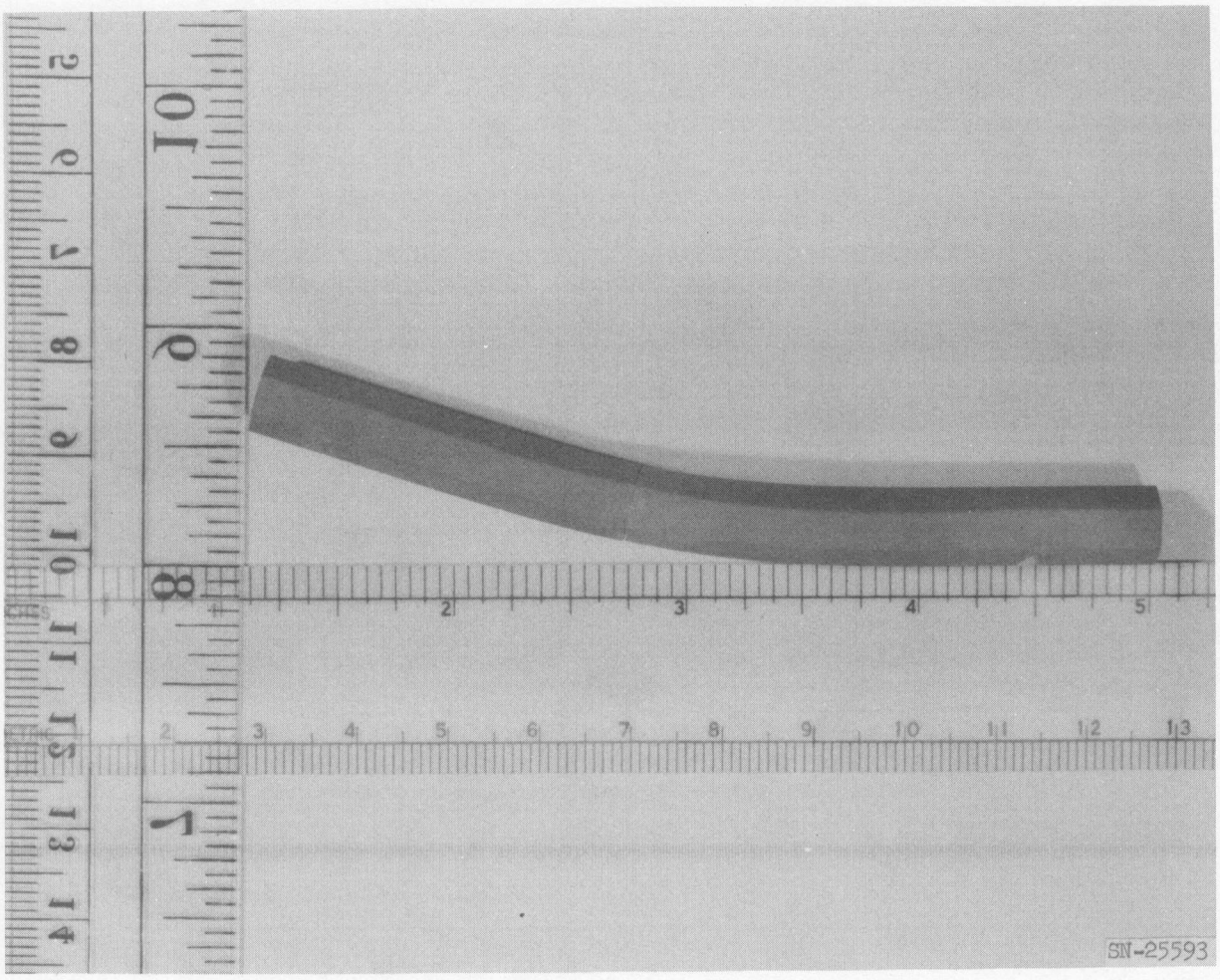

Fig. II-2. Sample No. 59-4, BeO-UO_2-ZrO_2 (8.0% UO_2); 6000 psi hot-bend load, 75 psia O_2, 1450°C; failure: approximately 2-1/2 hr.

Table II-12. Fuel Retention and Stability. $BeO-CeO_2-UO_2$ Tubes[a] at 75 psia O_2[b].

Test No.	Tube description	Test temp (°C) Time (hours)	Density before (9 m/cc)	% Wt change	$\%UO_2$ loss (by chem.)	Flex resonance ratio (R_B/R_A)	Mod. rupt. (psi)[c]
73-BF7B-19	Fired H_2, 1700°C, 3 hr – no air anneal	1450/94-100	3.10	-3.14	No test	No test	No test
74-BF7B-7	Fired H_2, 1700°C, 3 hr – no air anneal	1250/10	3.10	+0.25	No test	1.05	14,700
-10	Fired H_2, 1700°C, 3 hr – no air anneal	1250/10	3.10	+0.25	No test	1.03	14,500
78-BF7B-16	Fired H_2, 1700°C, 3 hr – no air anneal	1525/10	3.10	-1.00	-9.63	1.01[d]	16,700
-20	Fired H_2, 1700°C, 3 hr – no air anneal	1525/10	3.11	-0.85	No test	1.01[d]	16,400
78-BF7B-21	Fired H_2, 1700°C, 3 hr – no air anneal	1525/10	3.11	-1.12	No test	1.01[d]	16,000
BF7B-3	Fired H_2, 1700°C, 3 hr – no air anneal	No test	No test	No test	No test	No test	24,300 (28,300)[e]
-5	Fired H_2, 1700°C, 3 hr – no air anneal	No test	No test	No test	No test	No test	24,500 (26,900)
74-BF7B-12	Fired H_2, 1700°C, 3 hr – air annealed 1370°C, 2 hr	1250/10	3.12	+0.03	No test	1.04[d]	14,400
-15	Fired H_2, 1700°C, 3 hr – air annealed 1370°C, 2 hr	1250/10	3.11	-0.07	No test	1.03	15,500
78-BF7B-1	Fired H_2, 1700°C, 3 hr – air annealed 1370°C, 2 hr	1525/10	3.11	-1.60	-15.87	1.00	16,400
-14	Fired H_2, 1700°C, 3 hr – air annealed 1370°C, 2 hr	1525/10	3.11	-1.43	No test	1.04[d]	17,300
BF7B-28	Fired H_2, 1700°C, 3 hr – air annealed 1370°C, 2 hr	No test	No test	No test	No test	No test	(19,400)[e]
-30	Fired H_2, 1700°C, 3 hr – air annealed 1370°C, 2 hr	No test	No test	No test	No test	No test	(24,200)[e]
74-BF7B-24	Fired H_2, 1550°C, 3 hr – no air anneal	1250/10	3.08	+0.28	No test	1.01[d]	17,700
-25	Fired H_2, 1550°C, 3 hr – no air anneal	1250/10	3.06	+0.28	No test	1.00[d]	17,600
78-BF7B-8	Fired H_2, 1550°C, 3 hr – no air anneal	1525/10	3.08	-1.05	No test	1.00	17,600
-22	Fired H_2, 1550°C, 3 hr – no air anneal	1525/10	3.08	-1.57	-19.12	1.01	17,100
74-BF7B-9	Fired H_2, 1550°C, 3 hr – air annealed 1370°C, 2 hr	1250/10	3.08	+0.01	No test	1.00[d]	18,100
-23	Fired H_2, 1550°C, 3 hr – air annealed 1370°C, 2 hr	1250/10	3.09	+0.03	No test	1.02[d]	18,700
78-BF7B-11	Fired H_2, 1550°C, 3 hr – air annealed 1370°C, 2 hr	1525/10	3.08	-1.42	No test	1.00	15,200
-32	Fired H_2, 1550°C, 3 hr – air annealed 1370°C, 2 hr	1525/10	3.09	-1.55	-20.12	1.00	14,600

(a) All tubes nominal composition 8% wt UO_2-3.5% wt CeO_2.

(b) Sample 73-BF7B-19 tested under 40 psia O_2.

(c) 4-pt loading $\frac{3\text{-in. support}}{2\text{-in. downcomer}}$.

(d) Resonance frequency pressure sensitive.

(e) Values in parentheses represent samples broken on 1-1/2-in. centers.

Table II-13. Fuel Loss Testing at 1400°C and 1450°C, BeO-ZrO_2-UO_2 Tubes.[a]

Sample No.	Tube description	Nominal %UO_2/ %ZrO_2	Atm/ psia	Temp °C/time (hr)	% Weight loss	% UO_2 loss (γ count)	Mod. rupt. (psi)[b]
70-81	10X210Y, Fired 1700°C	1.0/0.6	O_2/75	1400/10	0.01	0.9	21,800
-73	10X210Y, Fired 1700°C	1.0/0.6	O_2/75	1400/10	0.01	0.9	17,200
70-60	10X210Y, Fired 1750°C	1.0/0.6	O_2/75	1400/10	0.01	1.0	22,100
-62	10X210Y, Fired 1750°C	1.0/0.6	O_2/75	1400/10	0.01	1.1	23,000
80-12	10X210Y, Fired 1725°C, surface ground	1.0/0.6	O_2/75	1400/10	0.07	5.3	25,100
-18	10X210Y, Fired 1725°C, surface ground	1.0/0.6	O_2/75	1400/10	0.04	3.9	24,100
70-160	80X211-212Y, Fired 1650°C	7.8/4.9	O_2/75	1400/10	+0.14	0.16	29,500
-153	80X211-212Y, Fired 1650°C	7.8/4.9	O_2/75	1400/10	+0.12	0.43	31,400
80-157	80X211-212Y, Fired 1650°C	7.8/4.9	O_2/75	1400/10	0.01	2.2	34,100
-163	80X211-212Y, Fired 1650°C	7.8/4.9	O_2/75	1400/10	+0.03	1.9	36,500
-121	80X211-212Y, Fired 1675°C, surface ground	7.8/4.9	O_2/75	1400/10	+0.10	1.4	22,000
-132	80X211-212Y, Fired 1675°C, surface ground	7.8/4.9	O_2/75	1400/10	+0.07	1.7	11,900
-119	80X211-212Y, Fired 1675°C, surface ground	7.8/4.9	O_2/75	1400/10	-1.25	18.9[c]	27,800
70-107	80X211-212Y, Fired 1700°C	7.8/4.9	O_2/75	1400/10	+0.13	0.86	21,100
-101	80X211-212Y, Fired 1700°C	7.8/4.9	O_2/75	1400/10	+0.10	0.86	26,500
-001	BeO control tube	0	O_2/75	1400/10	0	No test	No test
-007	BeO control tube	0	O_2/75	1400/10	0	No test	No test
76-26	244-800-192-21 (Fired 1700°C, 192C)	7.8/8.7	O_2/75	1400/10	+0.13	1.2	13,700
-47	244-800-192-21 (Fired 1700°C, 192C)	7.8/8.7	O_2/75	1400/10	+0.09	2.4	3,900
73-16	80X211-212Y, Fired 1700°C[d]	7.8/4.9	O_2/40	1450/94-100	0.61	8.2	13,600
-32	80X211-212Y, Fired 1700°C[d]	7.8/4.9	O_2/40	1450/94-100	0.42	7.7	No test
59-5	80X182, Fired 1700°C	7.8/5.0	O_2/40	1450/94-100	0.36	No test	9,600
73-8	BeO control, Fired 1725°C	0	O_2/40	1450/94-100	0.11	No test	17,600
-16	BeO control, Fired 1725°C	0	O_2/40	1450/94-100	0.06	No test	15,800
-28	100X151 control (BeO-UO_2 only)	10/0	O_2/40	1450/95-100	0.99	No test	13,100

(a) All samples have 60 m/o ZrO_2-40 m/o UO_2 except samples 76-26 and 76-47 which are 70 m/o ZrO_2-30 m/o UO_2.

(b) 4-pt. loading.

(c) One face resting against furnace wall had reacted giving glassy appearance.

(d) Change in thermal diffusivity after test was about 50%.

MUL-15051

Table II-14. Fuel Loss Testing at 1525°C and 1550°C, $BeO-ZrO_2-UO_2$ Tubes.[a]

Sample No.	Tube description	Nominal $\%UO_2/\%ZrO_2$	Atm/ psia	Temp °C/time (hr)	% Weight loss	% UO_2 loss (γ count)	Mod. rupt. (psi)[b]
67-1	10X210Y, Fired 1700°C	1.0/0.6	O_2/75	1525/10	0.33	12.8	18,100
67-3	10X210Y, Fired 1700°C	1.0/0.6	O_2/75	1525/10	0.34	13.2	15,800
67-4	10X210Y, Fired 1700°C	1.0/0.6	O_2/75	1525/10	0.18	12.8	16,700
71-72	10X210Y, Fired 1700°C	1.0/0.6	O_2/75	1525/10	0.12	13.6	15,000
71-80	10X210Y, Fired 1700°C	1.0/0.6	O_2/75	1525/10	0.08	8.2	21,700
71-54	10X210Y, Fired 1750°C	1.0/0.6	O_2/75	1525/10	0.08	10.7	18,000
71-66	10X210Y, Fired 1750°C	1.0/0.6	O_2/75	1525/10	0.06	8.0	16,700
81-7	10X210Y, Fired 1700°C, surface ground	1.0/0.6	O_2/75	1525/10	0.66	33.2	22,200
81-17	10X210Y, Fired 1700°C, surface ground	1.0/0.6	O_2/75	1525/10	0.35	30.7	22,400
72-7	10X210Y, Fired 1700°C	1.0/0.6	Argon/75	1525/10	0.07	0.9	19,500
72-9	10X210Y, Fired 1700°C	1.0/0.6	Argon/75	1525/10	0.08	1.2	21,300
68-5	10X210Y, Fired 1700°C	1.0/0.6	O_2/75	1550/10	0.64	35.0	21,300
68-10	10X210Y, Fired 1700°C	1.0/0.6	O_2/75	1550/10	0.58	34.4	17,100
71-145	80X211-212Y, Fired 1650°C	7.8/4.9	O_2/75	1525/10	0.05	3.9	8,800
71-148	80X211-212Y, Fired 1650°C	7.8/4.9	O_2/75	1525/10	0.19	6.2	11,700
81-144	80X211-212Y, Fired 1650°C	7.8/4.9	O_2/75	1525/10	2.88	36.3	7,000
81-158	80X211-212Y, Fired 1650°C	7.8/4.9	O_2/75	1525/10	3.06	38.7	4,800
81-122	80X211-212Y, Fired 1675°C, surface ground	7.8/4.9	O_2/75	1525/10	2.54	32.8	10,200
81-117	80X211-212Y, Fired 1675°C, surface ground	7.8/4.9	O_2/75	1525/10	3.66	45.8	9,500
71-88	80X211-212Y, Fired 1700°C	7.8/4.9	O_2/75	1525/10	0.27	6.3	14,200
71-61	80X211-212Y, Fired 1700°C	7.8/4.9	O_2/75	1525/10	0.21	5.7	15,000
67-17	80X209Y, Fired 1700°C	7.8/4.9	O_2/75	1525/10	0.85	6.3	11,400
67-18	80X209Y, Fired 1700°C	7.8/4.9	O_2/75	1525/10	0.85	9.4	9,700
67-19	80X209Y, Fired 1700°C	7.8/4.9	O_2/75	1525/10	0.82	9.8	13,100
85-106	80X211-212Y, Fired 1700°C	7.8/4.9	No test	No test	No test	No test	35,600
67-4	80X209Y, Fired 1725°C	7.8/4.9	O_2/75	1525/10	0.60	9.1	16,000
67-5	80X209Y, Fired 1725°C	7.8/4.9	O_2/75	1525/10	0.53	8.4	15,800
67-9	80X209Y, Fired 1725°C	7.8/4.9	O_2/75	1525/10	0.63	9.2	16,600
67-14	80X209Y, Fired 1750°C	7.8/4.9	O_2/75	1525/10	0.83	10.1	19,400
67-17	80X209Y, Fired 1750°C	7.8/4.9	O_2/75	1525/10	0.86	10.0	5,800
67-16	80X209Y, Fired 1750°C	7.8/4.9	O_2/75	1525/10	0.47	7.4	19,200
68-11	80X209Y, Fired 1725°C	7.8/4.9	O_2/75	1550/10	3.52	39.9	18,100
68-12	80X209Y, Fired 1725°C	7.8/4.9	O_2/75	1550/10	1.59	17.5	14,600
68-0	BeO control	0	O_2/75	1550/10	0.13	No test	No test
72-20	80X209Y, Fired 1700°C	7.8/4.9	Argon/75	1525/10	0.06	1.0	24,100
72-21	80X209Y, Fired 1700°C	7.8/4.9	Argon/75	1525/10	0.01	0.8	22,800
78-18	244-800-192-21 (Fired 1700°C, 192C)	7.8/8.7	O_2/75	1525/10	0.77	14.9	2,400
78-22	244-800-192-21 (Fired 1700°C, 192C)	7.8/8.7	O_2/75	1525/10	1.64	13.1	6,700
78-38	244-800-192-21 (Fired 1700°C, 192C)	7.8/8.7	O_2/75	1525/10	+0.24	9.9	10,800

(a) All samples have 60 m/o ZrO_2-40 m/o UO_2 except samples 78-18, 78-22, 78-38, which have 70 m/o ZrO_2-40 m/o UO_2.

(b) 4-pt. loading.

MUL-15101

a. 1% UO_2 Tubes

All tubes tested were 60 ZrO_2/40 UO_2 (mole ratio). Tubes (test 70) at 1400°C lost about 1.0% fuel in 10 hours. The average strength (4 samples) after testing was 21,000 psi. Firing temperatures of 1700°C and 1750°C had no effect on fuel loss or strength in this case. Surface-ground tubes (test 80, 2 samples) lost from 4% to 5% UO_2. Mean strength was 24,600 psi. Surface grinding thus increases fuel loss at 1400°C, but has no significant effect on strength.

Tubes at 1525°C (Table II-14, tests 67 and 71, 7 samples) lost an average of 11% UO_2 with a range of 8.0% to 13.6%. The mean strength was 17,500 psi. Surface-ground tubes (test 81, 2 samples) lost heavily (30% to 33% UO_2), but strength after test was still about 22,000 psi. There is reason to question whether surface grinding caused these high losses. Two 8% UO_2 unground tubes were tested as controls and they lost as much UO_2 as did the surface-ground 8% UO_2 tubes. Fuel loss is quite temperature dependent at these higher temperatures. A test at 1500°C (test 68) indicates that such high losses should be expected with a slight increase in temperature. In view of this it is believed that the temperature in test 81 may have been closer to 1550°C than 1525°C. This point will be checked in the future. It is interesting that no significant increased loss in strength accompanied these higher losses. It shall be seen later that this was not the case for 8% UO_2 tubes.

Finally, tubes tested in argon at 1525°C (test 72, 2 samples) lost about 1% UO_2 and had a mean strength of 20,000 psi. The argon purging was not complete and the oxygen partial pressure was at some low value. The fuel loss was, however, a factor of ten less than that in the 5 atmosphere oxygen tests.

b. 7.8% UO_2 Tubes

Tubes (60% m ZrO_2 and 40% m UO_2) tested at 1400°C lost an average 1.2% UO_2 with a range of 0.2% to 2.2% (test 70 and 80, 8 samples). Their average strength was 26,600 psi. Neither firing temperature (1650°C and 1700°C) nor surface grinding had any effect upon fuel loss. Again it is seen that tubes fired at 1650°C have higher strengths (average 33,000 psi for 4 samples) than those fired at higher temperatures.

A long-term (94 to 100 hours) test (73) was designed to simulate a concurrent irradiation test on similar specimens in order to asses the effects of irradiation. The average fuel loss was 8.0% UO_2, and the strength on only one sample was 13,600 psi. Even BeO control tubes (no UO_2) had low strengths after testing (average 16,700 psi). No explanation is offered for this as yet. The comparable irradiated sample (80X211-212Y, fired 1700°C), after 63 hours of irradiation at 1450° ± 50°C and 40 psia O_2, had a strength of 27,000 psi and a fuel loss of 3% UO_2. There were 5 reactor scrams and a total 7×10^{18} nvt. Thus oxidation effects tend to mask irradiation effects in these long tests.

Tubes (tests 67 and 71, 13 samples) containing 60-40 m/o ZrO_2-UO_2 when tested at 1525°C for 10 hours lost an average 7.8% UO_2 (range of 4% to 10%). The average strength after testing was 13,600 psi. Test 81 involved higher losses, but the temperature was questionable as previously stated in the discussion of 1% UO_2 tubes. One 8% tube (sample no. 85-106) was broken without testing. The strength (35,600 psi) checks well with virgin strengths reported in another section. (See Table II-14.) Test 72 was performed in argon atmosphere with some low partial pressure of oxygen. The results are like those for 1% UO_2 tubes. The average fuel loss was low (approximately 0.9%) at 1525°C and loss in strength not so severe (23,400 psi average).

c. 70% m ZrO_2 – 30% m UO_2 Tubes

The effect of thermal cycling has been covered earlier in this report. Fuel loss averaged 1.8% in 10 hours at 1400°C and 12.6% at 1525°C. Thus, no improvement is apparent compared to the 60/40 material. Average strengths after testing were low at both temperatures (7,500 psi with a range of 2,000 to 13,000).

4. Thermal Stress – Oxidation Tests

A high-pressure furnace has been constructed which is capable of producing thermal stresses in fueled tubes similar to the stresses found in all conditions in Tory II-C. A sample is heated over the center portion, with airflow adjusted to create the desired thermal stresses at the test temperature. Radial temperature gradients produce maximum tensile stresses, σ_θ and σ_Z, along the bore surface following the general pattern of Fig. II-3A. Stresses

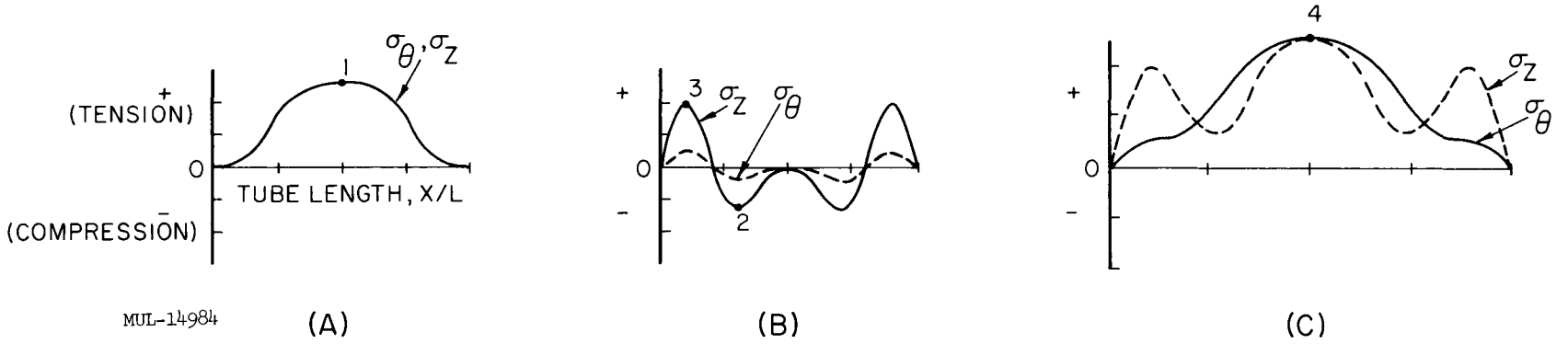

Fig. II-3. Thermal stresses along the bore surface during testing. (A) Stresses due to radial ΔT. (B) Stresses due to axial ΔT. (C) Combined thermal stresses.

due to axial gradients have been approximated according to Kent,[1] and follow the general pattern of Fig. II-3B. The result of these stresses combined is shown in Fig. II-3C. The real point of interest is at (4), which is believed to be close to the value calculated for (1) above. Good values for points (2) and (3) depend on exact axial gradients, but as long as axial gradients do not significantly affect point (4) or initiate failure elsewhere, their exact magnitude is not essential.

A summary of 24 tests is given in Table II-15. All tests were made with air flowing through the tubes at 275 psia, except 3 samples which had flowing nitrogen in place of air; and all tests were run for 2 hours at the test temperature, except for one run of only 90 seconds.

1. 10 of 12 fueled samples at 1150°C and 15,000 psi were cracked.
2. All samples — including pure BeO — at 1370°C and 15,000 psi were cracked.
3. 1 of 2 fueled samples at 1370°C and 10,000 psi were cracked.
4. In 2 hours, fuel losses in ZrO_2-stabilized samples varied from 1 to 17% at 1150°C by wet analysis. However, the wide variations require further study.

Note that the stresses quoted above are uncertain, and should be conditioned by the remarks made below.

Typical crack patterns after the samples were split lengthwise are shown in Fig. II-4. Fuel losses for a given condition vary widely from lot to lot with no apparent pattern, but with any given lot losses appear to be sensitive to both the test temperature and the stress level. Substitution of nitrogen for air through the bore eliminated fuel losses ($\pm 2\% \triangle UO_2$ is maximum error of wet analysis with no change in fuel present), but did not alter the tendency to crack. Many of the cracked samples broke during handling after testing, although pieces of some of these tubes had post-test strengths over 24,000 psi. Conversely, pure BeO sample 10 had no cracks or apparent damage, but the internal friction was at least doubled and the post-test modulus of rupture was low. The damage seen in the pure BeO samples suggests

---

[1] C. H. Kent, "Thermal Stresses in Thin-walled Cylinders," Trans. ASME, Appl. Mech. Div., 53, 167-180 (1931).

Table II-15. Thermal Stress – Oxidation Test Results (2 Hours, Except Where Noted).

	Test Conditions							Results				
Sample	UO_2 %	ZrO_2 (a) %	Firing temp %	Density g/cc	Test temp °C	σ_θ, σ_Z psi tension	Special conditions	UO_2 % by analysis	UO_2 % by count	Modulus of rupture psi	Cracks	Appearance, Comments
Pure BeO												
10	0	0	1750	2.96	1150	15,000		--	--	8,500	None	Dynamic E unchanged; internal friction increased.
11	0	0	1750	2.96	1370	15,000		--	--	6,500	L&T	
Lot 80X205												
29	7.87	4.5	1700	3.26	1150	10,000		-3	--	22,800	None	Black 0.04-in. deep along bore, outside brown.
16	7.87	4.5	1700	3.26	1150	15,000		-17	--	0 (b)	L&T	Black thruout, tan along cracks.
19	7.87	4.5	1700	3.26	1150	15,000		-15	--	0 (b)	L&T	Black thruout, tan along cracks.
Lot 80X209Y												
35	7.79	4.8	1700	3.27	1150	15,000		-1	--	0 (b)	L&T	Black along bore, brown interior.
43	7.86	4.8	1700	3.27	1370	15,000		-22	--	0 (b)	L&T	Black thruout.
Lot 80X206												
126	7.76	3.77	1600	3.02	1150	15,000			--	0 (b)	L	Black thruout.
142	7.76	3.77	1600	3.03	1260	10,000			--	20,300 (c)	None	Black thruout.
137	7.76	3.77	1600	3.04	1370	10,000			--	14,800 (c)	L	White 0.010-in. deep along bore, then black.
87	7.90	3.77	1650	3.10	1150	15,000			--	15,300 (c)	None	Black thruout except some brown extreme outside.
96	7.90	3.77	1650	3.12	1370	10,000			--	20,900 (c)	None	White coat along bore, then black.
170	7.92	3.77	1700	3.24	980	15,000		-1	--	24,100	None	Black 0.02-in. deep along bore, outside brown.
179	7.92	3.77	1700	3.23	1150	15,000		-6	--	24,700	L&T	Black thruout except some brown extreme outside.
175	7.92	3.77	1700	3.24	1150	15,000	Flowing N_2 used for inert atm	+1	--	24,200	None	Black along bore, brown interior.
176	7.92	3.77	1700	3.24	1370	15,000		+2	--	24,600	L&T	Black along bore, brown interior.
181	7.92	3.77	1700	3.24	1370	15,000		+1	--	0 (b)	L&T	Black thruout.
Lot 10X210Y												
34	1.06	0.8	1700	3.01	1150	15,000			--	(d)	L&T	Black thruout.
31	1.06	0.8	1700	3.01	1150	17,000			--	(d)	L&T	Black thruout.
33	1.06	0.8	1700	3.01	1370	17,000			--	(d)	L&T	Black thruout.
Lot BF-7B												
6	8.15	(3.1 CeO_2)	1550	3.10	1150	15,000			--		L&T	
13	8.15	(3.1 CeO_2)	1550	3.11	1150	15,000	Air annealed @ 1000°C					
Supplier Class 8, Tory II-A-1												
1	6.41	0		3.08	1150	15,000		-4	--	0 (b)	L&T	Black, discolored near cracks.
2	6.41	0		3.07	1370	15,000	90-second test	0	--	0 (b)	L&T	Max. stresses held only 90 seconds.

(a) ZrO_2 except lot BF-7B where additive is CeO.

(b) No M/R test; sample broke during handling.

(c) Four-point loading; all others three-point loading.

(d) No M/R test; sample cut for gamma count.

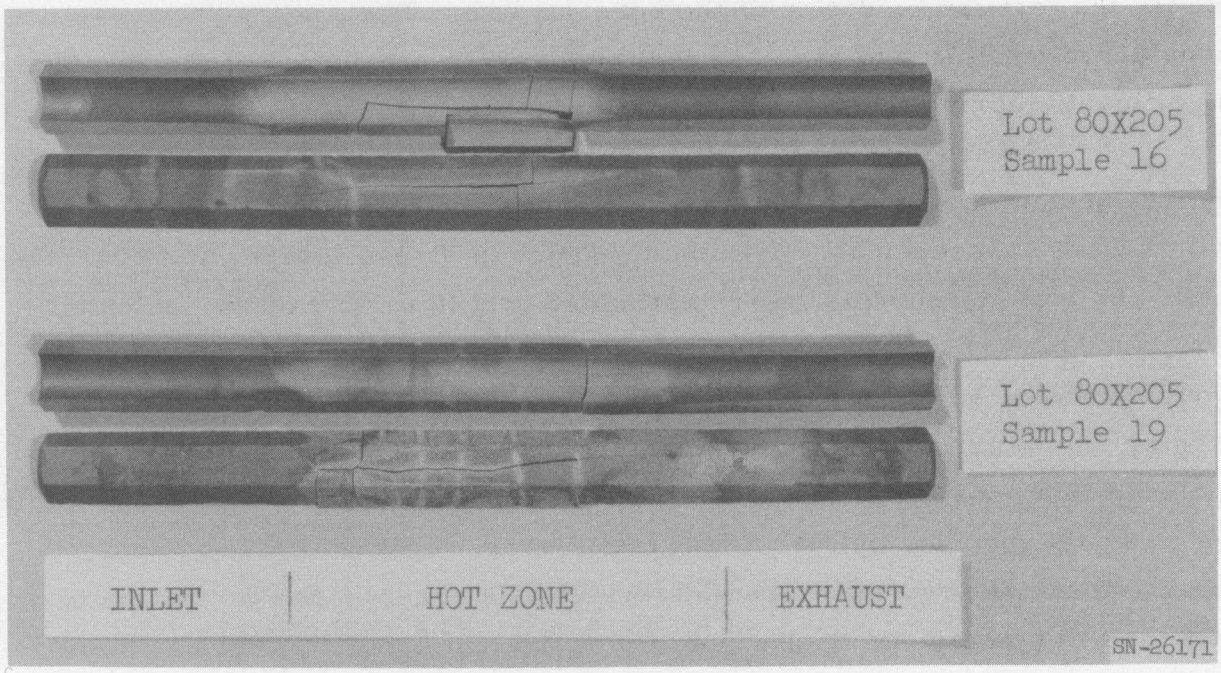

Fig. II-4. Typical longitudinal and transverse thermal stress cracks from similar thermal stress tests.

that the basic material limits have been reached in these tests, and the damage may be exaggerated by the presence of UO_2 and/or ZrO_2 in fueled tubes.

Two Class 8 tubes from a supplier were tested, and both cracked. One of these was held at the maximum stress for only 90 seconds, simulating a Nevada-type cycle. The point of origin of the cracks in both samples was determined and is shown in Fig. II-5. Arrows show the direction of crack propagation. In both cases, the point of origin was within the hot zone, although in sample 2 it was off-center.

Petrographic studies after testing have shown some grain growth during the test and oxidation at the bore surface. The grain growth was not considered sufficient to have altered the strength properties of the samples significantly during the test.

Several attempts have been made to determine test temperature by independent methods. Both thermocouples and temperature-indicating paints were unsuccessful. Maximum errors in stress levels due to calculations and test measurements are estimated at ±40 to 45% of the indicated stress. About half of this is due to convective heat transfer equations, and would probably be off in the same direction in all tests. The remainder is largely due to errors in measurements, and could be off in either direction. Included is a possible error of up to ±100°C in the reported test temperature, which would undoubtedly also affect fuel losses. This estimate of possible errors does not preclude a possible systematic error in the derivation of stresses in a hexagonal shape from its equivalent annulus, which is being checked. Continuing emphasis will be placed on ways to reduce these errors.

5. Corrosion Blowpipe

Two samples were run in the blowpipe, completing a series reported earlier. In general, BeO-UO_2 samples coated with aluminum paint and tested at 1170°C without thermal stresses had little apparent damage, while samples similarly tested but with 3800 psi tension from thermal stresses suffered oxidation (black color), crazing, and loss of strength. One exception was a ZrO_2-bearing tube (Lot 80X205) which had little apparent damage at 1165°C with 4100 psi tension.

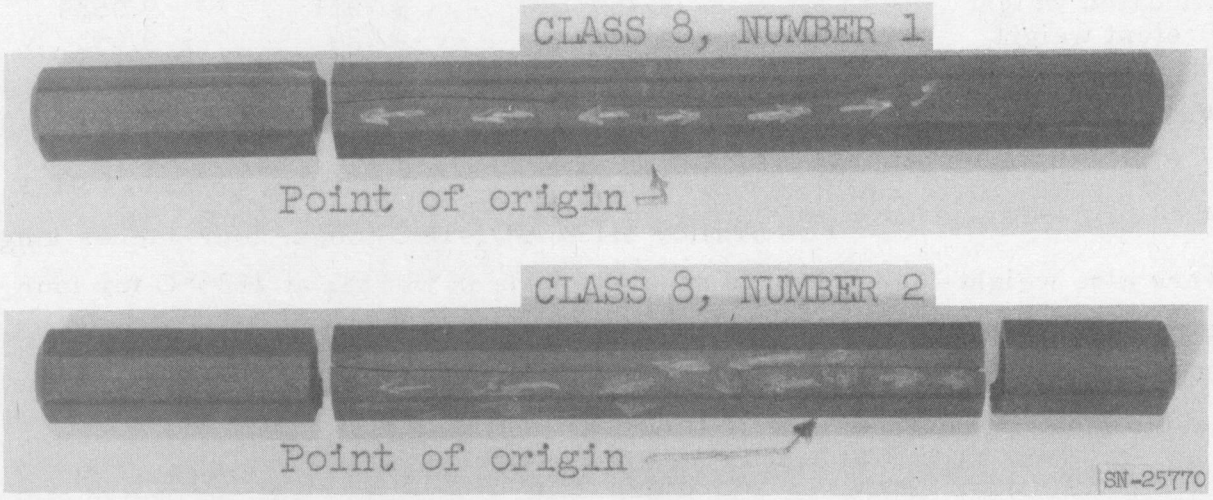

Fig. II-5. Location of point of origin of longitudinal crack; all other cracks propagated from first longitudinal crack.

C. Protective Coatings

1. Vapor-Phase Al_2O_3 Coatings

a. Water-Loss Testing

An oralloy 8.36% UO_2-BeO hex tube and a straight BeO tube were completely vapor deposited with Al_2O_3. These two tubes plus an uncoated BeO tube were weight-loss tested in wet air at 1525°C for four hours. Results were as follows:

Test One

	Uncoated BeO	Coated BeO	Coated UO_2-BeO
Coating thickness, mils i.d.		1.2	1.0
o.d.		2.7	1.6
Uncoated weight	8.769	8.7957	9.0529
Pretest weight	8.769	9.729	9.652
After test weight	8.749	9.719	9.635
Weight loss	0.020	0.010	0.017
% Loss	0.23	0.11	0.19

dew point --- 91°F

Two oralloy 8.15% UO_2-BeO tubes, four-inches long were also weight-loss tested in separate runs in wet air at 1525°C for four hours. These tubes had been vapor deposited with Al_2O_3. An uncoated 8.36% UO_2-BeO tube and an uncoated BeO tube were included in each test with the coated tube. Results were as follows:

Test Two

	Uncoated BeO	Uncoated UO_2-BeO	Coated UO_2-BeO
Coating thickness, mils i.d.			1.0
o.d.			0.7
Uncoated weight	8.200	9.060	9.168
Pretest weight	8.200	9.060	9.526
After test weight	8.185	9.034	9.526
Weight loss	0.015	0.026	0.000
% Loss	0.18	0.29	0.00

dew point --- 92°F

Test Three

	Uncoated BeO	Uncoated UO_2-BeO	Coated UO_2-BeO
Coating thickness, mils i.d.			1.2
o.d.			0.7
Uncoated weight	8.185	9.086	9.182
Pretest weight	8.185	9.086	9.575
After test weight	8.173	9.068	9.578
Weight loss	0.012	0.018	0.003*
% Loss	0.14	0.20	0.03*

dew point --- 88°F

* Weight gain.

The percent loss results indicate that the coating on BeO in Test One was effective to some extent in reducing water attack. However, the coating on the UO_2-BeO tube was not as effective as those in Tests Two and Three.

Visually, the difference in coatings on the UO_2-BeO tubes in the three tests were that of coating texture and the tendency to spall after test. The specimen in Test One showed considerably more tendency to spall on the o.d. than those in the latter tests. Its surface coarseness appeared rougher, which indicated a larger Al_2O_3 grain size in the coating. From these observations, an improvement in o.d. coating quality of tubes such as in Test One is desired. Such approaches as a two-step coating application to the o.d. and a study of coating temperature effect on coating quality should lead to improved coating protectiveness.

In all tests the tube surfaces of coated tubes turned black, indicating some UO_2 oxidation. Petrographic examination of sections of fueled coated and uncoated tubes from Test Two revealed that both had brown areas inside the tube wall. The uncoated appeared to have more brown (less oxidation) than the coated. About 1/4 of the uncoated tube section and about 1/2 of the coated tube section was oxidized.

Examination of a section of the coating after Test Two (on the fueled tube) showed two layers in the coating. Under the optical microscope the inner layer (next to tube) appeared to be chrysoberyl.

Since the coated fueled tubes in Tests Two and Three show less weight loss than the uncoated, it appears that a vapor-deposited coating can be beneficial in reducing water attack of BeO.

b. Coating Uniformity and Thickness Determinations

A good nondestructive method is needed to establish any variation in vapor-deposited Al_2O_3 coating thickness over the fueled tube surface. One method currently being set up is that of β counting over segments of the o.d. This is done by encapsulating the hex tube in a brass holder. The holder has a sliding window which allows exposure of various one-inch lengths along each hex flat. Attenuation of β can be calibrated against Al_2O_3 thickness. Since the i.d. is a confined surface, a special detector device is necessary to fit inside the hex tube. An anthracene scintillator counter which again detects β is in the process of being packaged. This will supposedly scan 1/4-inch cylindrical segments in the i.d.

Preliminary results using this method on the o.d. of an 8-percent tube were made and compared to weight gain and petrographic examination of the same tube. The values for β count represent the maximum and minimum thickness observed when one-inch lengths on all flats were examined. Petrographic values are for sections made at one-inch intervals on all flats, starting one-half inch from the tube end. Results were as follows:

1. β count – 0.5 mils to 0.8 mils
2. Weight gain – 0.7 mils
3. Petrographic section – 0.8 to 1.2 mils (average 1.0 mil).

Methods one and three indicate that the coating does vapor deposit fairly uniformly over the entire tube surface. Petrographic observation showed that the coating is deposited as a dense crystalline layer, except that some crystals project out as far as one mil from the Al_2O_3 surface.

c. Oxidation Protection

An 8.15% UO_2-BeO hex tube completely coated (weight gain calculated as 1.0 mil on i.d. and 0.7 mil on o.d.) was subjected to 1525°C for 10 hours under 75 psia oxygen. After testing, the tube surface was blackened. The coating completely adhered to the tube and showed only one small blister area. Test results on this tube and an uncoated 7.8% UO_2-BeO tube were as follows:

	Coated 8.15% UO_2-BeO	Uncoated 7.8% UO_2-BeO
Density before test	3.21 g/cc	3.36 g/cc
Percent weight change (loss)	0.06	1.64
% Gamma count change (loss)	4.90	13.10
Sonic resonance ratio (before/after test)	1.01	1.03
Modulus of rupture	11,900 psi	6,700 psi

These preliminary results indicate that the vapor-deposited Al_2O_3 coating may offer some degree of oxidation protection under these test conditions.

After modulus of rupture testing, the coating flaked off in several places from the tube o.d. X-ray examination of these flakes revealed two phases. These were chrysoberyl and alumina.

D. Mechanical Properties

1. Thermal Stress

BeO samples in the form of washers, 3/4-in. o.d. × 1/4-in. i.d. × 3/4-in. long have been evaluated for thermal stress using a one-minute rise to power. The results are listed in Table II-16. A plot of the materials parameter $\sigma K/E\alpha$ versus temperature is shown in Fig. II-6. Figure II-7 is a plot of the parameter $E\alpha/K$ wherein the parameters are taken from UCRL-6457 and are tabulated in Table II-17.

The data seem to indicate decreasing resistance to thermal stress as the temperature is increased up to about 1450°C. This is to be expected in the elastic range and reflects largely the decreasing strength and conductivity with increasing temperature.

The "washer" or thin-cylinder solution may not be applicable to a 3/4-in. long hollow cylinder, and so the thermal stress resistance data may be somewhat pessimistic. The maximum error would be the stress due to the $(1-\mu)$ term; hence the quoted $\sigma K/E\alpha$ values could be low by a factor of 1.4. Samples 3/8-in. long will be tested to determine the appropriate length for the washer solution.

Table II-16. Steady State Thermal Stress Resistance of BeO.

Sample No.	T mean °F	T mean °C	Q watts/inch	Calc. α psi	σK/Eα	No. fractured
8	2067	1130	230	13,400	13.3	3
5	2540	1393	156	11,000	9.0	3
32	2550	1398	116	8,200	6.7	0
26	2550	1398	203	14,300	11.7	4
40	1915	1045	213	11,500	12.3	0
7	1875	1024	208	11,000	12.0	1
24	1955	1068	253	13,900	14.6	2
30	2440	1338	208	14,100	12.0	4
39	2520	1382	197	13,700	11.4	2
43	2445	1340	127	8,600	7.3	0
22,29	2735	1502	156	11,000	9.0	4
28,29	2760	1515	130	9,000	7.5	0
44,29	2718	1492	136*	9,600	7.9	0
23,27	2685	1474	163*	11,600	9.4	0

$$\frac{K}{E} = 0.0577\ Q\ \frac{\text{Watts}}{\text{Inch}}$$

* 8 samples 3/8-in. long instead of 3/4-in. length.

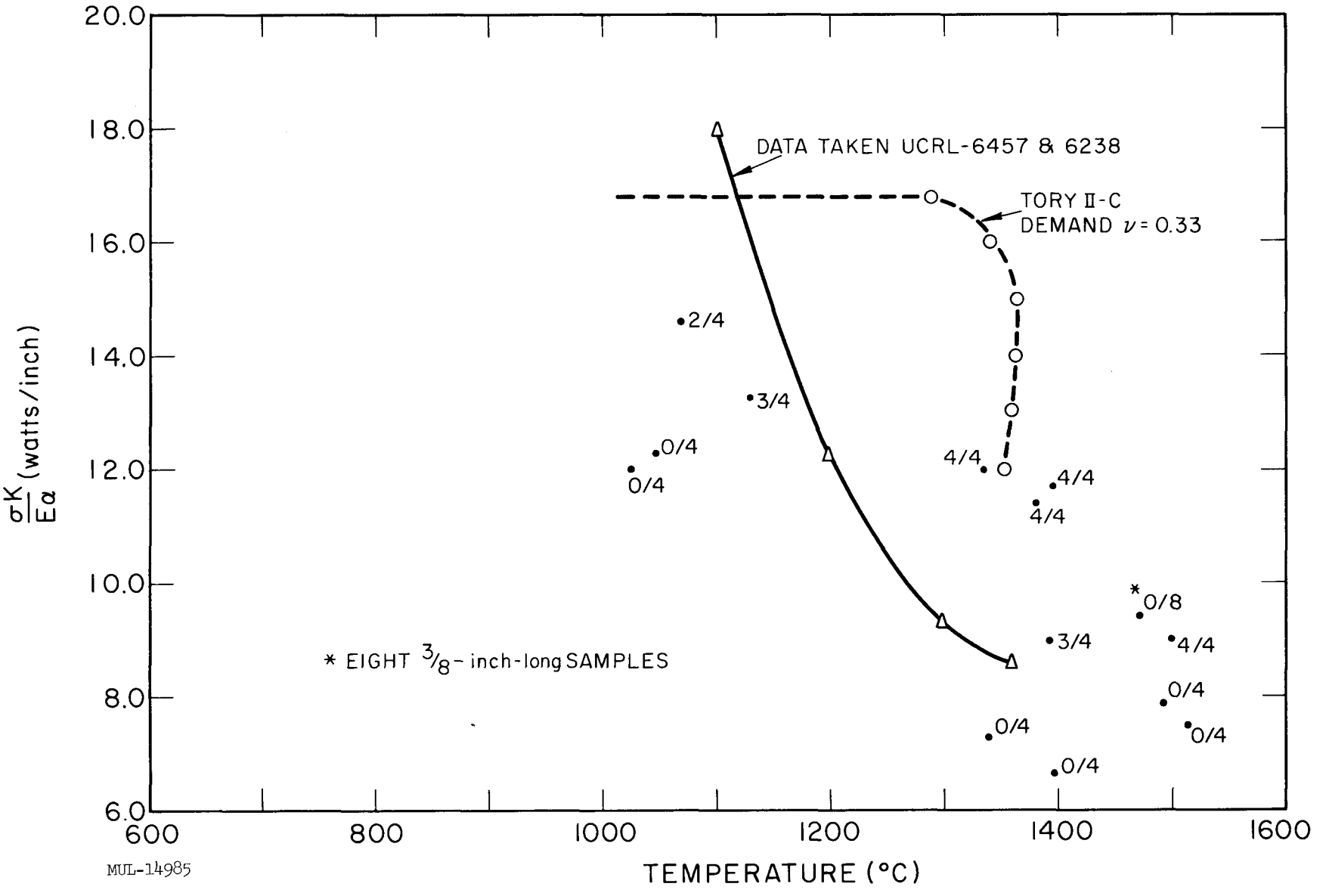

Fig. II-6. Plot of materials parameter $\sigma K/E\alpha$ vs temperature.

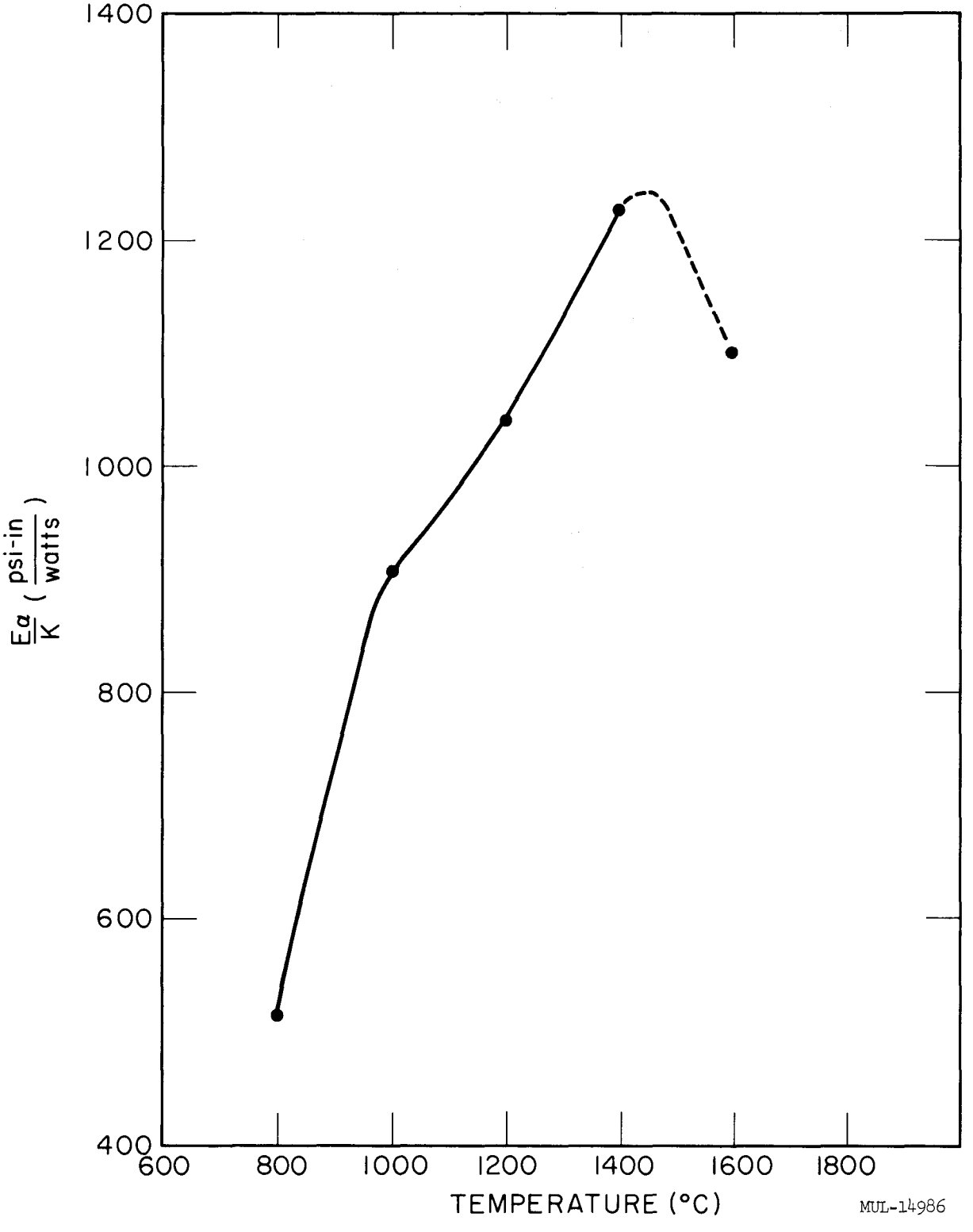

Fig. II-7. BeO thermal stress parameter as a function of temperature. Note: numbers refer to samples cracked out of samples tested, e.g., 3/4 means 3 samples out of 4 cracked.

Table II-17. BeO Materials Parameters.[a]

T(°C)	K watts cm-°C	K watts in.-°C	α in./in./°C	E (psi)	Eα	Eα/K
800	0.37	0.94	10.20×10^{-6}	47.7×10^{6}	486.5	517.5
1000	0.27	0.66	12.85	46.7	600.1	909.2
1200	0.22	0.56	12.85	45.4	583.3	1042
1400	0.18	0.46	12.85	43.9	564.1	1226
1600	0.17	0.43	12.85	(40.1)[b]	515.3	[1198]

(a) Data taken from UCRL-6457.

(b) Extrapolated.

2. Residual Strain in BeO Tubes by X-Ray Diffraction

The residual strain existing in a fabricated body can be measured by determining the change in interplanar spacings in various directions with respect to the spacing in unstrained material. When using a standard x-ray diffractometer, which requires a flat-surfaced sample, only spacings of planes that are normal to the bisector of the incident and diffracted rays can be measured. The sample holder was modified to allow rotation of the flat sample about the x-ray beam and detector support arm. Translation of the detector support arm will permit focusing the x rays reflected from the rotated sample. Thus, interplanar spacings may be measured in directions other than normal to the sample surface. The variation of strain with direction can be measured, and the sign of strain verified. The diffractometer modifications are described by Grossman and Fulrath.[1]

The strain measurement techniques have been applied to the determination of residual strains in Tory II-A-1 tubes. The 300 reflection of BeO has been used for all samples because it lies in the high back reflection region near the upper limit of the diffractometer and can be measured with

---

(1) L. N. Grossman and R. M. Fulrath, "Internal Stresses in Model Ceramic Systems. IIA – X-ray Strain Measurement Techniques for Ceramic Bodies," Second Technical Progress Report Air Force Office of Scientific Research Contract No. AF49 (638) – 4 (1959).

considerable accuracy. The value of 0.77883A for the interplanar spacing reported by Swanson and Tatge[1] has been used as the reference value. Because no evidence has been found for any change in cell dimensions in the presence of UO_2, all changes in spacing may be assumed to be due to strain in the sample. Five corrections on the diffraction angle are necessary. Horizontal and vertical divergence and the goniometer gear corrections are the same for all samples. Two other corrections must be made: (1) for the variable depth of penetration due to absorption, and (2) for the displacement of the reflecting surface from the axis of the goniometer due to the polyethylene bag. These corrections vary from sample to sample.

The stress is calculated using the relations

$$\epsilon_z = \Delta d/d$$

and

$$\sigma_x = \sigma_y = E\epsilon_z/2\nu ,$$

where d is the interplanar spacing, ϵ_z is the strain normal to the tube flats, ν is Poisson's ratio (approximately 0.3), E is Young's modulus (approximately 55×10^6 psig), and σ_x and σ_y are the axial and tangential stresses, respectively.

Table II-18 lists the data obtained from several Tory II-A-1 tubes and some additional miscellaneous samples. Two runs using UOX powder were made. The correction for the half-depth of penetration was based on the assumption that the absorption was negligible and the half-thickness of the sample could be used. The excellent agreement may be fortuitous. The stress in the BeO Tory II-A-1 tube was unexpectedly high, but the value of 13,000 psig is not unreasonable. The Tory II-A-1 fuel tubes were prestressed by heating them centrally and cooling the external surface. Several of the tubes showed cracks developed longitudinally along the tube before the strain was measured. Four of the tubes were reheated, after strain measurement, to 2150°F to relieve the stresses. The stresses were remeasured and found to be near zero. The discrepancy in one value for the untreated tube 3 is unexplained.

---

[1] H. E. Swanson and E. Tatge, "Standard X-Ray Diffraction Patterns," Vol. 1, National Bureau of Standards, Circular 539 (1953).

Table II-18. Strain Measurement in BeO Tubes by X-Ray Diffraction.

Sample	2θ measured	2θ corrected	d_{300}	Δd	$\epsilon_z (\times 10^4)$	$\sigma_x (\times 10^{-3})$	Remarks
Unfueled BeO							
BeO (NBS)		162.970	0.77883				Reference value
BeO (UOX)	162.884	162.973	.77883	0.00000	0.0	0	Powder
BeO tube (*)	162.805	162.853	.77895	.00012	1.5	12	Tory II-A-1 white tube
BeO crucible cover	162.887	162.935	.77886	.00003	0.4	3	
Tory II-A-1 Tubes (Class 10)							
T-245	162.930	162.961	.77884	.00001	0.1	1	Untreated tube
T-3	162.875	162.906	.77889	.00006	0.8	7	Prestressed at 3120°F (cracked)
T-4	162.811	162.842	.77896	.00013	1.6	13	Prestressed at 3120°F (cracked)
T-5	162.879	162.910	.77889	.00006	0.8	7	Prestressed at 3080°F
T-6	162.865	162.896	.77890	.00007	0.9	7	Prestressed at 3100°F
T-7	162.843	162.874	.77894	.00011	1.4	12	Prestressed at 3180°F (cracked)
T-3	162.807	162.893	.77891	.00008	0.9	8	
	162.862	162.948	.77885	.00002	0.3	2	Not retreated
T-4	162.859	162.945	.77885	.00002	0.3	2	Reheated at 5 atm O_2 to above 2150°F
T-5	162.848	162.934	.77887	.00004	0.5	4	
	162.820	162.906	.77889	.00006	0.8	7	Reheated at 5 atm O_2 to above 2150°F
T-6	162.860	162.946	.77885	.00002	0.3	2	
T-7	162.890	162.976	0.77882	-0.00001	-0.1	-1	
Tory II-A-type Tubes							
T-80-205-30	162.893	162.919	.77888	.00005	0.6	5	

(*) Supplier.

One Tory II-A-type tube was measured and found to have about 5000 psig stress. Additional Tory II-A-type tubes are now being run.

3. Compressive Creep

The high-temperature compressive creep properties of extruded fueled BeO are under investigation. The current effort is directed towards establishing creep stress laws for 10 w/o UO_2 material. The test results completed during this quarter are summarized in the table below:

Specimen	Percent UO_2	* Density % theoret.	Temp °F	Stress psi	Secondary creep rate in./in./hr × 10^4
L-140	10	99.0	2500	6000	3.6
L-146	10	98.8	2700	4500	18.1
L-109	10	99.1	2700	6000	23.0

* Based on a value of 3.2425 g/cc.

The above data, along with data previously reported can be utilized to complete the stress laws at 2500°F and 2700°F (Figs. II-8 and II-9). Early results on the 2500°F stress law indicated a deviation from linearity above 4500 psi; however, subsequent information has shown the strain-rate-stress relationship to be linear to 6000 psi. As is the case at 2500°F, the stress law at 2700°F is linear.

II. FABRICATION DEVELOPMENT

A. New Binder Additions for Extrusion

With the introduction of zirconia to our regular urania-beryllia fuel elements, it became necessary to obtain a new plasticizer and binder for the extrusion of ceramic fuel elements.

The new mix should have the following attributes:

1. Easy to prepare.
2. High chemical purity.
3. Release water fairly fast.
4. Easy to mix into dry fueled powder.
5. After extrusion, the extruded piece should be strong, tough, and resist external deformation.

A binder containing 3 w/o polyvinyl-alcohol, 2 w/o 400-cps viscosity methylcellulose, 27.5 w/o deionized water, and 67.5 w/o dry fuel element material was made using the following procedure:

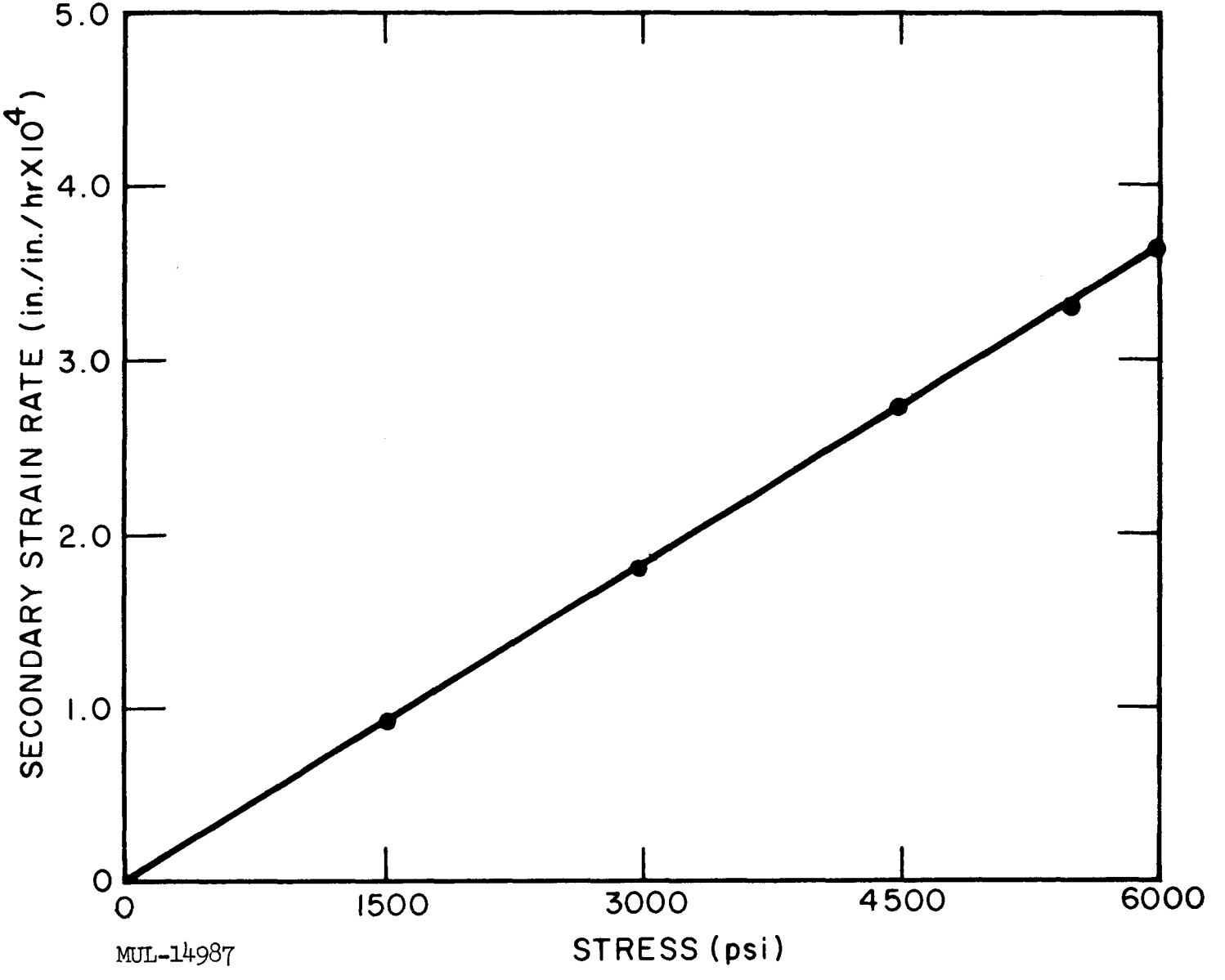

Fig. II-8. The effect of stress on strain rate for BeO – 10 w/o UO_2 at 2500°F.

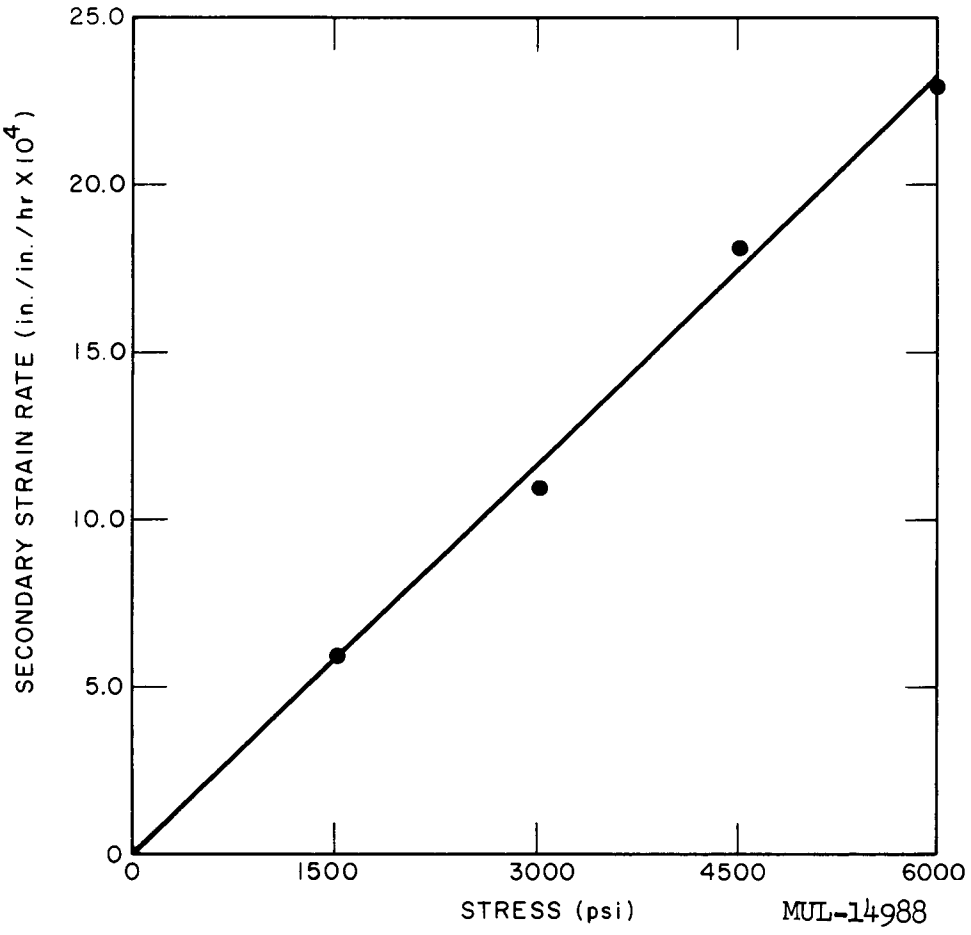

Fig. II-9. The effect of stress on strain rate for BeO – 10 w/o UO_2 at 2700°F.

1. The calcined cake is ground up in the mix muller.
2. Binder and lubricant are prehydrolyzed with water and then added to the ground cake.
3. Mix in muller for 13 to 15 minutes, or until large balls are formed.

4. Mix in a sigma mixer under vacuum for 20 minutes for extrusion.

Four 3600-gram batches were extruded with 29 percent total combustibles. The extrusion pressure and rate held constant at 1500 psi. The old die set (120° entrance angle and sharp-edge hex die) was used with full dielectric and radiant heater power. The extruded tubes appeared to be very straight on the belt. They were hard and readily handled at the lower end of the conveyor. After starch burning, fifty tubes were measured for camber. Three tubes had a camber below three mils while the other 47 varied from 3 mils to 5 mils. However, after they were sintered to 1750°C for 5 hours in a horizontal position, 95% of the tubes had cambers of 3 mils and less, as follows:

	Camber in mils										
	0 to 0.5	0.6 to 1.0	1.0 to 1.5	1.6 to 2.0	2.1 to 2.5	2.6 to 3.0	3.1 to 3.5	3.6 to 4.0	4.0 to 4.5	4.6 to 5.0	over 5.0
Starch burned (50 tubes)			1		2		18	10	12	7	
Sintered tubes 1750°C/5 hours (149 tubes)	20	30	31	34	19	7	3	2	1	1	1

Thin-walled tubes (35-mil wall thickness) were extruded using this binder and preliminary examination of the dried tubes showed no transverse cracking.

The surface porosity of sintered tubes using this new binder has been greatly reduced, as determined by Zyglo inspection.

B. Fuel Element Fabrication Facility

1. General

This quarter has given us considerable experience with zirconia stabilized mixes. We are still studying process variables and defining processing characteristics for the zirconia mixes.

The addition of zirconia has necessitated a change of extrusion binder to a methocel-polyvinyl alcohol system. Binder incorporation and mixing have been considerably revised and are still under close study.

A recent study of wall thickness variation shows that this dimension can be held to much closer tolerances than originally specified. This will allow appreciable relaxation of the Tory II-C camber specification, i.e., from 1.5 mils to 3 mils.

2. Wall Variation and Surface Roughness

From recent tube production we conclude that wall variation specifications for Tory II-C can be tightened without increasing production problems. This is based on wall thickness measurements from 375 tubes, 12 readings per tube. The 375 tubes represent 4 extrusions and 12 firings. On an over-all basis, 95.1 percent of all the wall thickness measurements were within ±0.001 inch of their averages.

Surface roughness is no problem. No reading on any tube was higher than 28 microinches (rms). The average reading is probably 20 to 25 microinches (rms).

Table II-19 summarizes the wall variation data. Note that the values calculated from predicted shrinkage are very close to the average values. Actually, for extrusions 1249, 1269, and 1270, the wall thickness averages about 0.0002 inch less than the calculated value. This is consistent with the cross-flats dimensions, which run about 0.002 inch lower than calculated, since the wall thickness is 1/10 of the cross-flats dimension. One assumes that closer control of the cross-flats dimension will bring the wall thickness on specification within the limits of inspection accuracy.

3. Mix Line

a. Raw Materials

We have two drums of wet-screened BeO (material not dried before shipment) which will be evaluated as time permits. This material should be somewhat easier to slurry free from agglomerates than the dried material.

Table II-19. Wall Variation Data.

Extrusion No.	Tube Nos.	No. of tubes	Wall thickness				% Within ± 1 mil of av	Average density	Remarks
			Min	Max	Av	Calc.			
1249	3-55	46	0.0459	0.0532	0.0477	0.0479	84.8		
1249	156-200	45	0.0457	0.0513	0.0476	0.0479	88.1	3.333	
1266	1-18	10	0.0447	0.0465	0.0457	0.0470	100	3.196	
1266	21-56	18	0.0473	0.0499	0.0486	0.0495	98.1	3.196	
1266	57-104	48	0.0445	0.0468	0.0457	0.0470	98.4	3.205	
1269	1-16	16	0.0468	0.0492	0.0481	0.0485	96.9	3.207	
1269	17-31	15	0.0474	0.0503	0.0487	0.0485	94.4	3.204	Densities not consistent with sizes. Likely due to inherent accuracy of both size and density measurements.
1269	32-46	15	0.0472	0.0499	0.0484	0.0485	92	3.210	
1269	47-61	15	0.0474	0.0510	0.0487	0.0485	96.1	3.201	
1269	63-77	15	0.0477	0.0505	0.0488	0.0485	94.4	3.204	
1269	78-92	15	0.0476	0.0497	0.0487	0.0485	99.4	3.194	
1269	93-107	15	0.0452	0.0469	0.0458	0.0461	100	3.199	
1270	1-16	16	0.0445	0.0462	0.0454	0.0462	100	3.161	
1270	17-31	30	0.0445	0.0465	0.0455	0.0462	99.7	3.160	
1270	47-61 33-46	15	0.0452	0.0469	0.0463	0.0462	98.9	3.163	
1270	63-77	15	0.0425	0.0442	0.0436	0.0462	98.9	3.159	Size anomaly. Measuring error.
1270	78-92	15	0.0443	0.0467	0.0455	0.0462	97.8	3.150	
1270	97-107	11	0.0447	0.0466	0.0458	0.0462	99.2	3.156	Tubes 93-96 same as 63-77.
Totals		375					95		

Note: The calculated wall thickness is about 1/2-mil over the actual. Excluding X1266 (which may have been calculated for an erroneous binder content) the calculated value is about 0.0002 inch high. This is consistent with cross-flats figures.

A small-scale slurrying and vibratory screening arrangement has been fabricated to determine how well the BeO (both wet and dry) meets particle size specifications. The apparatus consists of a container for slurrying the BeO and three vibratory screens in series: 50, 100, and 200 mesh. These screens may be replaced with other sizes as required. Material trapped on successive screens will be identified and calculated as percent of total.

Zirconyl nitrate stabilized with 6% HNO_3 is currently being used. This material shows no serious concentration change with time. The results from chemical analysis substantiate this and show considerable improvement as to both zirconia/urania mole ratio and urania content.

4. Binder

An MCPVA (methyl-cellulose polyvynl alcohol) binder is presently being used exclusively. This material has proved far superior to the so called "sticky" binder and permits extrusion at lower total combustibles than was previously possible. It is also possible to rework mixes initially too dry to extrude and obtain material which is (perhaps) more extrudable than virgin material of identical composition. Material which was too dry to extrude may be reworked in the sigma mixer and then consistently extruded at low pressures. This would seem to be a strong indication of poor mixing. The efficiency of the sigma mixer is poor at the batch moisture content normally extruded. For this reason a procedure of mixing at moisture levels 3% to 4% higher than required for extrusion was established. At these moisture levels the efficiency of the sigma mixer is perhaps 1000 times greater due to the extreme plasticity of the material. It was found that by mixing at 33.5% total combustibles for 1/2 hour and subsequently removing the moisture slowly over a period of 2 to 3 hours the gregarious character of the material could be preserved to combustible contents below those at which it had been possible to extrude at times in the past. The surprising thing was that two of these mixes still produced extrusions with all the characteristics of poor mixing, i.e., uneven extrusion and in general poor tubes. Attempts to rework this material, on the assumption that the 200°F or less temperature seen by the tubes on the drying belt should not alter the chemical character of the binder, ended in failure. (Note: in this case the tubes were extruded, not just pushed out of the extruder with the die removed.) The next attempts used essentially the same mixing program but faster water removal (~ 1 hour) and lower final

total combustibles. The character of the material was, at this point, individual pellets approximately 1/4 in. to 1/2 in. in diameter. For the most part a greater degree of success has been achieved with this material. On the surface this seems to present a paradox. Material initially mixed to the same uniformity, but added at different rates while mixing constantly, should certainly show different degrees of homogeneity, but in the opposite of that indicated by our extrusion results. Obviously it is not quite this simple, but as yet no explanation can be given. Recently we have been able to extrude thin-walled tubes (~47-mil green wall thickness) with loadings of 2% and 5%, which gave good to excellent preliminary results. The data are still insufficient to draw any quantitative conclusions, but, in general, it seems the new mixing procedure is greatly improved if one uses the criteria of extrusion pressure or extrudability versus total combustible level.

5. Cutter

The traveling cutter has been in operation for some time now and produces tubes free of upset (end bulging) when the extrusion speed is reasonably well matched with the belt. Slight upsets have been noted when the extrusion speed was faster than the belt speed. In addition, the automatic and steady operation of the cutter provides an accurate timing mark by which the extruder operator can synchronize the extrusion speed with belt speed. The matching of extrusion and belt speeds has done much to improve tube quality. Not only is cracking due to tensile and compressive stresses reduced, but curvature due to tensile stress has been largely eliminated.

6. Firing

Tungsten Kilns

Summary. Four new tungsten kilns were installed and tested. Eighty-four firings were made in these kilns. In most cases the density of tubes fired on the bottom rows was lower than that on higher rows. In one kiln fired at 1000°C, a temperature spread of 120°C between the low on the bottom row and the high on the top 3 rows was found.

III. METALLURGY

A. Hafnium Control Rod Oxidation Protection

Additional oxidation data on hafnium carburized 24 hours at 1600°F are presented below:

Table II-20. Hafnium Carburization Study.

Temperature	Condition	Weight gain mg/cm^2 3 hours	10 hours
1700°F	Carburized	1.05	9.27
	Uncarburized	1.78	9.90
1600°F	Carburized	0.67	
	Uncarburized	1.04	

B. Hastelloy C Heat Treatment Investigation

All-weld metal tensile specimens of Hastelloy C have been tested to determine the effect of various heat treatments on mechanical properties. These data, with correlative Charpy data, are presented in Table II-21.

SECTION II. GENERAL CHEMISTRY

I. ANALYTICAL AND SUPPORT ACTIVITIES

A. Analysis of Stabilized-Fuel Tubes

Procedures have been developed for the analysis of cerium, yttrium, magnesium, and zirconium oxides in beryllium oxide/uranium oxide mixtures. Since zirconium oxide is now added to fuel batches prepared at LRL Livermore, emphasis has been placed on developing a rapid and precise procedure for this element. (The procedure described below, although satisfactory, is somewhat time consuming.)

Since starch-burned samples containing zirconium oxide usually dissolve very slowly in 50 percent sulfuric acid, a one-gram sample of the mixed oxides of beryllium, uranium, and zirconium is dissolved by refluxing in one-to-one by volume concentrated perchloric and sulfuric acids. After dissolution, the excess acid is fumed off and the sample diluted to about 100 ml, resulting in an acid concentration of about 10-percent sulfuric. A 6-percent cupferron solution in water is added to the ice-cold sample to about two-fold excess, and the precipitate filtered on a Whatman #42 paper by means of a suction type filter. The precipitate is washed a few times with a dilute cupferron solution in 5-percent sulfuric acid. The precipitate and paper are returned to the original beaker and first wet-ashed with nitric acid and finally with fuming perchloric acid. The final determination is made by adding excess 0.05 M EDTA and back-titrating the EDTA with 0.05 M Bi at pH 2, using thiourea as an indicator.

Table II-21. Hastelloy C All-Weld Specimen Tensile and Charpy V-Notch Data.

Condition	Test temp °F	Ultimate tensile strength psi	0.2% Offset yield strength psi	Elong. in 2 in. %	Red. of area %	Charpy V-notch value ft - lb
As welded	70	106,375	70,310	19.5	16	17-1/2
2225°F, 50 min	70	107,310	44,790	48.3	46	
1100°F, 12 hr	70	109,860	68,650	21.4	22	17-1/4
1200°F, 12 hr	70	101,740	63,550	17.1	10	22-1/2
1300°F, 4 hr	70	103,290	69,470	16.3	12	19
1400°F, 4 hr	70	110,220	73,905	9.2	6	12-1/4
1500°F, 4 hr	70	125,495	78,480	9.2	9	7-1/4
1200°F, 12 hr + 1300°F, 12 hr	70	111,420	78,180	6.4	4	
1200°F, 12 hr + 1300°F, 12 hr	1300	97,235	50,785	22.7	16	
1200°F, 12 hr + 1400°F, 1 hr	70	115,540	70,930	13.5	14	
1200°F, 12 hr + 1400°F, 4 hr	70	119,930	77,510	7.1	8	
1200°F, 12 hr + 1400°F, 4 hr	1400	58,800	49,245	24.9	38	
1200°F, 12 hr + 1500°F, 1 hr	70	117,580	75,090	10.9	9	
1200°F, 12 hr + 1500°F, 1 hr	1500	43,055	36,640	22.7	33	
1300°F, 12 hr	70	--	--	--	--	12
1500°F, 1 hr	70	--	--	--	--	16

II. MATERIALS DEVELOPMENT

A. Oxidation of Hafnium

It has been shown (UCRL-6516, p. 77) that the rate and mechanism of oxidation of hafnium are strongly influenced by the condition of the surface. It is suspected that impurities on the surface and perhaps residual stresses left by the forming operation are responsible.

Preliminary tests have been run to investigate the effect of molybdenum trioxide vapor on the oxidation rate of hafnium. Before such results could be interpreted, it was necessary to establish the precision and reproducibility of results without added impurities. Measurements were made on: (1) "as received" metal exposed to static air, (2) metal which had been annealed 1 hour in vacuum at 970°C and pickled in 2% HF - 30% HNO_3, solution, and (3) pickled and annealed hafnium exposed to flowing air containing molybdenum oxide vapor. The results are given in Fig. II-10.

From the data it is seen that the pickled-annealed metal oxidized in a completely reproducible manner, with the rate increasing with increasing temperature. The rate of oxidation was parabolic with time and was not dependent on the flow of oxygen, which indicates that even in static air the rate determining step is probably a diffusion mechanism in the solid and not the rate of arrival of oxygen at the sample surface. The sample exposed to molybdenum oxide vapor behaved similarly to the one whose surface was not pretreated; both showed enhanced oxidation. It thus appears that the presence of molybdenum oxide vapor affects the oxidation behavior of hafnium.

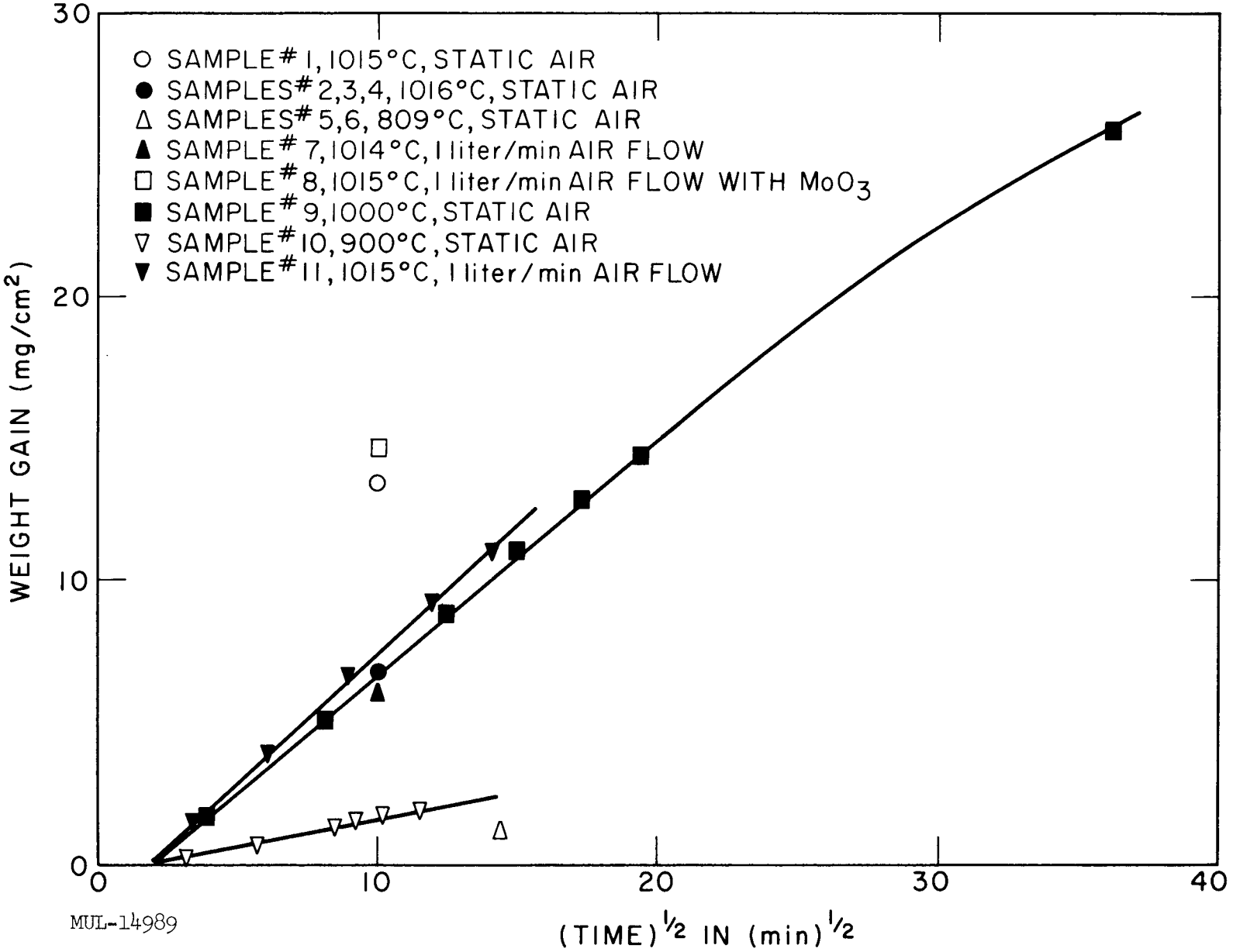

Fig. II-10. Oxidation of hafnium.

B. Thermal Diffusivity of Ta_2Be_{17}

The thermal diffusivity of Ta_2Be_{17} was measured with the room-temperature thermal diffusivity apparatus described previously (UCRL-5925, p. 136 and UCRL-6516, pp. 74-77). The Ta_2Be_{17} specimen was in the form of a rod that had been prepared by isostatic cold pressing of the reacted powder followed by sintering in an Ar atmosphere at about 1600°C. The density of the specimen was 4.61 g/cm^3. The results are as follows:

Average temperature of sample	150°C
Rise time, Δt, from 10% to 50% of level off	38.6 sec
Thermal diffusivity (corrected)	0.093 cm^2/sec.

C. Application and Testing of Coatings on F-48 Alloy

A niobium-rich alloy (F-48) has been chosen as a base plate material for the Tory II-C test reactor. F-48 consists nominally of 79% Nb, 15% W, 5% Mo, 1% Zr, and trace amounts of carbon, hydrogen, and oxygen. The alloy has marginal oxidation resistance under the anticipated operating conditions, hence a protective coating is required. A coating process has been selected and is currently being applied to F-48 test specimens by a supplier. The supplier's process is a double-coating process that applies a Si-rich undercoat and an Al-Cr-rich overlay. Coated specimens have been tested by another organization under high temperature, high flow rate oxidizing conditions, and have been found acceptable. Subsequent tests at LRL at lower temperatures and low flow rates showed failure of the coatings. At first, these failures were thought to be associated with impurities in the furnace environment, but later work showed the problem to be of more basic nature. The failure appears to be related to an intermediate temperature, rapid oxidation characteristic of silicides, and is referred to as the "silicide pest." In consideration of these problems, the following program was undertaken:

1. Determine the oxidation resistance of bare F-48 under controlled conditions.
2. Determine the oxidation resistance of supplier's coated F-48 under controlled conditions.
3. Duplicate the supplier's coating process and investigate the effects of process variables.
4. Investigate alternative coating processes.

1. Tests Performed on Bare F-48 and Coated F-48

Compatibility. Prior to undertaking the program outlined above, compatibility tests were performed on the supplier's coated F-48 specimens to establish if LRL furnace environments played a role in coating failures. Visual and spectroscopic analyses of furnace materials and mass spectroscopic analysis of evolved gases were used to identify possible contaminants. The following materials were tested: refractory cement, refractory brick, Fe_2O_3, V_2O_5, Cu_2O - $CuCl_2$ mixture, and several sources of SiO_2. The test consisted of containing the coated specimen together with the material of interest in a pure Morganite Al_2O_3 crucible closed with a lid. The crucible was then heated in an air environment to about 1260°C for various periods of time and examined. It was found that the degree of deterioration of the coats was a function of dwell time in the region of about 800°C. This effect, identified as the "silicide pest," was so extreme that it masked any effect that may have resulted from chemical incompatibility of materials, and further testing was discontinued.

2. Oxidation Tests on Uncoated F-48

The oxidation behavior of uncoated F-48 alloy is summarized in Figs. II-11 and II-12. Both dynamic (5°C/min) and isothermal testing techniques were used. Dynamic heatings were made in static air; the isothermal heatings in flowing oxygen at 100 cc/min, STP. Samples were discs of about 11-cm^2 surface area. The specimens were prepared for testing by washing with hexane, etching for 5 min in concentrated HF, rinsing with distilled water, then air drying.

The dynamic heating tests ranged from room temperature to either 1093 or 1260°C (see Fig. II-11). The samples showed a moderate amount of weight gain beginning at about 540°C and a more rapid weight gain at about 700°C.

Isothermal tests were run for 600 minutes each at temperatures ranging from 600 to 1000°C (see Fig. II-12). Oxidation products were adherent only for the 600°C heatings. In other cases, oxidation products were loose, powdery, and voluminous. X-ray diffraction patterns of the oxidation products indicated Nb_2O_5 plus unidentified phases.

The isothermal tests were also evaluated in terms of surface recession. Surface recession was calculated by assuming that all oxygen uptake resulted in formation of the stoichiometric oxides, Nb_2O_5, WO_3, and MoO_3,

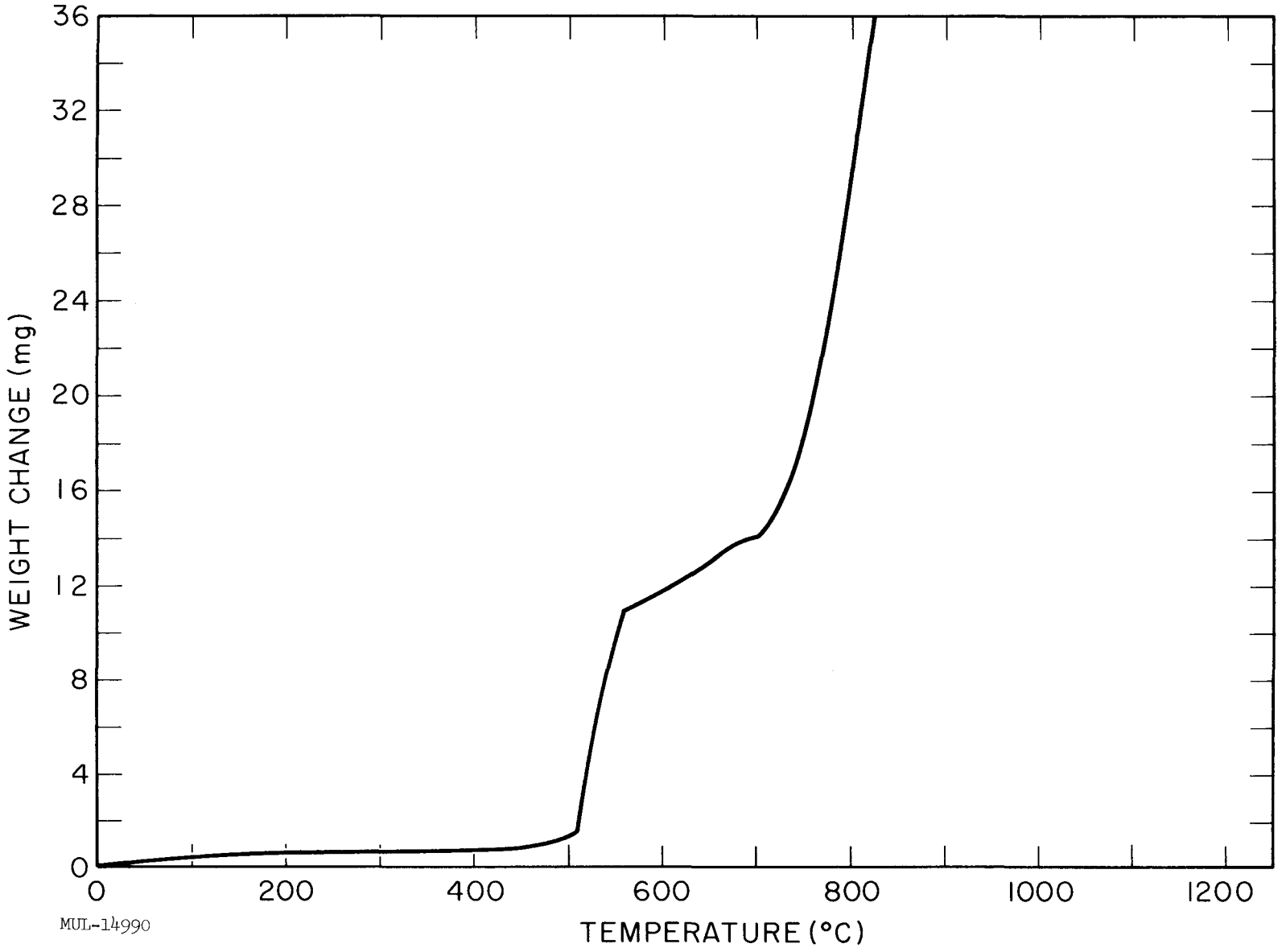

Fig. II-11. Thermogravimetric results for dynamic heating of F-48 alloy at 5°C/min in static air to 1093°C. Sample area is 11.1 cm^2. Note: rate of oxidation continued in the range 800°C to 1093°C, without change in character, to a total gain in weight of 96.6 mg.

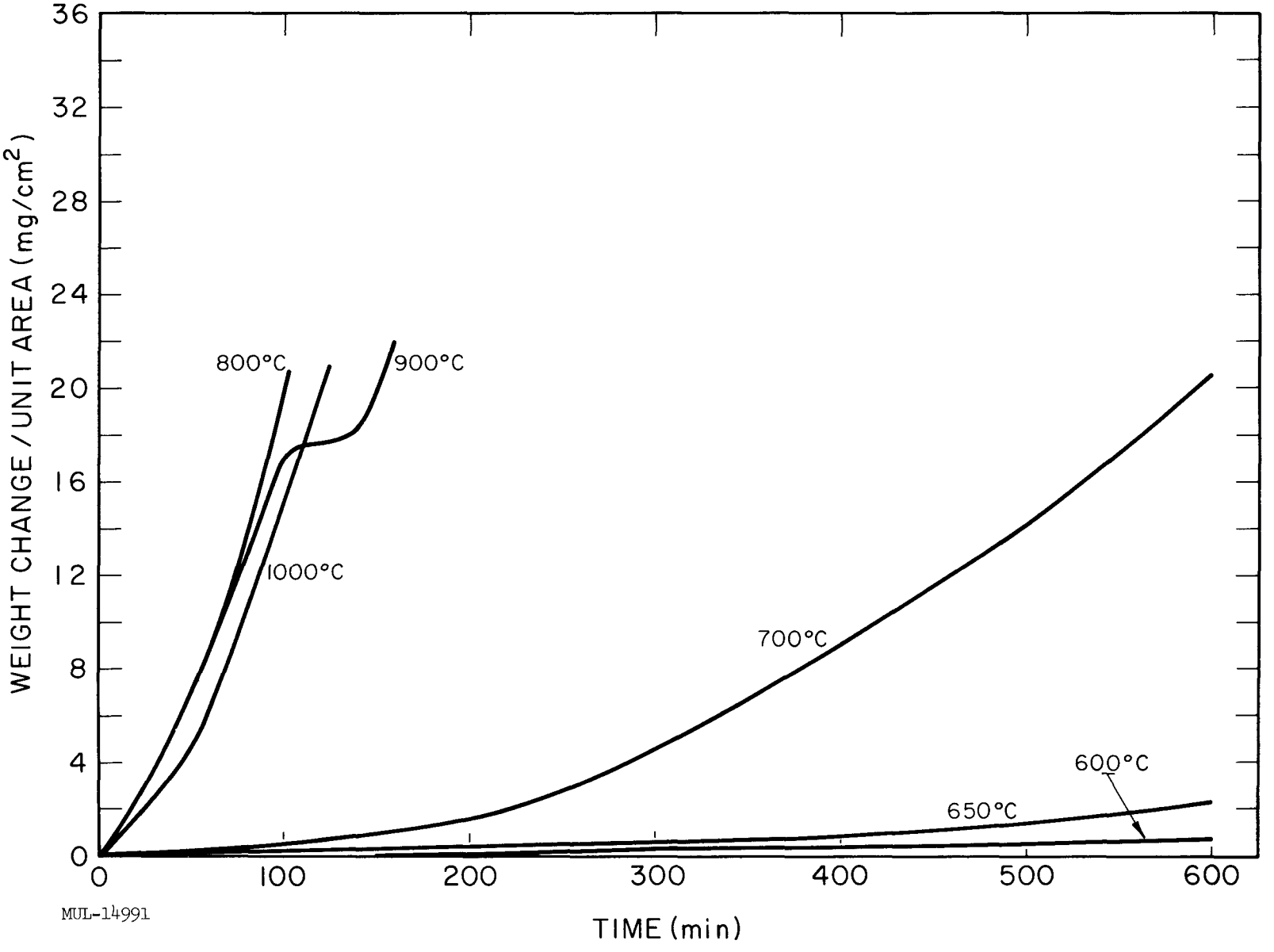

Fig. II-12. Thermogravimetric results for isothermal heating of F-48 alloy (uncoated) in oxygen (100 cc/min).

and that the surface receded at a uniform rate. Results are summarized in Table II-22.

Table II-22. Surface Recession of Uncoated F-48 Alloy, Isothermal Heating.

	Surface recession in mils calculated for period:		
Temperature, °C	120 min	300 min	600 min
600	0.015	0.040	0.064
650	0.025	0.051	0.229
700	0.047	0.423	1.95
800	2.08	--	--
900	1.58	--	--
1000	1.85	--	--

3. Oxidation Tests on Supplier's Coated F-48

The results of static oxidation tests on the supplier's coated F-48 alloys are summarized in Table II-23 and Figs. II-13 and II-14. One-half of the samples had been preconditioned by a one-hour firing in oxygen at 1093°C (2000°F); the other half by a one-hour firing in oxygen at 1260°C (2300°F). Both isothermal and dynamic heating tests were made, using a thermogravimetric apparatus. The heatings were made using a slow flow of oxygen. The samples were in all cases discs having about 11-cm^2 surface area.

The weight losses at 538 and 676°C are attributed to spalling of the coats. Some spalling may also have occurred in the 816°C run. The erratic behavior of the 1093°C experiment is due to poor furnace control.

Good intermediate temperature (about 800°C) protection results as long as the maximum temperature the sample has experienced does not exceed about 1100°C. In contrast, samples conditioned at 1260°C failed rapidly at about 800°C.

Dynamic heating tests in which the temperature was raised 5°C/min from room temperature to 1093°C gave a total gain of only 1.5 ± 0.3 mg for 3 specimens which had been conditioned at 1093°C. After heating, the sample had a faint greenish color, rather than the original dark gray color. The samples were heated from 1093 to 1260°C at 5°/min, held at 1260°C for one hour, then cooled. The corresponding weight gain was 2.6 mg during the temperature increase, and 1.7 mg during the hour-long soak. The surface

Table II-23. Results of Isothermal Heatings, Supplier's Coatings[a] on F-48 Alloy.

Sample	Conditions of treatment °C	°F	min	Total wt change mg[b]	Appearance after test
Samples conditioned for 1 hour at 1093°C (2000°F) in oxygen					
IE-1	538	1000	480	+3.0	No change
IE-2	676	1250	240	+0.5	No change
IE-3	816	1500	260	0.0	No change
IE-4	955	1750	260	0.0	No change
IE-5	1093	2000	260	+3.8	No change
IE-6	1260	2300	240	+14.0	Slight greenish color
IE-7	1316	2400	240	+49.5	Slight greenish color
Samples conditioned for 1 hour at 1260°C (2300°F) in oxygen					
IF-1	538	1000	1680	--	Coat spalled off between 8 and 23 hours
IF-2	676	1250	270	--	Coat spalled off immediately
IF-3	816	1500	340	+20 (~60 min)	Powdery flakes
IF-4	955	1750	244	+20 (~40 min)	Light powder
IF-5	1093	2000	355	+20 (~300 min)	No change

(a) The silicon-rich undercoat was applied at a nominal temperature of 1260°C for 16 hours, and the Cr-Al-rich overlay at a nominal temperature of 1037°C for 16 hours.

(b) Sample areas were all about 11 cm^2.

had become even darker green than before. X-ray diffraction patterns of the surface material were extremely complex and no compounds could be identified. Reheating one of the specimens at 1260°C for one hour gave 32-mg weight gain, and a subsequent heating gave rapid failure at an intermediate temperature during heat-up. The greenish color is found also in the samples conditioned at 1260°C, and seems to correlate with poor intermediate temperature oxidation resistance. It is believed that the color results from a chromium-containing compound, although Cr_2O_3 is not present according to the x-ray diffraction patterns. An investigation of all phases present is now underway.

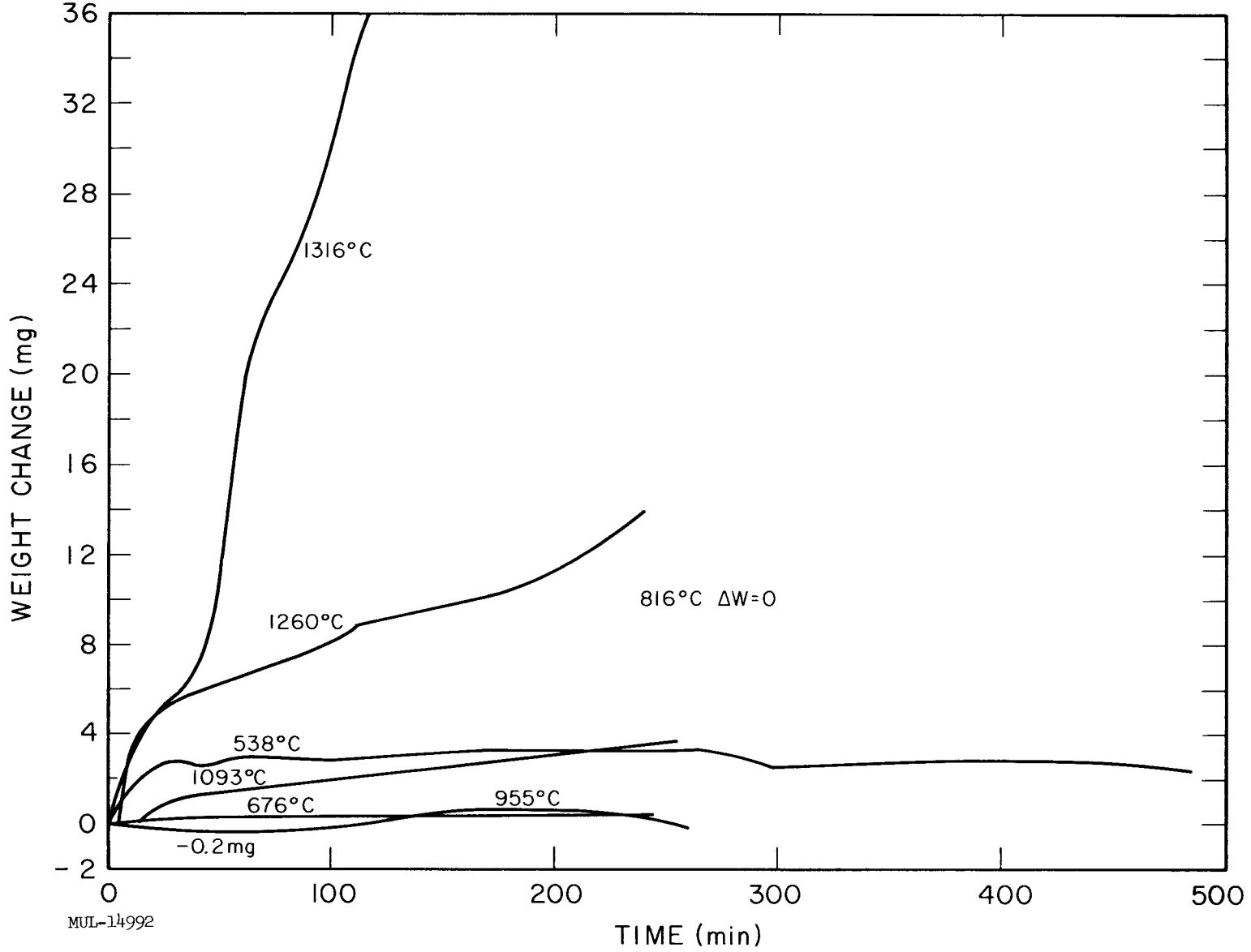

Fig. II-13. Thermogravimetric results for isothermal heating of supplier's coating on F-48 alloy. Coating samples conditioned at 2000°F for one hour.

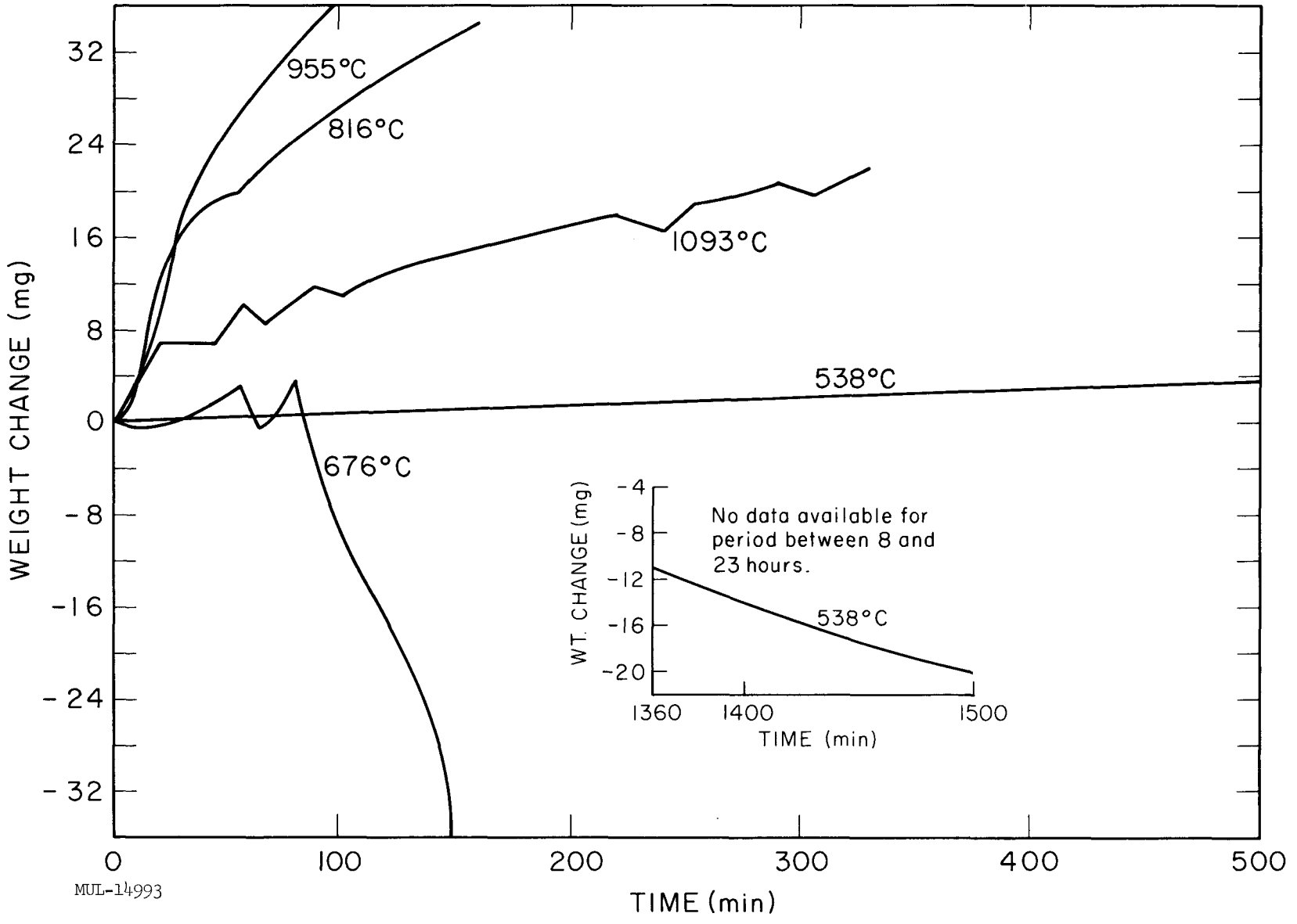

Fig. II-14. Thermogravimetric results for isothermal heating of supplier's coating on F-48 alloy. Coating samples conditioned at 2300°F for one hour.

4. Application of Coatings to F-48 Alloy

"Pack" Application of Silicide Coating. The work described here is a part of a study to develop coatings on F-48 alloy which will not undergo the low-temperature attack described previously. The immediate concern is to find optimum conditions for preparing silicide coatings on F-48 by a modification of supplier's "pack" process, and to prepare standard silicide-coated specimens for testing or for the application of additional coatings such as Al or Al-Cr.

The "pack" was an intimate mixture of 60 wt % Si powder, 30 wt % Al_2O_3 powder, and 10 wt % NaF powder. This corresponds to supplier's nominal composition, but reagent grade materials were used rather than the technical or commercial grade specified by them.

The apparatus consisted of an Al_2O_3 crucible and lid with a graphite black-body plate on top of the lid. This assembly was contained in a graphite susceptor and its temperature was measured by sighting on the black-body plate through a hole in the susceptor lid. The system could be evacuated or purged with Ar. Specimens were embedded in "pack" material inside the Al_2O_3 crucible.

Most specimens were rectangular blocks about 1.0 × 1.3 × 0.3 cm with rounded edges. They were etched for 1 min in concentrated HF, rinsed with distilled water, dried, and weighed before coating. During the siliciding runs the system was evacuated for at least four hours, heated under bacuum to about 1000°C, then under 1 atm Ar until the desired temperature was reached. All runs were for 8 hours except one for 4.17 hours. The pyrometry window was usually changed at least once during the run since the system evolved large amounts of vapor, presumably NaF. Samples were cleaned, reweighed, and measured after the run. Several were sectioned, and the coating thickness, d_o, measured directly with a microscope and filar eyepiece. The calculated coating thickness, d_c, was obtained from the weight gain, the surface area (usually about 4 cm^2), and an assumed coating density of 5.29 g/cm^3, corresponding to $NbSi_2$. Coatings were silver to dark bluish-gray, fairly uniform in thickness, with a metallic luster. They were cracked along edges where the original specimens had not been rounded off enough and also showed shallow pits corresponding to pits in the original specimens. The logarithm of d_o increased linearly with temperature from about 1090 to 1250°C.

Where a direct comparison was made between d_o and d_c on four specimens, d_c averaged 0.97 d_o. Since rounding of the specimen edges gave an actual surface area which was smaller than the values used in calculating d_c, the agreement is excellent, and supports the idea that the coating is primarily $NbSi_2$.

It is planned to continue systematic experiments to determine how d varies with temperature and time.

5. "Pack" Application of Aluminide Coatings

Pack mixtures consisting of 60 percent Al, 30 percent Al_2O_3, and 10 percent KI were used to coat F-48 specimens in Ar atmosphere. Al_2O_3 crucibles were used as containers and were heated by radiation in a tungsten helix furnace. Temperatures were varied from 900 to 1100°C, and times of 3 to 4 hours were used. The crucible was heated in vacuum up to about 600°C to outgas the materials, argon was then added, and the run completed. Coatings at the highest temperature were very thick (about 0.040 in.) and showed severe cracking at the edges. Coatings applied at the lowest temperature were about 0.005-in. thick and appeared to be free of cracks; however small nibs of material were present on the surface. These nibs appeared to be free aluminum.

An oxidation test run on one of the low-temperature coated specimens showed good resistance for 5 hours at 1260°C before noticable failure appeared.

6. Aluminide Coatings Applied by Melting Process

Attempts to coat F-48 by painting a sample with aluminum powder suspended in acetone and then melting the aluminum at 1100°C were, without exception, unsuccessful. Whether the F-48 surface was etched with HF, HF + HNO_3, grit blasted, or simply degreased with an organic solvent, the aluminum failed to wet the base material. The addition of NaF as a flux, or precoating the sample with copper or zinc did not aid wetting.

Using the same technique described above, aluminum was found to wet and coat samples of niobium, tantalum, tungsten, and chromium. Molybdenum was wet to a small extent, but the coating obtained was grainy and porous.

D. Irradiation of ZrO_2 - UO_2 Fueled BeO Tubes

A series of reactor irradiations has been made in the LPTR (Livermore Pool Type Reactor) to assess the effect of neutron irradiation

and/or oxidation on the thermal resistivity of fuel tubes. These tubes were $BeO-UO_2-ZrO_2$ material with about 7.8 percent UO_2, and irradiations were made in a thermal flux of about $3 \times 10^{13}/cm^2$-sec at the position of the tube. The results are given in Table II-24. The data show that the combined effect of irradiation and oxidation does not cause an enhanced increase in R/R_o.

E. Vapor-Pressure Measurements on Hafnium and Zirconium

Vapor-pressure measurements on hafnium and zirconium metals as a function of temperature have been initiated as part of a program to investigate the thermodynamic properties of intermetallic compounds of Ti, Zr, and Hf. No experimental measurements of the vapor pressure of hafnium are reported in the literature. There is one reliable investigation of the vapor pressure of zirconium over the temperature range 1950 to 2050°K [Skinner, Edwards, and Johnston, J. Phys. Chem. 73, 174, (1951)].

The vapor pressure will be determined by measuring the weight loss from a cylinder of the metal heated in an electron bombardment furnace which can be maintained at a vacuum of 4×10^{-7} mm Hg. Efforts are being made to develop an electron-beam configuration which will heat an unshielded specimen uniformly over its entire surface. At 1600°C the present system has a gradient of about 20 degrees from the middle to the ends of a cylinder 1-cm diameter by 2-cm long.

In addition to the weight loss determinations, experiments are being run in the mass spectrometer to determine the composition of vapor subliming from the zirconium surface under various conditions and to measure the enthalpy of sublimation over a large temperature interval. The source used for these experiments is a tubular filament folded from Zr sheet, 0.001-in. thick and 5-mm wide, to form a black-body cavity of triangular cross section. A slit about 1/2-mm wide is left in one side as a window for optical temperature measurements. Ion intensities were measured from 1375 to 1750°C with the mass spectrometer source pressure at 1.6×10^{-7} mm Hg. These data have been used to calculate $\Delta H°_{298}$ for the reaction $Zr_{(s)} = Zr_{(g)}$. The slope was taken from a plot of $\log I_{Zr} + T$ vs $1/T$ using a value of -1.0 cal/mole-deg for ΔC_P. The value obtained for $\Delta H°_{298}$ is 147.0 kcal/mole compared with 146.0 kcal/mole calculated by Stull and Sinke [D. R. Stull and G. C. Sinke, "Thermodynamic Properties of the Elements," American Chemical Society (1956)], from the data of Skinner, Edwards, and Johnston.

Table II-24. Results of Reactor Irradiations on ZrO_2 - UO_2 Fueled BeO Tubes.

Experiment	Atmosphere	time (hr)	T(°C)	NVt (thermal)	R/R_o [a]	Modulus of rupture psi	Fuel loss (%)
1[b]	~36 psia O_2	62.6	1450 ±50	6.8×10^{18}	<2.0		
2[b]	"	102.5	"	1.1×10^{19}	<2.0		
3	"	63.0	"	6.8×10^{18}	1.5 ±0.1	~27,000	~3
4	~75 psia O_2	100	1450	0	1.15 ±0.1		
5	"	100	1450	0	1.25 ±0.1	~17,000	
6	Neon	52.5	1425 ±25	5.7×10^{18}	1.6 ±0.1	34,990	
7	Helium	53.7	1000 ±100	5.8×10^{18}	3.0 ±0.2	14,200	

(a) R/R_o is ratio of thermal diffusivity before irradiation to thermal diffusivity after irradiation.

(b) Alundum thermocouple shields were cemented to these tubes, and therefore the measured values of R/R_o are too high. An estimate of the excess mass would result in a decrease in R/R_o of about 20 percent.

The data for ZrO^+ are very erratic, and seem to be time dependent. The source pressure was constant at 1.60 ± 0.05 mm Hg throughout the experiment. At this pressure and at temperatures where Langmuir sublimation experiments are feasible, the ratio of ZrO^+ to Zr^+ is less than 0.03.

The data of this work and that of Skinner, Edwards, and Johnston are presented in Fig. II-15.

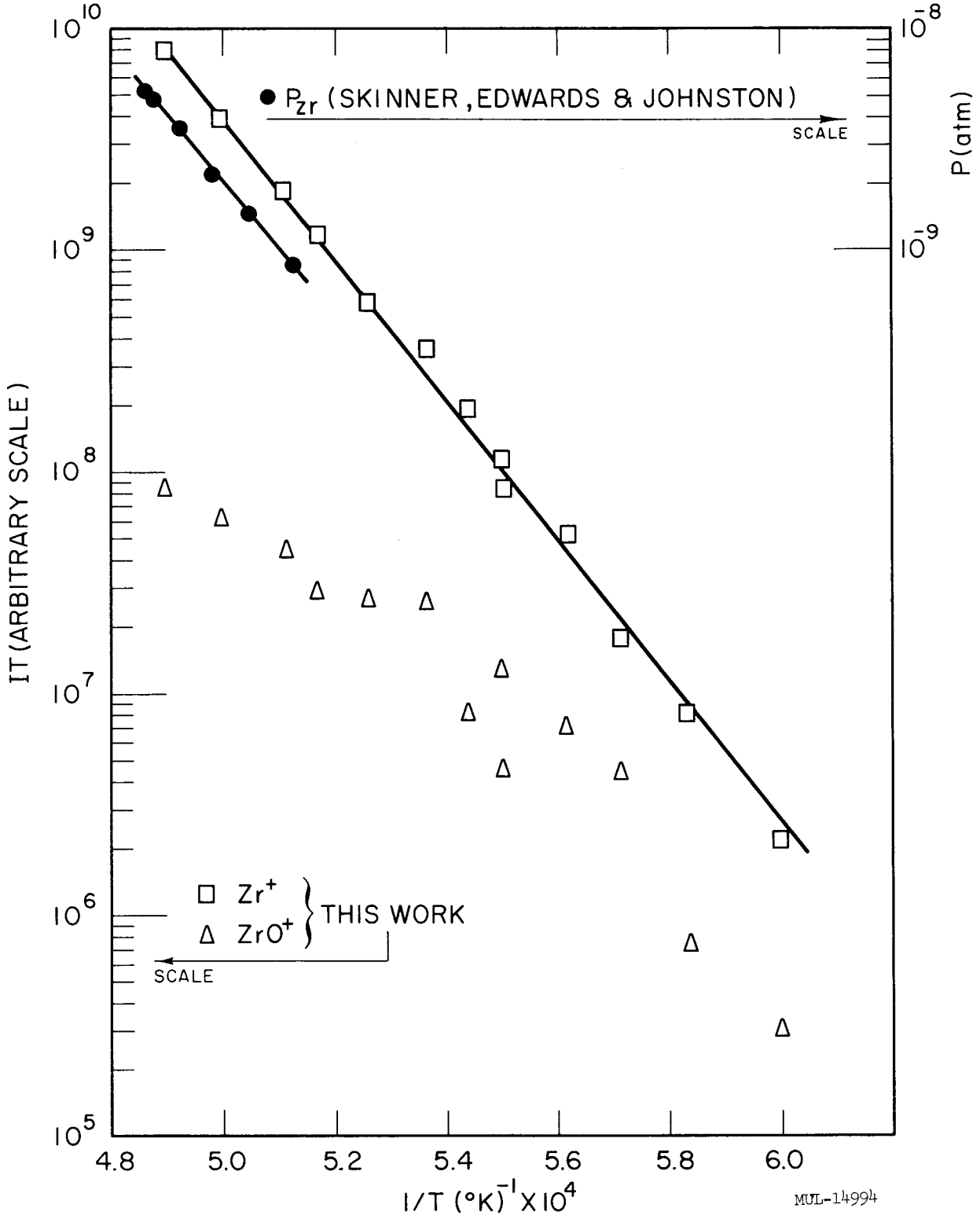

Fig. II-15. Plot of log IT vs 1/T for Zr^+ and ZrO^+, and log P vs 1/T for Zr from Skinner, Edwards, and Johnston.

CHAPTER III. HOT BOX

BeO EXPERIMENTS

INTRODUCTION

The bare BeO assembly (Fig. III-1) was set up again and experiments started the first week in July. The object of this new experimental series was to check the precision of the earlier experiments (UCRL-6329), to improve the experimental procedure, and to extend the experiments to BeO/U^{235} ratios other than the 560:1 ratio of the original experiments.

The main areas of distrust in the earlier experiments were the reproducibility of the BeO block spacing, the effect on the temperature coefficient of reactivity due to the large unfueled BeO regions in the center and at the edge of the core, the contribution to the temperature coefficient of reactivity of the relative thermal expansion of the BeO blocks and the supporting graphite box, and the determination of the critical condition for the shorter core which had a minimum amount of excess reactivity at room temperature.

EXPERIMENTAL IMPROVEMENTS

The blocks were stacked on edge due to the incompatibility of the 9-inch-wide Hot Box fuel-element foils with the 5-3/8-inch-wide, 15-mil-deep recesses in the $6 \times 6 \times 1$-inch blocks. Spacing between the blocks was left for the fuel-element foils, for differential thermal expansion of the blocks over the graphite supporting box, and for reduced friction between the blocks and foils in the event of a foil retraction. This spacing was obtained originally by inserting two extra 10-mil stainless steel sheets with the foils between blocks and then by compressing the layers of blocks and foils as much as the strength of the graphite structure would allow. When the stainless-steel spacer sheets were withdrawn prior to nuclear experiments, the blocks could not be kept from moving into the resulting spaces under the forces of compression. A sequence of spacer-sheet withdrawal was followed in earlier experiments to distribute this motion as uniformly as possible. The disturbance in the local effective BeO density due to this motion could not be readily measured. In the present experiments, a single 10-mil spacer sheet was used, and the crinkles in the fuel elements, which caused the springiness of the former assembly under compression, were allowed to provide the remaining spacing without using any appreciable compression forces on the core. When the

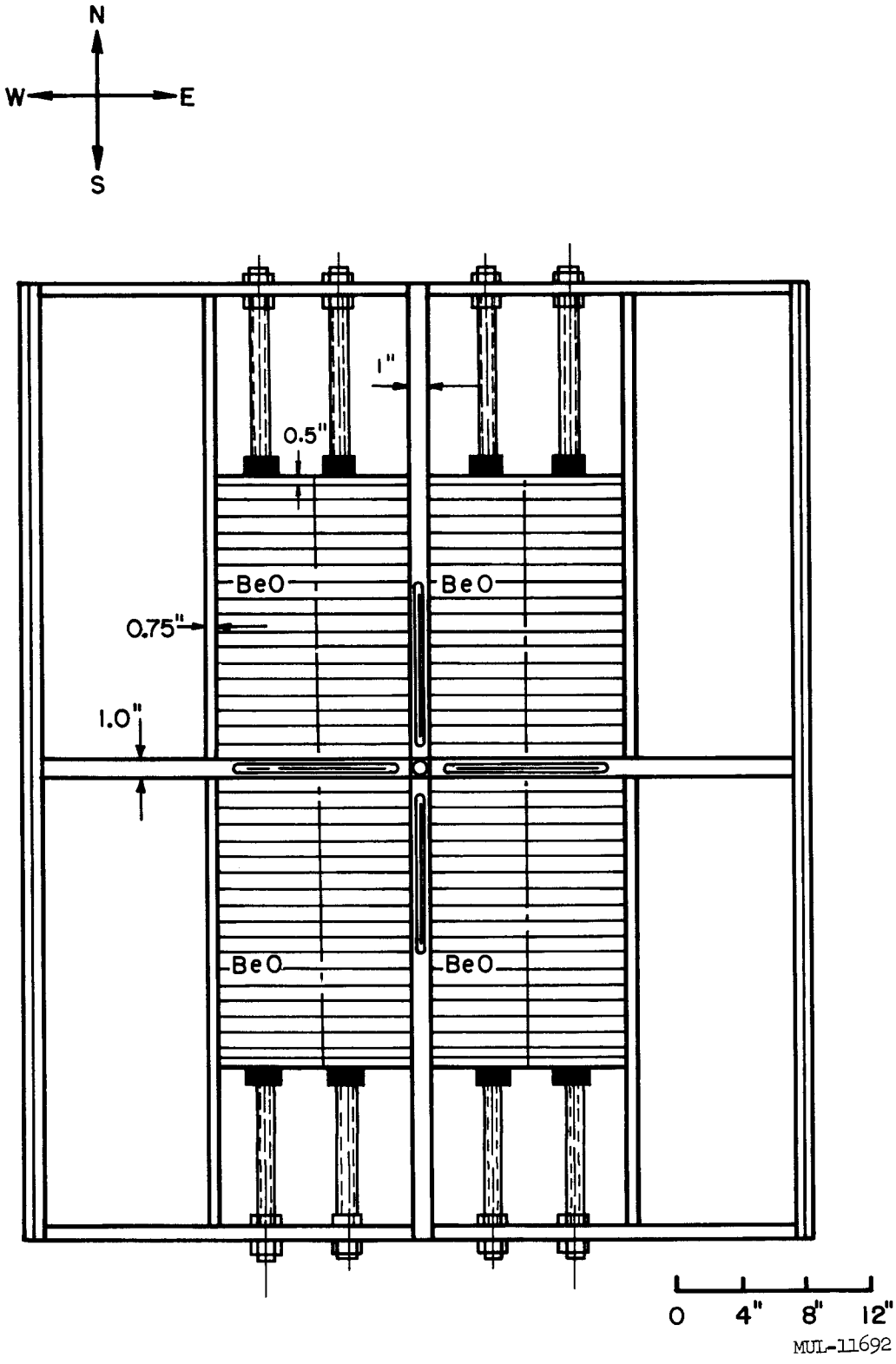

Fig. III-1. Bare BeO assembly.

spacer sheets were withdrawn, no motion of the blocks occurred, but a much smaller uncertainty in spacing is admittedly introduced due to the nonuniformity of the crinkles in all foils. This was felt to be the best workable solution to the spacing problem, short of making special fuel elements to fit into the block recesses. It must be emphasized that the spacing uncertainty exists in both the cold and hot systems such that the differential temperature effect is insensitive to the spacing distribution.

To give the 560:1 BeO/U^{235} ratio, two 2-mil-thick oralloy fuel-element foils were used for each 1-inch-thick layer of blocks in a 12-inch-wide quadrant. The 9-inch-wide foils were originally placed together, leaving a 1-1/2-inch-wide unfueled region along each side of a quadrant. At the center plane, the 1-1/2-inch slabs on each side formed a three-inch-thick unfueled "island" causing a large deviation in thermal neutron concentration from the desired simple cosine distribution. The revised arrangement was with the two foils in a pair staggered to fill the full width of a slot. This produced two 3-inch-wide regions of half-loading on each side of a quadrant and reduced the full-loading-region width to six inches. The resulting power distribution was much more nearly a cosine shape.

The center cruciform and the supporting-box side walls were spaced 12.090 inches apart to take two 6-inch-wide BeO blocks side-by-side. The extra spacing was for differential thermal expansion. The location of the blocks, i.e., whether they are all placed tightly against the cruciform or all tightly against the side wall, makes a large difference in the contribution of the BeO expansion to the temperature coefficient at reactivity. With the blocks against the cruciform, they expanded outward giving a decrease in reactivity with temperature, whereas with the blocks against the side wall, they expanded outward much less, or even had a net inward expansion when the thermal expansion of BeO was more than double that of graphite. This latter resulted in a small positive reactivity contribution with increasing temperature from expansion in this dimension of the core. (This does not, however, override the large negative effect of the BeO expansion in the vertical direction and the smaller negative effect of the graphite expansion in the longitudinal direction.) In the earlier experiments, no special care was taken to place the blocks either all against the cruciform or all against the side walls, so there was a large uncertainty in the correction of the over-all temperature coefficient of reactivity to give the nuclear effect alone by subtracting the thermal expansion

contribution. In the present experiments with a BeO/U^{235} ratio of 560:1, two comparative high-temperature critical runs were made, first with the blocks all against the cruciform and second with the blocks all against the outer wall to give a measure of the actual uncertainty in the previous experiments and to give a much better determination of the nuclear temperature coefficient of reactivity.

The high-temperature experiments involved finding the temperature at which the existing longer assembly would be critical with all vanes removed. The comparison shorter assembly always had some excess reactivity, and the practice in the past was to convert this excess to a length correction and modify the longitudinal dimension to give the size that would have been critical. The problem of the treatment of this length modification for diffusion code calculations has not been clearly resolved due to the layered arrangement of the core. In the present experiments, the shorter core was heated also to determine its critical temperature, which was, in general, within a few-hundred degrees of room temperature, and the length correction was thereby made unnecessary.

RESULTS

Only preliminary results from the high-temperature experiments are available at this time. Differential room-temperature experiments giving the reactivity worths of core length increments and control vanes have not yet been completely reduced.

Two high-temperature critical experiments were performed with the 560:1 BeO/U^{235} assembly (four, counting the lower elevated temperature criticality determinations for the shorter comparison assemblies). Another high-temperature critical run was made with a 280:1 BeO/U^{235} ratio. The latter assembly and the shorter comparison assembly were poisoned with additional stainless steel, one 2-mil, 11-3/4 × 24-in. sheet per slot, to bring the critical temperature of the shorter core closer to room temperature. The shorter core was heated to its critical temperature with heat lamps only. Table III-1 gives the vital statistics of the above experiments: the number of layers in the north and south halves of the core, the measurement between the cruciform and the inside of the pusher plate north and south (at room temperature), and the resulting critical temperatures.

Table III-1. Preliminary Results of New Bare-BeO High-Temperature Critical Experiments.

BeO/U^{235}	Description	N, S	L_n (in.)	L_s (in.)	T_c (°F)
560:1	Blocks against cruciform				
	long	16,16	16-3/4	16-3/4	1115
	short	15,15	15-23/32	15-23/32	360
560:1	Blocks against side walls				
	short	15,16	15-23/32	16-3/4	420
	long	16,16	16-3/4	16-3/4	785
280:1	Blocks against side walls				
	short	14,13-1/2	14-27/32	14-11/32	90
	long	14,14-1/2	14-27/32	15-3/8	850

CONCLUSIONS

Placing the BeO blocks against the side walls instead of the cruciform did not decrease the magnitude of the temperature coefficient of reactivity significantly, even though there was a definite decrease in room-temperature reactivity accompanying the change. The present experiments are in excellent agreement in temperature coefficient with the previous experiment (UCRL-6329) in spite of the different arrangement of fuel elements.

Finally, the temperature coefficient of reactivity for the 280:1 BeO/U^{235} ratio assembly was, as expected, a little more than one-half that of the 560:1 ratio assembly, following the same rough proportionality to moderator-to-U^{235} ratio as did the graphite experiments (UCRL-6504).

GRAPHITE-MODERATED ASSEMBLIES

Preliminary results from experiments with graphite-moderated assemblies constructed in the Hot Box facility covering the entire range of graphite-to-fuel ratios attainable were reported in UCRL-6516. These results have subsequently been refined and the corrected experiments used to check the accuracy of 9-Zoom calculations to predict the temperature dependence of reactivity. The calculations were made with eighteen energy groups, using

library tape material cross sections. Comparison of calculated and experimental differential temperature effects showed that the calculations consistently over-predict the nuclear temperature dependence by 25 to 55%.

The corrected experimental densities, temperatures, and critical heights used in the calculations are listed in Table III-2. Included are corrections for room return, poisoning due to the presence of thermocouples in the assembly, and the effect of external apparatus necessary for the removal of fuel elements.

The calculated k_{eff} for each assembly critical at room temperature is plotted in Fig. III-2. The marked deviation from unity, particularly with the larger assemblies is regrettable, but is not expected to interfere seriously with calculations of the differential effect of temperature on reactivity.

As a measure of the experimental effect and a standard for comparison with calculations, k_{eff} was calculated for each assembly, first with the room-temperature critical height and again with the height of the overstacked assembly which becomes critical at the determined high temperature. Room-temperature transfer coefficients were used for both sets. The difference between these values is the gross excess reactivity at room temperature to be overcome by elevating the temperature (column 7, Table III-2).

The extent to which thermal expansion alone contributes to the temperature effect is called the buckling effect (column 8, Table III-2). Its contribution was calculated by using the graphite linear thermal expansion curve of UCRL-6516 to convert the assembly dimensions to their high-temperature values and then reducing the density correspondingly. k_{eff} is calculated for the resulting assembly using the same cross sections as for the room-temperature case. The buckling effect is greatest (20%) in the smallest assembly where neutron leakage during slowing down is a relatively important factor, and decreases rapidly as the assembly size increases. This portion of the reactivity change is derived from the experimentally measured thermal expansion of graphite and should be subtracted from the gross reactivity change to leave the portion due to the changing neutron energy spectrum (column 9, Table III-2).

The major effect of temperature on reactivity is through changing the neutron energy spectrum in the assembly. Absorption cross sections for low-energy neutrons vary rapidly with neutron energy, and consequently competitive absorption processes are very energy-sensitive. The neutron energy spectrum

Table III-2. Corrected Hot Box Graphite Assemblies.

C/U^{235} Atomic ratio	ρ Graphite density (g/cm^3)	L × W[a] (feet)	T_c °F	H_c[b] (inches)	k_{eff}	Δk_{exp} (Experimental excess reactivity at room temp	Δk Buckling effect only	Δk_{exp} Nuclear only	Δk Calc. (room temp minus high temp)	Over-prediction of calculation (% nuclear effect)
1,184	1.4658	4 × 5	63	50.4	1.0280					
			850	52.6	1.0237	0.0168	0.0034	0.0134	0.0043	32.1
2,380	1.4731	4 × 5	46	59.0	1.0147					
			950	65.7	1.0007	0.0341	0.0040	0.0301	0.0140	46.5
			(1620)[c]	69.7	0.9910	0.0505	0.0079	(0.0426)	0.0237	55.6
7,164	1.4781	6 × 6	66	54.8	0.9807					
			85	61.1[d]	0.9822					
			1110	72.2[d]	0.9599	0.0599	0.0040	0.0559	0.0223	40.0
8,956	1.4781	6 × 6	50	62.0	0.9716					
			880	74.1	0.9466	0.0662	0.0032	0.0630	0.0250	39.7
9,546	1.4770	6 × 6	66	63.3	0.9605					
10,760	1.4799	6 × 6	60	71.5	0.9590					
14,440	1.4897	8 × 8	81	61.0	0.9337					
			723	68.8	0.9170	0.0563	0.0023	0.0540	0.0167	31.0
			1060	72.7	0.9144	0.0791	0.0035	0.0756	0.0193	25.5
16,850	1.4897	8 × 8	51	68.7	0.9235					
			961	83.3	0.9014	0.0718	0.0029	0.0689	0.0221	32.1
21,690	1.4919	8 × 10	46	78.8	0.8914					
			552	88.8	0.8786	0.0392	0.0013	0.0379	0.0128	33.8

(a) These dimensions are accurate to 0.050 inch.

(b) All dimensions reported are for 70°F.

(c) Estimated by extrapolation.

(d) Extra 2.41-kg of stainless steel (type 304) per kg of oralloy present in the form of tubes.

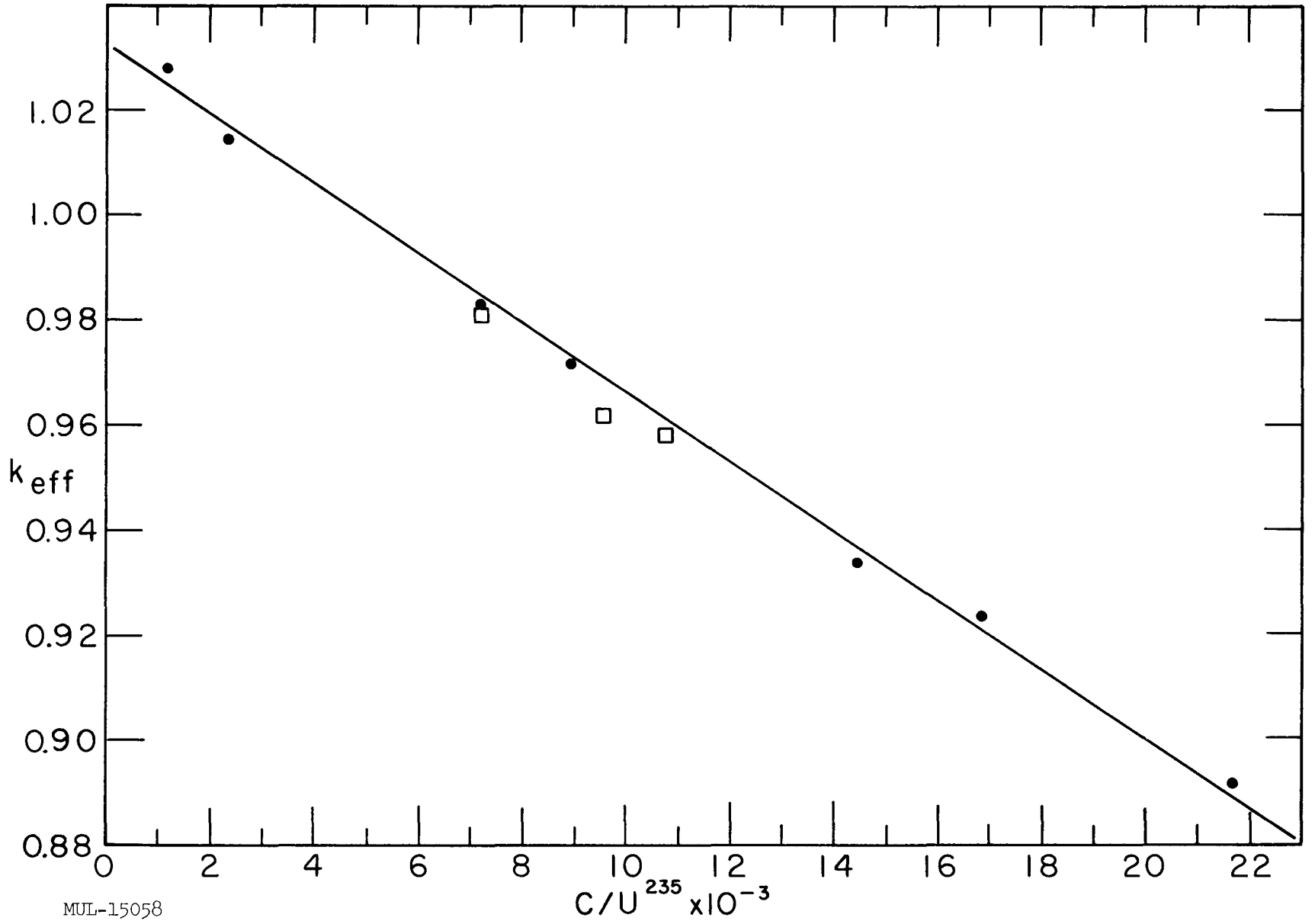

Fig. III-2. Hot Box assemblies critical at room temperature. Squares mark assemblies not made critical at high temperatures.

in these calculations was influenced by varying the transfer coefficients which control the rate at which neutrons are transferred between energy groups. The cross sections and cell factors (used to correct for flux depression in the fuel foils), were taken as temperature independent.

An accurate calculation of the temperature effect on reactivity would give the same k_{eff} for both room-temperature and high-temperature assemblies since criticality was achieved in each case. In actual practice the k_{eff} calculated at high temperatures is always seen to be lower than that calculated at room temperature. The difference between these values is given in the last column of Table III-2, expressed as percent of the experimental nuclear effect. These experiments clearly show that 9-Zoom calculations, using library tape transfer coefficients, overpredict the nuclear temperature dependence of reactivity by 25 to 55%.

CHAPTER IV. TORY II-C

SECTION I. NEUTRONICS

During the present quarter two tasks relating to the neutronic calculations of the Tory II-C reactor were completed.

1. A detailed study of the reactor configuration was made. The importance of this study stems from the fact that this summary of an up-to-date reactor description has been used to bring Tory II-C machine code representations numerically into agreement with the confirmed status of the reactor. Thus, methods of interpretation pertaining to geometry and constituent materials, have been documented and will be open to suggestions and criticism.

2. Radial and axial fuel maps have been prepared. Based on reactor representations in codes, as they evolved from the above study of the reactor configuration, fuel maps exhibit the best radial and axial fuel class assignments for the present reactor configuration. This marks the first time that step-by-step procedures have become established to outline the complex process which leads to the final picture of radial and axial fuel class assignments. A summary of the outline follows:

PREPARATION OF FUEL LOADING MAP FOR THE TORY II-C REACTOR

The Tory II-C reactor signifies several significant advances in the progress towards the construction of a nuclear ramjet. In contrast to the Tory II-A-1 reactor, the advanced version exhibits not only a radial variation of the fuel loading, but also includes a variation of fuel in the axial direction. The latter permits more advantageous operation of such a vehicle because of the optimized axial power distribution.

Specifically, in order to achieve a maximum power efficiency with fuel elements of identical flow orifices, a flat radial power profile is anticipated, while the axial power profile is planned to be of a shape as shown on Fig. III-2 of Pluto Quarterly Progress Report No. 7.

In order to achieve a flat radial power profile, certain fuel-element classes are assigned to certain annuli such as to correspond as closely as possible to an idealized smooth radial fuel allocation.

For the axial fuel distribution, the desired power profile is achieved by an axial variation of fuel in layers, or axial loading stations. These axial

loading stations have the same, or nearly the same, boundaries between radial fuel classes, however, all classes in any one layer are shifted by one, two, or three classes with respect to the corresponding classes of adjacent axial fuel layers. The axial fuel layer nearest to the inlet BeO reflector has the highest over-all fuel loading.

Basic Assumptions:

Several basic assumptions form the premise for the formulation of the power profiles and the correlated fuel loading distributions;

1. The reactor configuration used is that of August 17, 1961.

2. A nominal core radius at room temperatures of 23.625 in. is assumed. Expansion due to camber and twist enter via an adjustment of the over-all critical mass, as discussed on page 96 of Pluto Quarterly Report No. 8, (UCRL-6516).

3. Fuel loading classes are shown in Table IV-1. Adjacent classes differ in fuel content by 8% (by weight).

4. The effect of control rods, or of oversize control rod tension tubes, upon power profiles has not been taken into account. While the perturbation due to the latter is small, the effect of partially inserted control rods on the power profiles is significant.

5. Distribution of R-235 and René-41 tension tubes in the core is assumed to be at random. The reader will recall that these two materials of different neutron-absorbing capability have been selected to provide means of adjusting not only reactivity, but also radial power profiles. The mass ratio of René-41 to R-235 is about 2:1.

6. Base problems of machine calculations used in the preparation of the fuel maps have neutronic densities in the active core which are characteristic of the typical, symmetric, hexagonal tension-tube modules. The simplification introduced by this method is thought to be more important than the slight reactivity and power perturbations caused thereby.

7. The axially integrated power per tube column is considered to represent the main criterion for design for the assignment of fuel classes. This consideration is quite essential because of its immediate effect upon the temperatures of the gas stream at the base plate. Inasmuch as 2180°F is not to be exceeded by the exit gas, optimum efficiency of the system can only be achieved with an axially integrated power per tube column as uniform as it is practical to achieve.

Table IV-1. Tory II-C Fuel Tube Distribution at Different Axial Stations.

Class av fuel wt per in. (g of OyO_2)	Fuel Tube Running Length at Various Axial Stations (inches × 10^3)							
	Station 1 (2.6 in. av length)	Station 2 (3.9 in. av length)	Station 3 (3.9 in. av length)	Station 4 (3.9 in. av length)	Station 5 (3.9 in. av length)	Station 6-14 (32.5 in. av length)	Total all stations	Fuel Mass (kg of OyO_2)
0.0188	--	--	--	--	--	22.230	22.2300	0.4179
0.0203	--	--	--	--	4.3992	43.485	47.8842	0.9720
0.0219	--	--	--	4.3992	5.3586	33.345	43.1028	0.9440
0.0237	--	--	--	5.3586	3.8610	30.615	39.8346	0.9441
0.0256	--	--	4.3952	3.8610	4.0716	40.755	53.0868	1.3590
0.0277	--	--	5.3586	4.0716	4.1418	21.450	35.0220	0.9701
0.0299	--	4.3992	3.8610	4.1418	3.3462	41.535	57.2832	1.7128
0.0324	--	5.3586	4.0716	3.3462	4.9608	38.025	55.7622	1.8067
0.0350	2.9328	3.8610	4.1418	4.9608	4.2822	33.735	53.9136	1.8870
0.0379	3.5724	4.0716	3.3462	4.2822	4.5162	37.635	57.4236	2.1764
0.0409	2.5740	4.1418	4.9608	4.5162	3.8220	30.095	50.1098	2.0495
0.0442	2.7144	3.3462	4.2822	3.8220	3.9624	36.595	54.7222	2.4187
0.0479	2.7612	4.9608	4.5162	3.9624	5.0154	40.755	61.9710	2.9684
0.0518	2.2308	4.2822	3.8220	5.0154	5.0544	63.765	84.1698	4.3600
0.0560	3.3072	4.5162	3.9624	5.0544	8.8452	46.800	72.4854	4.0592
0.0606	2.8548	3.8220	5.0154	8.8452	7.6986	120.705	144.6588	8.7663
0.0656	3.0108	3.9624	5.0544	7.6986	8.4474	--	28.1736	1.8482
0.0710	2.5480	5.0154	8.8452	8.4474	--	--	24.8560	1.7648
0.0769	2.6416	5.0544	7.6986	--	--	--	15.3946	1.1838
0.0832	3.3436	8.8452	8.4474	--	--	--	20.6362	1.7169
0.0901	3.3696	7.6986	--	--	--	--	11.0682	0.9972
0.0976	5.8968	8.4474	--	--	--	--	14.3442	1.4000
0.1058	5.1324	--	--	--	--	--	5.1324	0.5430
0.1147	5.6316	--	--	--	--	--	5.6316	0.6459
0.1243	--	--	--	--	--	--	0	47.9119 kg Total fuel mass

MUL-15053

In order to prevent oscillations of the gas stream which would reflect the discrete class jumps of 8% in fuel content, radii between fuel classes are not kept alike throughout the length of the active core. Instead, boundaries between classes are shifted outward by a certain distance in the upstream section of the core, and are shifted inward by that very same amount in the downstream section of the core. The shift corresponds to 1/4 of the distance between boundaries of the adjacent outer fuel class. Although the front section extends only over 40% of the active core length, it contributes half of the total power developed in the reactor. The above determination of delimiting radii between fuel classes, therefore, does not affect significantly the overall power of the system.

Summary of Effects which Cause Perturbations of Power Profiles

Certain power perturbations either were not, or could not be, included in neutronic machine calculations. The effects of these parameters enter our considerations, therefore, as perturbations or corrections of a basic power profile.

The basic power profile is taken from a machine problem which includes the side support structure of 20.14 g/cm^2. Fuel variations in the radial and axial plane are also included. The gamma-ray heating distribution is typical of items not implicit in the neutronic calculations.

The miscellaneous perturbations of the power profiles, and the resulting corrections to the fuel loading, are summarized in Table IV-2.

Table IV-2. Perturbations of Power Profiles.

No.	Subject	Radial	Axial	Comments
1	0.942-in.-thick nickel shim	X		
2	Gamma and neutron heating	X	X	
3	Side reflector at 1100°K	X		
4	Requested 16.8% power drop-off in outer tube layer	X		Corrections apply to final maps, requested by aero-thermodynamics group
5	20.14 g/cm^2 side support structure	X		Included in base problem
6	Axial temperature gradient		X	
7	Effect of front support structure		X	Negligible
8	Effect of rear base plate		X	Not significant
9	Front reflector SS-inserts		X	Included in axial base problem
10	Upstream axial power deviation		X	Experimental finding from Tory II-A-1
11	Axial stagger of columns		X	Not considered

Determination of the Radial Fuel Distribution

The first three perturbations, as listed on the preceding table, must be taken into account prior to the formulation of boundaries between fuel classes. A graphical representation of the composite deviation from a flat power average due to these perturbations is illustrated by Fig. IV-1.

Inasmuch as a 1% increase in local fuel density causes, in general, the power to increase also by 1%, deviations in percent from flat radial power are applied in the opposite sense to correct the radial fuel profile. The corrected resultant profile is shown on Fig. IV-2. The range of fuel classes is also entered on this graph. Intercepts between the delimiting fuel concentrations in each class and the distribution profile render idealized, average boundaries between fuel classes. However, these boundaries are not final. As mentioned before, radii are shifted slightly outward and inward in the front and after sections of the core, respectively. The resulting stagger of boundaries helps to decrease power and temperature variations in the exit gas stream.

Once the idealized radial boundaries for the upstream and downstream regions of the active core are established, it remains to determine equivalent zig-zag boundaries between actual fuel tubes in the radial plane. This has been done on Fig. IV-3 which shows a typical fraction of the core, i.e., one-sixth. Specifically, Fig. IV-3 depicts boundaries and fuel classes for the downstream region of the core, or that fuel map which is common to downstream axial stations.

At this point in our procedure to determine radial and axial fuel assignments, the anticipated axial power profile must be approximated by discrete fuel class shifts between axial fuel stations. This method, similar to that which leads to radial class assignments, is outlined in the next section.

Determination of the Axial Fuel Distribution

Fuel variation in the axial direction occurs in six steps. Because of fuel-tube stagger in the axial direction, it is necessary to specify six fueling planes whereby all tubes intersected by a fueling plane have a common radial fueling map. All tubes intersected by the last (sixth) plane, as well as all tubes aft of the plane, have a common fueling map. The minimum fuel variation possible is 8% by weight of fuel (OyO_2). For some steps a 16% by weight (of fuel) variation is necessary.

The first five axial loading stations have distinct fuel loading maps. All stations thereafter are characterized by one and the same fuel loading map.

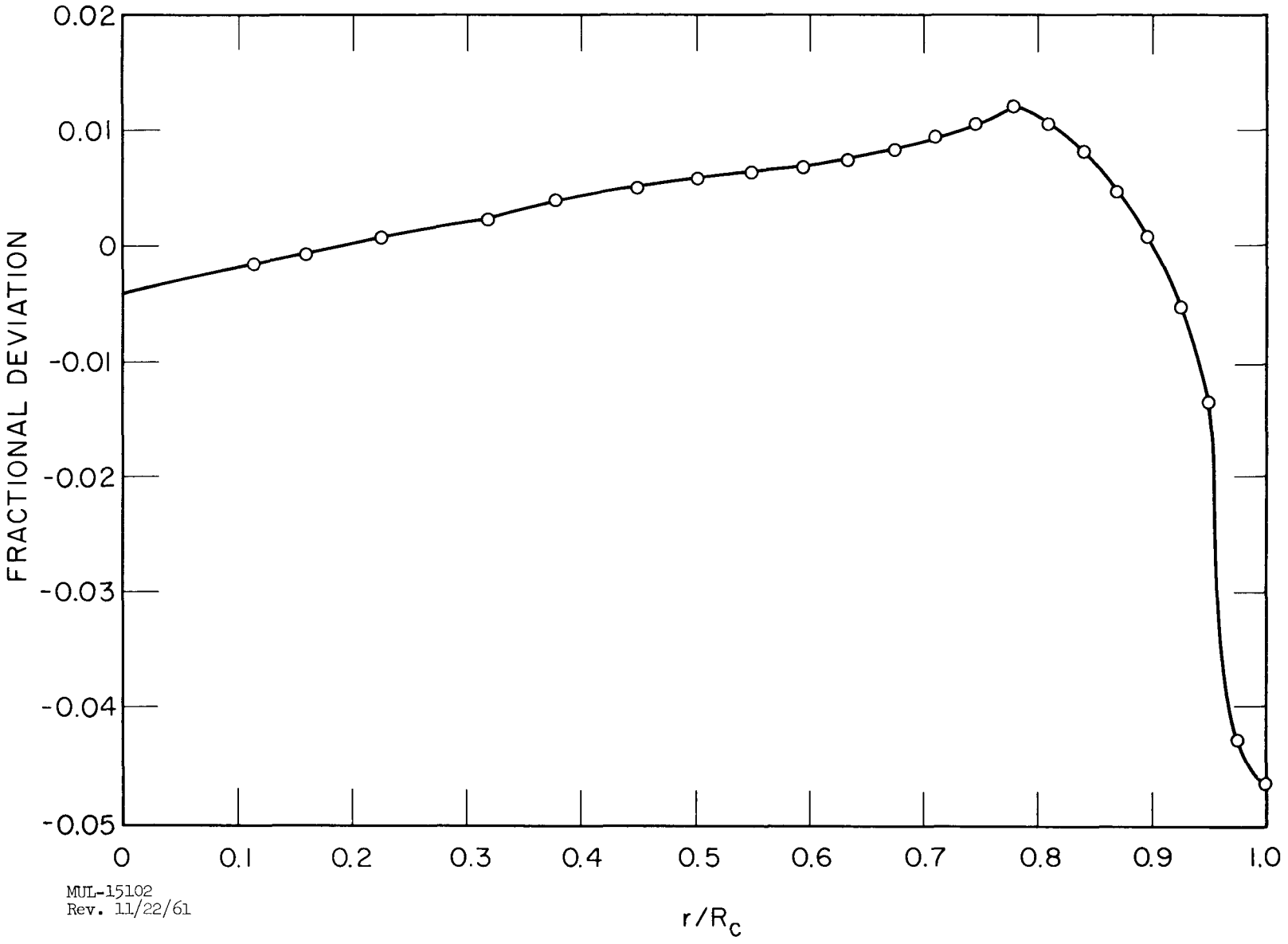

Fig. IV-1. Total deviation of axially integrated power density from a flat profile in radial direction of active core. (Fractional deviation vs r/R_c, where R_c = 23.625 in. at ambient room temperature.)

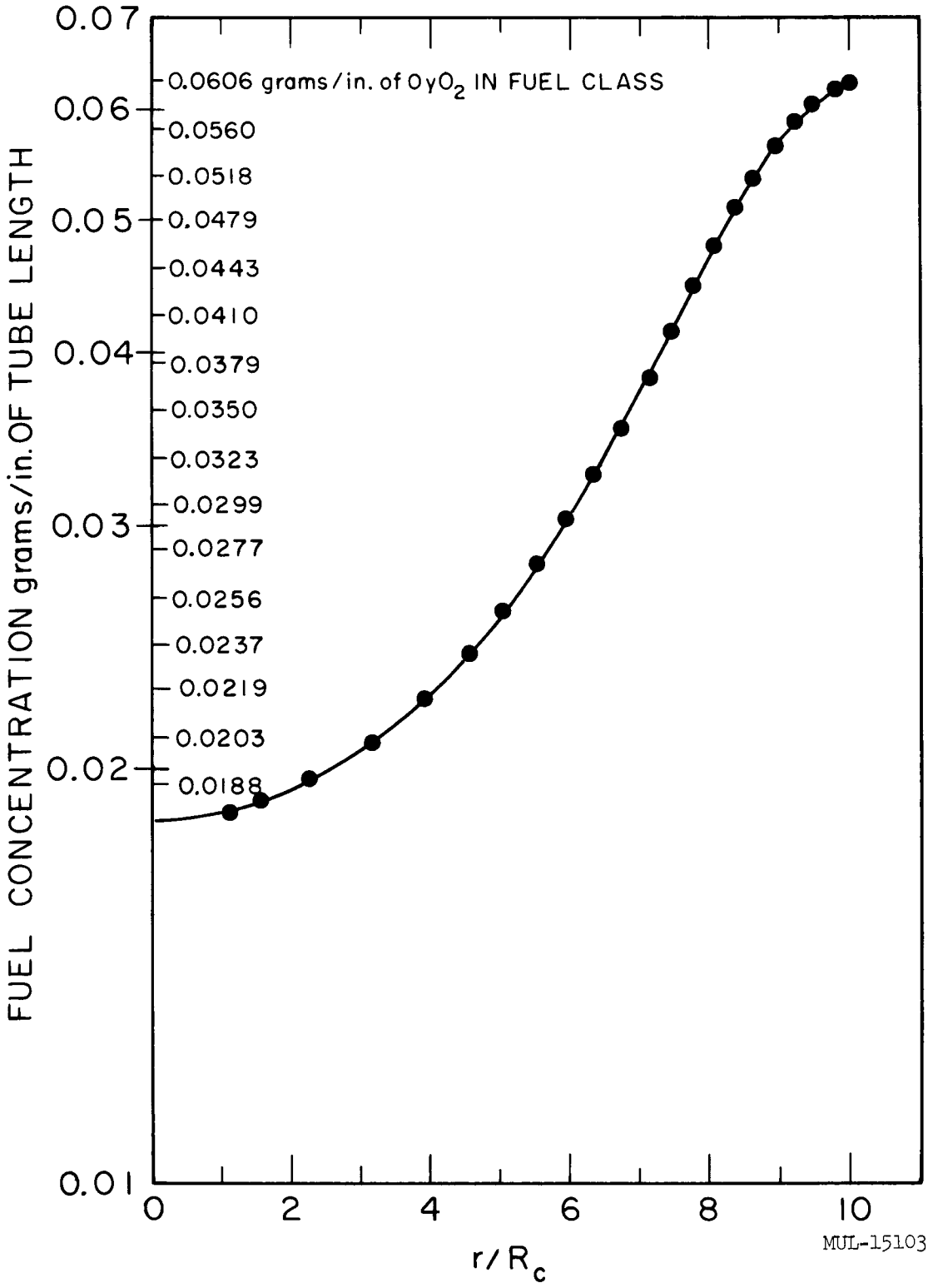

Fig. IV-2. Final corrected fuel concentration as a function of distance from core center. Numerical values pertain to downstream fuel loading stations of core, i.e., fuel loading stations 6 through 14. (R_c = 23.625 in. at ambient room temperature.)

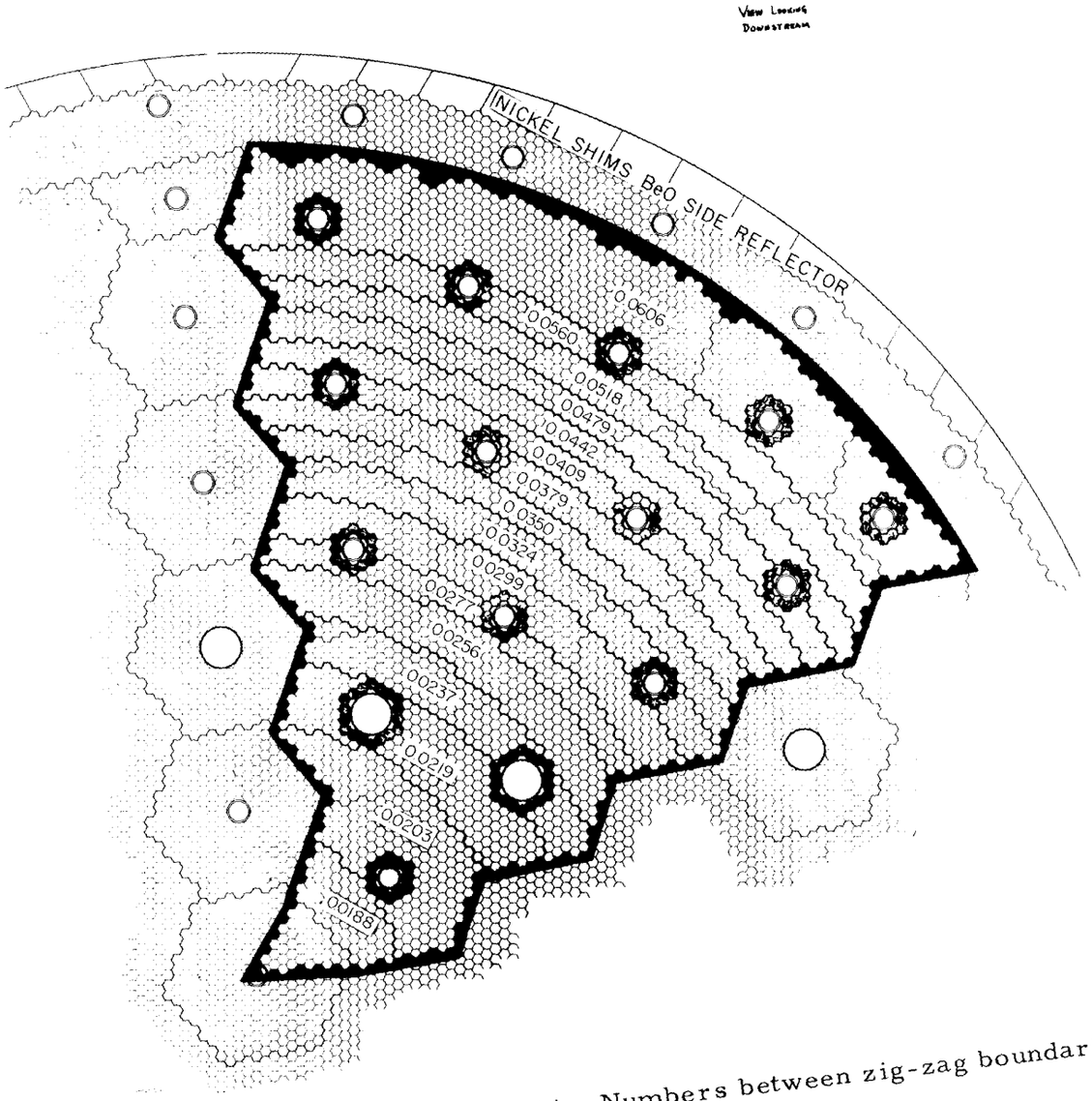

Fig. IV-3. Fuel map for station 6 through 14. Numbers between zig-zag boundaries specify fuel tube classes by the weight of O_yO_z in grams per inch length of tube.

Stations are identified by loading patterns which apply to all tubes which intersect certain axial planes. Axial positions of these planes are measured from the front reflector core interface, as shown in Table IV-3.

Table IV-3.

Station	Dist. from FR-core interface (in.)	Axial loading map	Equivalent width, in.*
1	1.00	I	2.925
2	4.925	II	3.925
3	8.850	III	3.925
4	12.775	IV	3.925
5	16.700	V	3.925
6	20.625	VI	3.925
7	24.550	↓	↓
8	28.475	↓	↓
9	32.400	↓	↓
10	36.325	↓	↓
11	40.250	↓	↓
12	44.175	↓	↓
13	48.100	↓	↓
14	49.700 (Stub)	↓	1.300

* Dimensions at room temperature.

This arrangement of axial stations results in equivalent widths of each successive tube layer as shown in the last column of Table IV-3. Note the shorter width of the first upstream layer of 2.9 in. The smaller dimension permits a better adjustment of fuel classes in the upstream region of the core.

Similarly as in the procedure for the preparation of the radial fuel map, those perturbations are considered which either were not or could not be included in the base problem as perturbations to the power profile. The resultant deviation from the desired axial power shape is a measure of the corrections which are to be applied to the axial fuel distribution. In Table IV-2, which lists the different power perturbations yet to be considered, it is noted that only the following perturbations must be taken into account:

1. The deviation of the base problem from the desired power profile.
2. Local variations of gamma and neutron heating.
3. Axial temperature gradient corrections. (Angie problems utilize the theoretical volume, weighted average core temperature in the description of the core, although the core temperature of Tory II-C will vary axially.)

4. Upstream axial power deviation from calculated values. (This is a correction which arises from a comparison between predicted and measured axial power densities of the Tory II-A reactor. Refer to page 11 and Figure I-5 of Pluto Quarterly Report No. 7.

The composite deviation from the anticipated axial power profile, due to all of the above causes is shown in Fig. IV-4. It is noted that the deviation oscillates with an amplitude of about ± 2%, that is, corrections to the axial fuel distribution should be almost 2% at certain axial stations. Yet we recall that the smallest fuel change permissible is that between two adjacent classes, which is 8%, so that an axial change in fueling over that of the base problem is not appropriate. Thus, the axial fueling pattern used is retained: a 2-class jump between loading planes one and two, two and three, and three and four; and a 1-class jump between loading planes four and five, and five and six. Loading plane six is identified by the loading plane which is 20.625 in. downstream of the front reflector-core interface. The radial fueling map appropriate to this plane is to be used for all tubes downstream of this plane. Fig. IV-3 shows this fuel map.

The above axial fuel class assignment is based on the notion that shim control rods are fully withdrawn.

Summary of Radial and Axial Fuel Class Assignments

The procedures for radial and axial fuel class assignments as outlined in the preceding sections leads to a summary of fuel class requirements as summarized in Table IV-1. In this table the requirements of fuel tube classes in each axial fuel layer are noted in running inches, rather than in tube numbers. The incremental class increase between adjacent fuel layers mentioned earlier is clearly recognized. Similarly, the total requirements in each fuel class are shown. We note that 24 fuel-tube classes are utilized with the greatest numerical demand in the class with 0.0606 grams of OyO_2 per inch of tube, which corresponds to 3.43 weight percent of OyO_2. The highest loading registered is 6.34 weight percent.

A graphical illustration of fuel class assignments as listed in Table IV-1 is shown in Fig. IV-5. Six different radial fuel allocations are distinguished which pertain to the first five axial stations and to those of the remaining downstream section of the active core. This representation depicts the latest fuel loading of Tory II-C in Angie two-dimensional machine code calculations. The description shown supercedes that of Fig. III-3 of Pluto Quarterly Report No. 7.

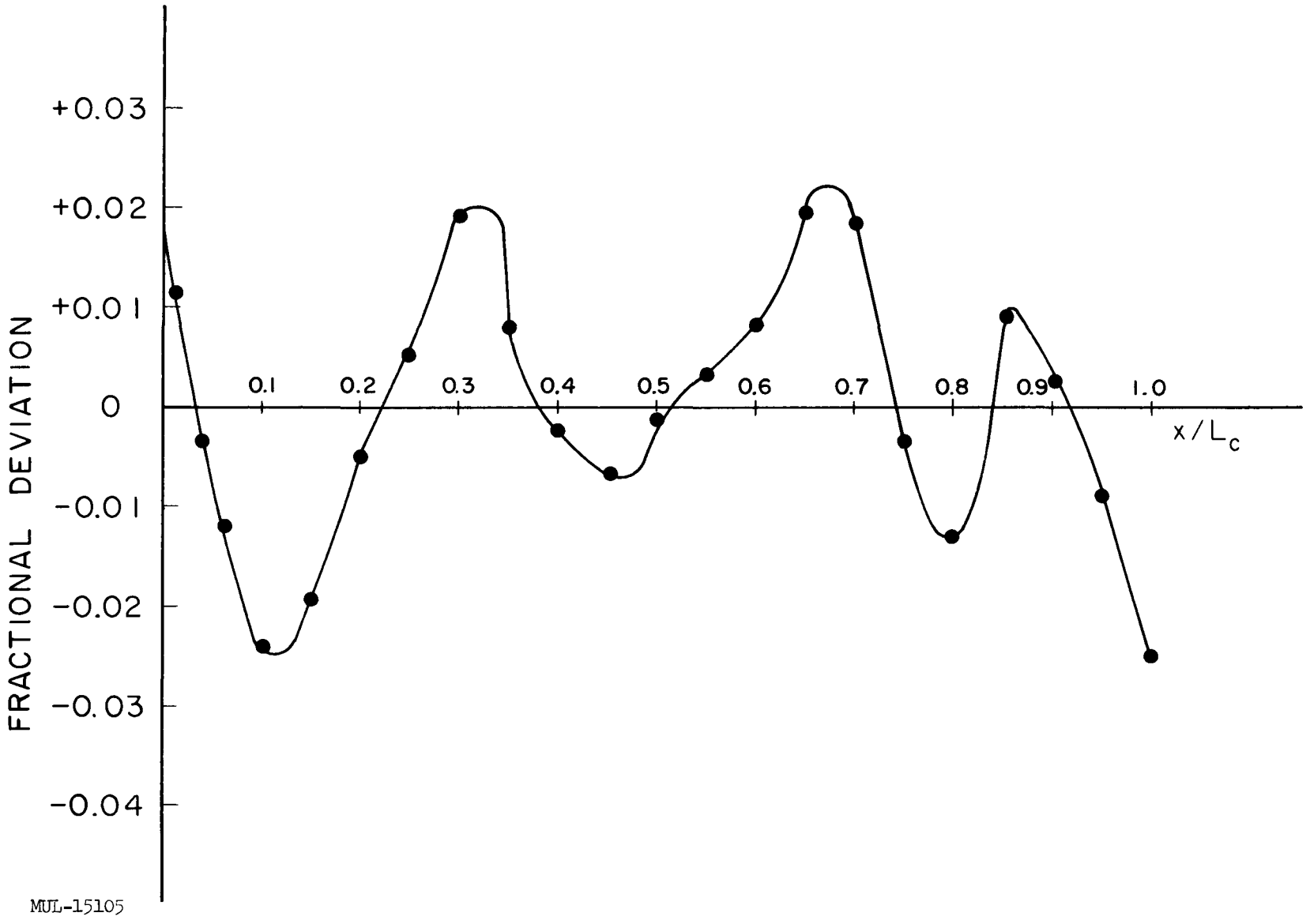

Fig. IV-4. Deviation of axial power from anticipated power profile. L_c = 50.7 in. at ambient room temperature.

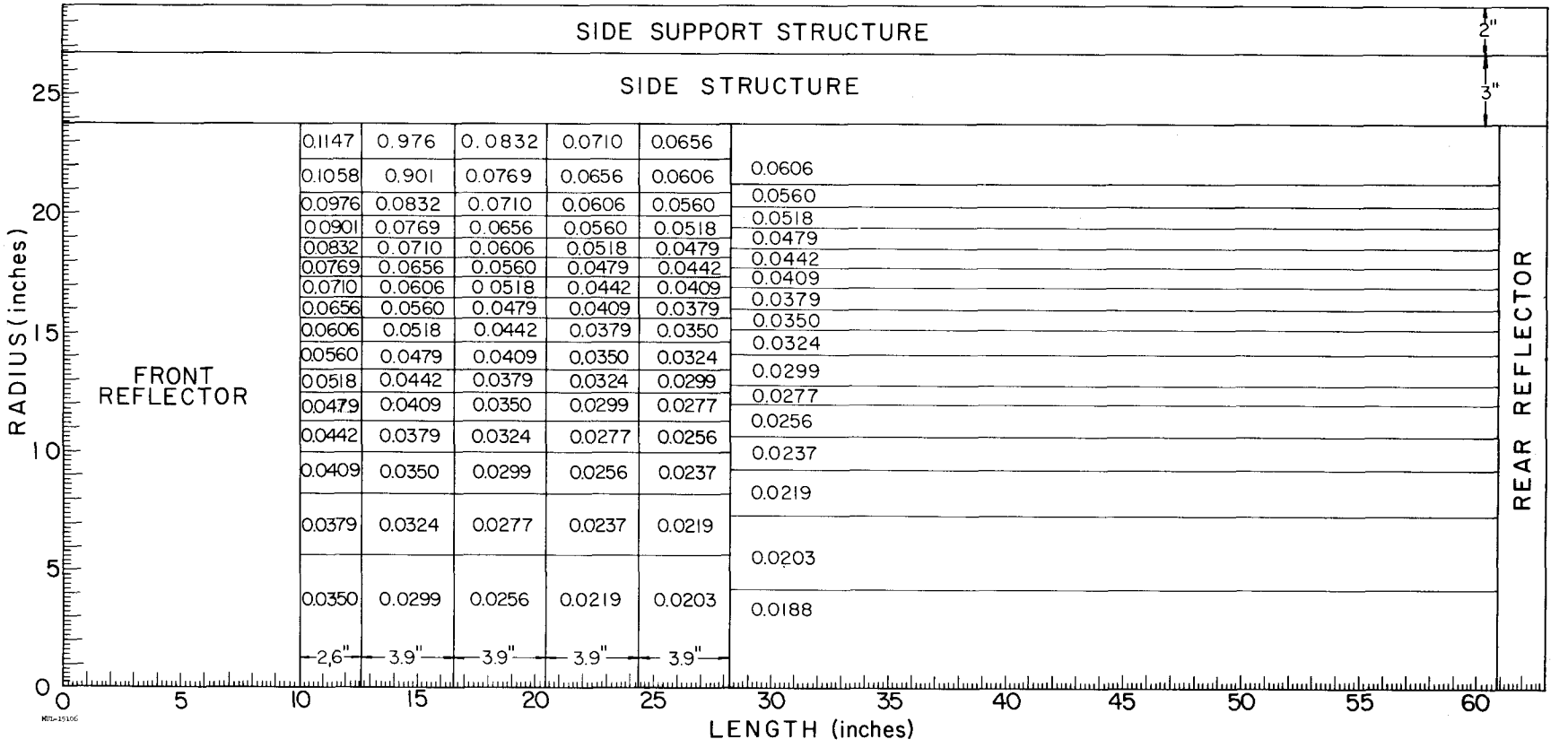

Fig. IV-5. Tory II-C: Angie representation showing fuel tube class in each core region. Fuel tube class is in terms of average $O_y O_2$ weight in grams per inch of length.

On the basis of this summary, a total of 47.9 kg of OyO_2 are realized in the Tory II-C core. This is felt to be within 4 kg of the critical mass of the reactor at high-power operation. Equivalently, the reactor should be within a $\Delta K = \pm 0.01$ from the critical condition.

The Effect of Partially Inserted Shim Control Rods on Power Profile

Radial and axial fuel maps as determined by the procedures which were outlined above were performed on the assumption that shim control rods are fully withdrawn from the core. However, in anticipation of a flyable ramjet, xenon poison effects must be considered. This necessitates partial insertion of shim rods during start-up with a gradual withdrawal during the specified 10-hour operating period of the reactor. This xenon poisoning was estimated by Zoom calculations to be $(\Delta k/k)_{Xe} = -0.025$ for this duration (UCRL-6376, p. 79). In consideration of this time-dependent poisoning effect, it appears advisable to specify the fuel loading, taking into account the poison build-up during 5 operating hours. To put it differently, we wish to account for the power disturbance caused by partially inserted shim rods having a reactivity worth equivalent to about $\Delta k = -0.0125$.

In addition, an excess capability of 0.5% in the multiplication factor should be included for miscellaneous control requirements. Thus, radial and axial fueling of the Tory II-C reactor should be designed for a shim rod insertion depth equivalent to -0.0175 in the multiplication factor, 5 hours after start-up.

Obviously, the presence of poison rods in the active core has a pronounced effect upon the power profile adjacent to these rods. However, of greater importance to the reactor operation is the concurrent rise of the volume-weighted local power density in the downstream section of the active core. This dependence is shown in Fig. IV-6 where isopower lines are drawn for a shim rod insertion depth equivalent to $\Delta k = -0.016$.

NUCLEAR HEATING OF TORY II-C HAFNIUM CONTROL RODS

Use has been made of the Yogi Monte Carlo code to determine the heating of the hafnium control rods in the Tory II-C reactor by gamma radiation from various sources.

A. External Source

The results obtained for the heating of the rods by fission gamma rays are listed in Tables IV-4 and IV-5. In these problems, the source spectrum

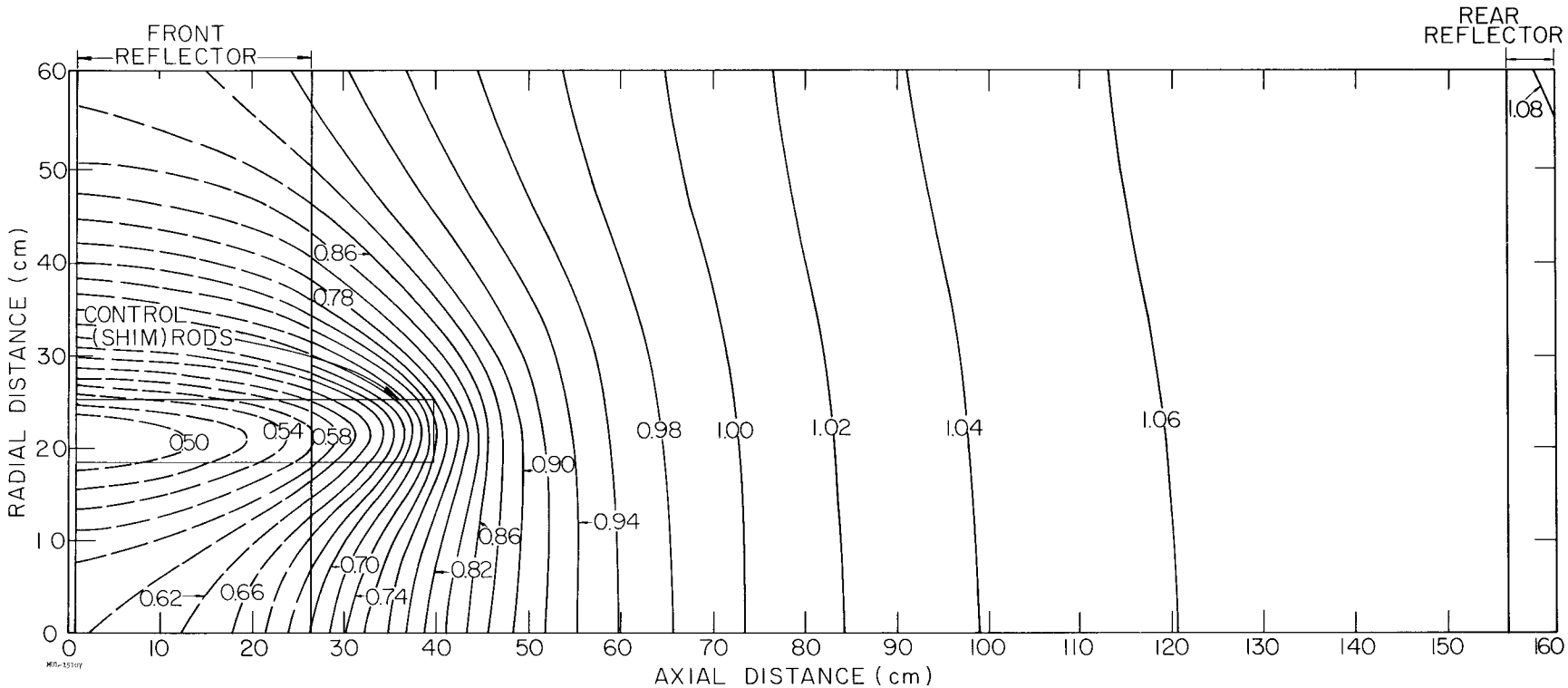

Fig. IV-6. Ratio of local power density in reactor containing partially inserted rods to that containing no rods. (Both configurations at equal power.) Control rod worth = $\Delta k/k$ = 1.59%.

Table IV-4. External Source.

Problem	Rod description	Cell size (in. × in.)	BeO:U^{235}	In cell, area (in^2) of rod	In cell, area (in^2) of moderator	f(a)	H(b)	Description of cell
1	cruciform,	2 × 2	951:1	0.0586	3.94	0.181	0.94	rod in direct
2	1/8 in. × 1/2 in. blades	2 × 4			7.94	0.099	1.04	contact with
3		2 × 8			15.94	0.047	1.00	fueled moderator
4	cruciform, 1/16 in. × 1/2 in. blades	2 × 4	951:1	0.0303	7.97	0.074	1.51	same as 1-3 except for rod thickness
7	slab, 1/8 in. ×	$2.06 \times (3.94 \times 10^9)$	951:1	2.46×10^8	7.87×10^9	0.352	0.87	slab in direct
9	3.94×10^9 in.	$4.06 \times (3.94 \times 10^9)$			15.75×10^9	0.216	1.07	contact with
11		$8.06 \times (3.94 \times 10^9)$			31.5×10^9	0.117	1.16	fueled moderator
13	asterisk, 0.08 in. × 1/2 in. blades	2 × 4	951:1	0.0572	7.94	0.103	1.10	rod in direct contact with fueled moderator
17	(See Fig. IV-7a)				7.78	0.099	1.04	rod separated from moderator by rectangular cavity containing air(c)

(a) f = fraction of source energy deposited in rod.

(b) H = average heating of rod in Mw/ft^3 per Mw/ft^3 local power density. See text for explanation and discussion.

(c) In all cases in which a cavity containing air exists, the fraction of energy deposited in air < 0.001.

Note:

1. 10^4 particles were followed in each problem.
2. At ratio of BeO:U = 951:1, the molecular density of BeO is 3.18×10^{22} cm^{-3}; at all other ratios, the molecular density of BeO is 2.95×10^{22} cm^{-3} (corresponding to a change in module).

Table IV-5. External Source[a] — Continued.

Problem	$BeO:U^{235}$	In cell, area (in ^{2}) of				Fraction of source energy deposited in				Heating (Mw/ft^3 per Mw/ft^3) of				Description of cell
		Rod	Moderator	Hastelloy[b] R-235	Unfueled BeO	Rod	Hastelloy R-235	Unfueled BeO	Tie tube	Rod	Hastelloy R-235	Unfueled BeO	Tie tube	
26	951:1	0.0586	7.75	--	--	0.102				1.04				same as 17, but asterisk replaced by cruciform
27			7.71	0.0296	--	0.093	0.024			0.95	0.48			rectangular Hastelloy shell separates air cavity from fueled moderator
29			7.35	0.0296	0.357	0.091	0.023	0.020		0.88	0.45	0.03		pure BeO rectangular shell surrounds Hastelloy
31	951:1	0.0586	7.35	0.0296	0.357	0.090	0.024	0.019		1.02	0.54	0.04		same as 29, but new input source distribution used — 90% fission product saturation
34	423:1	0.0586	7.35	0.0296	0.357	0.089	0.020	0.019		1.01	0.45	0.04		same as 31 except for BeO:U.
33						0.083	0.020	0.019		0.94	0.45	0.04		same as 34, but Hastelloy[c] smeared throughout moderator medium
35	423:1	0.0586	7.35	0.0296	0.357	0.079	0.020	0.017		0.90	0.45	0.03		same as 33, but fueled moderator has density of that adjacent to control rod
37	423:1	0.0586	7.06	0.0296	0.357	0.095	0.021	0.022	0.022	1.03	0.44	0.04	0.47	same as 34, but rectangular Hastelloy tie tube added 4 in. from control rod

(a) In all cases, the rod was described by a cruciform with 1/8 in. × 1/2 in. blades in a cell of dimensions 2 in. × 4 in. (see Fig. IV-7b).

(b) Hastelloy surrounding the control rod. The areas of the Hastelloy surrounding the rod and the tie tube 4 in. away were the same; a change in density of the tie tube was made to account for its smaller size.

(c) In Problems 33 and 35, Hastelloy R-235 was smeared throughout fueled moderator medium to represent the normal tie tubes.

MUL-15055

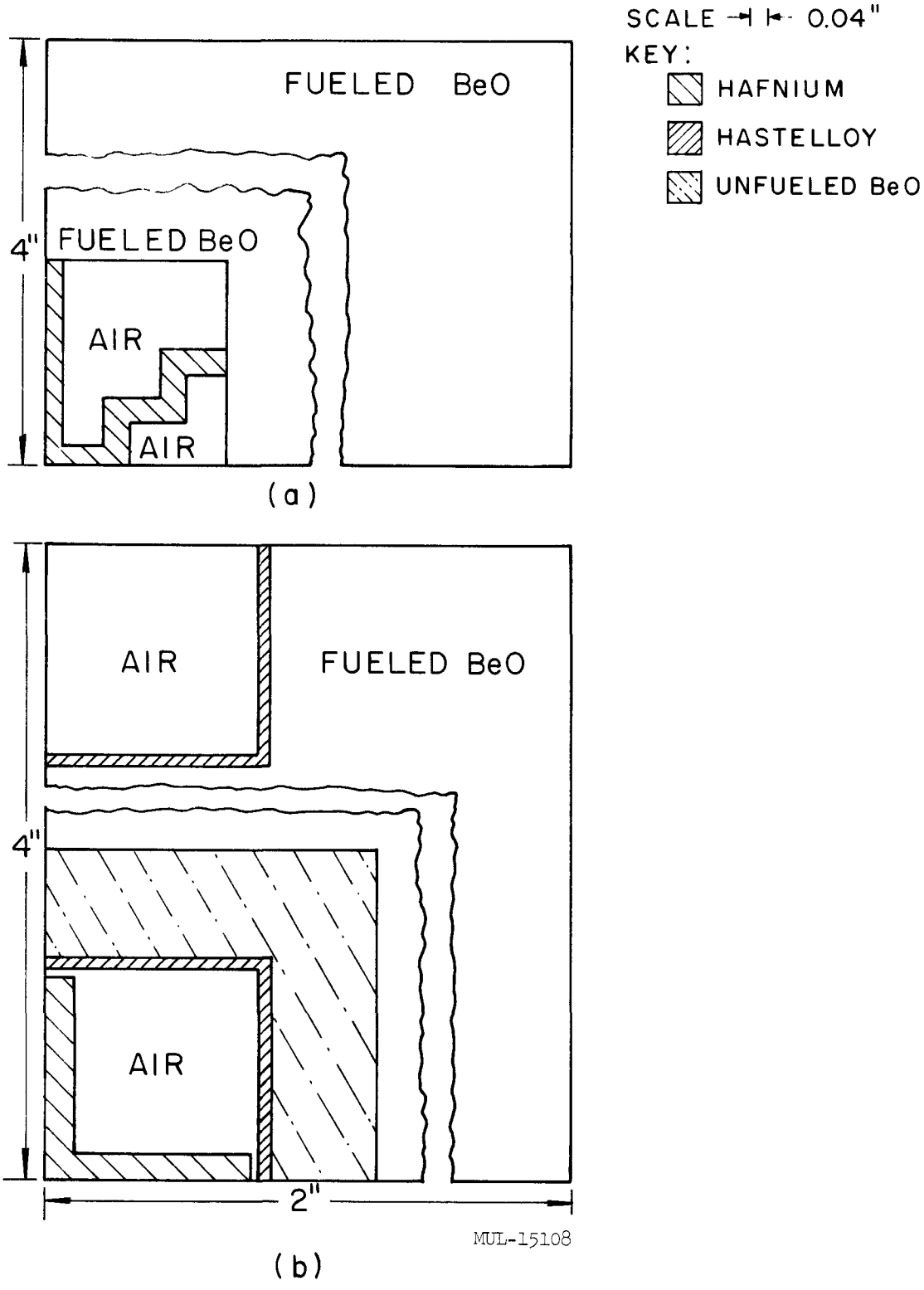

Fig. IV-7. Cell configuration.

of radiation originating in the fueled moderator region included gammas from prompt fission, fission product decay at 50% saturation,[1] and radiative capture reactions in the tie rods and fuel elements. This source is designated as "external."

The average heating of a component in Mw/ft^3 per Mw/ft^3 local power density was obtained by multiplying the fraction of source energy deposited in the component by the factor,

$$\frac{E_\gamma / A_c}{E_m / A_m}$$

where E_γ = gamma energy available — 14.8 Mev/fission at 50% fission product saturation,

E_m = total energy produced in the fueled moderator adjacent to the control rod — 191 Mev/fission,

A_c = area of the component in the cell,

A_m = area of the fueled moderator in the cell.

Problems were run in which the rod was of asterisk or cruciform shape. In order to determine the effect that each of the components surrounding the control rod has on the heating value, problems were run in which each component was added successively to the cell. In these latter instances, it was necessary to describe the rod by a cruciform because of the limitation on the number of zones handled by the Yogi code. Similar problems (3, 13 and 17, 26) run with the asterisk and cruciform descriptions of the rod indicated that the descriptions were essentially equivalent. (It should be noted that the mass of hafnium was approximately conserved in going from one description to the other. In the case of the asterisk, the blade thickness was 0.080 in. while the cruciform blade thickness was 0.125 in.) The following conclusions may be drawn from the results listed in Tables IV-4 and IV-5.

1. The heating results of problems 1, 2, and 3 indicate that the 2 in. × 4 in. cell was a reasonable choice for use in subsequent problems since there was little coupling between rods. This is not an unexpected result since

---

[1] For problem numbers greater than 30, the external source spectrum included gamma rays from fission product decay at 90% fission product saturation — 17.3 Mev/fission available in this case.

the mean free path of the gamma rays in the moderator is approximately 8 inches. This cell size, in addition, approximated the actual distance between adjacent rods quite well. These results, then, justified the manner in which the heating values in Mw/ft^3 per Mw/ft^3 local power density were obtained.

Problems 7, 9, and 11, in which the rod was described by a slab, led to similar conclusions about the coupling between rods.

2. From a comparison of the results of problems 2 and 4, in which the rod was a cruciform with blades 1/8 in. × 1/2 in. and 1/16 in. × 1/2 in., respectively, it is apparent that the 1/8-in. rod is self-shielded. The heating of the 1/8-in. rod is 1.04 (Mw/ft^3 per Mw/ft^3) as opposed to that of 1.51 for the 1/16-in. rod.

3. A comparison of the results obtained in problems 2, 26, 13, and 17 indicates that, with the present statistical accuracy, the introduction of the air cavity between rod and fueled moderator has no perceptible effect on rod heating.

4. Problem 27 indicates that the Hastelloy tie tube absorbs more than 2% of the energy of the external source thereby reducing the heating of the rod as described in problem 26 (without the Hastelloy shell) by (9 ±6) % .

5. From a comparison of problems 27 and 29 it appears that the ring of unfueled BeO surrounding the tie tube has little shielding effect – (3 ±5) % – on rod heating since the results agree within the statistical accuracy.

6. Because of the variation in uranium loading within the core, it was of interest to determine the effect that a change in loading has on rod heating. A comparison of the results of problems 31 and 34, in which the various materials surrounding the rod have been added, leads to the conclusion that an increase in uranium loading, even by a factor of 2, has little effect on rod heating.

7. Since the density of fueled moderator utilized in earlier problems was one that had been averaged over the core, a problem was run with the density increased to that of the moderator adjacent to the control rod. A comparison of the heating values obtained in problems 33 and 35 indicates that a density increase of 14% results in a slight reduction – (4 ±5) % – of rod heating.

8. A comparison of the results of problems 34 and 37 indicates that the presence of Hastelloy tie tubes in the vicinity of the control rods, other than those enclosing the rods, has little effect on rod heating.

B. Internal Source

Problems were also run with gamma rays originating in the control rod. The input spectrum was that due to radiative capture of thermal neutrons in the hafnium. From the results listed in Table IV-6, it is seen that the introduction of the various materials surrounding the control rod has little or no effect on the fraction of internal (hafnium) source energy deposited in the rod, within the present statistical accuracy.

A final problem was run using as the source of radiation thermal neutron capture occurring in the Hastelloy shell surrounding the control rod. The results given in Table IV-6 indicate that 16% of this source energy is deposited in the rod, while 4% is deposited in the unfueled BeO.

Heating results obtained with the Trikl code may be compared with those obtained by use of Yogi, in which the rod is described by a slab. Yogi 9 and the Trikl problem, treating an average moderator medium with $BeO:U^{235}$ ratios of 951:1 and 963:1, yielded heating values of 1.07 and 1.10 Mw/ft^3 per Mw/ft^3, respectively. The results therefore agree quite well.

Finally, an analytical treatment of self-absorption of gamma radiation by the control rod, considering a cylinder of mass equivalent to that of the cruciform or asterisk, yielded a fraction of internal source energy deposited in the rod of 0.26, the same result as obtained with Yogi.

C. Total Heating of Hafnium Control Rod

Total hafnium control rod heating density normalized to the average core power density had been calculated from those Yogi problems which describe the control rod assembly most realistically; these are:

1. Yogi No. 37 for the external core gamma source of 17.3 Mev/fission,
2. Yogi No. 36 for the (n, γ) source in the hafnium,
3. Yogi No. 32 for the (n, γ) source in the control-rod tie rod.

All heating power density values are given in Mw/ft^3 in solid, hot component material normalized to 1 Mw/ft^3 of average core power density based on the active hot core volume of 53.42 ft^3. The anticipated power of the Tory II-C reactor is 510 Mw; the corresponding average core power density will be 9.55 Mw/ft^3. Normalization of the heating density realized by the control rod due to the three contributing sources was performed in the following manner:

1. External source: if one assumes the rod to extend throughout the length of the fueled core, the average heating density of 1.03 Mw/ft^3 per

Table IV-6. Internal Source.

Problem	Rod description	$BeO:U^{235}$	Fraction of source energy deposited in Rod	Hastelloy	Unfueled BeO	Description of cell
A. Hafnium						
14	asterisk, 0.08 in. × 1/2 in. blades (see Fig. IV-7a)	951:1	0.243			rod in direct contact with fueled moderator
19			0.255			rod separated from fueled moderator by air cavity
24	cruciform 1/8 in. × 1/2 in. blades (see Fig. IV-7b)	951:1	0.259			rod in direct contact with fueled moderator
25			0.266			rod separated from fueled moderator by air cavity
28			0.260	0.033		Hastelloy shell separates air cavity from fueled moderator
30			0.265	0.030	0.029	pure BeO shell surrounds Hastelloy
36	cruciform 1/8 in. × 1/2 in. blades	423:1	0.256	0.035	0.031	same as 30, but fueled moderator has density of that adjacent to control rod
B. Hastelloy						
32	cruciform 1/8 in. × 1/2 in. blades	951:1	0.157	0.060	0.040	same as 30.

Mw/ft^3 obtained directly from Yogi is normalized to the power in the fueled moderator; renormalization to power density in the total active core yields the average heating density value of

$$\overline{H}_{\gamma} = 1.13 \frac{Mw/ft^3 \text{ of full density Hafnium}}{Mw/ft^3 \text{ of average core power density}} .$$

However, the maximum insertion distance of the control rod is 40 in. from the front reflector face. If, then, one extends the gamma heating curve into the front reflector, assuming an E_2 fall-off, and averages over the 40-in. length, the average heating density value along this rod length becomes

$$\overline{H}_{\gamma} = 0.93 \frac{Mw/ft^3 \text{ of full density Hafnium}}{Mw/ft^3 \text{ of average core power density}} ,$$

with a peak-to-average ratio of 1.33.

2. Internal (n, γ) source: the (n, γ) heating of the control rods has been calculated on the basis of a rod of minimum reactivity, or one that absorbs 0.0127 neutrons/fission. For each neutron captured by the control rod, 6.6 Mev are released in the form of high-energy gamma rays. Since the rod length is 40 in., the heating density and its normalization must necessarily be based on this value. The total (n, γ) energy source in the hafnium rod normalized to unit fission density in the active core volume (V_c = 53.42 ft^3) is 1.27×10^5 Mev/sec per fission/cm^3 sec.

The energy fraction remaining in the control rod, 0.256, was determined by Yogi No. 36. For a rod volume of 0.00529 ft^3 (hot), the average (n, γ) heating density normalized to unit core power density (based on a hot core volume of 53.42 ft^3) was found to be

$$\overline{H}_{(n, \gamma)} = 1.16 \frac{Mw/ft^3 \text{ of full density Hafnium}}{Mw/ft^3 \text{ of average core power density}} ,$$

with a peak-to-average ratio of 1.39.

3. (n, γ) source in control rod tie rod: based on 0.00111 neutrons per fission absorbed by an average tie rod, the total (n, γ) energy source in an average tie rod normalized to unit fission density in the active core is 1.47×10^4 (Mev/sec)/(fission/cm^3). The fraction of the energy made in the tie rod which is absorbed by the control rod was calculated by Yogi No. 32 to be 0.157. Assuming the hafnium rod to extend the full length of the reactor, one finds

that the average heating density is 0.0513 Mw/ft^3 per Mw/ft^3. The peak heating (using the peak-to-average ratio of 1.54 corresponding to an average taken over the full length of the reactor) would be 0.079 Mw/ft^3 per Mw/ft^3. The peak-to-average ratio corresponding to an average taken over the 40-in. insertion distance is 1.39, so that the average heating contributed by an average tie rod is

$$\bar{H}_{n,\gamma} = 0.0567 \frac{Mw/ft^3 \text{ of full density Hafnium}}{Mw/ft^3 \text{ of average core power density}} .$$

So far, this heating contribution was assumed to result from an average tie rod; in the core there are a total of 121 tie rods, 14 of which are control tie rods; of these 4 are expected to be Hastelloy R-235, and 10 René 41. Furthermore, these control tie rods can be located at two possible radial positions, $R \cong 8.92$ in. and $R \cong 17.54$ in. These variations in material and position change the average worth of these tie rods. The factors by which the average worth must be multiplied are listed in the following table:

	R-235	René 41
Inner control tie rod ($R \cong 8.5$ in.)	1.147	2.423
Outer control tie rod ($R \cong 17.2$ in.)	0.692	1.494

The contribution to the control rod heating from this source will therefore vary depending upon what material is being used at either location. Even though this heating contribution is small in comparison with the total, the choice of Hastelloy R-235 over René 41 will cut the total heating by approximately 4%.

4. Total heating: The average heating contributions from the three components to the total heating density of a shim rod (i.e., one at R = 8.92 in.) is:

	$\bar{H}$ (Mw/ft^3 per Mw/ft^3)
External gamma source	0.93
Internal (n, γ) source	1.16
External (n, γ) source (from René 41 tie rod)	0.14
Total average heating density	2.23

The volume of one control rod at the temperature realized at full power is 0.00529 ft^3, so that the integrated power in the control rod inserted 40 in. into

the reactor and normalized to an average core power density of 1 Mw/ft^3 (based on a hot core volume of 53.42 ft^3) is

$$P = 11.77 \text{ kw per } Mw/ft^3 .$$

The axial distribution of the total heating density was compiled from the individual contributions described above, each modified by its proper axial dependence. For the case of the control tie rod (n, γ) contribution, René 41 was considered. The use of an R-235 tie rod reduces the heating by about 4%. The axial distribution of the total heating density in the control rod at maximum insertion, at 90% fission product saturation (10-hr operation), is given in Fig. IV-8.

The foregoing analysis treated fully inserted rods (i.e., 40 in. into reactor). However, the expected mode of high-power operation is one in which the shim rods will project approximately 13 in. into the core. This corresponds to a $\Delta k_{rods} \cong -0.03$. Therefore, the peak power density will, in normal operation, exist at the rod tips and should be 2.6 (Mw/ft^3 of solid hafnium)/(Mw/ft^3 of average core power density). The more comprehensive treatment reviewed here allows one to estimate the hazardous condition which might arise if a single shim rod were fully inserted at high power levels.

PRODUCTION OF PHOTONEUTRONS BY THE $Be^9(\gamma, n)$ REACTION IN TORY II-C

The yield of photoneutrons from the Be^9 (γ, n) reaction in the Tory II-C core material has been calculated for three different times after start-up. Because of the fission product build-up during operation, the gamma-energy source as well as its associated energy distribution changes with time; the gamma-energy source rises from an initial value of about 7.9 Mev/fission at start-up (due solely to the prompt fission gammas) to 14.2 Mev/fission at 90% saturation of fission products. An additional source of gammas in the Tory II-C core is due to the (n, γ) process in both fuel and tie rods. This contribution amounts to about 3 Mev/fission and is constant during operation. The times considered in this report are (1) at start-up, considering the prompt gamma rays only, (2) at 50% fission product saturation, or 2 min after start-up, and (3) at 90% fission product saturation, or 10 hr after start-up.

The gamma flux in the core was calculated by the Trikl code for an average core material composition of BeO:U = 423 (where $N_{BeO} = 0.0294 \times 10^{24}$ atoms/cc). The flux obtained from Trikl is applicable to an infinite medium

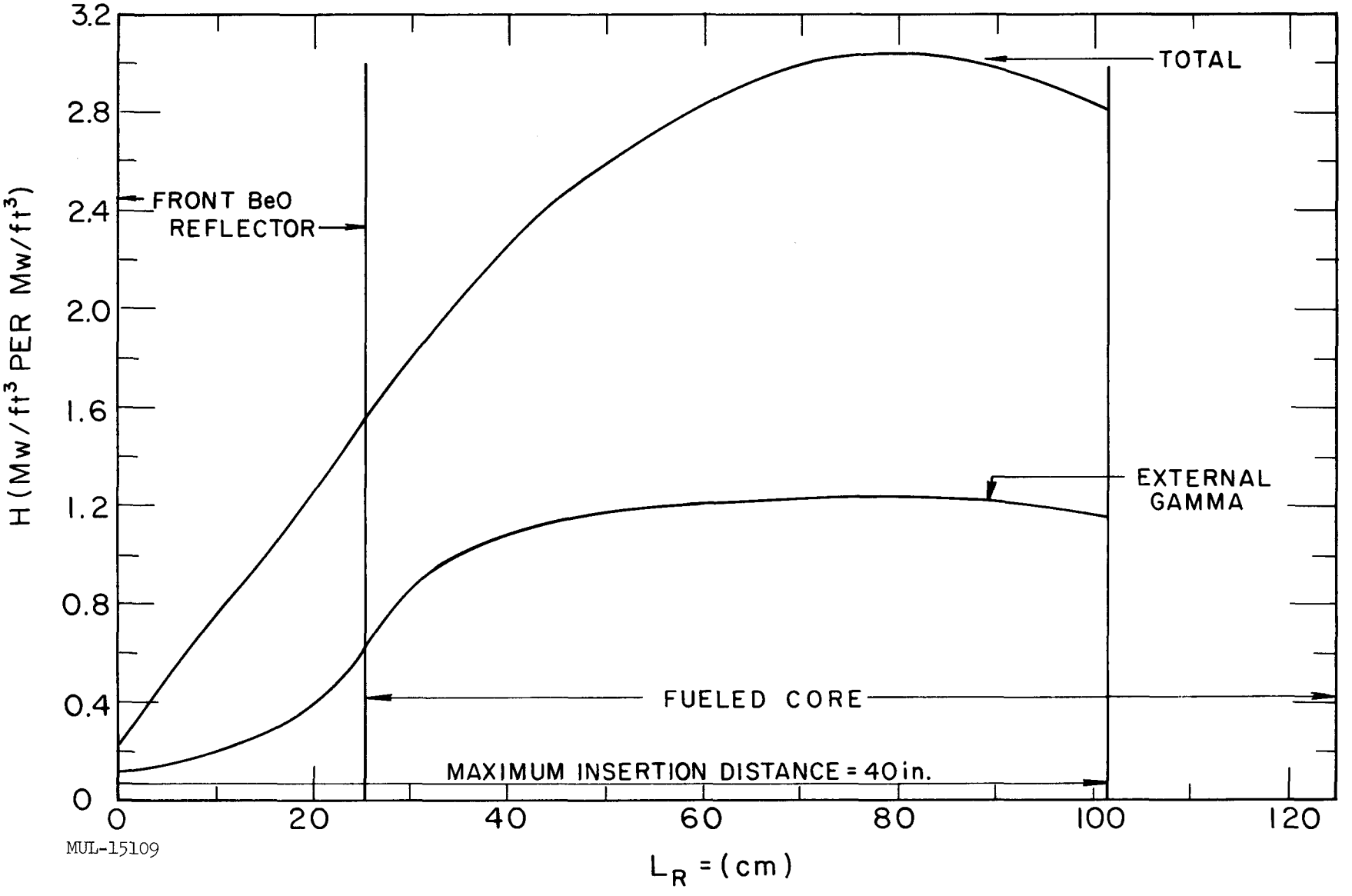

Fig. IV-8. Nuclear heating of the Tory II-C hafnium control rod as a function of axial position. Assumptions: (1) 90% fission product saturation, (2) 80-mil wall thickness, asterisk shape, and (3) minimum reactivity requirement.

(leakage is neglected) and the photoneutron yield values calculated should be interpreted as such.

In order to obtain the photoneutron yield, a summation of $\Sigma_{(\gamma, n)}\phi$ was performed, using the (γ, n) reaction cross-section data published in UCRL-5996.[2]

The photoneutron spectra and the total yield per fission for the three considered cases are given in Table IV-7. The reason for the fine subdivision of the energy spectrum at the low-energy end was to obtain a detailed neutron spectrum at the low energies. The average energy of the photoneutron was obtained from the relationship

$$E_n = E_\gamma - (\text{binding energy}) \quad .$$

PERIPHERAL SHIMS

The Tory II-C side reflector has been modified significantly by thickening the nickel peripheral shims to approximately one inch at the expense of reflector BeO. This change was made to reduce the heat load on the side support structure elements, and in particular the pressure pads which are in direct contact with the peripheral shims. The move was also encouraged because the costs of nickel parts are far less than those of BeO parts.

Before the substitution was made, a series of Spade experiments were performed where nickel plates replaced BeO. These pulsed neutron experiments showed conclusively that displacement of reflector BeO with a density of 2.86 g/cc by nickel with a density of 8.90 g/cc resulted in an increase in assembly reactivity in meaningful cases. Experiments involving R-235 did not show as dramatic an effect, presumably because of the lower macroscopic scattering cross section in the alloy.

The usual Spade assembly was employed with 8-mil oralloy foils spaced one-inch apart to give a moderator-to-fuel ratio, $BeO/U^{235} = 247$. The fueled core in all cases had the base dimensions 24 × 24 inches, and a height adjusted to keep the complete assembly subcritical. Measurements were made using the pulsed neutron technique to determine α, the neutron decay constant, and have an estimated accuracy of ±5 to 8%.

---

[2] J. M. Prosser and W. J. John, "Photodisintegration Cross Section of Beryllium Near Threshold," UCRL-5996, 12 May 1960.

Table IV-7. Photoneutron Spectra from (γ, n) in Be in Tory II-C 423:1 Core Medium.

$\bar{E}_n$	ΔE_n	0% Sat.[a] 7.926 Mev/fission neuts/fiss. $\times 10^{-4}$	0% Sat.[a] 7.926 Mev/fission neuts/fiss. Mev $\times 10^{-4}$	50% Sat. 14.75 Mev/fission neuts/fiss. $\times 10^{-4}$	50% Sat. 14.75 Mev/fission neuts/fiss. Mev $\times 10^{-4}$	90% Sat. 17.29 Mev/fission neuts/fiss. $\times 10^{-4}$	90% Sat. 17.29 Mev/fission neuts/fiss. Mev $\times 10^{-4}$
7.25	2.057	0.	0.	1.101	0.535	1.27	0.617
5.42	1.633	0.076	0.047	0.998	0.611	1.138	0.697
3.96	1.298	0.127	0.098	0.447	0.344	0.506	0.390
2.81	1.031	0.33	0.32	0.539	0.523	0.597	0.579
1.89	0.819	0.501	0.612	0.688	0.84	0.758	0.926
1.16	0.65	1.28	1.96	1.755	2.70	1.90	2.92
0.8	0.11	0.1552	1.41	0.2406	2.18	0.279	0.279
0.69	0.1	1.149	1.49	0.2496	2.50	0.279	0.279
0.59	0.1	0.158	1.58	0.2832	2.83	0.31	0.31
0.49	0.1	0.1706	1.71	0.3261	3.26	0.352	3.52
0.39	0.1	0.1961	1.96	0.3897	3.10	0.417	5.165
0.315	0.05	0.1386	2.77	0.283	5.66	0.298	5.96
0.265	0.05	0.1566	3.13	0.3179	6.36	0.336	6.72
0.215	0.05	0.1855	3.71	0.3785	7.57	0.397	7.94
0.165	0.05	0.2325	4.65	0.4713	9.4	0.494	9.88
0.13	0.02	0.1113	5.565	0.2242	11.2	0.235	11.74
0.11	0.02	0.1234	6.17	0.2459	12.3	0.257	12.86
0.09	0.02	0.1359	6.795	0.2721	13.6	0.283	14.16
0.09	0.02	0.1504	7.52	0.2975	14.9	0.309	15.47
0.05	0.02	0.1759	8.795	0.3463	17.3	0.362	18.09
0.03	0.02	0.1465	7.325	0.2862	14.3	0.299	14.94
0.01	0.02	0.0526	2.63	0.10215	5.11	0.107	5.33
Total yield neuts/fission		0.0004752		0.001024		0.001118	

(a) The 0% saturation spectrum is based on prompt fission gammas only, the other two include the 3 Mev/fission due to the (n, γ) reactions in the core.

MUL-15056

The first measurements were made on the bare core at various heights, and the results are shown in Fig. IV-9. A series of Zoom problems using standard library tape materials and self-shielding factors gave k_{eff} at each stack height, and these calculated values are plotted with the corresponding measured α in Fig. IV-10. The result is a straight line whose slope is ℓ^*, the prompt neutron lifetime, which has the value 33.3×10^{-6} seconds. It is important to recognize that ℓ^* is a function of the absorption cross sections and is dependent on the use of self-shielding factors. A calculation based on a similar critical assembly with no self-shielding gives 18.4×10^{-6} seconds.

Measurements of α were also made on several assemblies involving the core capped with reflectors of unfueled BeO and combinations with nickel and R-235. Zoom problems were run, giving a calculated k_{eff} for each assembly which may be related to a predicted α through Fig. IV-10 for comparison with the experimental values. The basic assumption underlying this is that systems having the same decay constant must have the same k_{eff}. Experimental and calculated results are listed in Table IV-8. Assembly components are listed in the order of their stacking.

Self-shielding factors were not used for the reflector materials in the calculations except in the last case. The last two assemblies listed were calculated using a new set of nickel cross sections; all others are standard library tape values.

The experimental assemblies are very well represented by the calculations. The internal consistency is within $\Delta k = \pm 0.003$ when the standard cross sections are used. With the new set, k_{eff} is reduced by 0.003 for a one-inch nickel layer. The standard set is being used in the Tory II-C calculations.

PRESENT STATUS OF TORY II-C CONTROL ROD SYSTEMS: NEUTRONIC ASPECTS

Shim Rods

In UCRL-6376 (p. 79) the considerations pertinent to the neutronic worth of the Tory II-C shim rods are outlined. Since then, work has continued to reduce the uncertainties in the value for rod worth. Experiments done have furnished input data for a series of Angie problems. The results, discussed in UCRL-6516 (p. 108), show that diffusion theory overpredicts the worth of hafnium rods by 10%. The hafnium cross sections were determined from basic constants, and conventional resonance self-shielding techniques were employed.

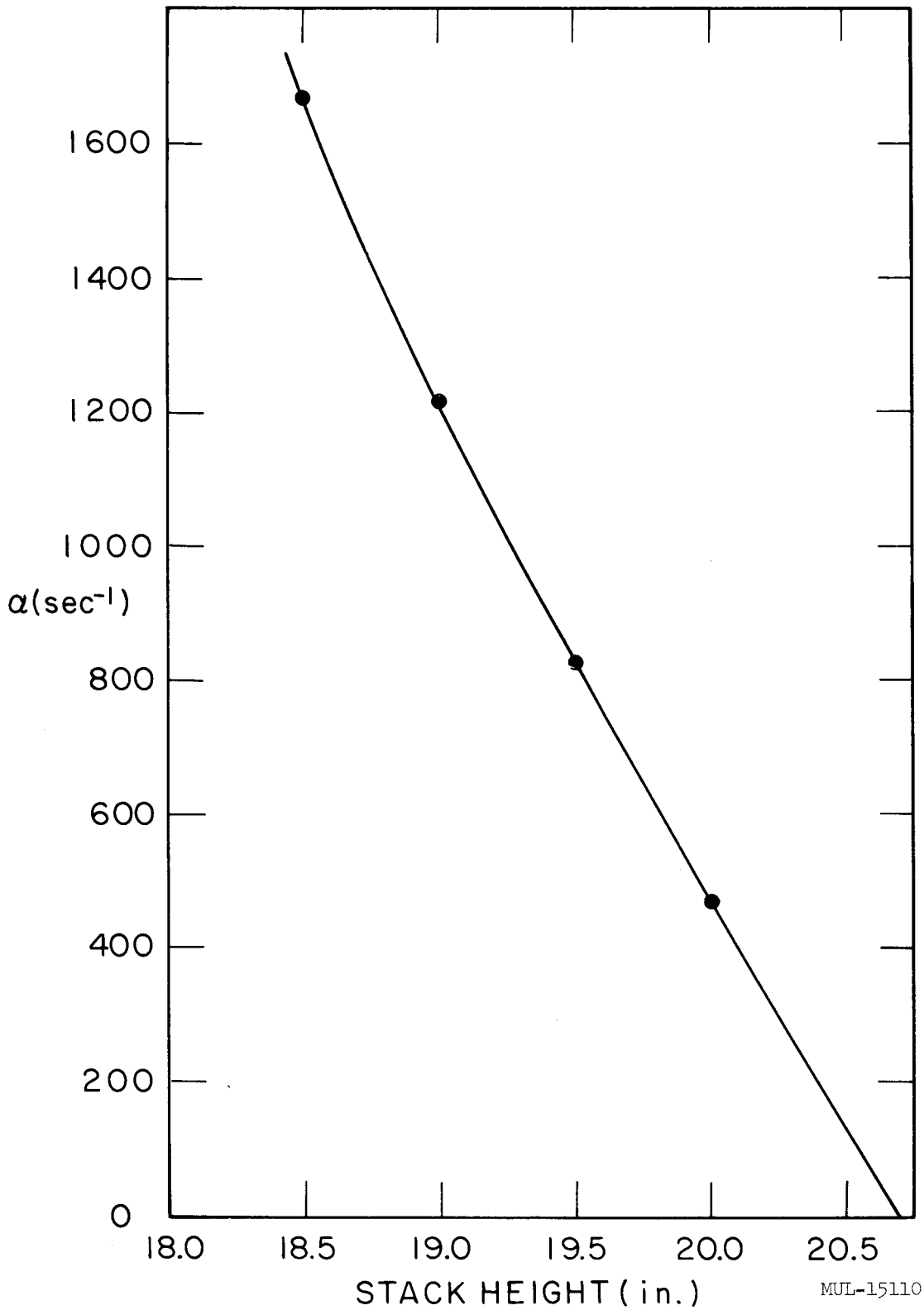

Fig. IV-9. Measurements on bare core at various heights.

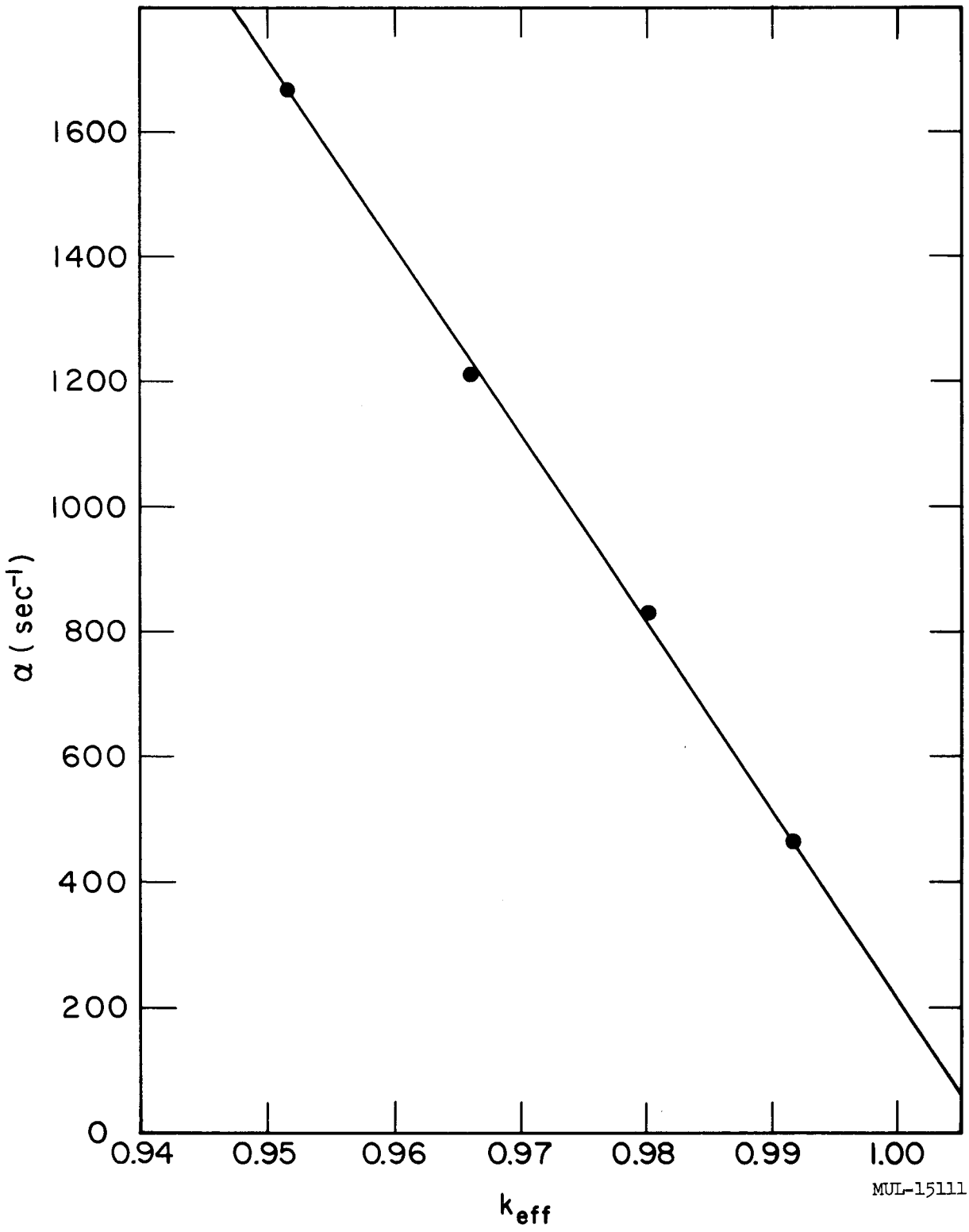

Fig. IV-10. Experimental decay constant vs k_{eff} from Zoom for same assembly. $\ell^* = \Delta k/\Delta \alpha = 33.3 \times 10^{-6}$ sec.

Table IV-8. Experimental and Calculated Results.

	Assembly composition										
	Core height (in.)	Unfueled BeO (in.)	Unfueled BeO (lb/ft^2)	Nickel (in.)	Nickel (lb/ft^2)	R-235 (in.)	R-235 (lb/ft^2)	k_{eff} Calculated	$\alpha(sec^{-1})$(a) Predicted	$\alpha(sec^{-1})$ Experiment	$\Delta\alpha$ Predicted minus experiment(b)
1	16.5	3.0	44.4	--		--		0.97290	1024	939	85
2	16.5	2.5	37.0	0.5	23.04	--		0.97972	821	736	85
3	16.5	2.0	29.6	1.0	46.08	--		0.98088	785	729	56
4	16.5	1.5	22.2	1.5	69.12	--		0.97933	834	848	-14
5	16.5	1.0	14.8	1.5	69.12	0.5	20.16	0.97452	979	1042	-63
6	16.0	2.0	29.6	1.0	46.08	--		0.96713	1202	1163	39
7	16.0	2.0	29.6	1.0	46.08	0.25	10.08	0.97211	1052	1069	-17
8	16.0	2.0	29.6	1.0	46.08	0.5	20.16	0.97478	969	1007	-38
9	16.0	2.0	29.6	1.0	46.08	0.75	30.24	0.97704	903	956	-53
10	16.0	2.0	29.6	1.0	46.08	1.00	40.32	0.97896	845	895	-50
11	16.5	2.0	29.6	1.0	46.08	--		0.97734	893	729	164
12	16.5	2.0	29.6	1.0	46.08	--		0.97773	880	729	151

(a) Value of α is found from Fig. IV-10. Self-shielding factors were applied only to the fuel except in number 12, where they are applied also to nickel. Numbers 11 and 12 are identical to 3 except for the use of a new set of cross sections for nickel. Experimental accuracy is ±5 to 8%.

(b) An error in $\Delta\alpha$ of ±300 is equivalent to $\Delta k = \pm 0.01$.

These nuclear cross sections were then employed in Angie R-θ calculations where the Tory II-C geometry, composition, and fuel distribution were faithfully represented. Inasmuch as the original experiments involved hafnium bars of rectangular cross section, some Tory II-C Angie calculations treated such shim rods, and used a mesh similar to that employed in the Spade Angie calculations. After applying the 10% correction, the worth of twelve shim rods, 0.080-in. thick and 1.00-in. wide, and inserted 40 in. into the reactor from the entrance end was found to be:

$$\Delta k_{\square} = -0.095 \ .$$

Recall from UCRL-6376 that $\Delta k = -0.13$ is required. Actually, the shim rods will be of asterisk cross section. It is estimated that these will be worth twice as much:

$$\Delta k_{*} = -0.19 \ .$$

The estimate is made on the basis of experimental observations that a cruciform of uniform wall thickness is worth 1.7 times that of a slab which is identical to two opposite arms of the cruciform. This was shown in an experiment involving tantalum, and also by others using hafnium rods in a hydrogenous medium.

If, upon initial nuclear operation of Tory II-C, it is found that the shim rods are worth more than needed for minimum control of the reactor, the rods will be modified to make their worth equal to the minimum requirement. If Δk (temp) = -0.075, the minimum reactivity requirement is Δk (total) = -0.130. (See UCRL-6376 for a breakdown.) The above value of $\Delta k_{*} = -0.19$ is reassuring.

The minimum reactivity requirement is submitted to assure the lowest possible heat load on the control rods, for if they are worth more neutronically than necessary, the (n, γ) heating mechanism will be greater than necessary. The cooling problem would thereby be aggravated.

CRITICALITY CALCULATIONS OF D_2O-REFLECTED, GRAPHITE-MODERATED, ENRICHED URANIUM SYSTEMS (PUPPY I)

The 18-energy-group code-9 Zoom (UCRL-5682 and 5913) has been used to perform criticality calculations for a series of D_2O-reflected, graphite-moderated, enriched uranium systems. Reasonably good agreement was found between calculation and experiments in spite of the fact that odd arrangements

of fuel foils were used in some cases, while in others the fuel foil spacing was so small that the validity of diffusion theory in calculating flux disadvantage factors was questionable.

Experiment

The core, a lattice of graphite blocks (13 ppm boron) and oralloy foils, was approximately octagonal in cross section. This was surrounded by an aluminum container which was filled with D_2O of better than 99.7% purity; the inner wall of the container conformed to the shape of the core, while the exterior wall was cylindrical. Because Zoom is a one-dimensional code, the actual assembly was reduced to a supposedly equivalent cylindrical system. The thickness, rather than the mass of the inner aluminum wall was conserved and the dimensions of the external wall were not altered. The validity of this model was checked (for one experiment only) with the two-dimensional code-9 Angie which agreed with 9 Zoom to within 0.1%.

In these experiments the critical height had been determined for various values of the following parameters:

1. Fuel foil thickness, spacing, and arrangement.
2. Graphite density.
3. Moderator-to-fuel ratio.
4. Wall thickness of aluminum container.
5. Thickness of D_2O reflector.

The experimental run number as assigned at the time has been retained.

The cross sections and transfer coefficients for the several materials involved are available. The Cohen self-shielding approximation was used to determine the disadvantage factor resulting from the finite thickness of the oralloy foils and the foil spacing in the graphite moderator. This permitted the core to be represented as a homogeneous system.

The results of the calculations are presented in Fig. IV-11. The general tendency for the effective multiplication factor to decrease as the moderator-to-fuel ratio increases is similar to that found in previous calculations with BeO-U^{235} systems.

EFFECT OF RESONANCE SCATTERING ON NEUTRON ABSORPTION

A neutron Monte Carlo code has been written which treats, in simple geometry, the problem of neutron resonance absorption and the effect of resonance scattering on the resonance absorption. A cell geometry is employed,

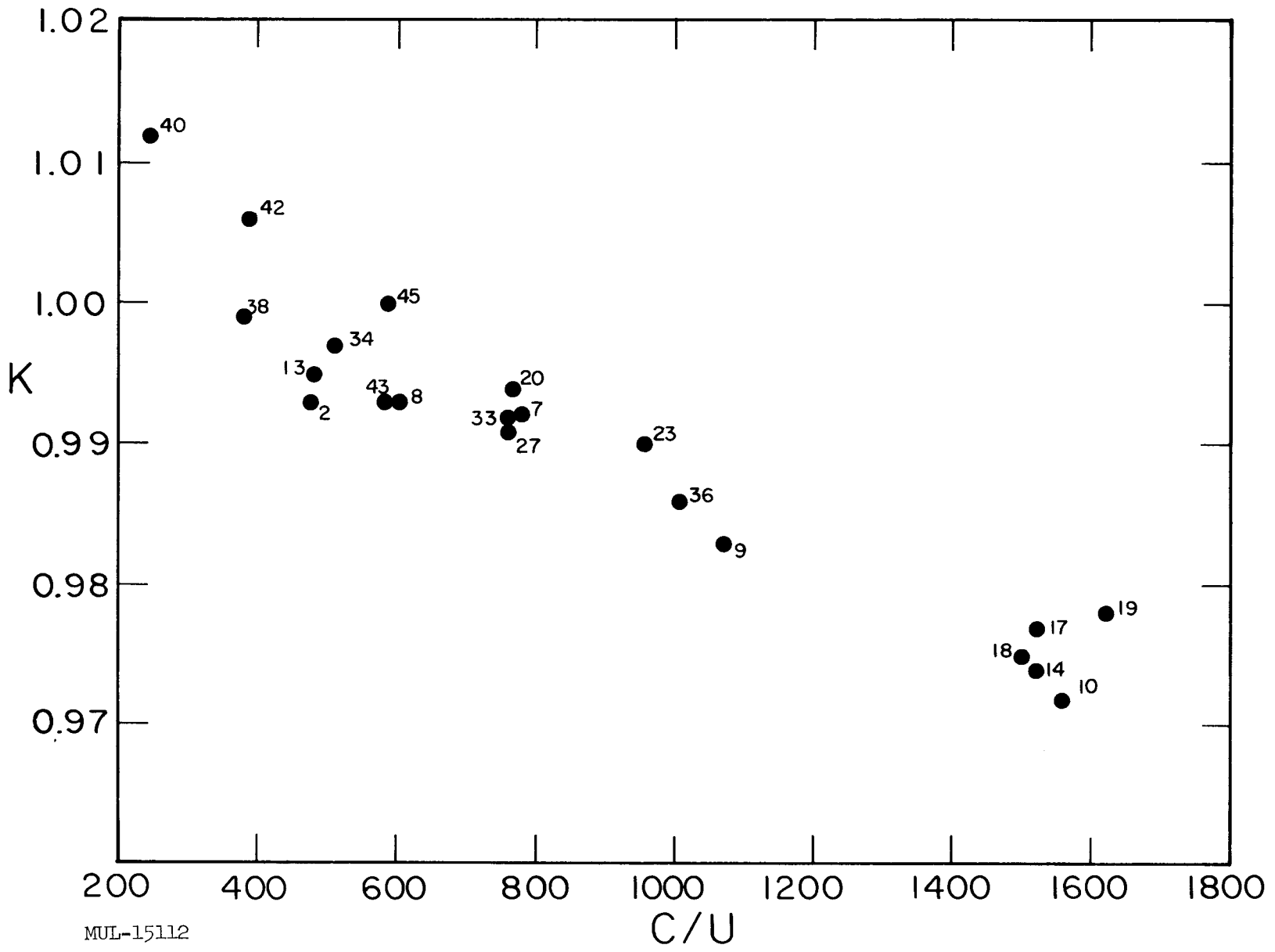

Fig. IV-11. Effective multiplication factor vs moderator-to-fuel ratio.

and slab absorption is easily treated. Concern over the matter of resonance absorption is warranted, since Tory II-C utilizes structural materials containing cobalt. This element noticeably affects the neutron economy and the radiation heating levels of the tension tubes and side support structure.

The initial study dealt with the 44.6-ev resonance of Mo^{95}. Parameters given in the literature were employed.[3] Several problems were run with different values of initial neutron energy ranging from 100 ev to 3000 ev. The capture probability was found to be insensitive to the initial energy for $E_o \geq$ 300 ev, in accord with previous predictions.[4] Results yield an effective resonance absorption integral of 2.33 barns for a molybdenum sheet of 0.120-in. thickness. The moderator was BeO (ρ = 2.86 g/cc) and the spacing between sheets was 8.0 in. When resonance scattering was suppressed, this value rose to 2.49 barns. The latter value compares very favorably to the Roe[5] value of 2.5 barns and is expected to, for the Roe treatment neglects scattering effects. If one assumes that all resonance scatters degrade the neutron energy so that no resonance absorption is possible, a slight modification of the Roe procedure leads to a value of 1.9 barns. Therefore, the Monte Carlo results show that the resonance scatter has an effectiveness of only 25% in preventing neutrons from being absorbed in the resonance.

Attention is currently being given to the 132-ev resonance of cobalt, which is primarily a scattering resonance.

SECTION II. ENGINEERING

I. GENERAL ARRANGEMENT OF REACTOR

The general arrangement of the core and reflector remains basically the same as shown in the previous progress report. Figures IV-11a-d reproduce Figs. IV-23a-d from Quarterly Report No. 8 for reference. A change has been made in the thickness of the peripheral shims. Figure IV-12 shows a mockup of the original shim design assembled with steatite tubes. The new shims are three times thicker. Figure IV-13 shows this shim assembled with the reactor and duct. The additional thickness provides sufficient shielding of the side support system and duct to eliminate the need for an auxiliary

[3] J. A. Harvey, et al., Phys. Rev. 99, 10 (1955).

[4] Weinberg and Wigner, The Physical Theory of Neutron Chain Reactors, p. 290 (1958).

[5] G. M. Roe, KAPL-1241, pp. 39-49 (1954).

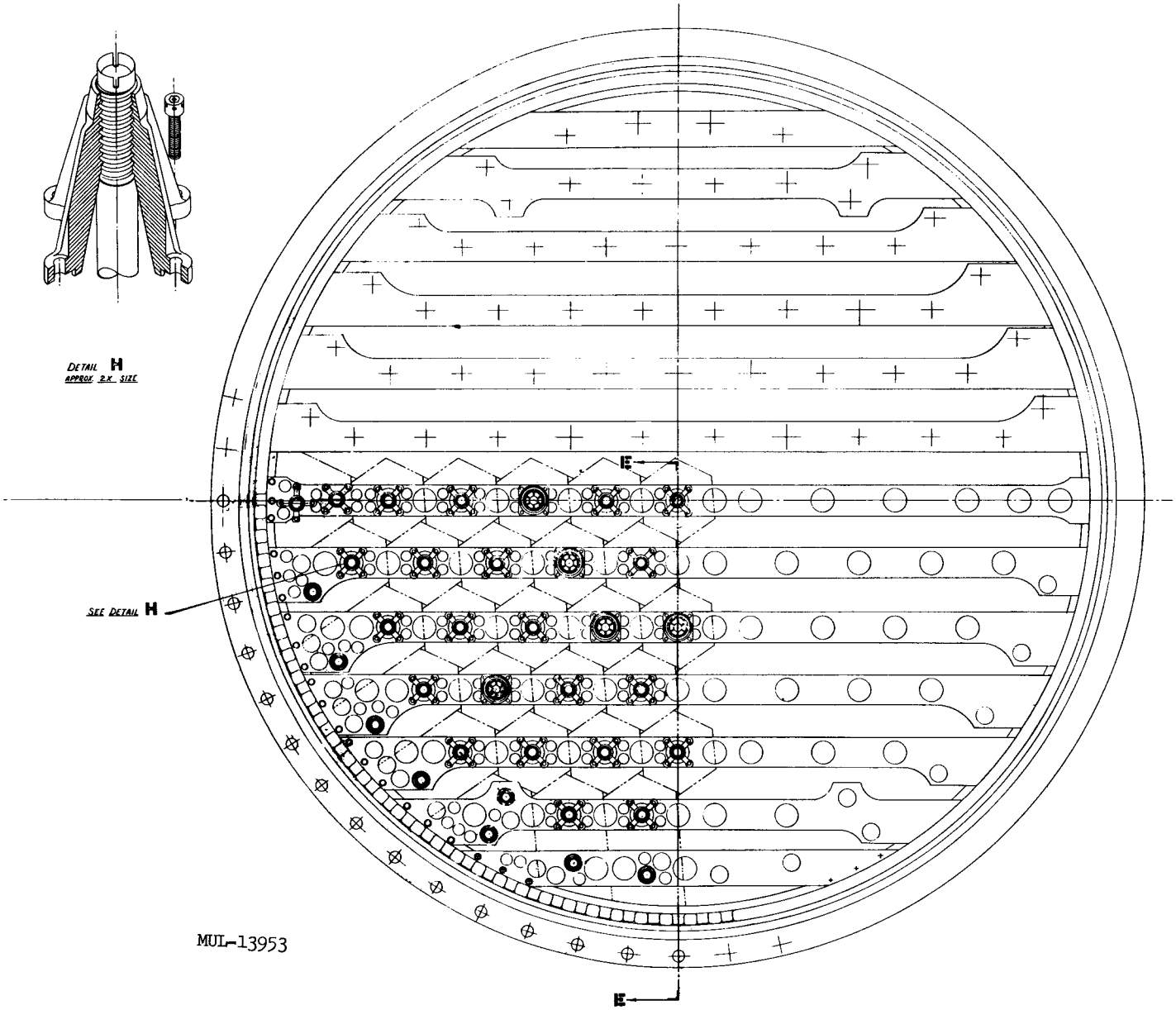

Fig. IV-11a. Reactor assembly.

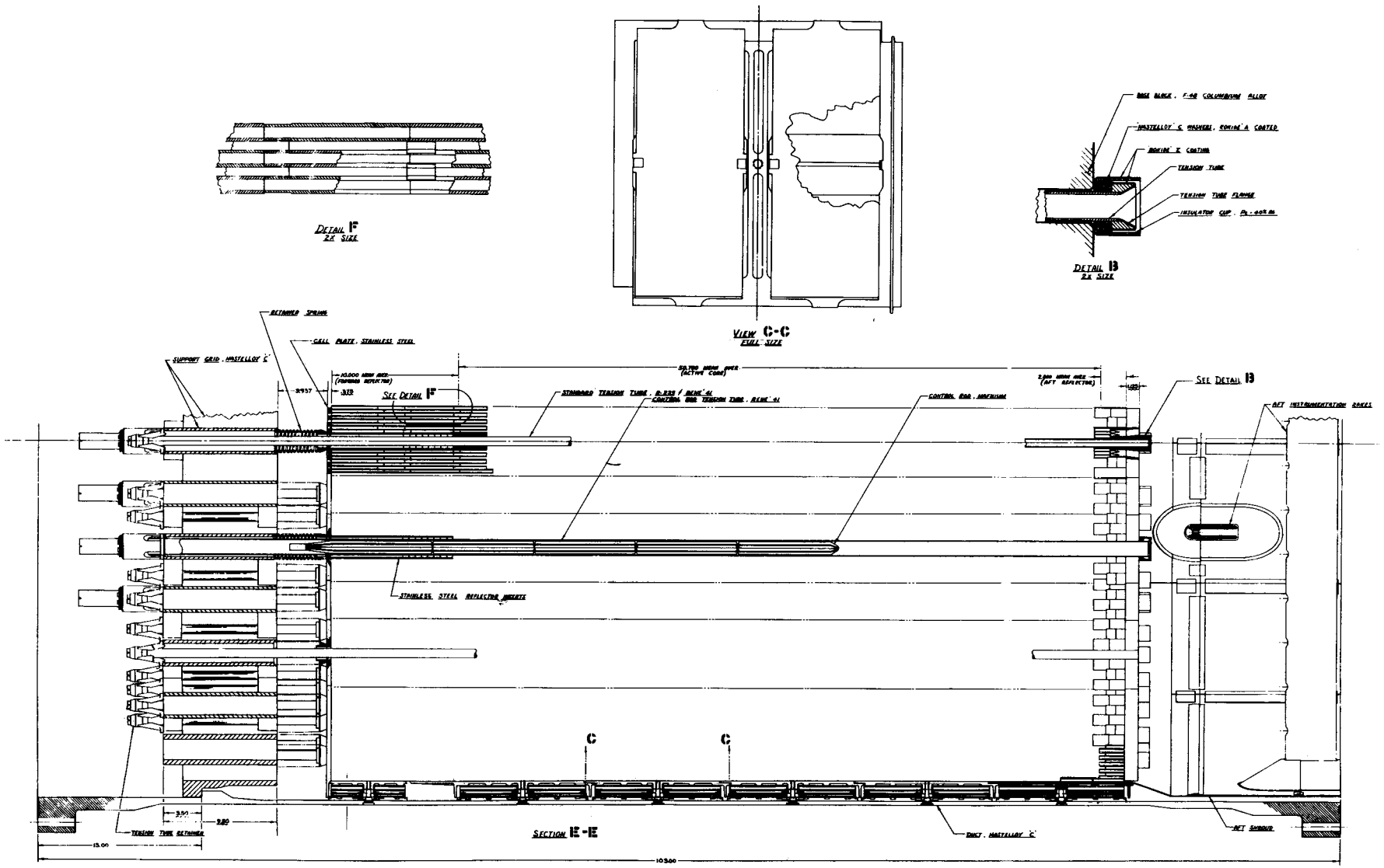

Fig. IV-11b. Reactor assembly.

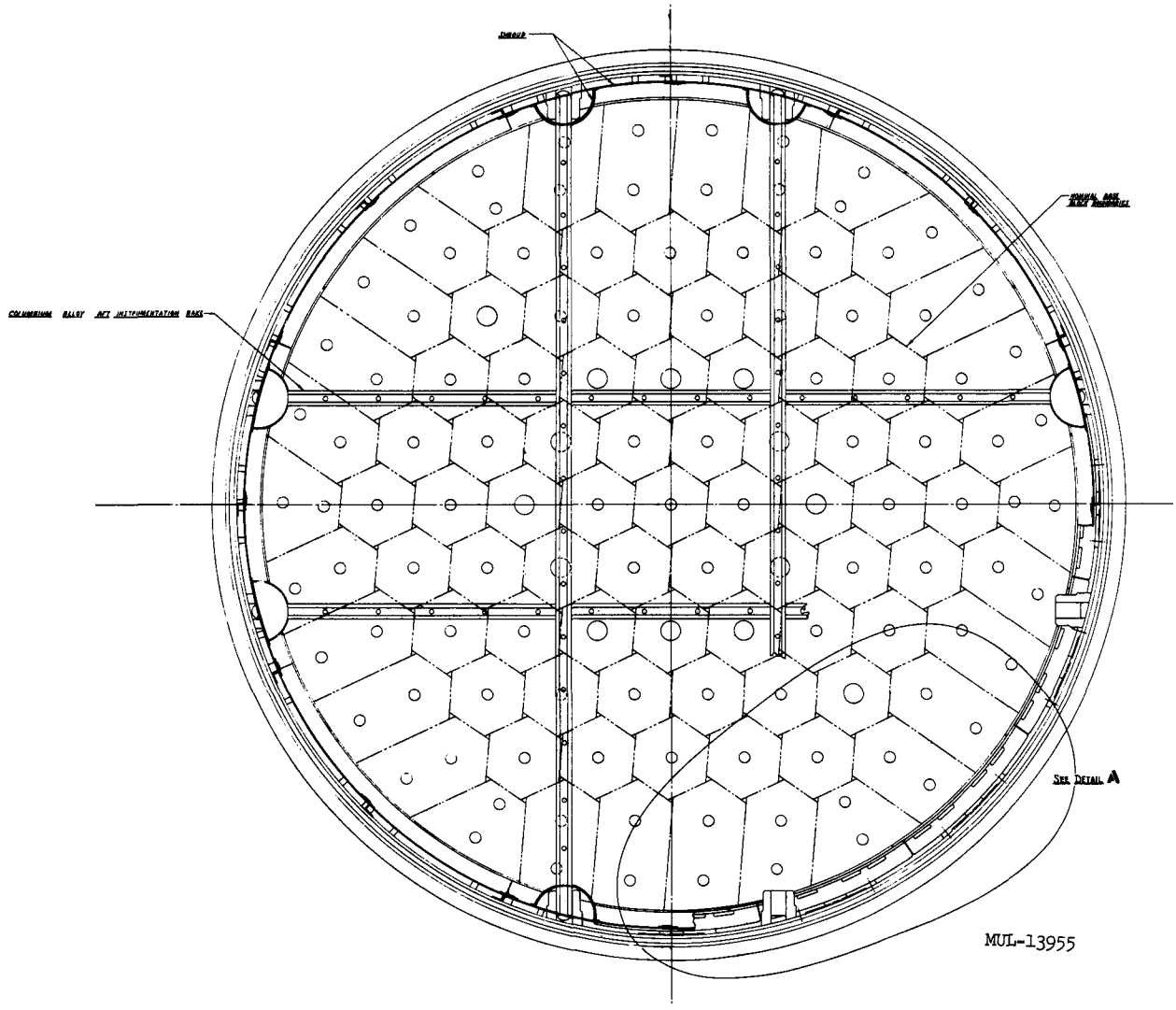

Fig. IV-11c. Reactor assembly.

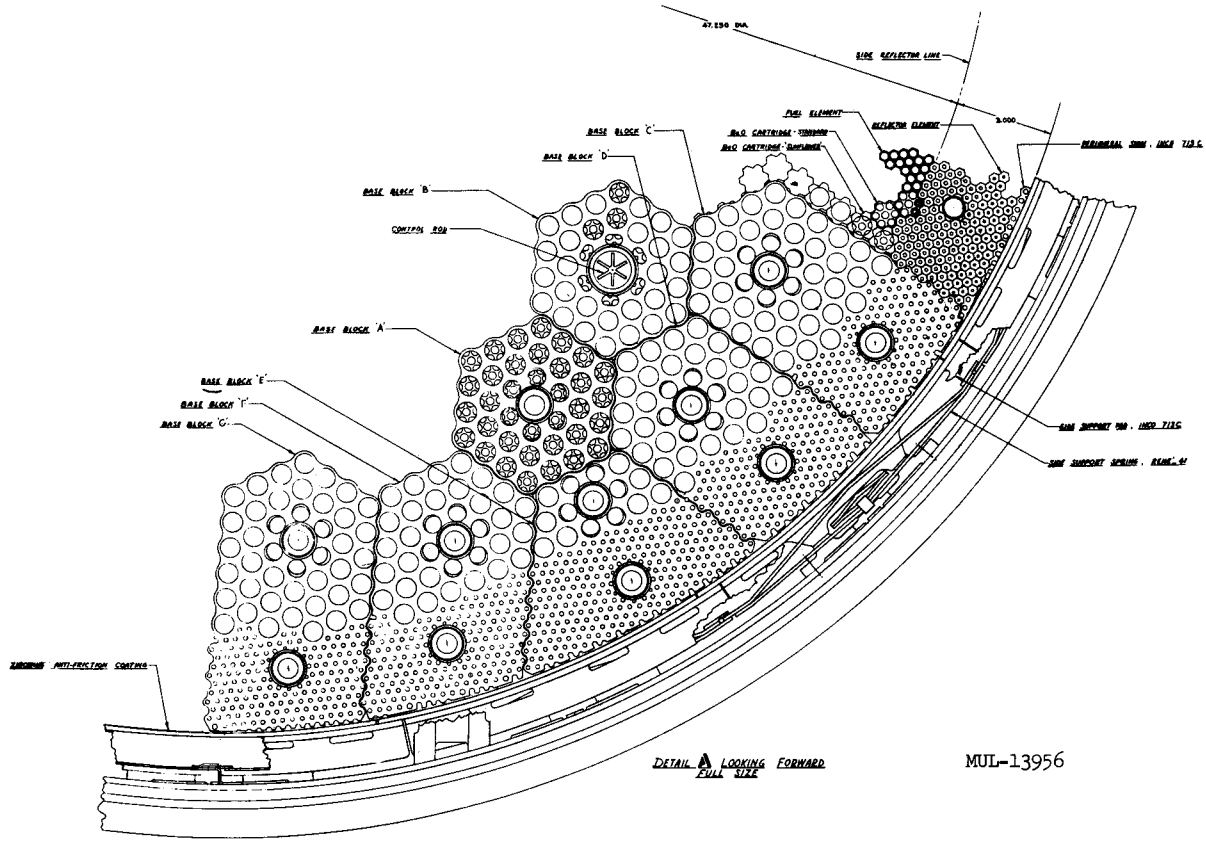

Fig. IV-11d. Reactor assembly.

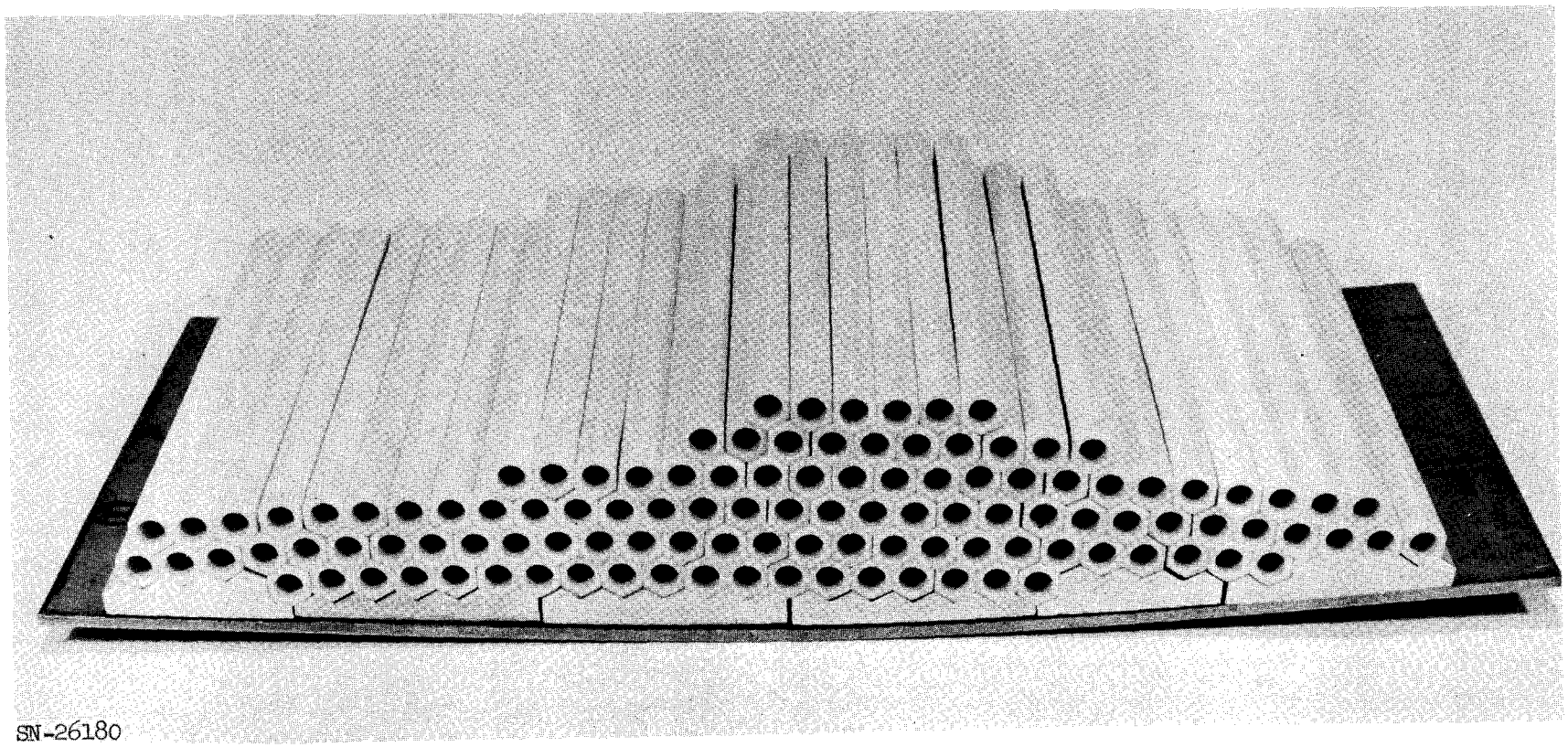

Fig. IV-12. Photo of first shim design.

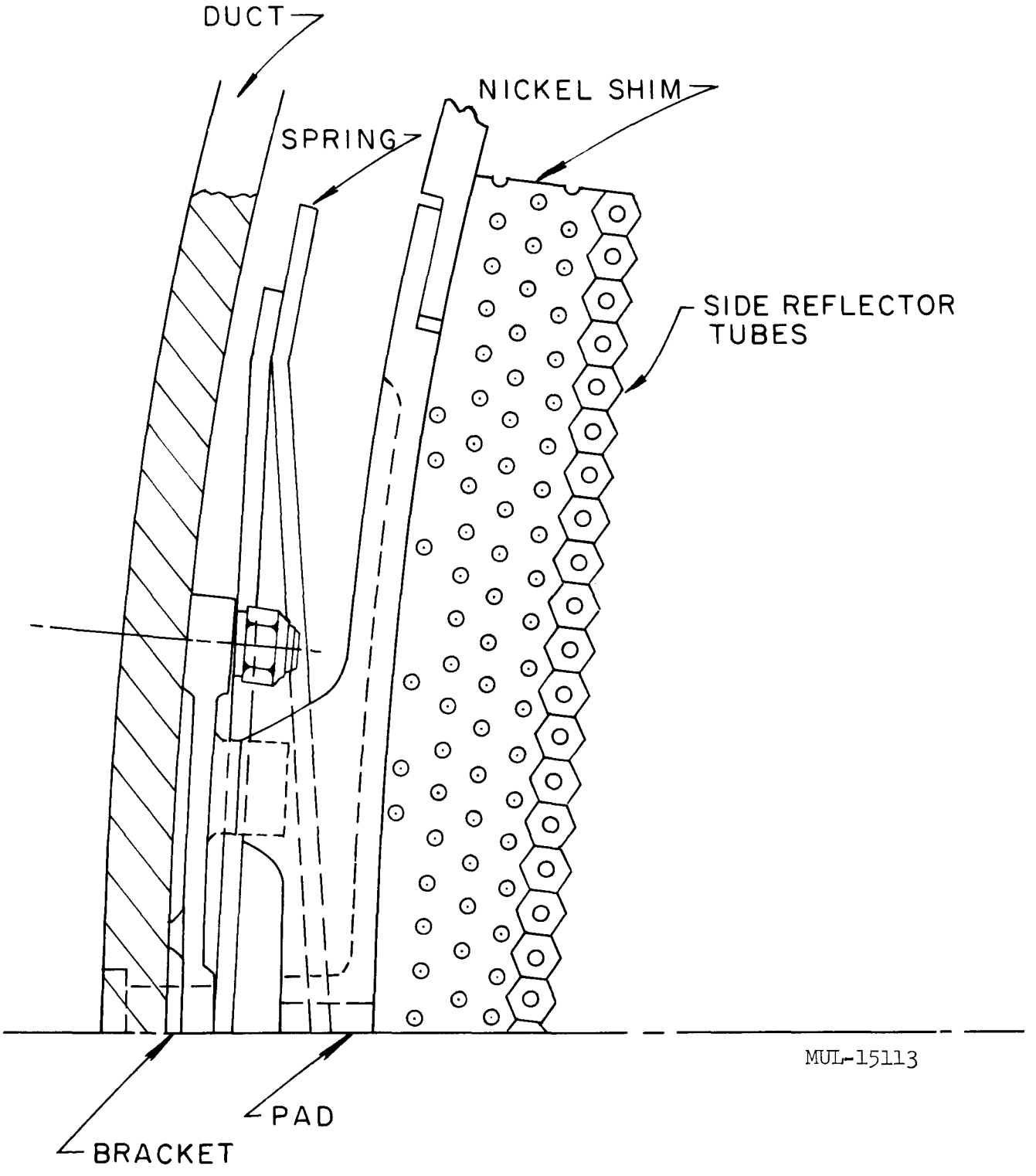

Fig. IV-13. Shims assembled with side support system.

system to externally cool the duct for the Tory II-C experiment. The shim material has been changed to cast electrolytic nickel, eliminating all elements with less neutron-reflecting or more neutron-absorbing properties.

At the periphery of the reflector, the nickel thickness chosen is as effective a reflector as BeO and can thus replace some BeO reflector tubes. The softness and ductility of the nickel shim is of advantage in avoiding high point-loads on reflector tubes, and in general providing a physically soft and geometrically compatible transition from the side support system to the ceramic reactor.

Figure IV-14 shows the stress-rupture properties of electrolytic nickel plotted on Larsen-Miller parameter coordinates. The maximum operating temperature of the shims is 1500°F to 1800°F, depending upon axial position. The mechanical stress imposed is 150 psi in compression. The nickel will yield under thermal stress with plastic strains of less than 1%.

II. TIE RODS

The tie rod brazing development program is under way with three vacuum-brazing companies. The objective of the program is to develop satisfactory vacuum-brazing cycles and techniques for brazing the forward and aft tie-rod fittings for both the standard and the control-rod tie rods. Operating temperatures are 1400 ±200°F. To date, the main objective has been to obtain 100% braze-filled joints without eroding or undercutting of the parent metal or holding for excessive time at temperature, which adversely affects the parent metal mechanical properties. The braze material selected, J-8100, a nickel-base alloy, has produced about 30% perfect brazes so far. Study of the braze cycle and gap indicates that a gap of 0.004 to 0.005 in., a vacuum of 2×10^{-6} mm, and a holding time of 6 to 8 minutes at 2160°F produces a completely filled joint. Further development in this and other alloys is being continued to provide the optimum brazed joint configuration.

Ultrasonic and x-ray test methods have been developed to provide complete confidence in determining the quality of brazed joints. These methods will be used to nondestructively test the reactor quantity of brazed tie-rod assemblies.

Test quantities of R-235 and René 41 tubing of both welded-to-size and redrawn types have been received. A test program is being conducted to determine if there is any significant difference in the ductility in tension between

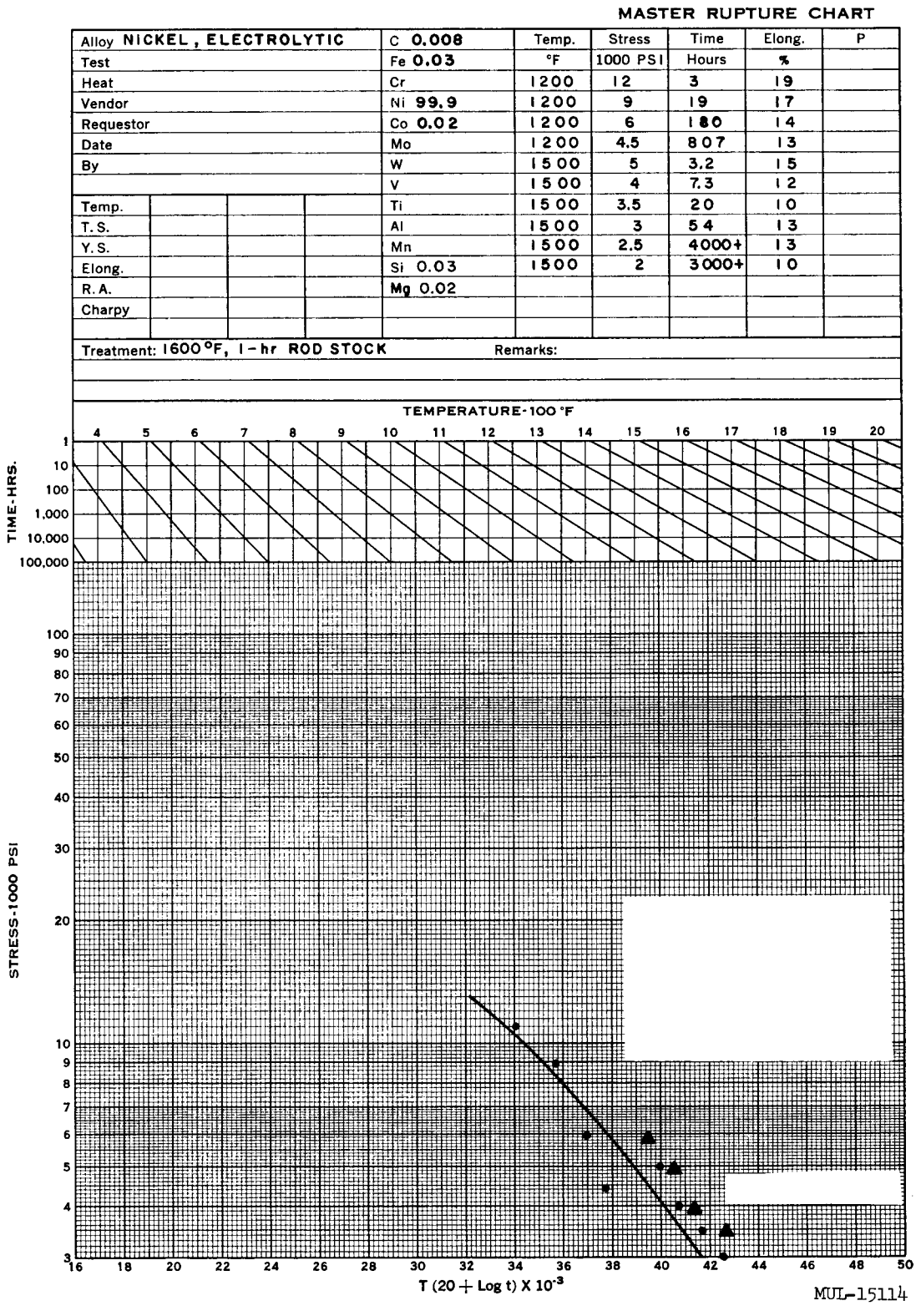

Fig. IV-14. Stress-rupture properties of electrolytic nickel.

nonworked welded tubing and welded and redrawn tubing. The first results of stress-rupture tests on the welded-to-size tubing are shown in Fig. IV-15, plotted on Larsen-Miller coordinates. Elongation is shown at the top of the figure.

III. FRONT RETAINER SYSTEM

Figure IV-16 shows one standard unit cell of this system. The function of the retainer plates and springs is to hold the front reflector in contact with the active core against forward-acting G loads, vibrational loads, and differential thermal movement. The front retainer plates transfer the spring load to the BeO reflector tubes and protect the BeO from the possibility of impact of foreign particles originating in the tank farm, air heater, and other parts of the air-supply system.

The retainer plate and spring adapter material is 410 stainless steel. Design of these parts is complete. Figure IV-17 shows the stress-rupture properties of 410 stainless steel. This alloy has been selected from many candidates because of its low thermal expansion to match the BeO reflector expansion, adequate strength, ductility and impact resistance, machinability, and availability.

The design of the springs is complete. Coil compression springs in triple-treated Inconel-X have been received and are being tested to determine spring constant vs temperature, stress relaxation vs time, and number of cycles to failure at maximum temperature. The design stress of the springs is 36,000 psi and the operating temperature 1100°F.

IV. AFT REFLECTOR

Test quantities of the aft reflector cartridges have been received, but have not conformed fully to the specification. The main problem is one of dimensional accuracy of hole location. Hole location must be precise to prevent offset losses in the flow channels. A second problem is the presence of inclusions of a size and quantity larger than acceptable. Aside from these points, the quality of the parts is good. A small amount of LRL-directed manufacturing development is expected to bring the parts within the specification. Figure IV-18 shows a group of the two types of cartridges assembled as if in the reactor.

MASTER RUPTURE CHART

Alloy R-235 0.670 o.d. TUBING				C	Temp.	Stress	Time	Elong.	P
Test CREEP RUPTURE				Fe	°F	1000 PSI	Hours	%	
Heat				Cr	1400	90	3	1.3	
Vendor				Ni	1400	85	2	3.1	
Requestor				Co	1400	90	3	4.7	
Date 9-15-61				Mo	1400	90	1	2.2	
By				W	1400	85	3.6	3.7	
				V	1400	66.8	22	5.9	
Temp.				Ti					
T.S.				Al					
Y.S.				Mn					
Elong.				Si					
R.A.									
Charpy									

Treatment: 1975, 30 min ac; -1400, 16-hr ac Remarks: L R L DATA

WALL THICKNESS 0.045 in., WELDED TO SIZE, NOT REDRAWN.

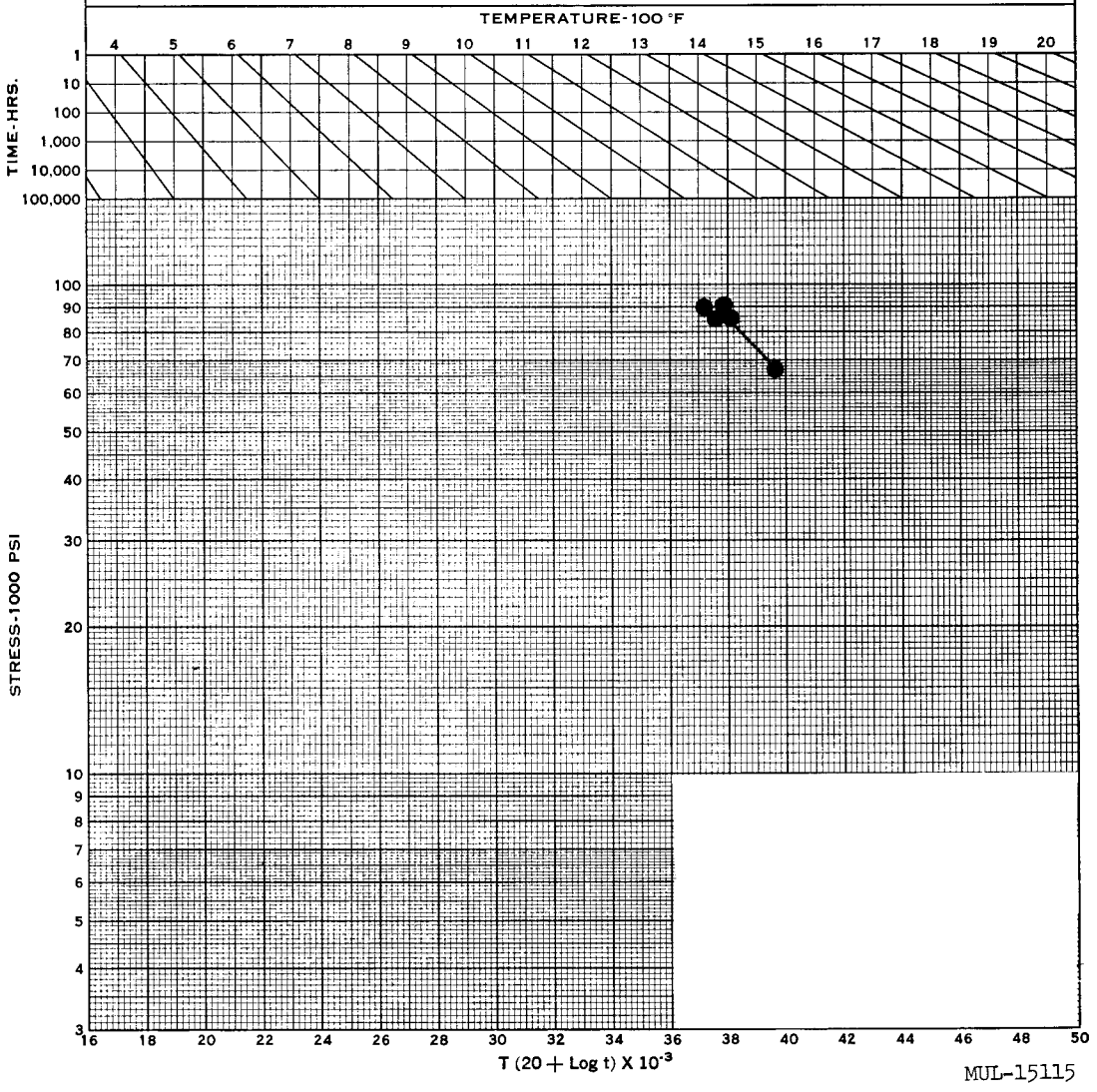

Fig. IV-15. Stress-rupture properties of R-235 welded (not redrawn) tubing.

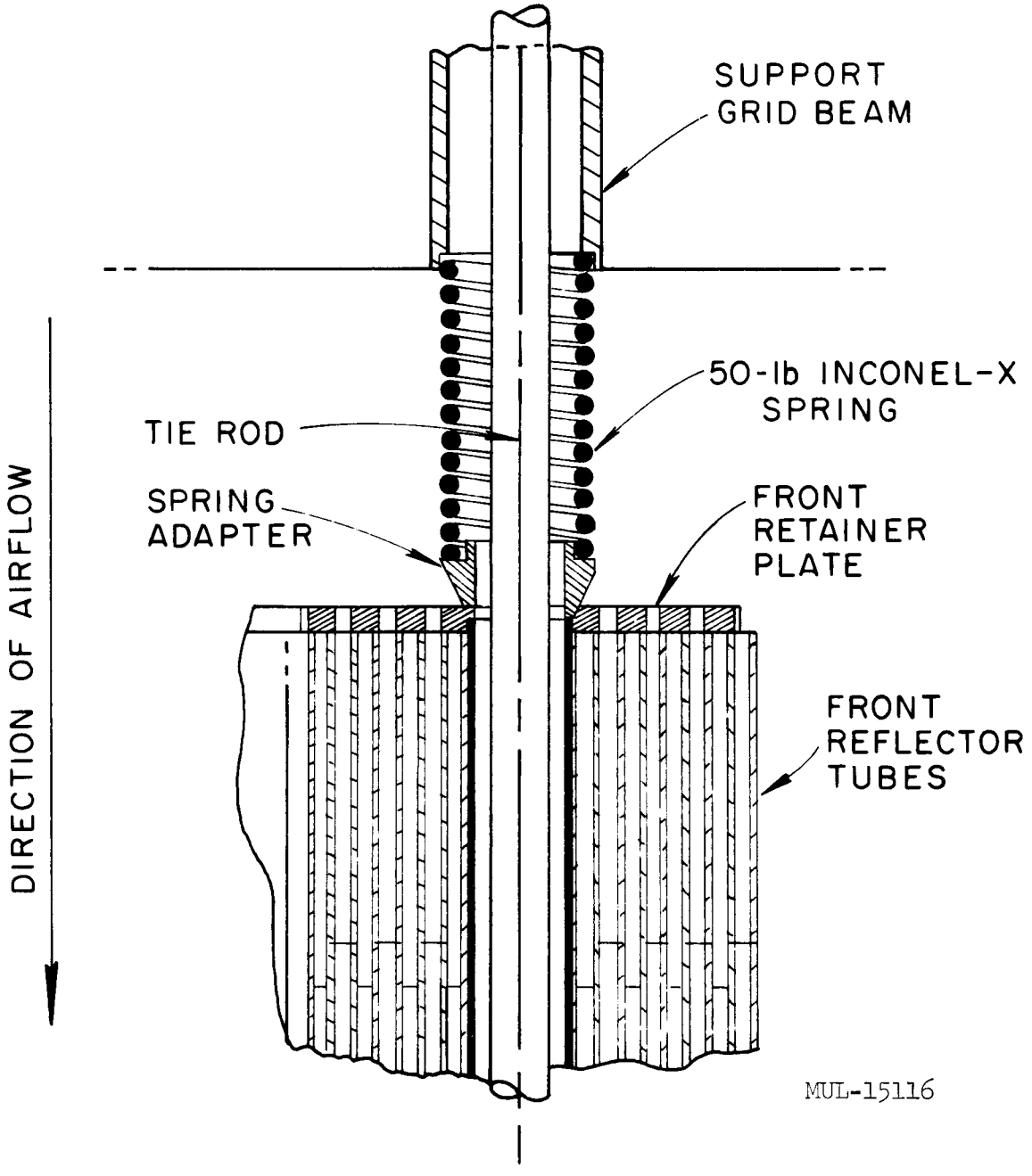

Fig. IV-16. Front reflector axial support system.

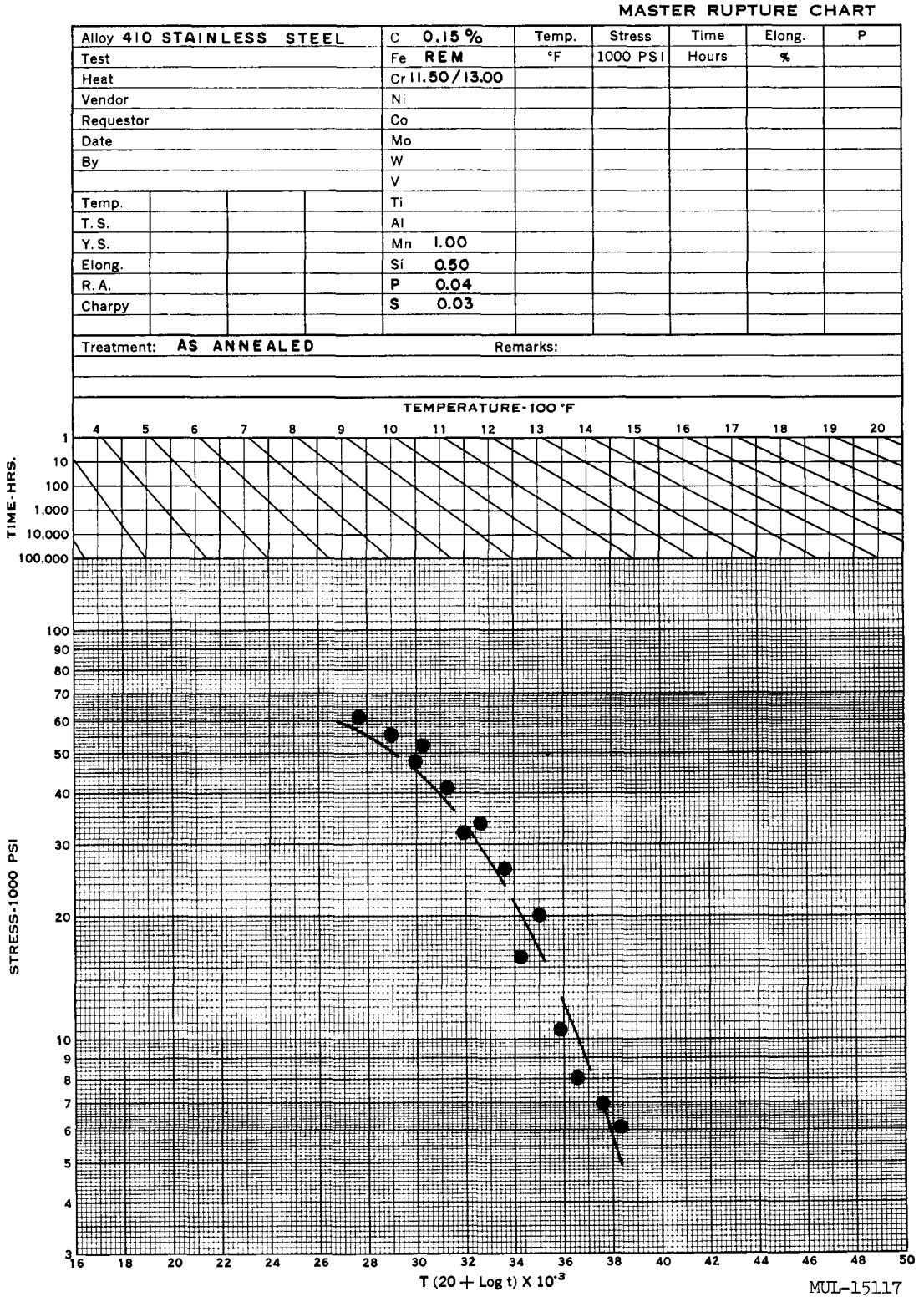

Fig. IV-17. Stress-rupture of 410 stainless steel.

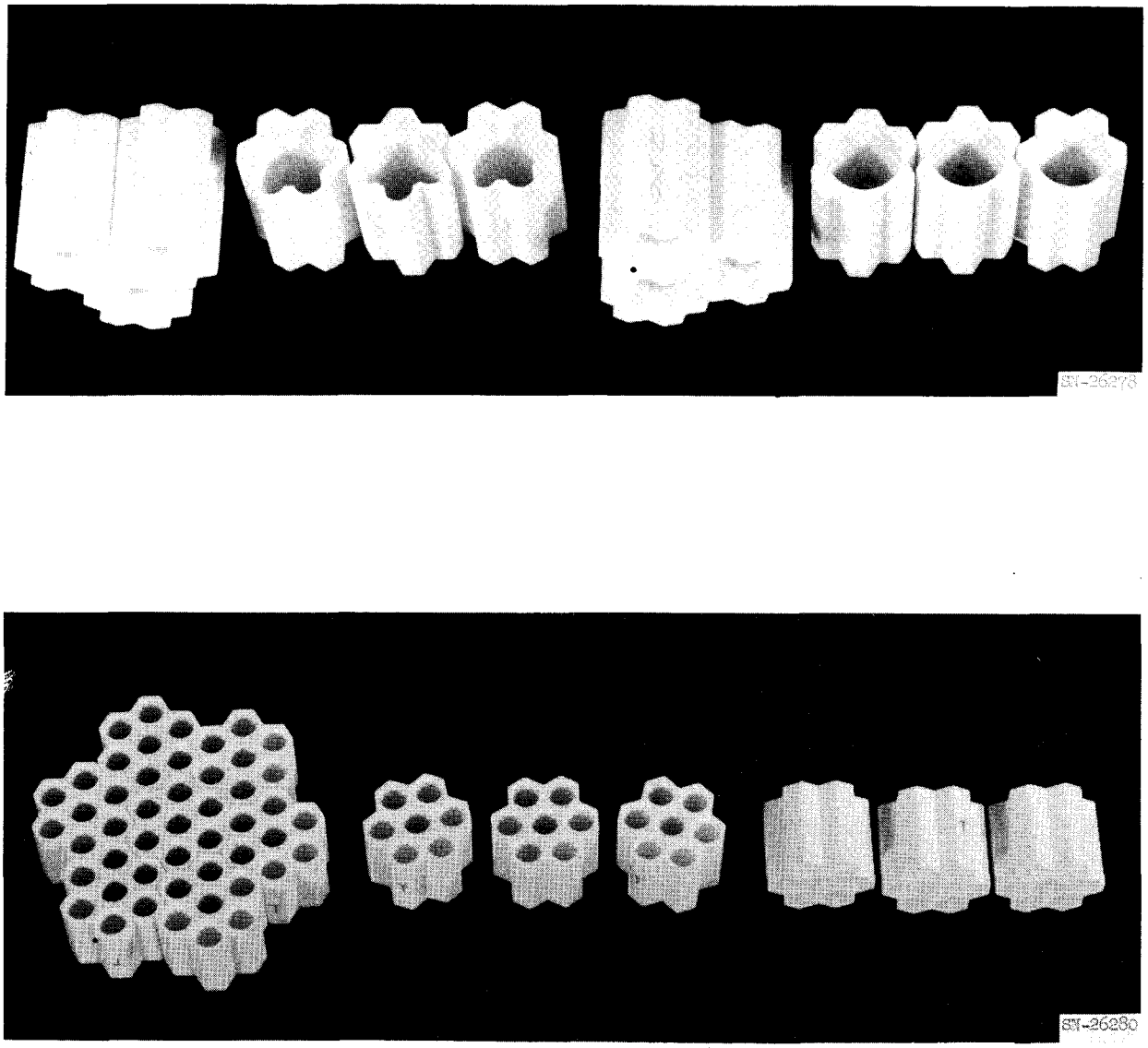

Fig. IV-18. BeO aft reflector cartridges.

V. CONTROL RODS

1. Coefficient of Friction Between Hafnium and R-235 at Elevated Temperatures

LRL performed preliminary coefficient of friction tests between hafnium and Hastelloy R-235 bars at temperatures of 1300, 1500, and 1700°F. The surfaces of the hafnium bar were cleaned ultrasonically before they were run. The surface finish of the hafnium and the R-235 were, respectively, 16 and 3 microinches (not typical in the reactor). The test assembly is shown in Fig. IV-19.

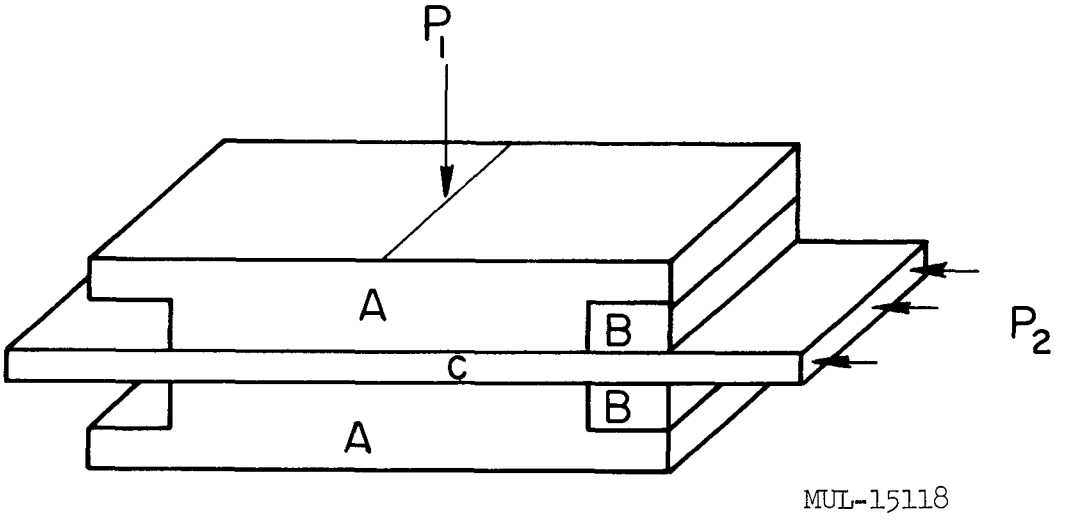

Fig. IV-19. Coefficient of friction specimen. Parts A and B are R-235, part C is hafnium.

The assembly was held at test temperature for 2 hours. Part B of the assembly was then removed to expose a uniformly oxidized surface. The assembly was then heated in a Leppel unit until the hafnium bar reached test temperature. The R-235 parts ran at a lower temperature than the hafnium, which simulates somewhat the actual core environment. A load, P_1, of 16.87 pounds was applied to the specimen giving a bearing pressure of 10 psi. The hafnium bar was then loaded as shown in Fig. IV-19. The load P_2 required to move the hafnium and the load required to maintain motion at a constant speed were measured.

The test was repeated after a soaking time of 5 hours, using the same velocities and pressure.

Preliminary results are given in Fig. IV-20. Additional tests are planned.

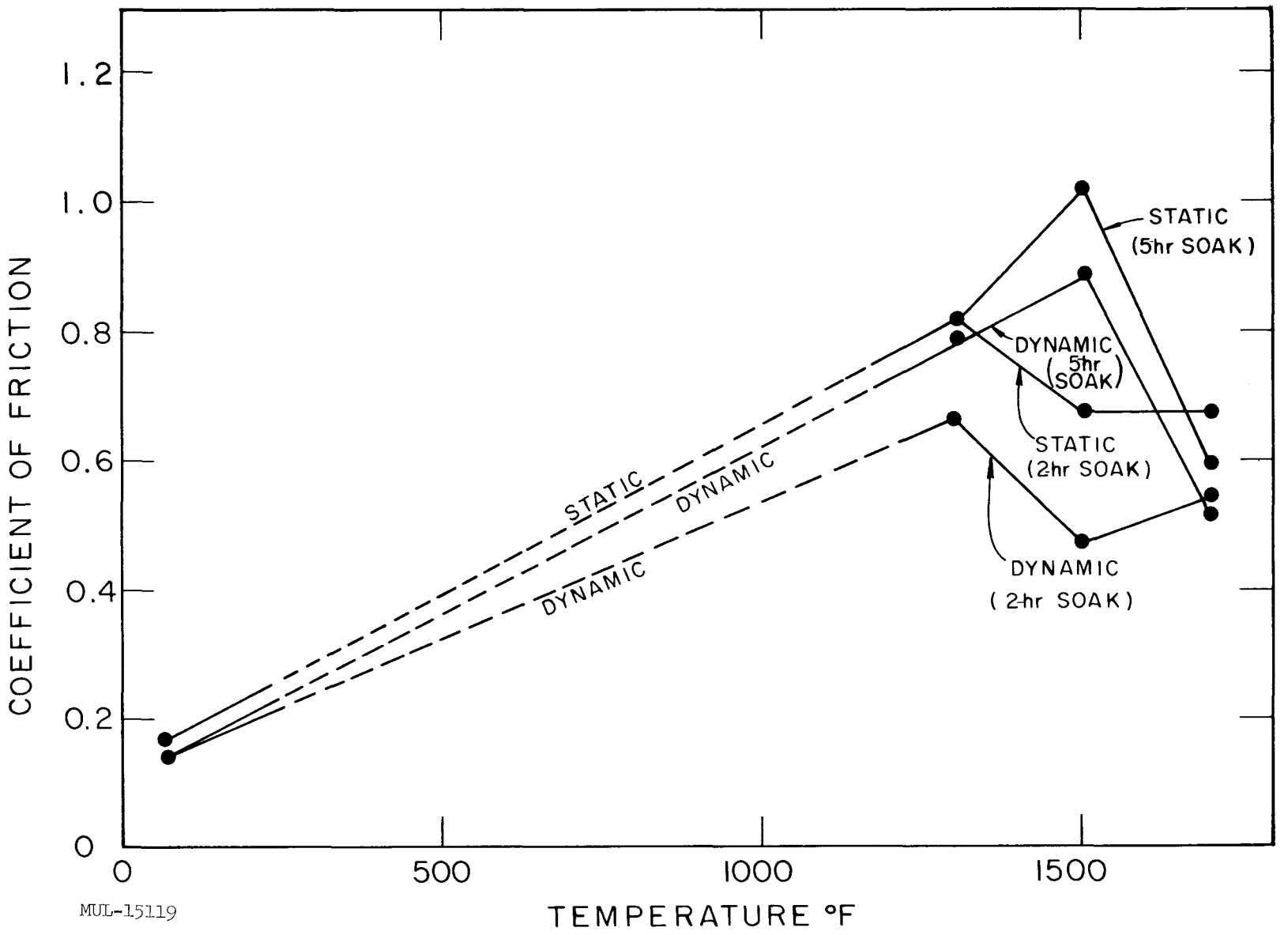

Fig. IV-20. Coefficient of friction vs temperature between hafnium and Hastelloy R-235.

2. Oxidation of Hafnium

LRL has continued hafnium oxidation studies. Pack carburizing of hafnium specimens at 1600°F for 24 hours has improved oxidation resistance as shown in Fig. IV-21.

SAFETY RODS

A transient heat transfer analysis was made on a bare boron-nitride circular rod in an air stream. The internal (maximum) temperature in the boron-nitride rod is given by:

$$T_i(0,t) = \frac{GR^2}{2K} + \frac{GR}{2h} + T_g - \frac{2Gh}{RK^2} \sum_{n=1}^{\infty} \frac{e^{-\alpha\beta_n^2 t}}{\beta_n^2\left[\left(\frac{h}{K}\right)^2 + \beta_n^2\right] J_0(R\beta_n)}$$

where T_i is internal temperature of boron nitride

T_g is temperature of air stream

t is time

h is convection coefficient

k is thermal conductivity

α is thermal diffusivity

G is internal heat generation rate

R is radius of cylinder

β_n are positive roots of

$$R\beta J_1(R\beta) = \frac{h}{K} RJ_0(R\beta) \quad .$$

Using a 0.300-inch-diameter rod, an internal heat generation rate of 1.75 Mw/ft^3, and a 1060°F air stream, the internal temperature is plotted on Fig. IV-22.

The specific heat of boron nitride is given by

$$C_p = 0.212 + 1.79 \times 10^{-4} T \quad \text{Btu/lb-°F}$$ [1]

where T is in °F. For this calculation, the specific heat is determined at the average of the gas temperature and the steady state temperature at the center of the rod.

---

[1] High Temperature Materials, Inc., to U. S. Navy, Bureau of Naval Weapons, Special Projects Office, Contract NOw 60-0202 [FBM], First Quarterly Progress Report, June 1960.

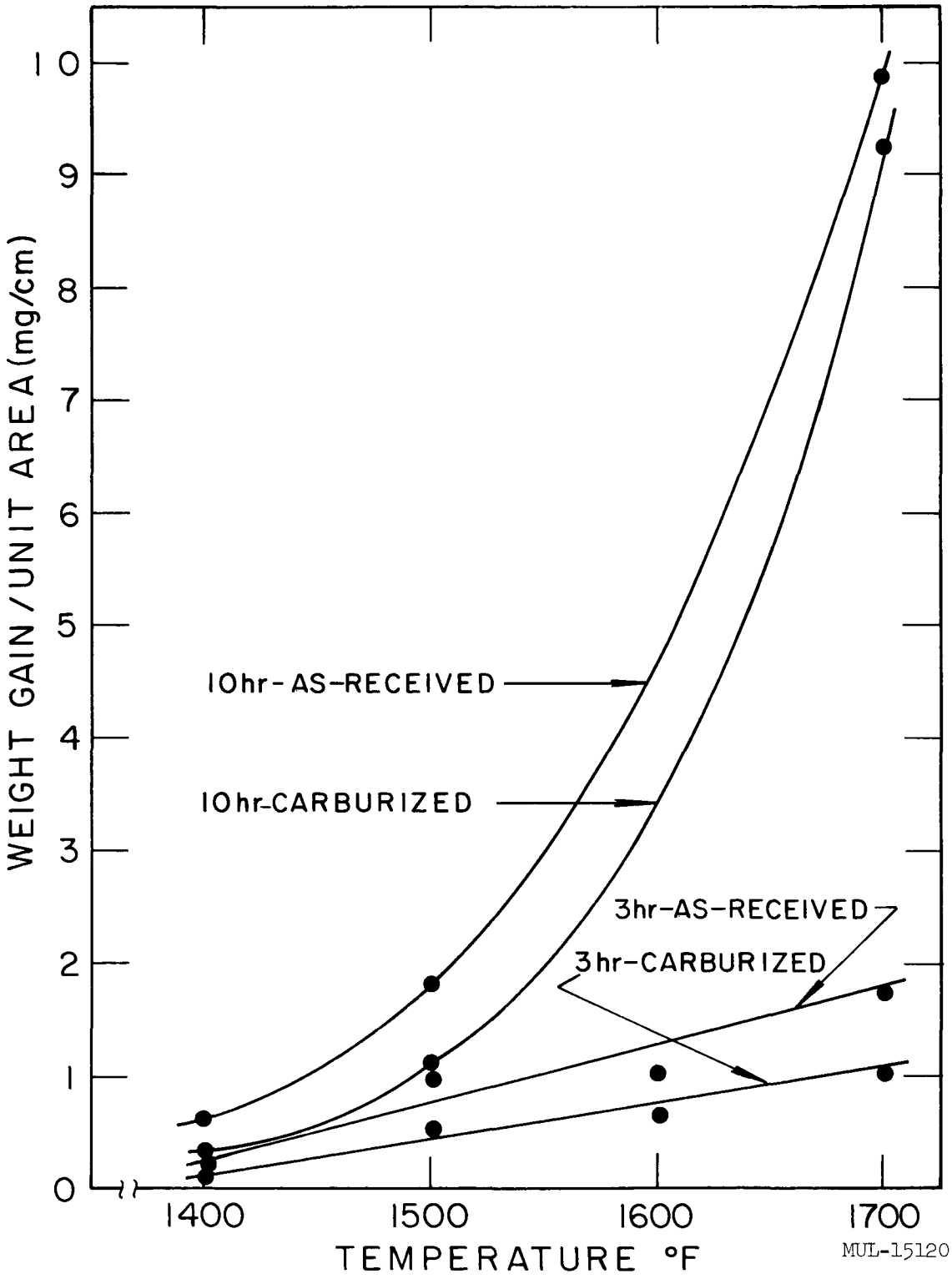

Fig. IV-21. Oxidation of hafnium in still air at one atmosphere for 3 hours and 10 hours at various temperatures. Results are shown for material oxidized in the as-received condition and after carburizing treatments.

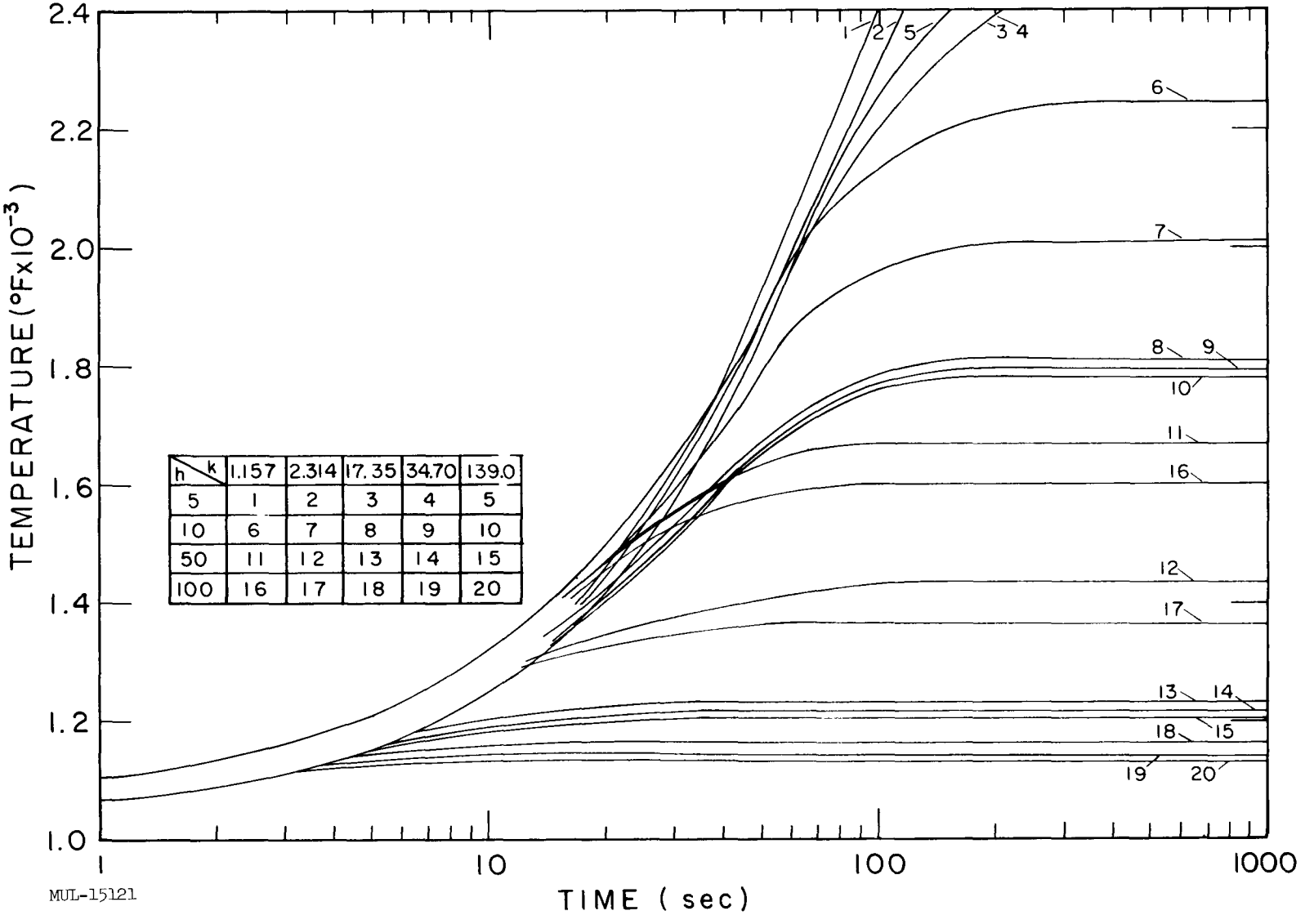

h \ k	1.157	2.314	17.35	34.70	139.0
5	1	2	3	4	5
10	6	7	8	9	10
50	11	12	13	14	15
100	16	17	18	19	20

Fig. IV-22. Transient temperature in the center of a 0.300-inch-diameter boron-nitride rod with internal heat generation in a 1060°F air stream for various heat transfer coefficients and conductivities. G = 0.96 Btu/sec-in^3 (1.75 Mw/ft^3). h – Btu/sec-in^2-°F × 10^5. K – Btu/sec-in. -°F × 10^5.

Since boron nitride is highly anisotropic, the thermal conductivity varies with grain orientation. For hot-pressed boron nitride at 1800°F, the thermal conductivity parallel to the pressing direction is about 17.35×10^{-5} Btu/sec-in.-°F, while perpendicular to pressing direction the conductivity is 34.7×10^{-5} Btu/sec-in.-°F.[2] For pyrolytic boron nitride, Kc ranges from between about 1.157×10^{-5} [3] and 2.314×10^{-5} Btu/sec-in.-°F,[4] and Ka is about 139×10^{-5} Btu/sec-in.-°F.[3]

The most probable convection coefficients lie between 10×10^{-5} and 50×10^{-5} Btu/sec-in^2-°F. Thus, after 5 minutes of run time, the rod is within 50°F of steady state temperature.

VI. SUPPORT GRID

A full size test beam, a duplicate of the center beam, was machined from Hastelloy-C plate (Fig. IV-23). This beam has been tested at room temperature to 1-1/2 times the design load. The measured strains and deflections agreed with the structural analysis.

VII. SIDE SUPPORT SYSTEM

Buggy Springs (Brazed)

Design of the production buggy spring (pressure + flight spring) has been completed and released for procurement of an evaluation quantity of 40. Brazing has been selected over the "riveted" end fasteners as a result of the very successful fatigue testing on brazed assemblies. This testing is being conducted both at an outside laboratory and at LRL. Table IV-9 shows some room temperature and 1200°F, 1300°F, and 1400°F fatigue data.

Three braze alloys are being investigated — 4778A, J-8100, and J-8600; 4778A has been tentatively selected. Figures IV-24 and IV-25 show a comparison of the effect on the mechanical properties (René 41 sheet) of 6 brazing and heat-treat cycles. The lower brazing temperature of 4778A (1950°F) produces a significantly stronger material than does J-8100 (2150°F) or J-8600 (2180°F). It follows that the 4778A alloy is less ductile. This decrease in

---

[2] W. G. Bradshaw and C. O. Matthews, Lockheed Aircraft Corporation.

[3] High Temperature Materials, Inc., to U.S. Navy Fifth Quarterly Progress Report, 30 June, 1961, Contract NOw 60-0202 [FBM].

[4] High Temperature Materials, Inc., to U.S. Navy Fourth Quarterly Progress Report, February 1961, Contract NOw 60-0202 [FBM].

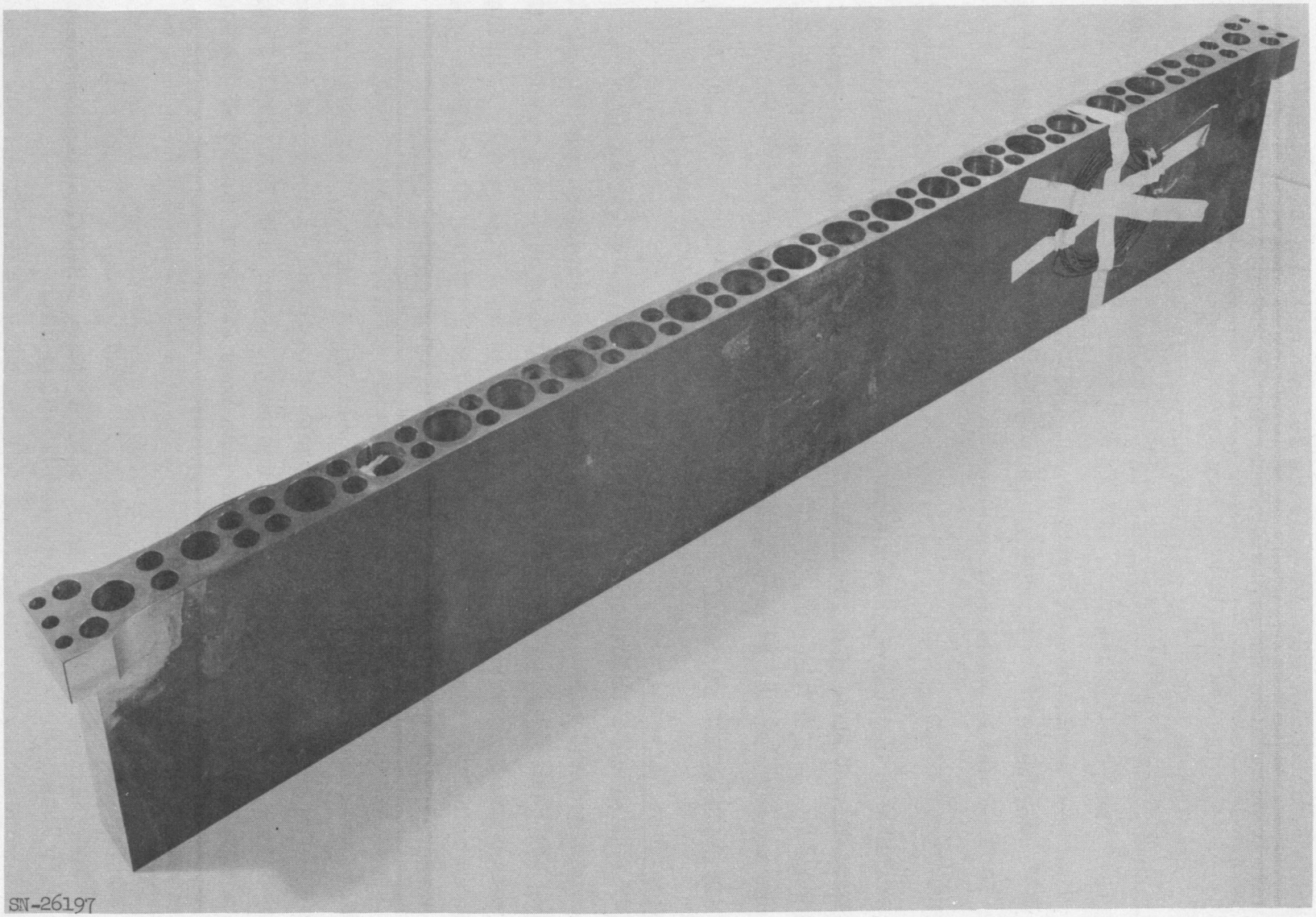

Fig. IV-23. Support grid test beam.

Table IV-9. René 41 Buggy Spring Fatigue Test.
(Supplier's laboratory.)

Braze alloy	Temp	Total* initial load lb	Total terminal load lb	No. cycles × 10^3	Measured permanent set	Remarks
4478A	Room	1160	1040	180	0.005	No cracks, braze sound
J-8100	Room	1240	970	500	0.012	No cracks, braze sound
4778A	1200°F	1200	1170	180	0.006	No cracks, braze sound
J-8100	1200°F	1200	1180	180	0.009	No cracks, braze sound
4778A	1300°F	1200	1080	188	0.029	No cracks, braze sound
J-8100	1300°F	1200	--	134	--	Fracture
4778A	1400°F	1200	--	36	--	Fracture
J-8100	1400°F	1200	--	45	--	Fracture

4778A Heat treatment:

1950°F - 1975°F - 30 min - F. C.
1950°F - 1975°F - 30 min - A. C.
1400°F - 1425°F - 16 hr - A. C.

J-8100 Heat treatment:

2150°F - 2170°F - 30 min - F. C.
1950°F - 1975°F - 30 min - A. C.
1400°F - 1425°F - 16 hr - A. C.

* Note: All springs were preloaded 200 lb.
Oscillating deflection for all runs was 0.345.
Springs are 0.125 gage × 4.49 wide.

ductility, however, has not proven to be a problem. Figures IV-26, IV-27, and IV-28 show microhardness surveys of a typical brazed joint of each of the 3 alloys. Figures IV-29, IV-30 and IV-31 show photomicrographs of René 41 sheet following exposure at the brazing and tempering cycles of the three braze alloys. Creep data at 1400°F are presented in Fig. IV-32. Ductility and shear and tensile strength data on the 3 braze alloys are being developed.

Several fatigue tests were conducted on the side support springs (buggy springs) at 1400°F. Figure IV-33 shows the test apparatus. Figure IV-34 is a sketch of a side support spring. The results of all the tests to date are summarized in Table IV-10.

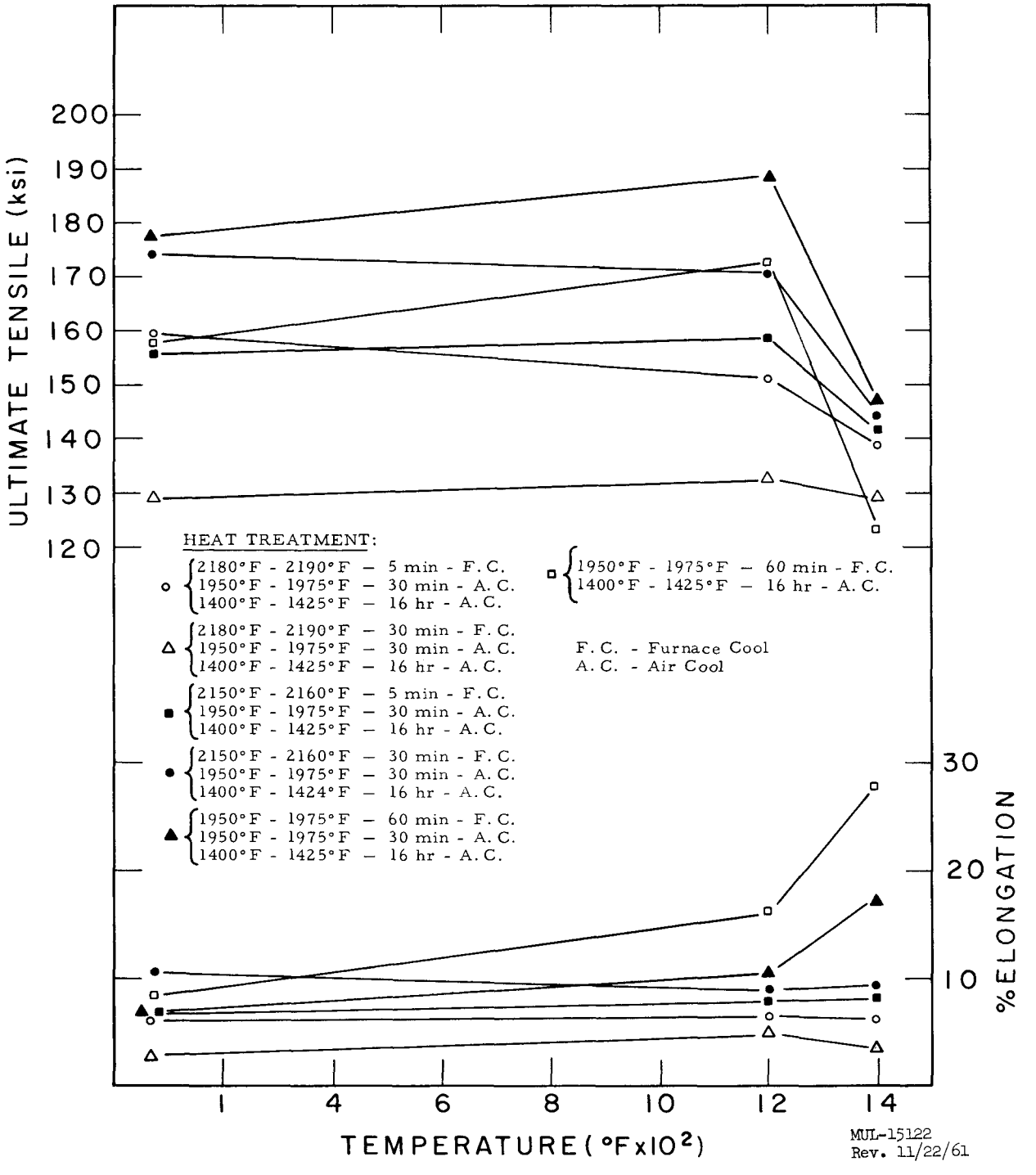

Fig. IV-24. Mechanical properties comparison, 0.125 René 41 sheet after exposure to six brazing and aging cycles.

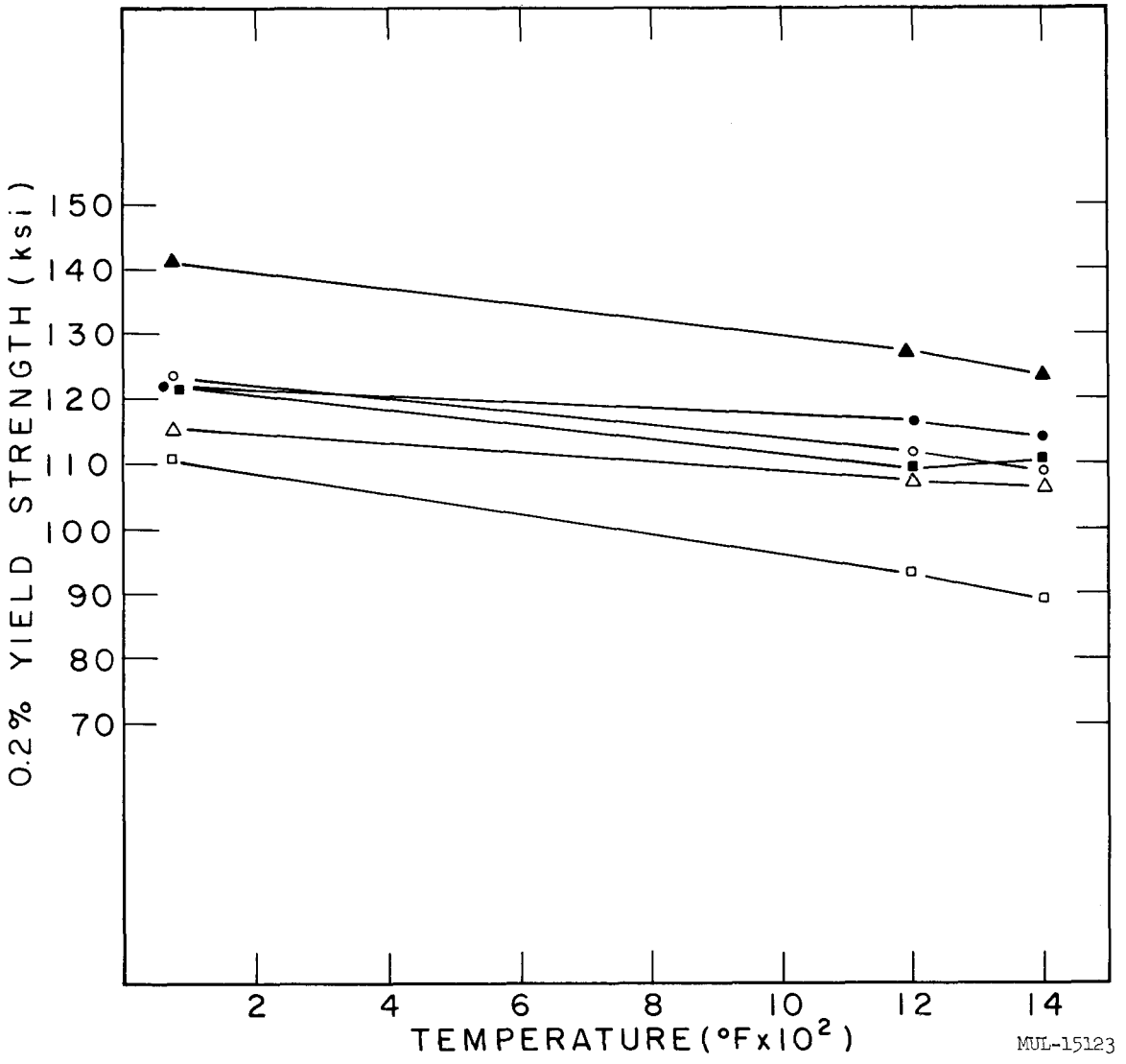

Fig. IV-25. Mechanical properties comparison, 0.125 René 41 sheet after exposure to brazing and aging cycles. See Fig. IV-24 for heat treatment.

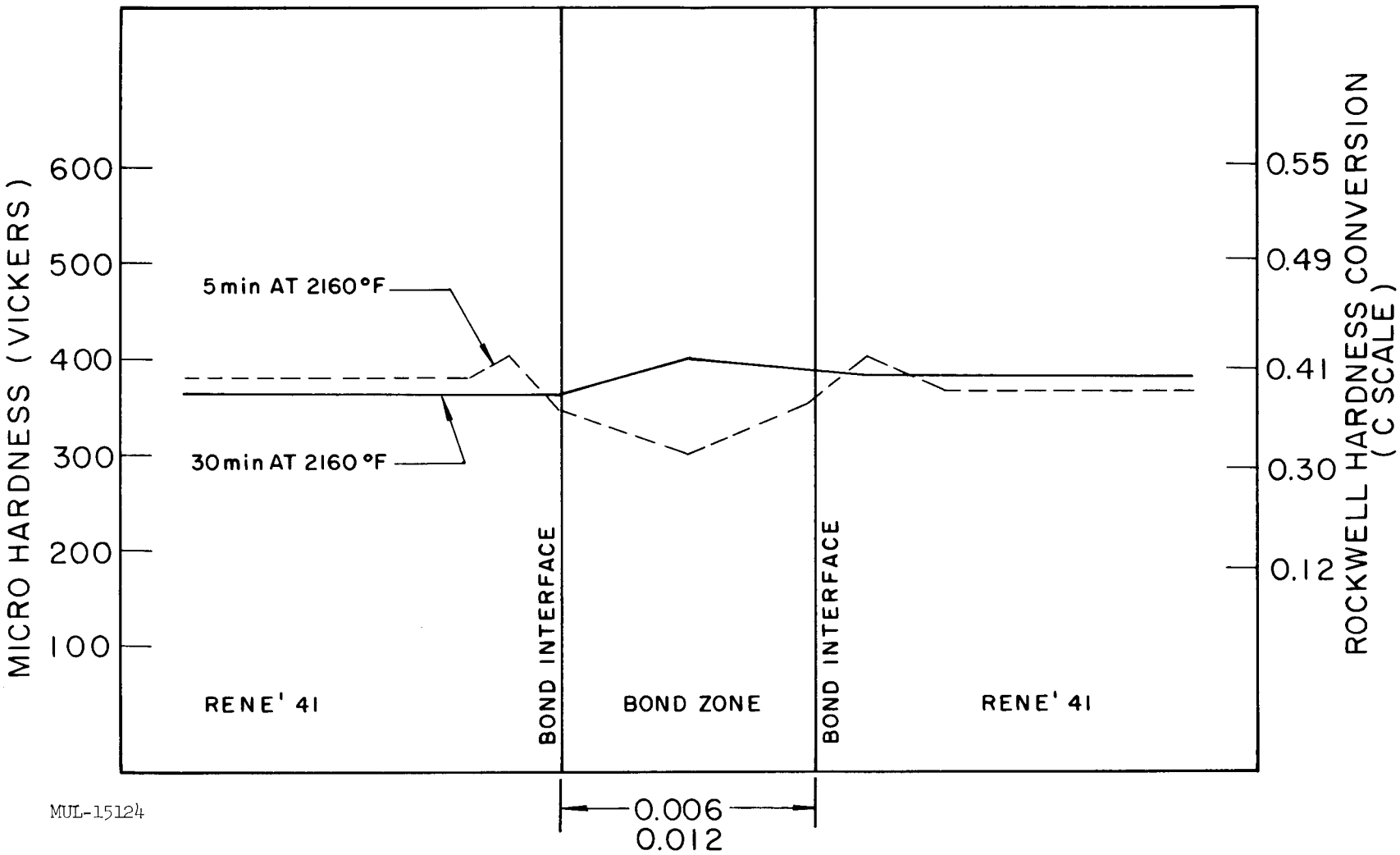

Fig. IV-26. Microhardness traverse, J-8600 braze.

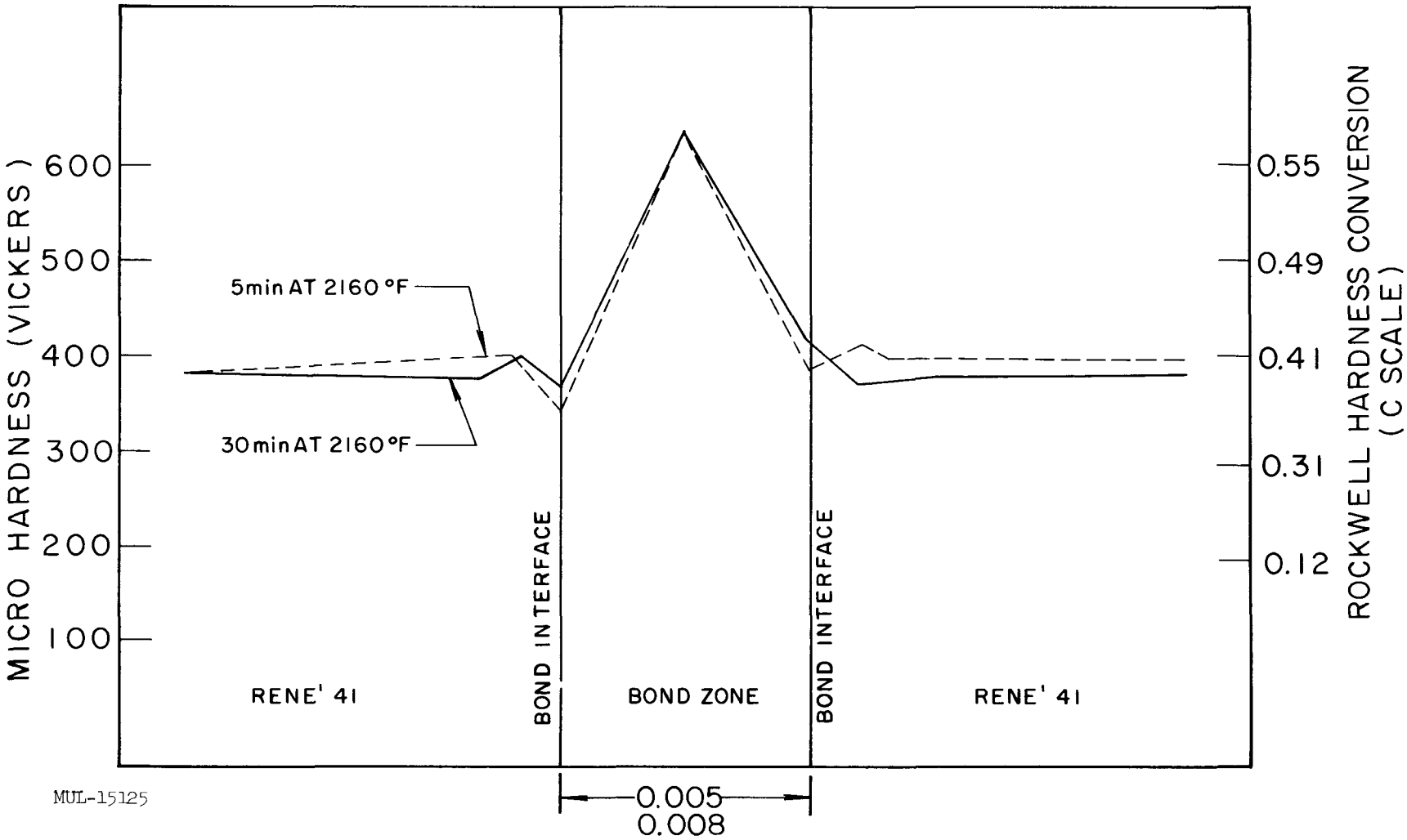

Fig. IV-27. Microhardness traverse, J-8100 braze.

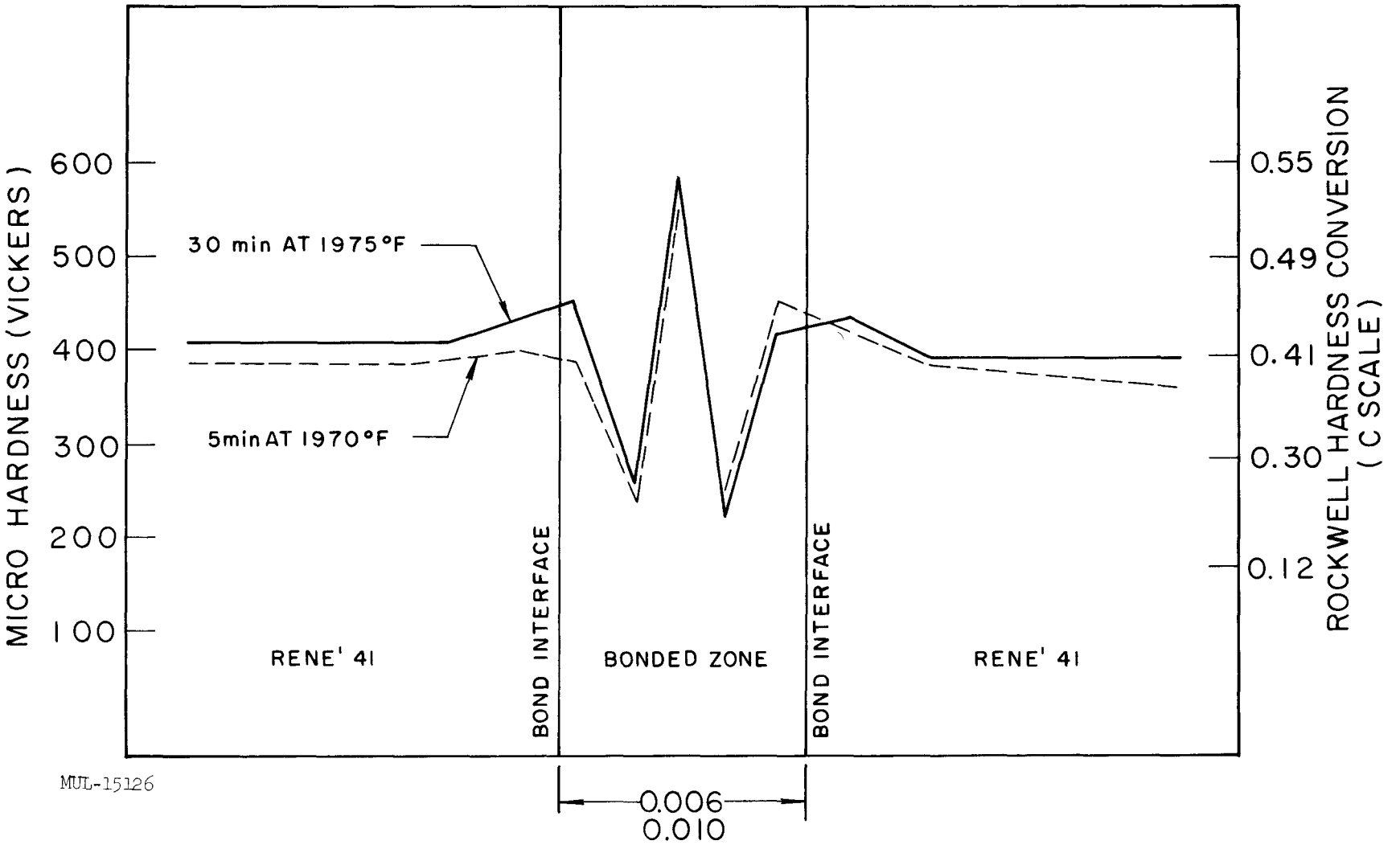

Fig. IV-28. Microhardness traverse, 4778A braze.

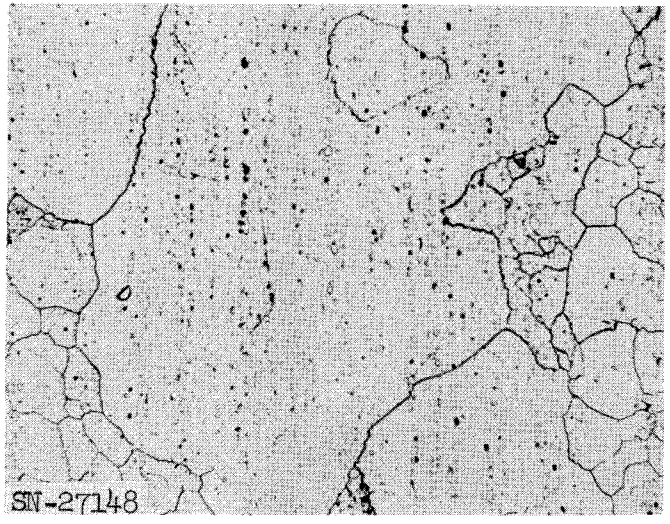

100X

2180–2190 °F – 5 min – F. C.
1950–1975 °F – 30 min – A.C.
1400–1425 °F – 16 hrs – A.C.

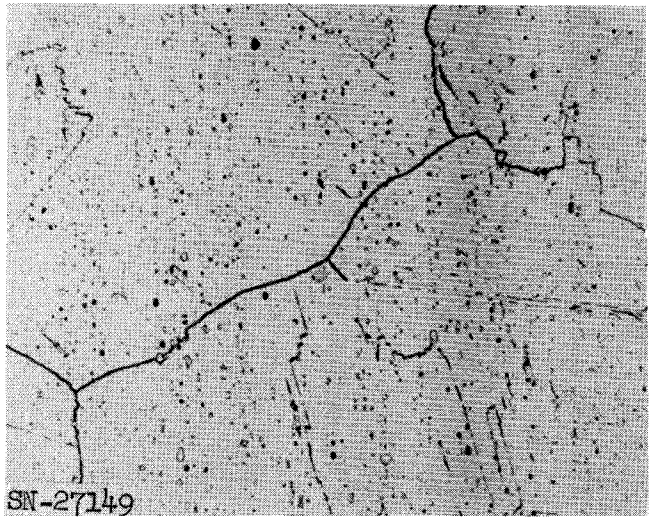

100X

2180 – 2190 °F – 30 min – F.C.
1950 – 1975 °F – 30 min – A.C.
1400 – 1425 °F – 16 hrs – A.C.

Fig. IV-29. Photomicrographs showing effect of J-8600 brazing cycles on 0.125 René 41 sheet. (Marble's reagent.)

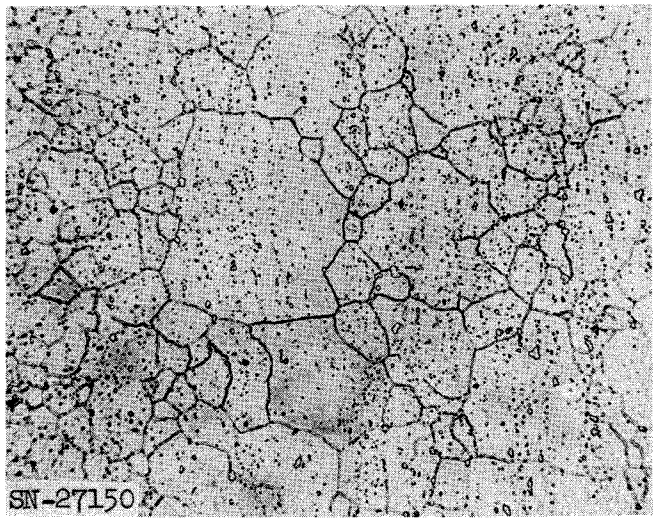

100X

2150-2160°F-5min-F.C.
1950-1975°F-30min-A.C.
1400-1425°F-16 hrs-A.C.

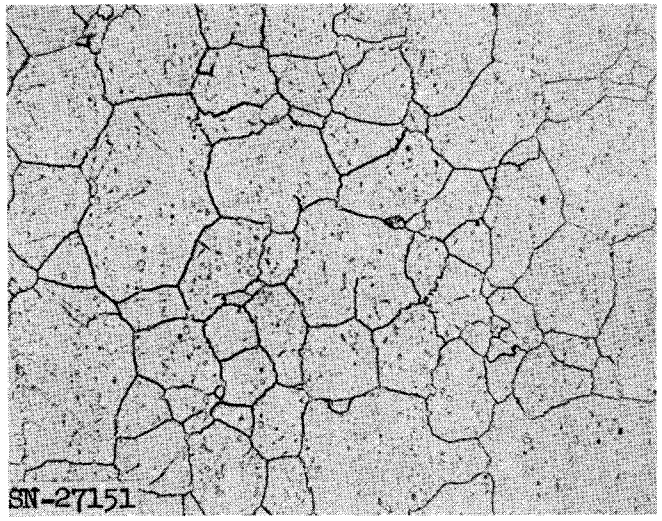

100 X

2150-2160°F-30 min-F.C.
1950-1975°F-30min-A.C.
1400-1425°F-16 hrs -A.C.

Fig. IV-30. Photomicrographs showing effect of J-8100 brazing cycles on 0.125 René 41 sheet. (Marble's reagent.)

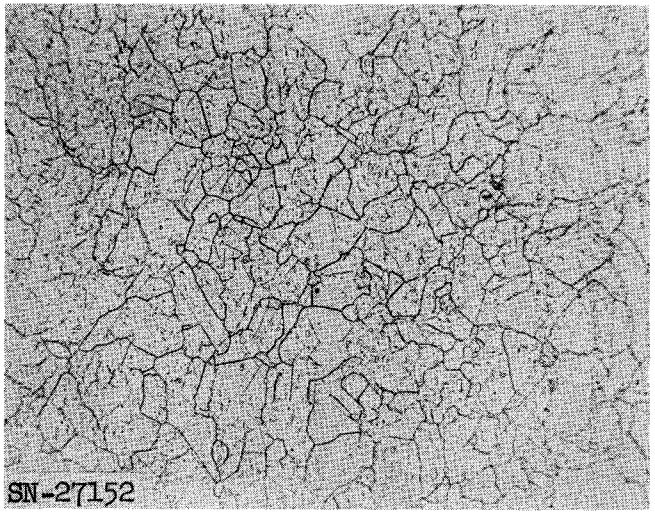

100X

1950-1975°F-60min-F.C.
1950-1975°F-30min-A.C.
1400-1425°F-16min-A.C.

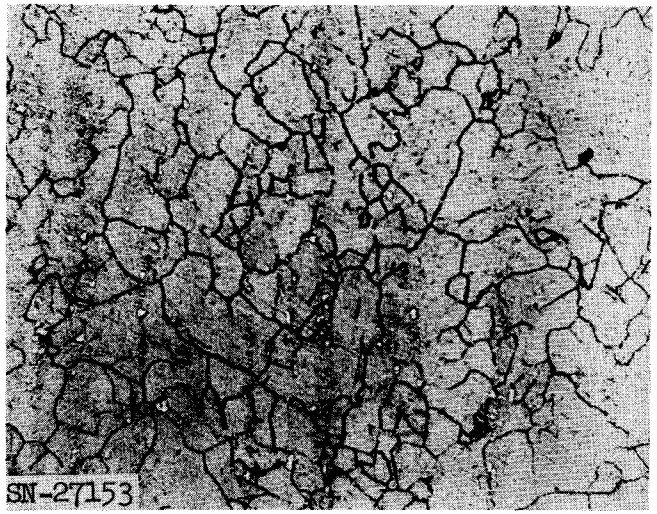

100X

1950-1975°F-60 min-F.C.
1400-1425°F-16 min-A.C.

Fig. IV-31. Photomicrographs showing effect of 4778A brazing cycles on 0.125 René 41 sheet. (Marble's reagent.)

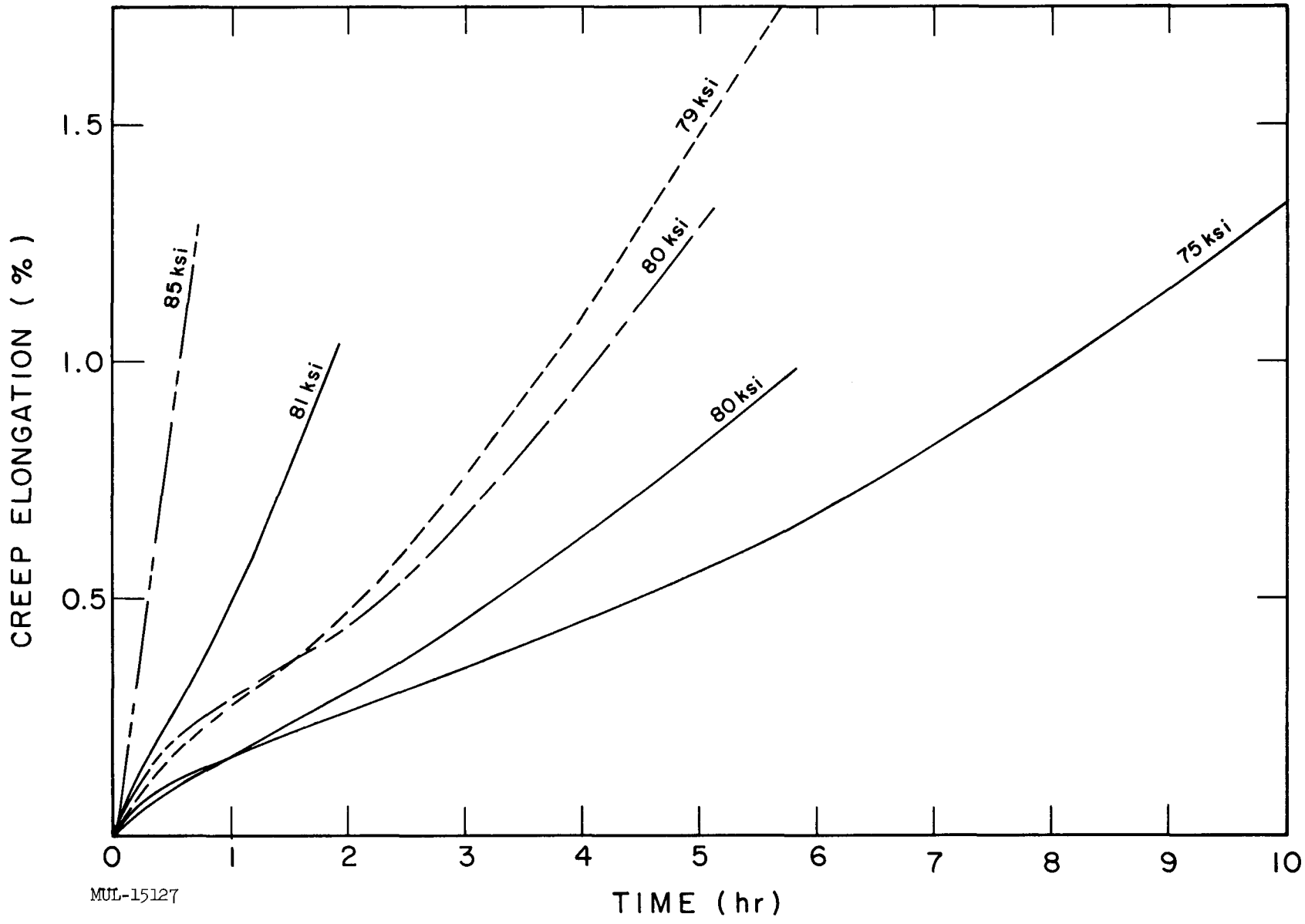

Fig. IV-32. 1400°F creep elongation of René 41 sheet. Heat treatment: 1950-1975°F – 30 min – A.C.; 1400-1425°F – 16 hr – A.C.

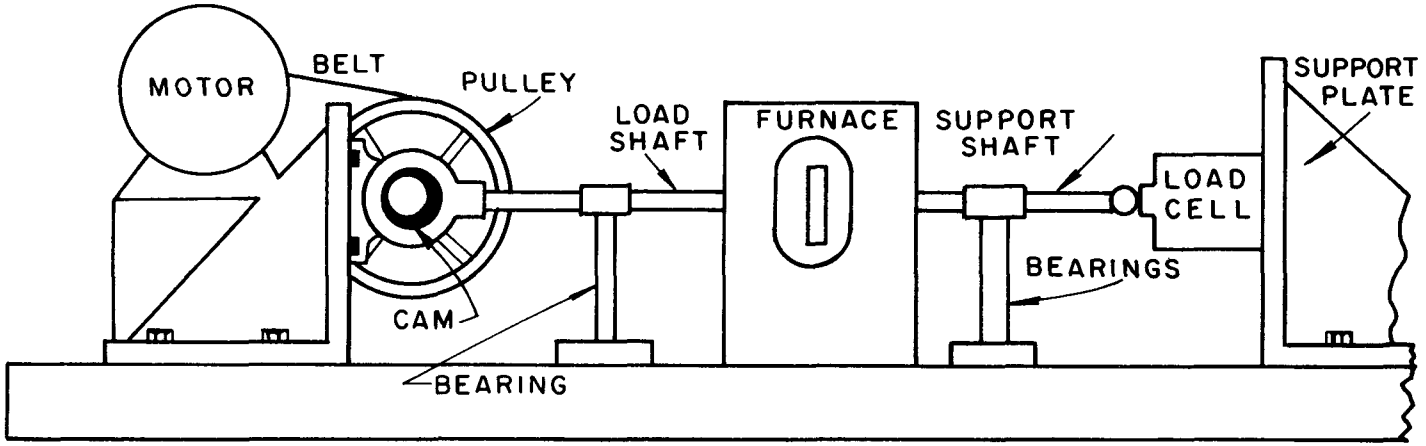

METHOD OF SUPPORTING AND LOADING SPECIMENS:

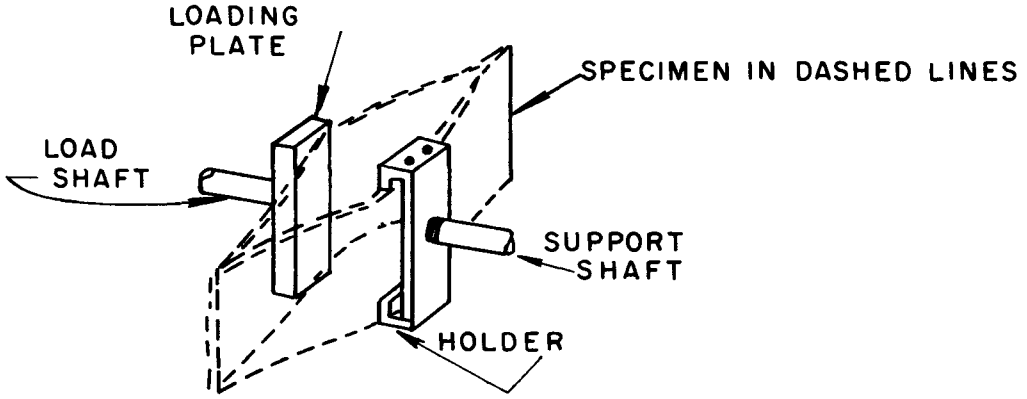

THE LOADING PLATE IS NOT ATTACHED TO THE SPECIMEN

MUL-15128

Fig. IV-33. Side support spring fatigue test apparatus.

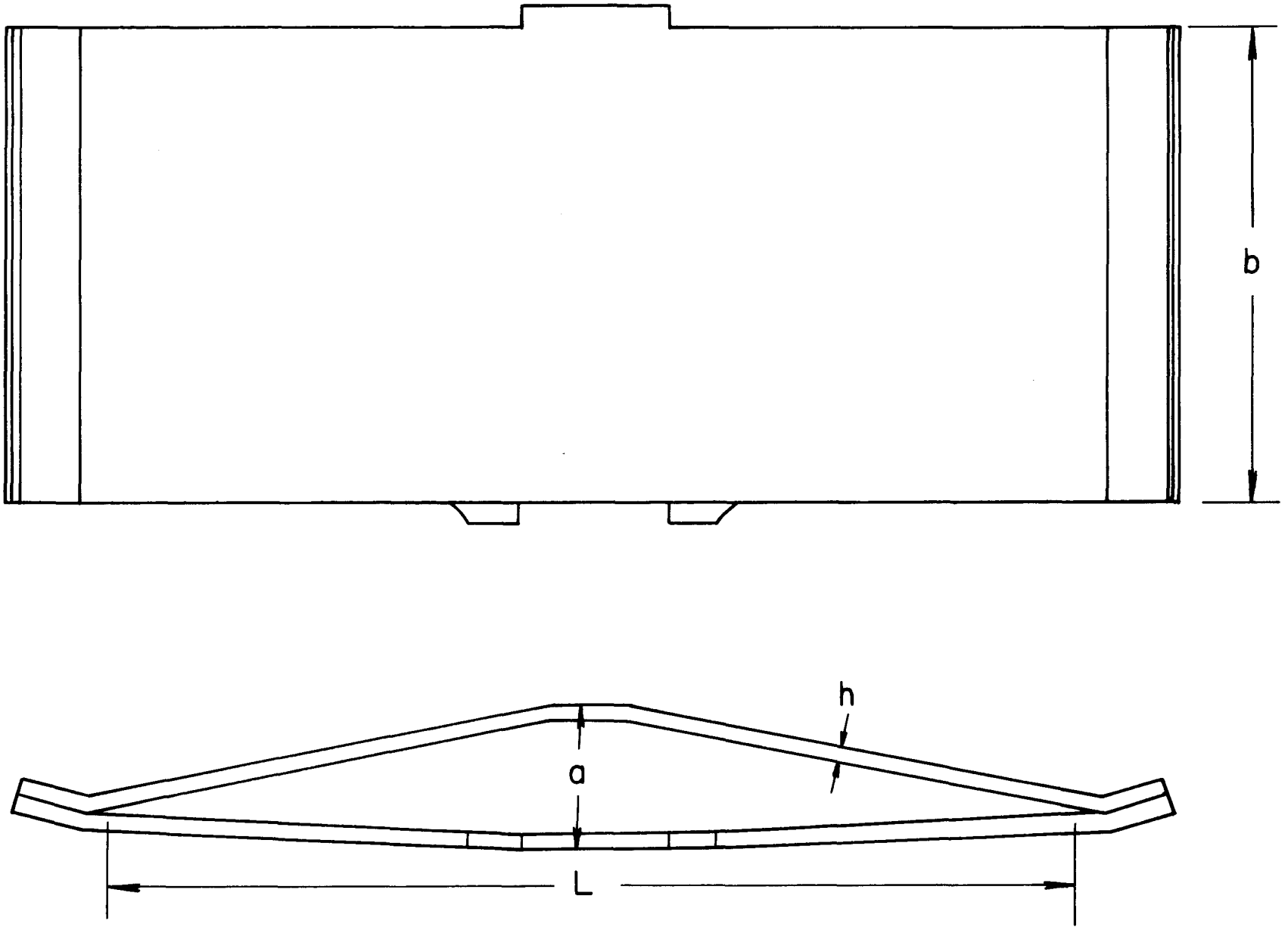

MUL-15129

Fig. IV-34. Sketch of side support spring.

Table IV-10. Summary of Test Results.

Run No.	Spec. No.	Description	Material	Geometry - inches (see Fig. IV-34) L	b	h	a av	Δa av	Room temp spring rate lb/in.	T °F	Def. in.	Rate rpm	Therm. exp load lb	Initial load - lb max	min	Initial stress-ksi max	min	No. of cycles	Fail	Remarks
1	2	First generation spring. Braze:J-8600	René 41	9.375	4.5	0.124	--	--	2190	1400	0.225	700	200	600	200	60	20	105	No	--
2	8	"	"	"	"	"	--	--	"	Rm	0.350	--	--	750	--	75	--	1	Yes	At braze.
3	1	"	"	"	"	"	--	--	"	1400	0.350	550	160	670	160	67	16	12,000	Yes	At braze on first cycle, but test continued.
4	5	"	"	"	"	"	--	--	"	1400	0.350	--	--	750	--	75	--	1	--	--
5	A	Decay in transmitted load of 24%. Slice test spring. Braze: J-8100	R-235	"	"	"	--	0.150	--	1400	0.350	550	160	720	160	72	16	5000	Yes	Decay in transmitted load of 24%.
6	6	This is same as #2 but had riveted edges. First generation spring.	René 41	"	"	"	--	--	2190	1400	0.145	500	200	240	20	24	20	60,000	No	--
7	6H	Second generation spring, no tab, half-width spring. Braze: J-8100	"	8.57	2.185	0.131	1.05	--	1950	1400	0.303	500	120	560	120	96	20	50,000	No	--
8	5H	Half-spring with tab. Braze: 4778A	"	8.62	"	"	1.08	--	"	1400	0.303	500	140	490	140	84	24	50,000	No	Increase in both max & min load observed during run.
9	5H	—	"	"	"	"	1.08	--	"	1400	0.303	500	180	540	180	92	31	150,000	Yes	Broke at tab.
10	6H	—	"	8.57	"	"	1.05	--	"	1400	0.303	500	200	600	200	102	34	55,000	Yes	Broke at braze.
11	25	Full-size second generation spring. Braze: J-8100	"	8.375	4.5	0.131	1.054	0.013	3940	1400	0.294	500	350	1320	540	106	44	100,000	Yes	Broke in center.
12	17	Full-size second generation spring. Braze: 4778A	"	"	"	"	1.060	0.060	3940	1400	0.303	500	350	1440	520	116	42	180,000	No	No cracks, although load decreased by 20%.
13	2	Modified end tabs, narrower spring. Braze: 4778A	"	8.935	4.24	0.129	1.277	0.123	3330	1400	0.296	500	250	1050	350	100	33	5×10^5	No	25% decrease in transmitted load during run.

The apparatus used in this test is shown schematically in Fig. IV-33. The motor pulley is a spring-loaded variable sheave which can vary from 230 to 850 rpm. The present cam arrangement allows for continuous variability of stroke from 0 to 0.5 inches. The furnace is capable of a maximum of 1650°F. The associated instrumentation includes a furnace controller, load cell, and recorder for the load cell.

A typical test procedure follows:

a. The support plate is loosened and pulled back to allow insertion of the specimen and its holders in the furnace. The cam is placed in its most retracted position.
b. The support shaft is screwed into the threaded receivers in the specimen holder and the support plate is slid forward until contact is made with the load shaft.
c. The furnace is brought up to test temperature.
d. The specimen is cycled by hand to determine the maximum load.
e. If the corresponding stress is insufficient, the support plate is slid farther forward to compress the specimen, or, the cam deflection is changed.
f. When temperature and initial stress requirements are met, the motor is started.

It appears that the 4778A braze is the better choice since the required heat treatment is less detrimental to the spring's fatigue life. Figure IV-35 shows the failure.

VIII. BASE BLOCKS

Material Evaluation

A base block material F-48 has recently been put into production for possible Tory II-C applications. The results on the mechanical properties of this are given below.

The extruded bar was cut into three lengths to be rolled to plate. The cuts were arranged so that all the high-density inclusions observed by radiograph were contained in one length. Rolling temperature was 2400°F. Thickness was reduced from the extruded dimension to 1-1/8 inch in five passes through the rolls with reheat to 2400°F between each pass. After the rolling operation, some curvature remained in each plate. This was straightened by a hard blow from a forging hammer at 2400°F after the last pass.

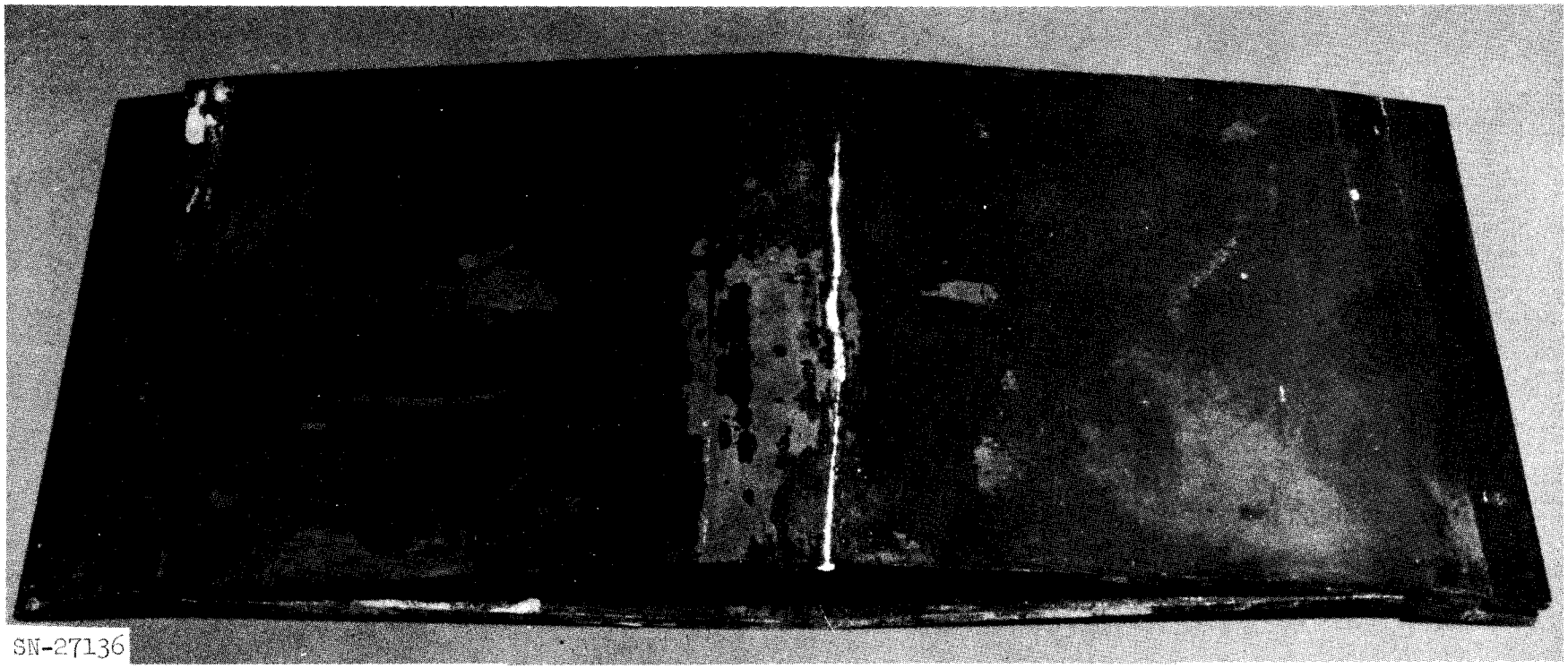

Fig. IV-35. Braze failure.

After a final stress-relief annealing operation (one hour at 2200°F) the plates were declared ready for use.

Test Results

Laboratory: Outside No. 1

Source piece: The plate containing the high-density inclusions. Test material was removed so that none of the included material occurred in a test specimen.

1. Short-time tensile tests
   a. Standard button-head specimen, 0.160-in. diameter over one-inch gage length.
   b. Tested in vacuum.
   c. Strain rate = 0.005 per min.

Temp °F	Direction	0.2% Yield,ksi	Ult., ksi	% Elongation
R.T.	long.	82.9	97.6	6
		87.9	93.3	4
	trans.	87.0	90.1	4
		94.4	101.8	5
	45°	86.8	97.5	5
		84.7	92.0	4
2200	long.	42.1	45.8	14
		42.4	45.6	20
		42.0	44.2	18
	trans.	42.3	44.8	17
		42.6	44.5	18
		42.8	45.3	14
	45°	41.1	42.2	16
		41.1	43.0	12
2500	trans.	27.4	30.1	27
		28.3	30.5	21
		25.9	29.2	28

2. Creep rupture tests
   a. Standard button-head specimen.
   b. Tested in vacuum.
   c. Temp = 2300°F.
   d. Testing direction parallel to extrusion.

Stress, ksi	Time to rupture, hr	% Elongation
26.0	23.1	19
26.0	No failure after 30 hr. Tested short-time at 0.005 per min to 42.3 ksi ult. and 15% elong.	
28.0	13.4	22
30.0	4.8	16
30.0	7.0	21
30.0	7.0	17
35.0	1.9	21
38.0	0.6	11
40.0	14 min	16

The above results are plotted in Fig. IV.-36.

Laboratory: Outside No. 3

Source piece: Plate from midportion of the extruded bar. No high-density inclusions were observed.

1. Short-time tensile tests
   a. Button-head specimen, 0.200-in. diameter, over one-inch gage length.
   b. Tested in vacuum.
   c. Strain rate = 0.005 per min.

Temp °F	Direction	0.2% Yield, ksi	Ult., ksi	% Elongation
R. T.	long.	--	89.5	--
		92.2	102.5	5.3
		94.8	103.5	2.0
	trans.	90.7	103.5	6.7
2200	long.	45.8	50.9	22
	trans.	42.9	43.6	11
		47.5	48.2	11

Chemical Analysis

Testing organization	Sample		W/O W	W/O Mo	W/O Zr	PPM C	PPM O	PPM N
Outside No. 2	1	Top	15.0	4.6	0.97	200	100	40
		Bottom	15.9	4.7	0.96	400	200	30
Outside No. 1	2					164	62	54
Outside No. 3	3	Top	13.0	4.37	0.67	950	640	120
		Bottom	15.5	4.52	0.55	620	340	180

Sample 1. Turning from top and bottom of ingot.

Sample 2. Material taken adjacent to position of test specimens machined from finished plate.

Sample 3. Turnings from top and bottom of billet as it was being turned down to 4-3/4-inch diameter.

The following observations are considered of significance:

1. Short-time strength and ductility equaled or exceeded the present acceptance level for base plate material.
2. Consistency of test results by Outside Laboratory No. 1 is the best obtained to date. This probably is due to their efforts in improving testing techniques, particularly at room temperature.
3. The wide difference in carbon, oxygen, and nitrogen content obtained from three independent sources needs to be explained. Outside Laboratories 1 and 2 agree reasonably well considering sampling location and techniques. The Outside Laboratory No. 3 analysis is suspected of being too high in light of the room temperature ductility observed.

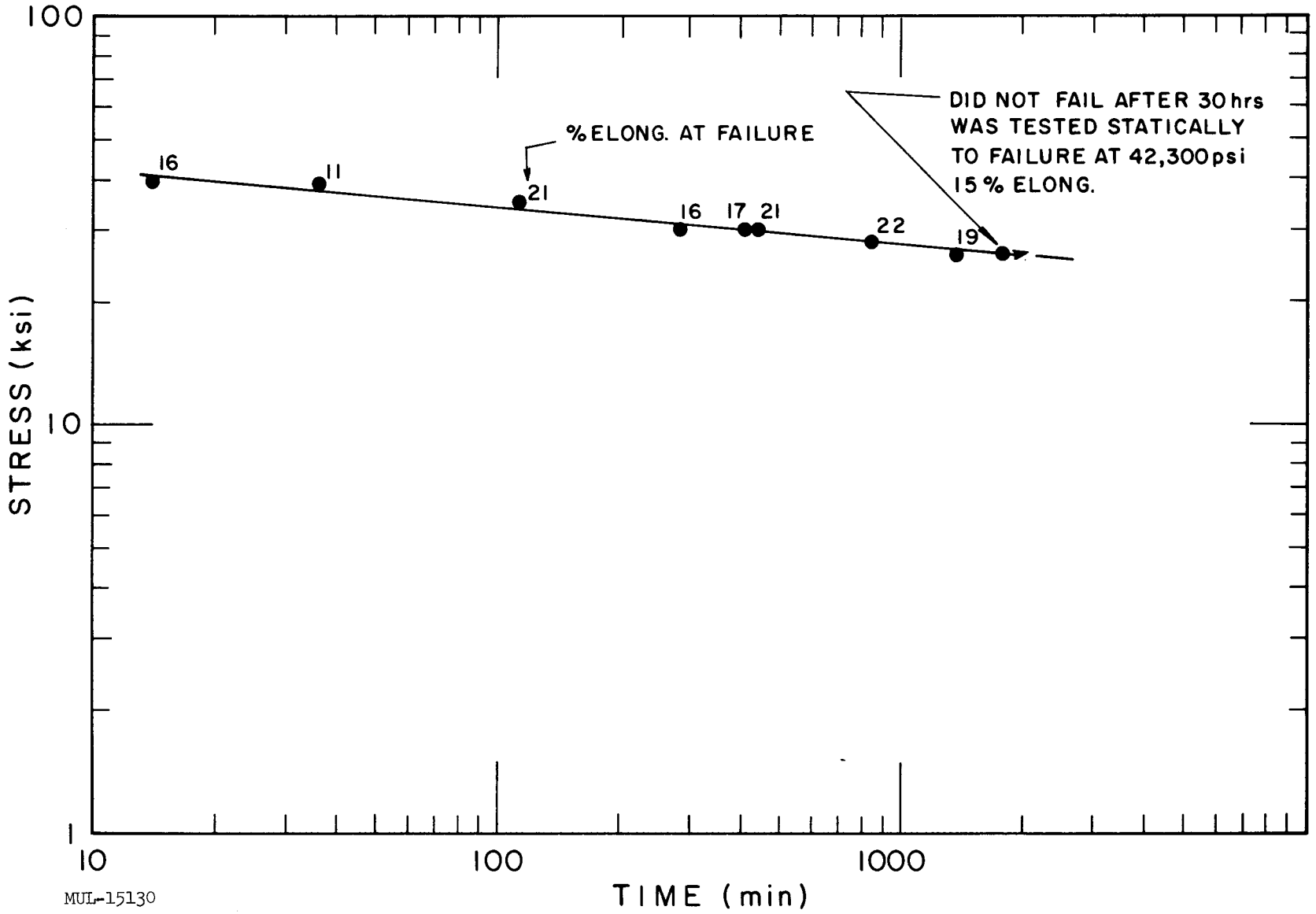

Fig. IV-36. Creep rupture of F-48 at 2300°F. (Plate LRL-1-3.)

4. The difference between Outside Laboratory No. 1 and Outside Laboratory No. 3 short-time tensile strengths at room temperature is not considered significant. The 2200°F values agree very well.
5. The Outside Laboratory No. 3 test at room temperature which showed no ductility was probably due to load misalignment during the test. Analysis shows that a loading eccentricity of 0.003 to 0.004 inch at the fracture point would be sufficient to cause the apparent low ultimate strength and accompanying zero ductility.
6. In general, the material was surprisingly good considering the questionable quality of the starting billet.

High-Temperature Coating Evaluation

Reproducibility tests on coated F-48 material parts for base plates have been approximately 25% completed. These tests were performed in a high-temperature blowdown facility under conditions which duplicate, to a reasonable degree, the Tory II-C environment. Test results were favorable. Test temperatures selected for reproducibility studies were alternately 2300 and 1950°F. To qualify, the specimens needed to survive for ten hours without loss of coating.

The typical temperature transients to produce the test temperatures for reproducibility are as listed in the following chart:

Temperature (°F)	Rate of change (°F/min)
Start up	
Ambient to 700°F	100°
700 to 1000	300° (H_2 burner ignition)
1000 to 1700	300°
1700 to 2300	100°
Shut down	
2300 to ambient	300°F

Oxidation Coating Test Results

Results of the reproducibility tests are indicated in Table IV-11. This table shows the number of hours of cumulative testing achieved before the first signs of coating failure appeared.

Table IV-11. Reproducibility Test Results.

Specimen	Material and coating	Hours of testing prior to appearance of effect				Total hours tested
		A*	B	C	D	
EA	F-48-CV-Rok	10				12
EB	"				16	17
EC	"	5	8	10	14	15
ED	F-48-CV			26	42	47
EE	"			23	47	47
EF	F-48-CV-Rok	5	15	29		39
EG	"		5	26		39
EH	F-48-CV			8		39
EI	"			5	10	10
EK	"			2	4	10
EL	"			6	10	10
EM	"			10		10
EO				10		10
EP				5	7	10
EQ				11		11
ER					11	11
ES					11	11
FA						10
FB				10		10
FC				10		10

* A = Rokide cracking.
B = Rokide flaking.
C = Silicide coating failure (first signs).
D = Unrestricted oxidation of base metal.

Coating Tests at Moderate Temperatures

Recently, in checking the base block coating against all possible modes of failure, it was observed by a series of tests that the present coating did not offer protection at moderate temperatures. This lack of protection was quite pronounced. For example, coated specimens utilizing the standard

coating process and which had been preconditioned (exposed in air to convert the $CbSi_2$ to SiO_2) at 2300° F for one hour, failed in less than 15 minutes at 1500° F under static test. This was the worst case of failure. Subsequent changes in the coating cycle and/or the preconditioning temperature have increased this moderate temperature life to approximately two hours. Current test observations on this moderate-temperature phenomenon may be summarized as follows:

1. Si-Cr/Al coating ranges from nonprotective to two-hour protective in the temperature region from approximately 1000° F to 1900° F.
2. The reaction is associated with the silicide portion of the coating and the so-called "Disilicide Pest," which is common to silicides of molybdenum and tungsten also.
3. The "Disilicide Pest" is oxygen dependent and does not occur in inert or reducing atmospheres.
4. Preconditioning or heat treatment of the coated parts prior to test exposure influences the rate of failure.
5. Specimens do not fail in two hours in the 1000° F to 1900° F range which have been preconditioned at 2000° F and which have not been exposed to higher temperatures.
6. Thermal gravimetric measurements from 1000° F to 2000° F have shown the following:
   A. Specimens preconditioned at 2000° F did not change. Weight gain was negligible.
   B. Specimens preconditioned at 2300° F failed as follows:
      1000° F - no failure in 8 hours
      1250, 1500, and 1750° F - rapid weight gain beginning immediately, with total loss of coating in 4 hours or less
      2000° F - no failure in 8 hours.

The Tory II-C design requirements are such that the moderate-temperature oxidation problem need only be confronted when coming from ambient to operating conditions. The normal rate of temperature rise will be such that the region will be passed through quickly (> 100° F/min) and hence the problem is one for which adaptation can be made. The operating restrictions at this time would be: first, to pass through the critical region at a rate

of 100°F/minute minimum for normal full-temperature operation, and second, to limit sustained running at moderate temperatures to times approaching two hours.

IX. TUBE CRUSHING

Crushing of fuel element specimens was performed using 1-inch-long sections of LRL and supplier's fuel elements. The stresses induced in the specimen were estimated from photoelastic tests.[1,2]

Following the determination of the short-time fracture strength (load rates of 30 lb/min) at three test temperatures, 1400, 1800, and 2200°F, a series of long-time (10-hour) tests was run in which similar specimens were loaded to lower stresses to determine the magnitude of stress which could be supported for 10 hours. Figure IV-37 shows the data obtained from the short-time tests. Figure IV-38 shows the long-time results. The abscissa is the ratio of applied stress to short-time strength and the circled number is the number of elements which failed (positive) or passed (negative). It appears that the relative strength differs at different temperatures and more data will be gathered.

At 1800°F, for example, one would assume that a specimen loaded to about 0.4 of its short-time fracture stress should survive a ten-hour exposure. This corresponds to a bearing pressure of about 290 psi, which is nearly ten times greater than the maximum expected bearing pressure. The corresponding load on a 4-inch-long specimen is about 200 lb.

Such a specimen would be expected to fail at a lower loading because of the greater stressed volume.

X. IRRADIATION TESTING

A wafer of coated F-48 was irradiated for 10^{19} nvt at a flux of about 5×10^{13} nvt in the Livermore Pool Type Reactor. The temperature of the specimen was not measured, but it is estimated that it did not exceed 300°F. Examination in the hot cell after irradiation revealed no visible changes in the coating.

---

[1] P. D. Flynn, Stresses in Hollow Hexagons under External Pressure, SESA, October, 1959, Paper No. 572.

[2] I. B. Mantle, Hydrostatically Loaded Cylinders with Noncircular External Boundaries, SESA, October, 1960, Paper No. 618.

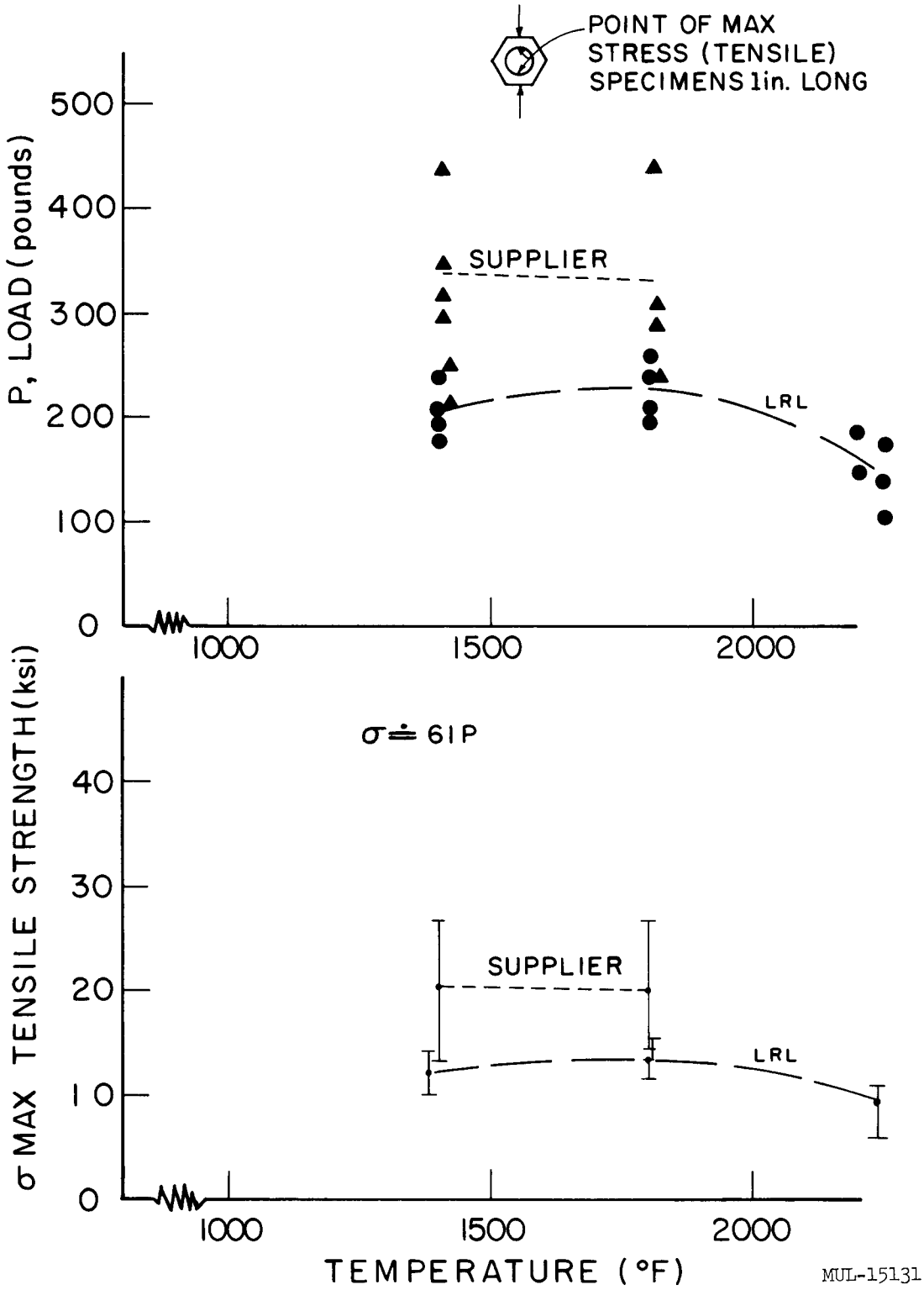

Fig. IV-37. Short-time strength.

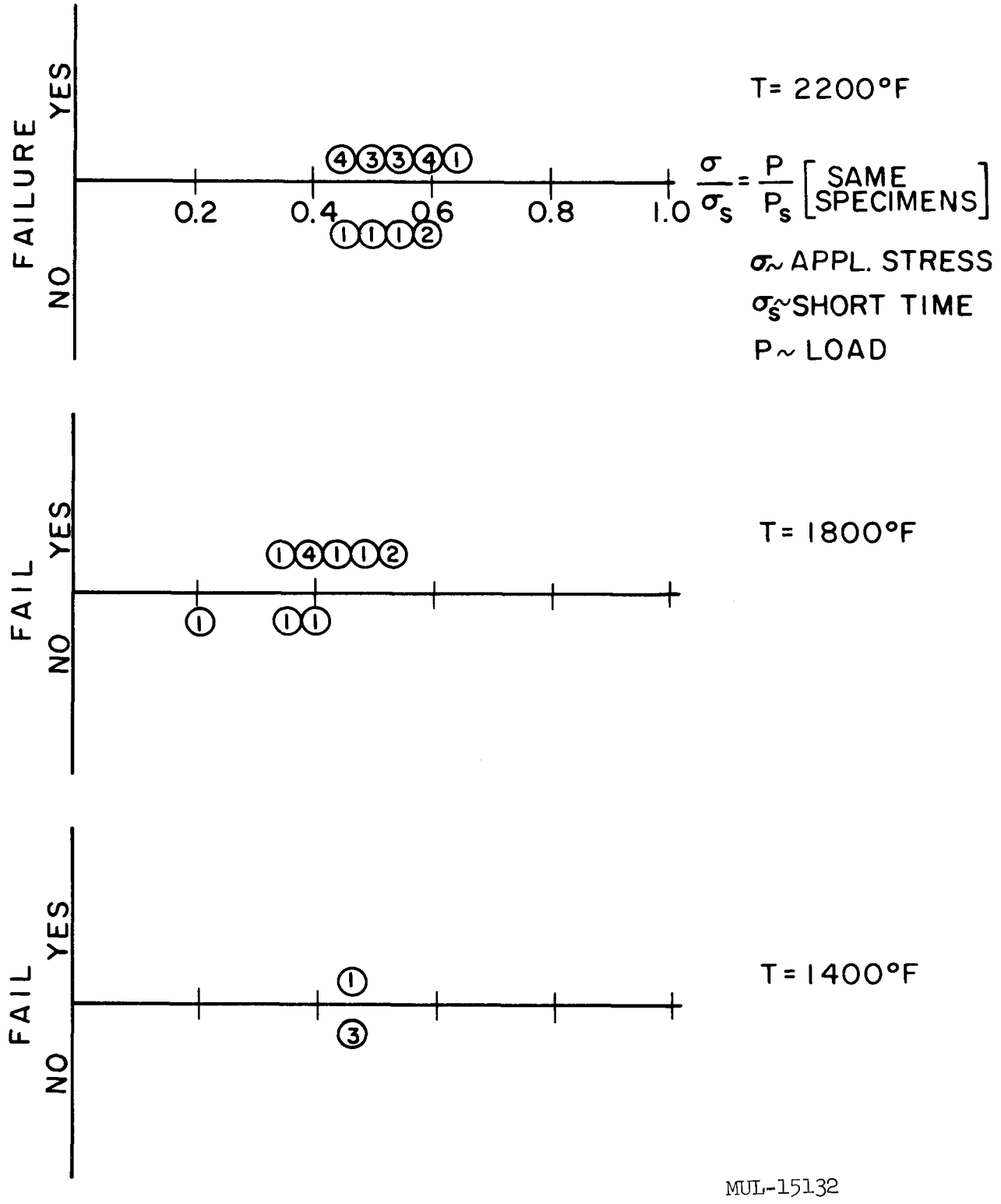

Fig. IV-38. Survival of one-inch-long fuel elements subject to 10-hour loading at indicated fraction of short-time strength.

XI. STACK TEST

The load deflection characteristics of a stack of 1000 Tory II-A fuel elements in a 4 in. × 6 in. × 12 in. (approx.) array were measured at room temperature and at 2150°F. Also tested were steatite mockups of two lengths and surface finishes at room temperature. A summary of the experimental results appears in the Table IV-12. The results are plotted in Fig. IV-39. All of the room-temperature data were well approximated by parabolas, while the high-temperature data were so badly spread that they were approximated by least squares. Figure IV-40 shows the arrangement of the fuel elements in the furnace. At a and b, quartz tubes were placed which were roughly as high as the stack. The top of these tubes, as well as the bottom of the loading plate at c, were visible through a port and were viewed through the cathetometer, a vertically graduated telescope. Changes in the difference between the top of the quartz and the edge of the loading plate were taken as stack compression.

XII. REACTOR SLICE

During the past quarter the slice assembly was rebuilt using shims in the core periphery and reworked springs. Static tests were completed at 5 and 10 psi spring pressures. Vibration tests were completed at the same spring pressures. Figure IV-41 shows the test item.

It is of interest to see how close the core approximates a hydrostatic condition. Consequently, the spring pressures were measured when the slice assembly was turned vertical after being set to 5 psi in the horizontal position.

Figure IV-42 shows the pressure distribution obtained from strain-gage readings on the springs and compares these with the theoretical hydrostatic distribution. The theoretical distribution is given by

$$P = P_0 + \rho R \cos\theta ,$$
$$= 5 - 2 \cos\theta .$$

During assembly, it was found that the steatite tubes nest more closely during the processes of setting pressures and moving the slice assembly. The length of 165 tube rows varied from 49.74 inches to 49.47 inches depending on the spring pressure and past history of the item. The decreases in dimension are the result of (1) taking up tube camber, and (2) shifting of the tube arrays into more compact arrangements.

Table IV-12. Load Deflection Characteristics, Summary of Experimental Results.

Material	Element length (in.)	Surface finish Axial (rms)	Surface finish Trans. (rms)	Temp (°F)	Cond.	Side load (lb)	Loose tubes 25 psi Exp.	Loose tubes 25 psi Theoret.	Equation	Mean deviation
Steatite	3-1/2	108	149	room	loose	~150			$P = 0.65Y + 0.25Y^2$	± 5 mils
	"	"	"	"	tight	"	205	239	$P = 2.25Y + 0.52Y^2$	
Steatite	4	32	16	"	tight	100	123		$P = 2.05Y + 2.12Y^2$	± 3 mils
BeO	4	64	64	"	loose				$P = 13.9Y + 1.82Y^2$	± 2 mils
	"	"	"		tight				$P = 42\ Y + 1.82Y^2$	
	"	"	"	2150	tight	100			$P = 32Y$	± 200 lb
	"	"	"	"	tight	250			$P = 105Y$	± 200 lb

The condition column indicates whether or not the stack had been preloaded prior to the runs. All results are based on at least 30 runs each. In the equation column, P is in pounds and Y in mils. The side load was calculated for the steatite and controlled for the high-temperature BeO test.

MUL-15057

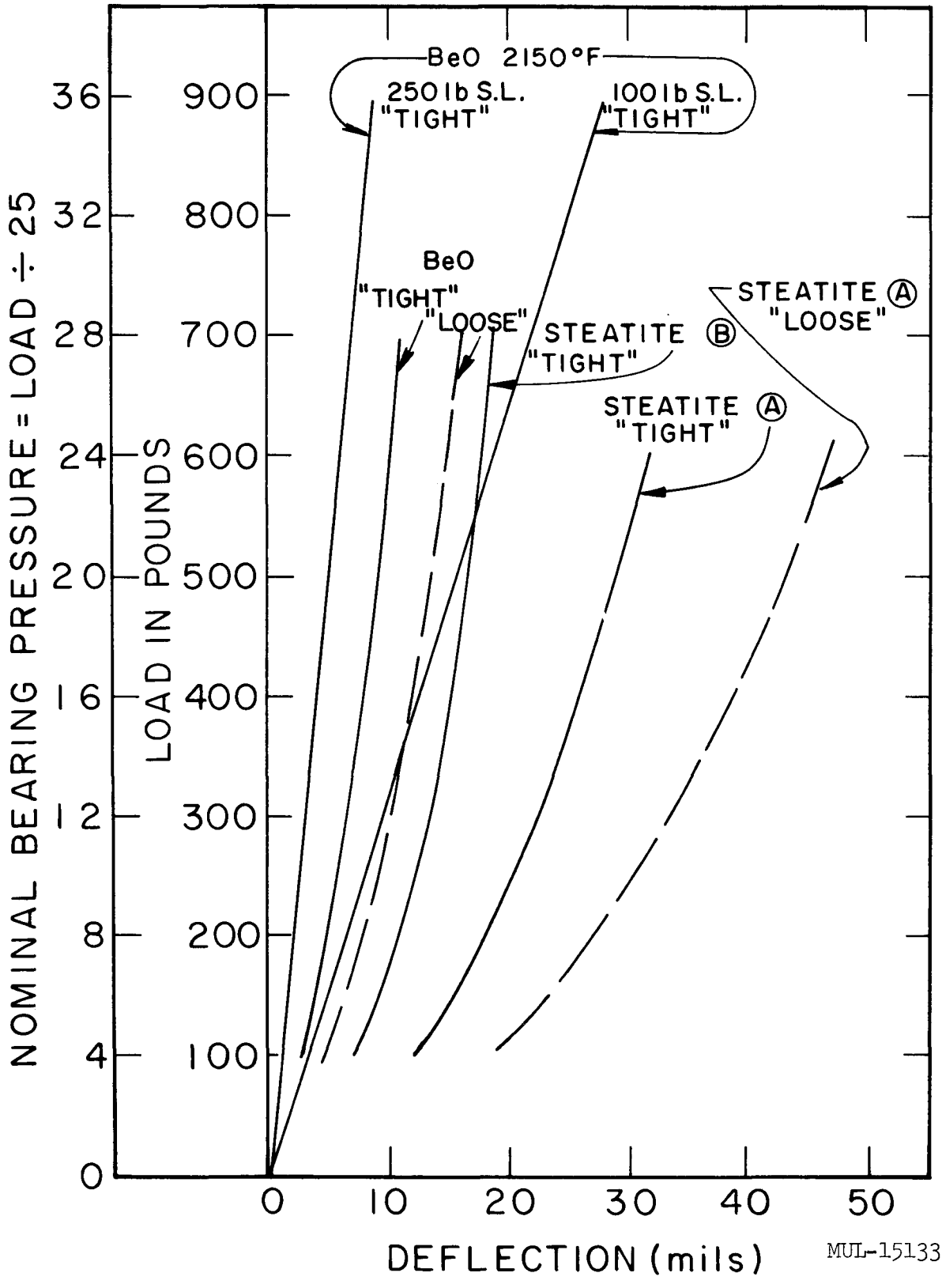

Fig. IV-39. Load vs deflection for hex-tube stack, 12 × 6 × 4 loaded in 12-in. axis.

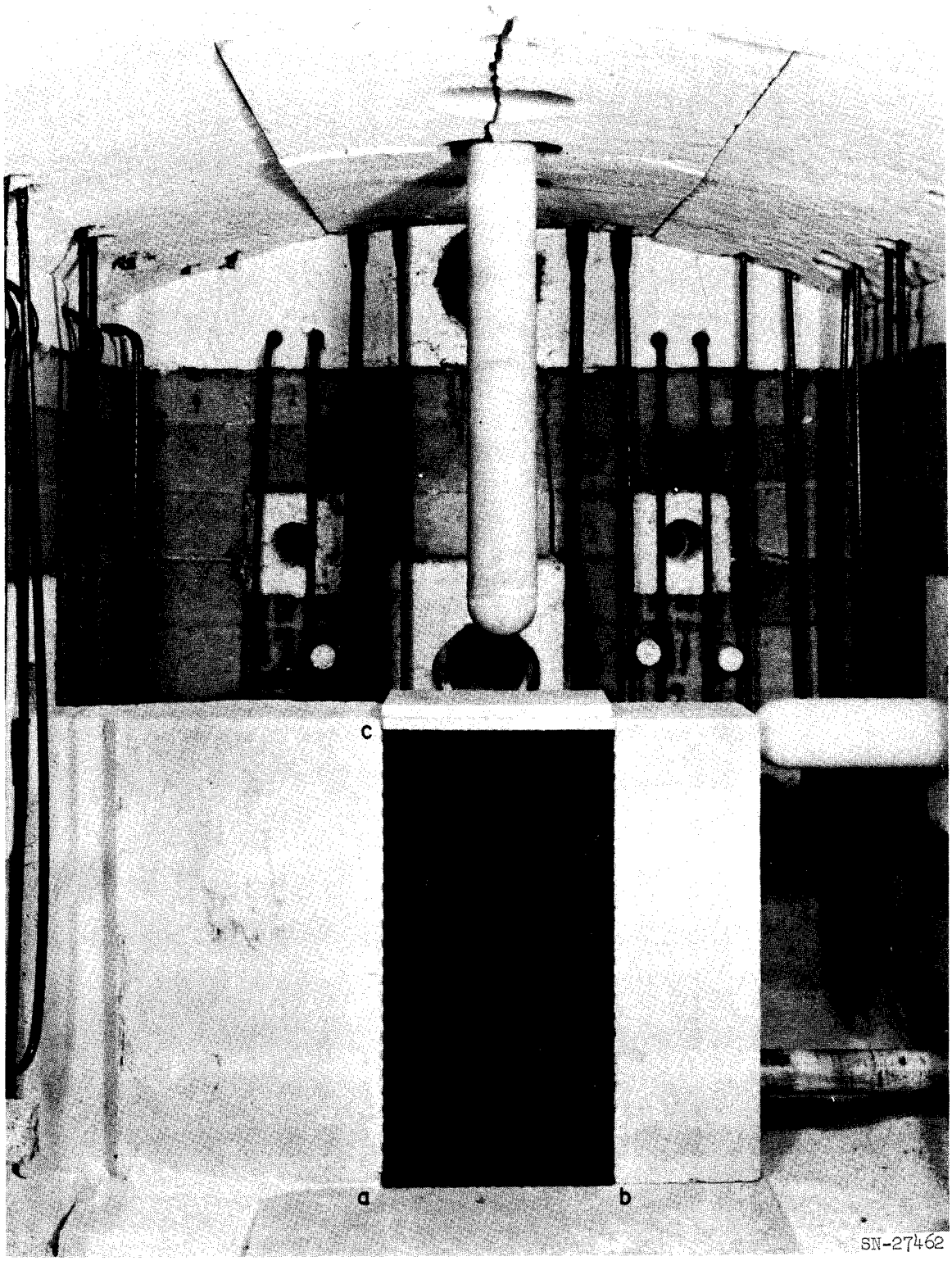

Fig. IV-40. Arrangement of fuel elements in the furnace.

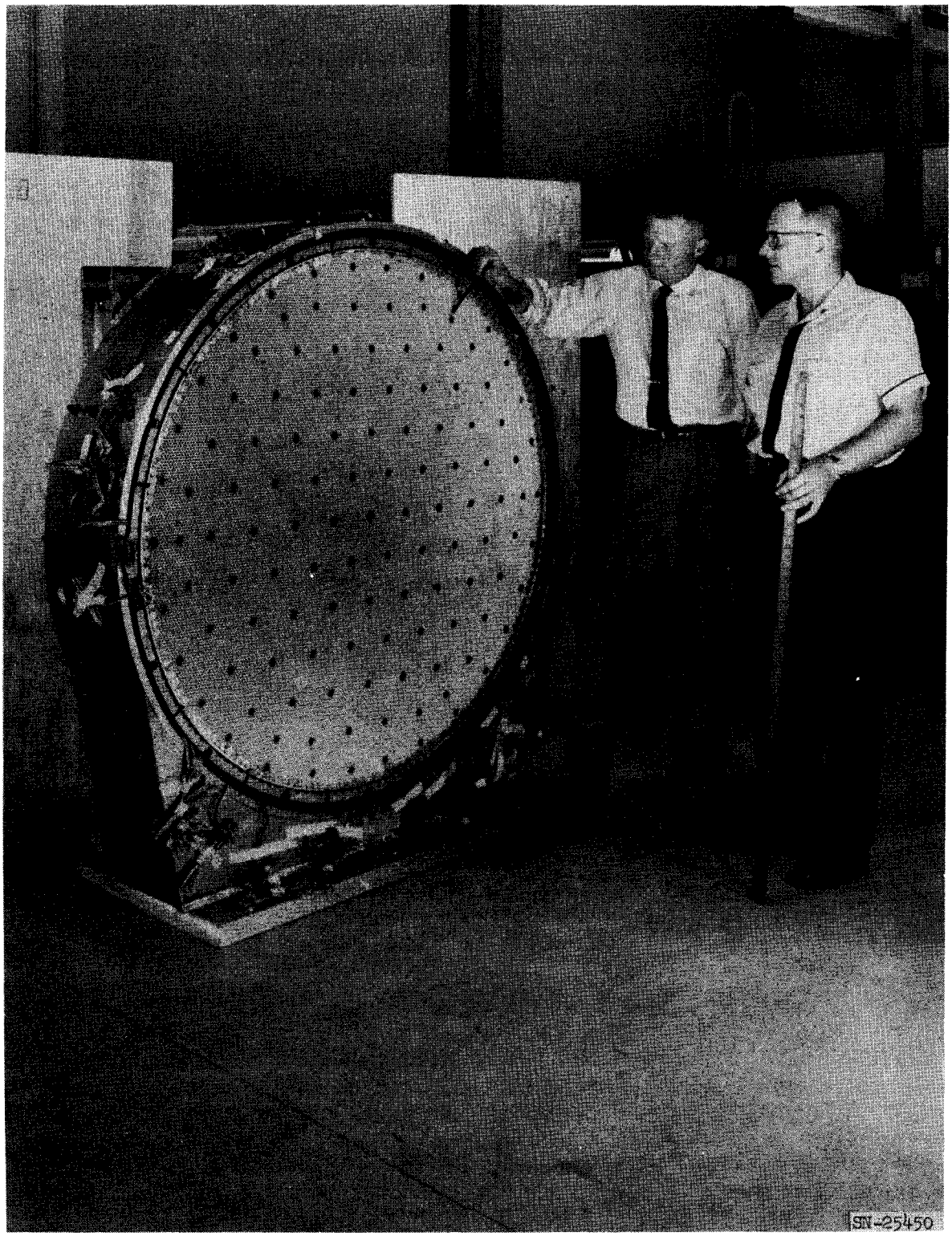

Fig. IV-41. Reactor slice test item.

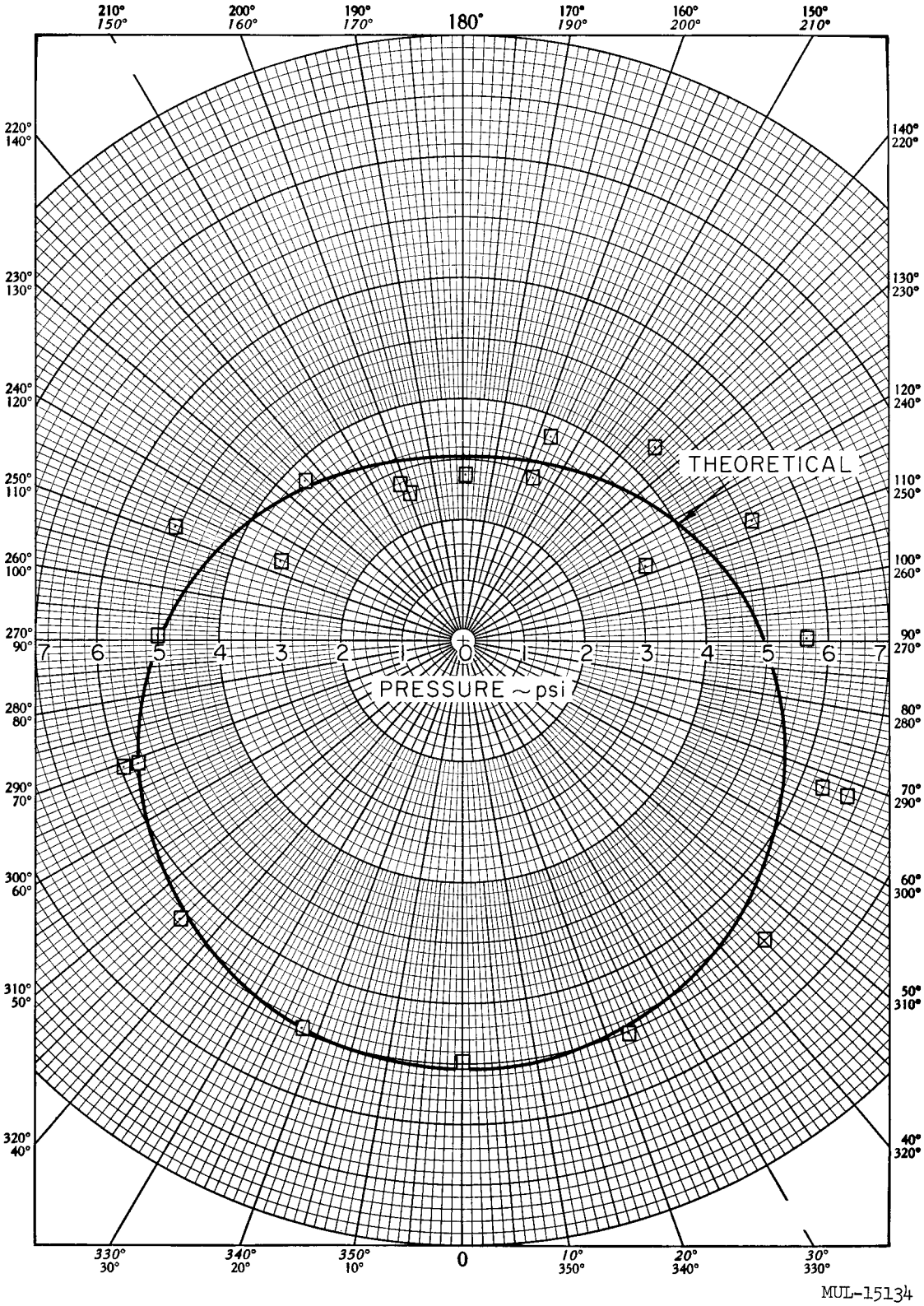

Fig. IV-42. Spring pressure distribution (measured with slice assembly in vertical position after being set to 5 psi in the horizontal position.

The static tests performed on the slice assembly were to determine the slip-loads at which first slipping occurred for the large hexagonal groups, the smaller 7-tube clusters, and the two bottom liners. The slip-loads were determined for two pressure settings of peripheral springs (5 and 10 psi). Figure IV-43 shows the installation for these tests. The slip-loads tests were performed in the large static jig in the following sequence:

a. With the peripheral springs set at 5 psi, the 13 large hexagonal groups were pulled one at a time with a hydraulic jack. The resulting loads are given in Table IV-13.

b. The two bottom liners (numbers 8 and 10) were also pulled with the hydraulic jack. The friction loads are listed in Table IV-13. Next to each liner was a compression spring, strain-gaged with two rosette strain gages for determining the shear stress while the liner was loaded to slippage. The shear stresses were negligible.

c. A survey of slippage loads was then made of the eighty-five 7-tube clusters by manually pulling on a 200-pound spring scale. The cluster locations and the recorded loads (in pounds) are shown in Fig. IV-44. For this test the peripheral springs were at 5 psi.

d. The above tests were then repeated for the peripheral springs setting of 10 psi. The slip-loads for the large groups are also given in Table IV-13. The average slip-load increased from 514 pounds at 5 psi to 1039 pounds per group at 10-psi spring setting.

e. The slip-loads on twenty-one 7-tube clusters were determined for the 10-psi spring setting. The results are shown in Fig. IV-45.

f. One liner (number 10) was pulled at the 10-psi spring pressure. The slip-load on it was 583 pounds, as compared to 330 pounds average for the two liners at 5-psi spring setting.

The slice assembly was next supported with elastic cords above an electromagnetic shake table. See Fig. IV-46 for the test arrangement. The support system was used in order to take the static weight off the table. The table then just had to drive the inertia of the test item. The natural frequency of the combined system was so low as not to affect the test. The driving input was made in the vertical direction.

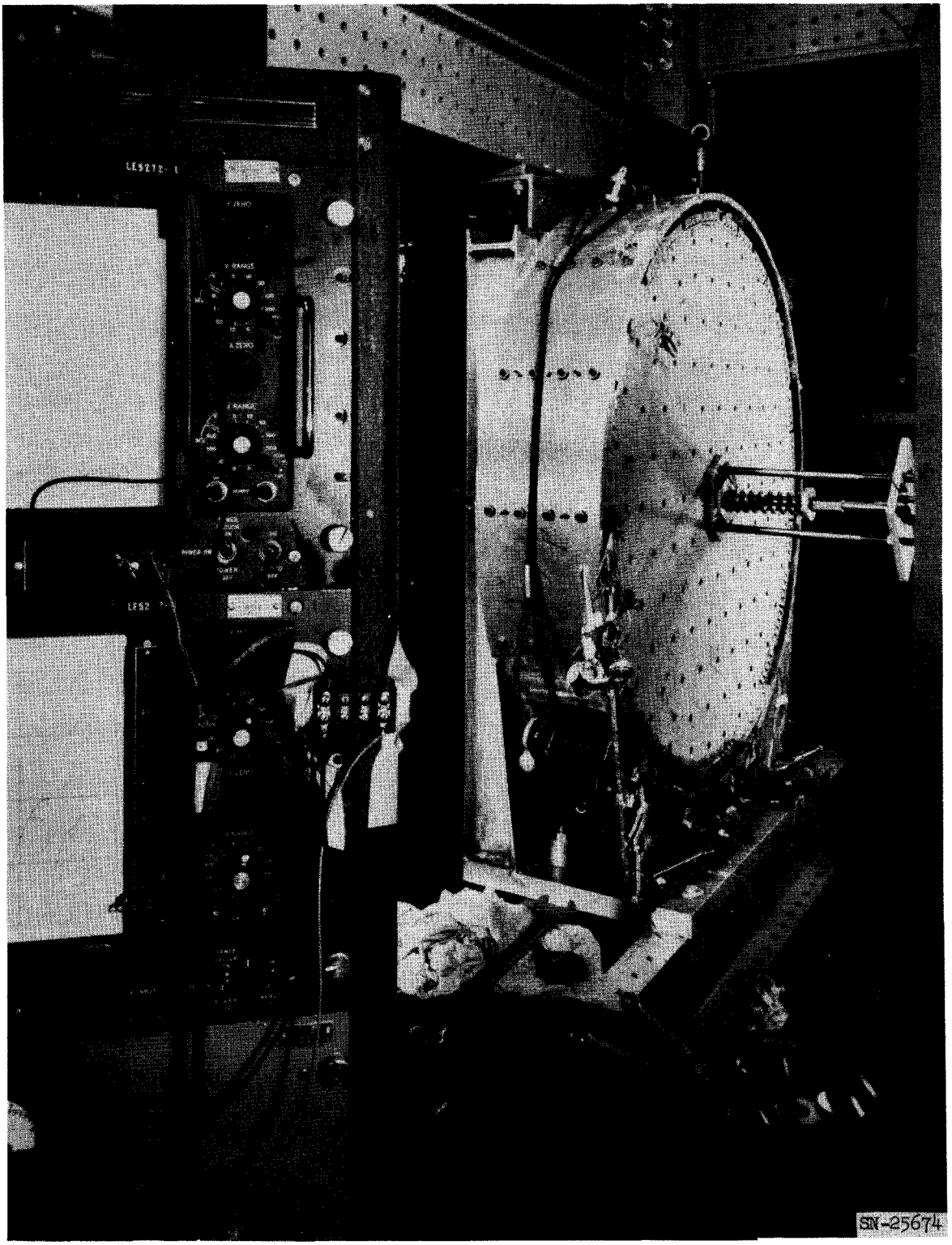

Fig. IV-43. Slip-loads test setup.

Table IV-13. Slip-Loads on Large Hexagonal Groups, Slice Test No. 2 @ 5 psi & 10 psi Spring Pressures.

	Group No.	Slip-load (lb) Springs @ 5 psi	@ 10 psi	
Upper 1/3 of slice	1	av 428 lb	400	925
	2		465	1220
	3		420	1020
				av 1055 lb
Middle of slice	4	av 480 lb	410	1000
	5		440	960
	6		385 & 335	1010
	7		455	1020
	8		500	--
	9		650	1040
	10		500	930
				av 993 lb
Lower 1/3 of slice	11	av 685 lb	790 & 665	1145
	12		640	1100
	13		625	1100
				av 1115 lb
	Liner No. 8		310	--
	Liner No. 10		350	583
			av 514 lb	av 1039 lb

Tests accomplished at 5-psi spring pressure were as follows:

1. 1/2-g input sweep from 6 to 600 cps. This test was to determine at what level of input acceleration one could operate without yielding the springs. The test showed that tests at 2 g's did not cause yielding.
2. Several sweeps from 6 to 600 cps with accelerometer and strain-gage instrumentation.
3. Tests at all observed natural frequencies with 2-g input. These tests were made to investigate more thoroughly the mechanisms of core motion through phase-lag instrumentation.

Tests accomplished at 10-psi spring pressure were as outlined above for parts 2 and 3.

Only preliminary results of the vibration test are given, as data analysis is continuing at the present time.

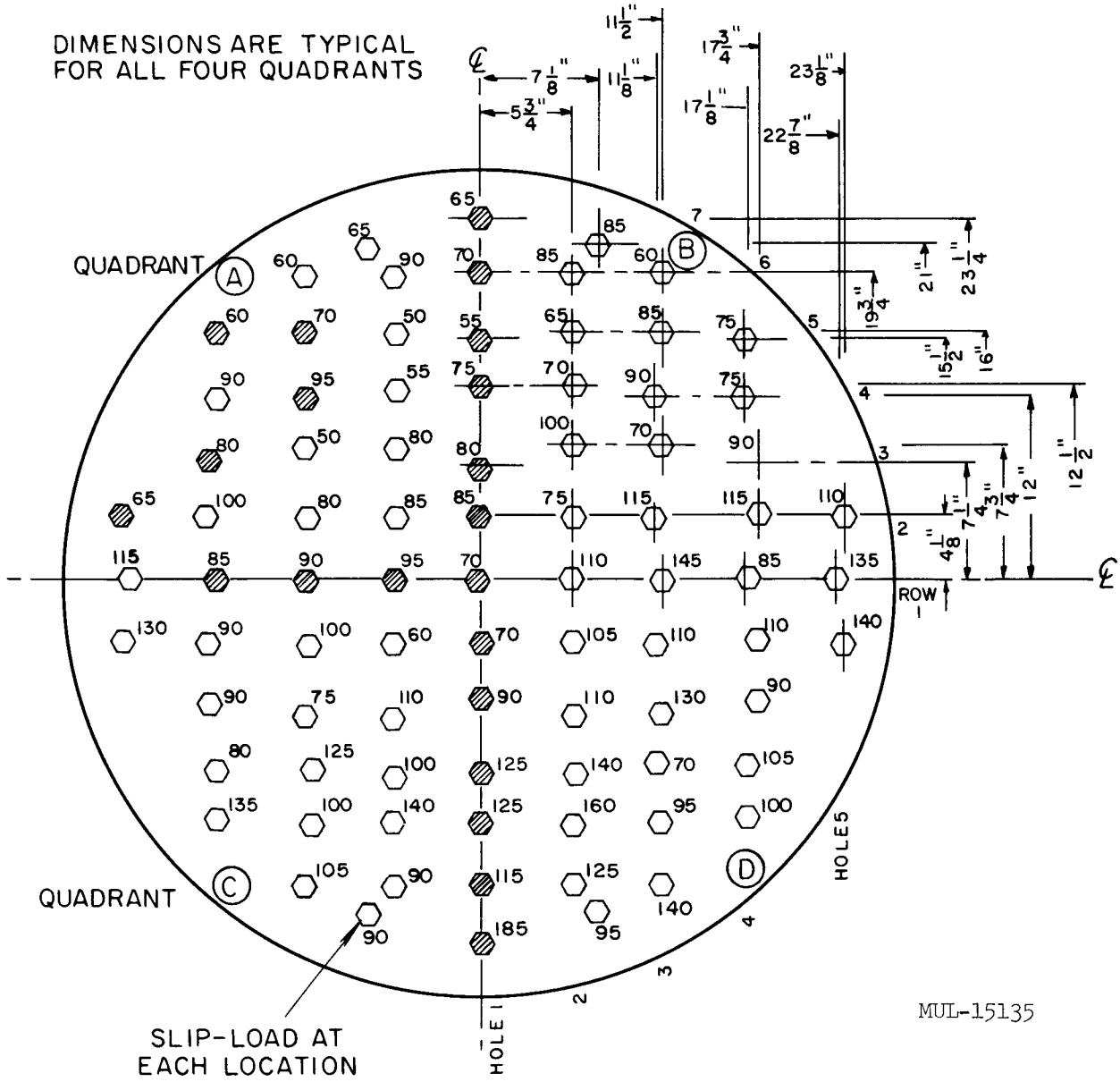

END VIEW
(NOT TO SCALE)

Fig. IV-44. Locations of the 7-tube clusters and slip-loads (lb) at 5-psi spring pressure. Average slip-load = 88 lb/cluster for the 21 cross-hatched locations (the cross-hatched locations match the 21 clusters pulled at 10 psi).

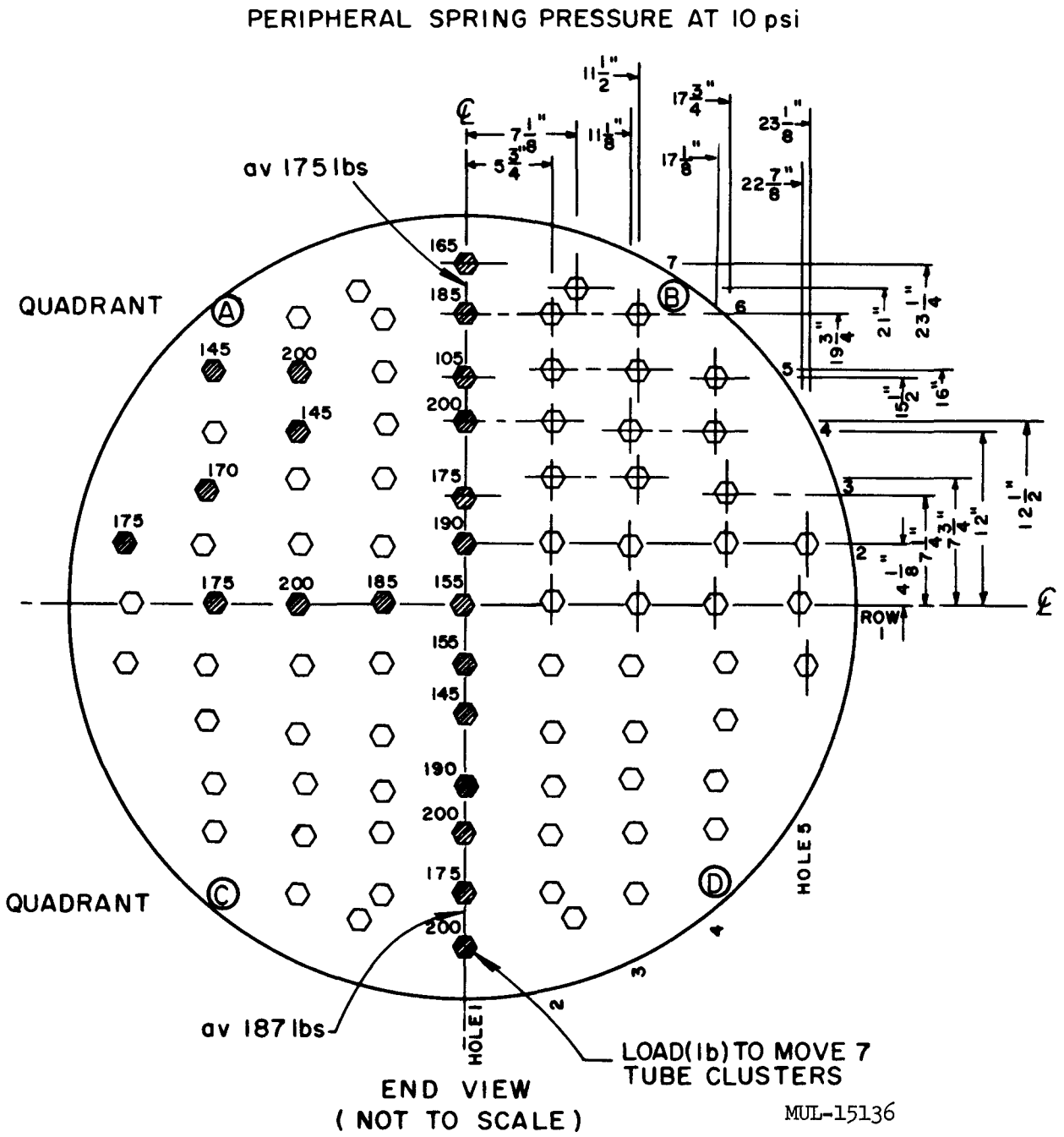

Fig. IV-45. Peripheral spring pressure at 10 psi. Average slip-load of 21 clusters = 168.5 lb.

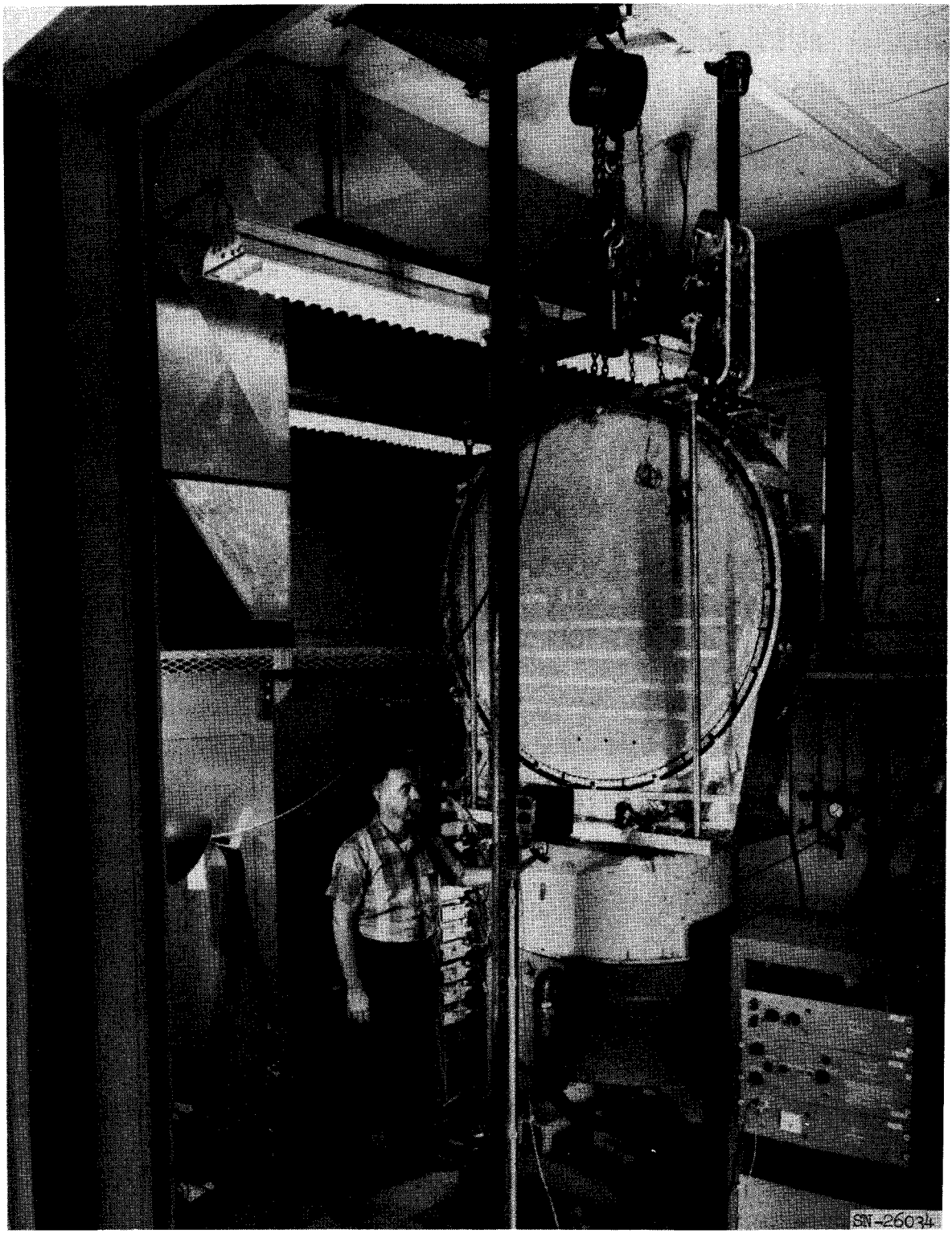

Fig. IV-46. Vibration test setup.

Figures IV-47 and IV-48 show the response of the core as measured by two of the 12 accelerometers used during 2-g sweeps at 5-psi spring pressure. These results indicate a "breathing" of the core horizontally as it vibrates vertically. This horizontal motion is more damped at the higher spring pressure, no doubt due to the increased friction in the core. A more detailed knowledge can be gained as the phase-lag data and Fourier analysis data become available.

All strain-gage information is still being analyzed, but it has been determined that the maximum dynamic strains measured were of the order of 200 microinches, corresponding to a stress change of 6000 psi. This magnitude of stress is seen only at the lowest natural frequencies, i.e., 50 cps at 5 psi, and 70 cps at 10 psi. At frequencies higher than 100 cps, the stress becomes negligible. Of interest are possible loads on the spring tangential to the periphery and in the plane of the spring. No such loads could be seen in these tests.

XIII. REACTOR UNIT CELL TESTS

A Tory II-C unit cell mockup was flow tested at an outside facility. This first cell was composed of steatite tubes, a 1% zirconium-columbium base plate, and an actual reactor tie-rod assembly. The purpose of the test was to check out operating procedures and instrumentation for a more exact BeO cell test now in preparation. As a result, most of the data are only secondarily of interest for the reactor development.

Three runs of approximately 20-minutes duration each were made, one with cold flow, one with flow at 1100°F and no cooling flow in the tie rod, and one at 2000°F with coolant flow in the tie rod. Flow rates for each run were adjusted to give design pressure drop across the cell. The cell mockup survived the test in good shape, but considerable damage to the pressure vessel insulation resulted, necessitating minor changes in the BeO module.

Extensive inspection of the tie rod after the test showed no metal damage of any sort. However, the flame-sprayed ceramic coating on the rear hub had almost completely separated from the metal and flaked off in several large pieces during disassembly. (Fig. IV-49.) This coating is probably not necessary for the design, a point which the next tests will determine. The flame-sprayed ceramic coating on the platinum cup survived in excellent shape (Figs. IV-49, IV-50, and IV-51). There is some discoloration and pitting

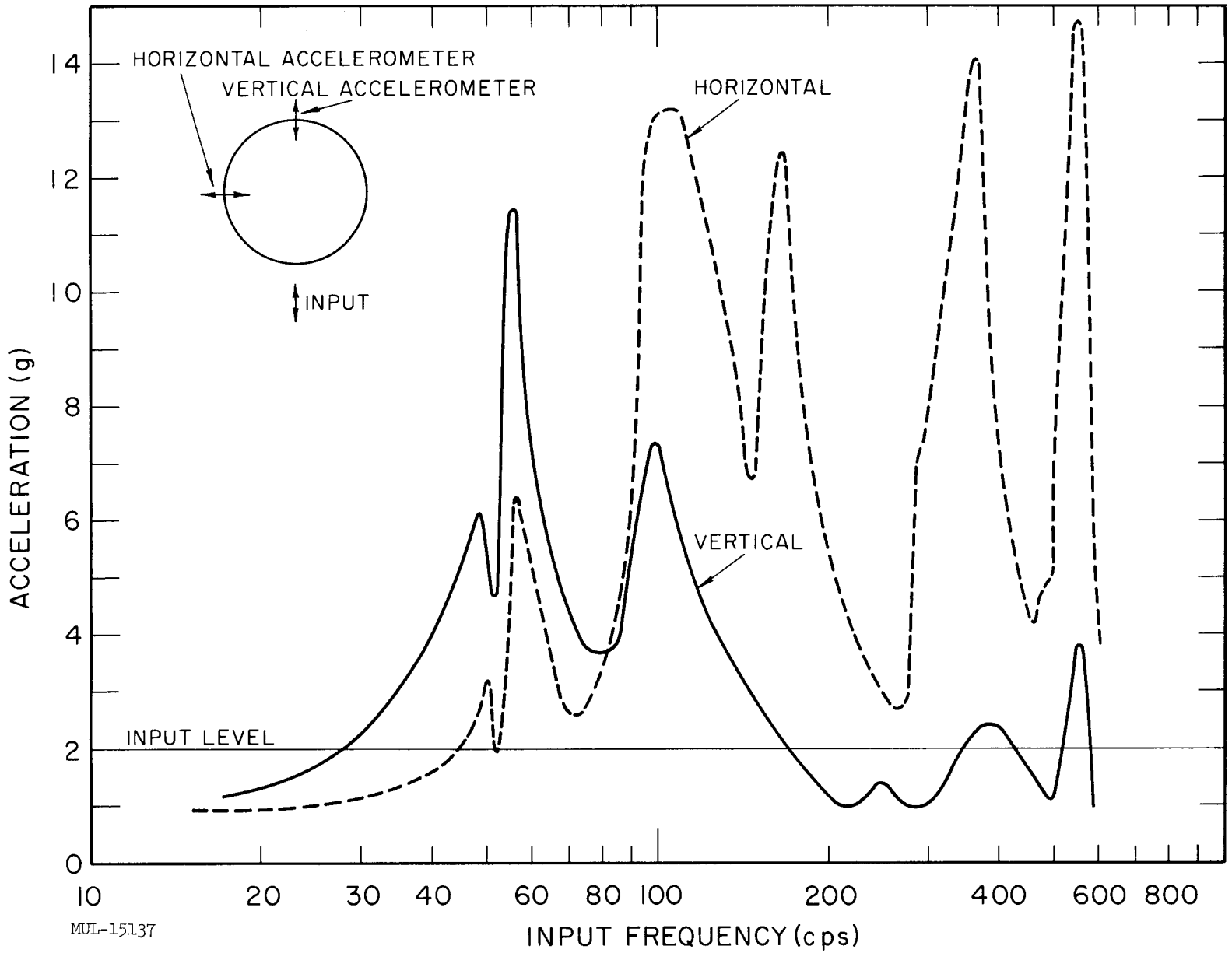

Fig. IV-47. Vibration response at 2-g input, spring pressure at 5 psi.

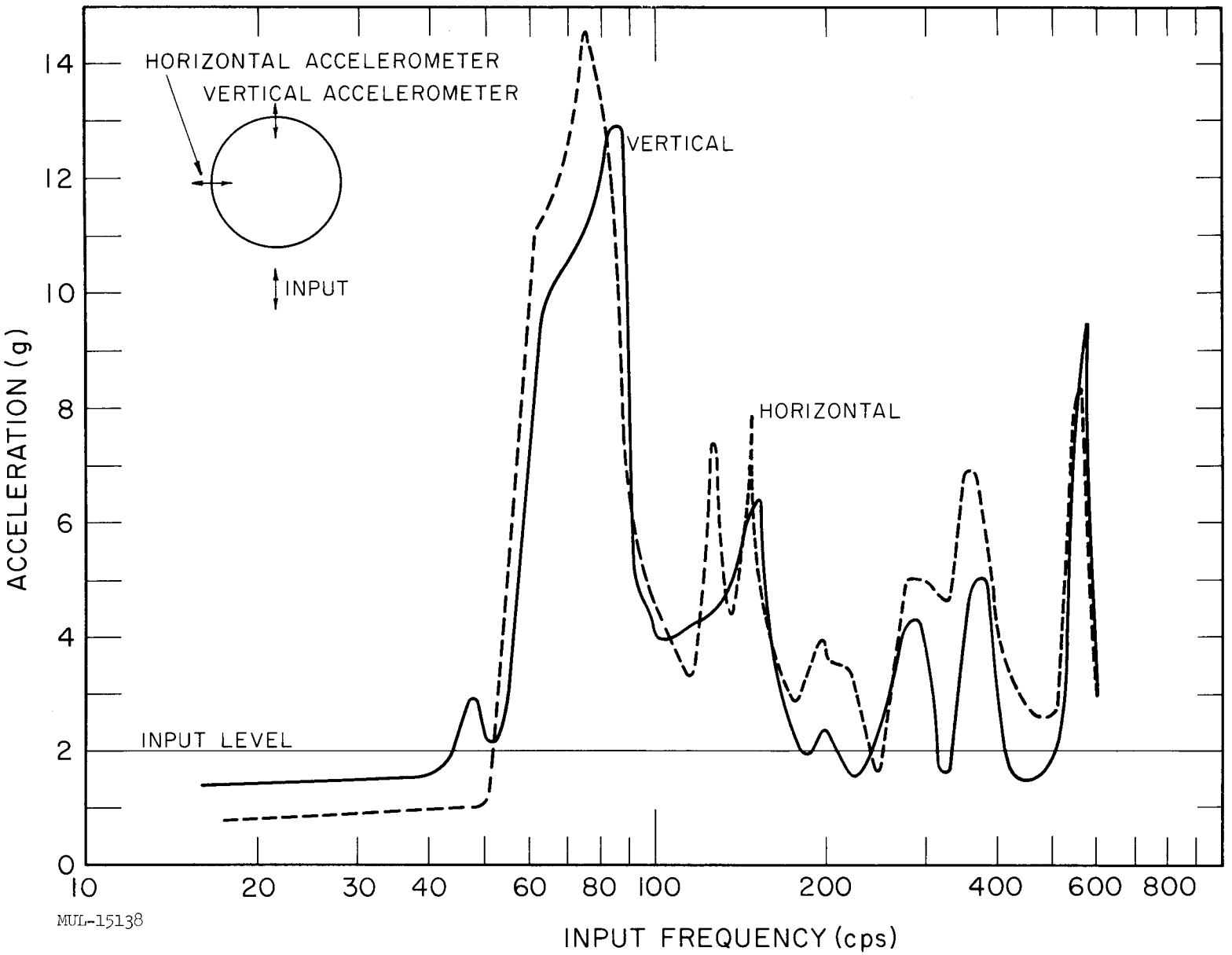

Fig. IV-48. Vibration response at 2-g input, spring pressure at 10 psi.

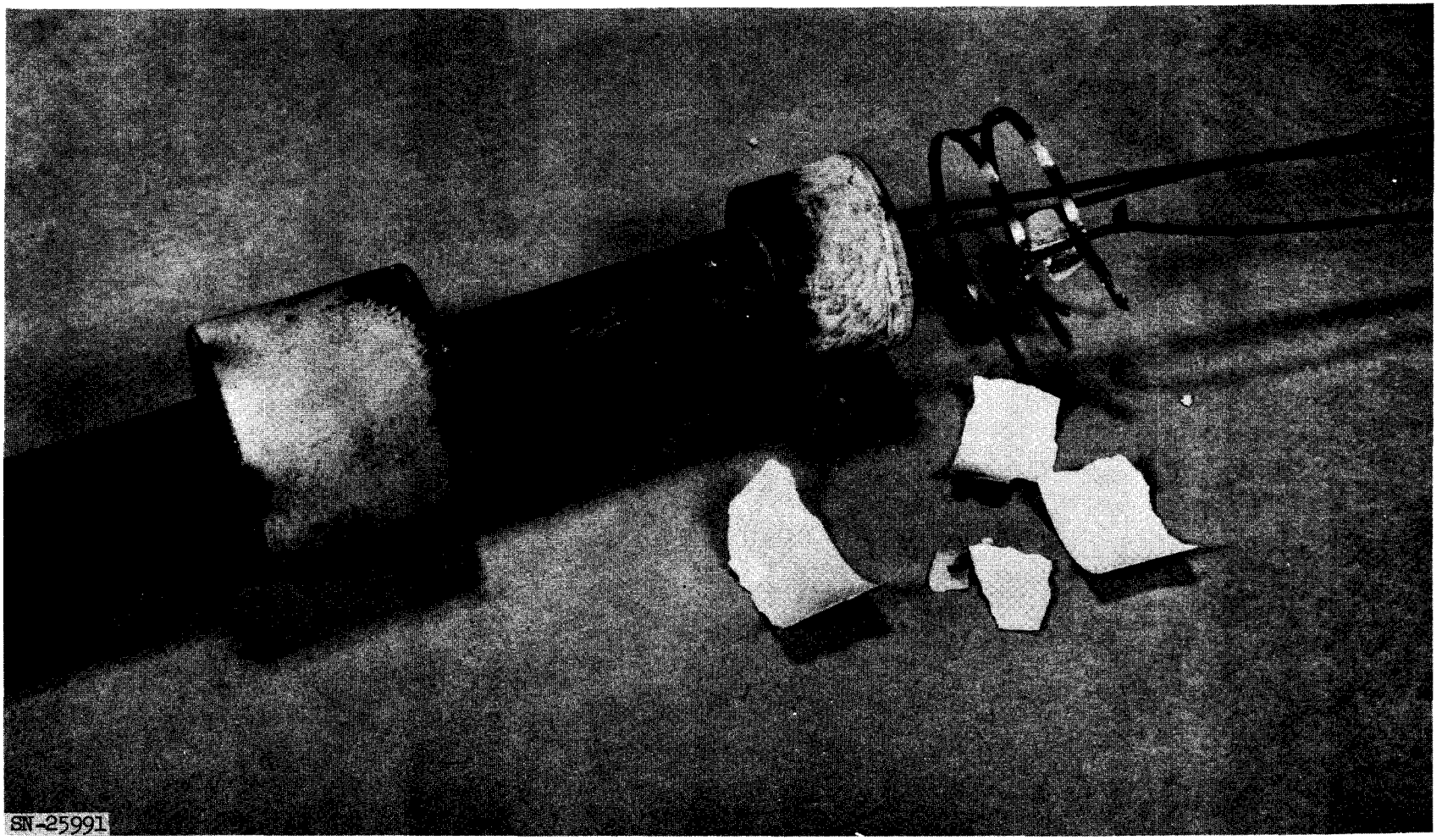

Fig. IV-49. Flame-sprayed ceramic coating after test.

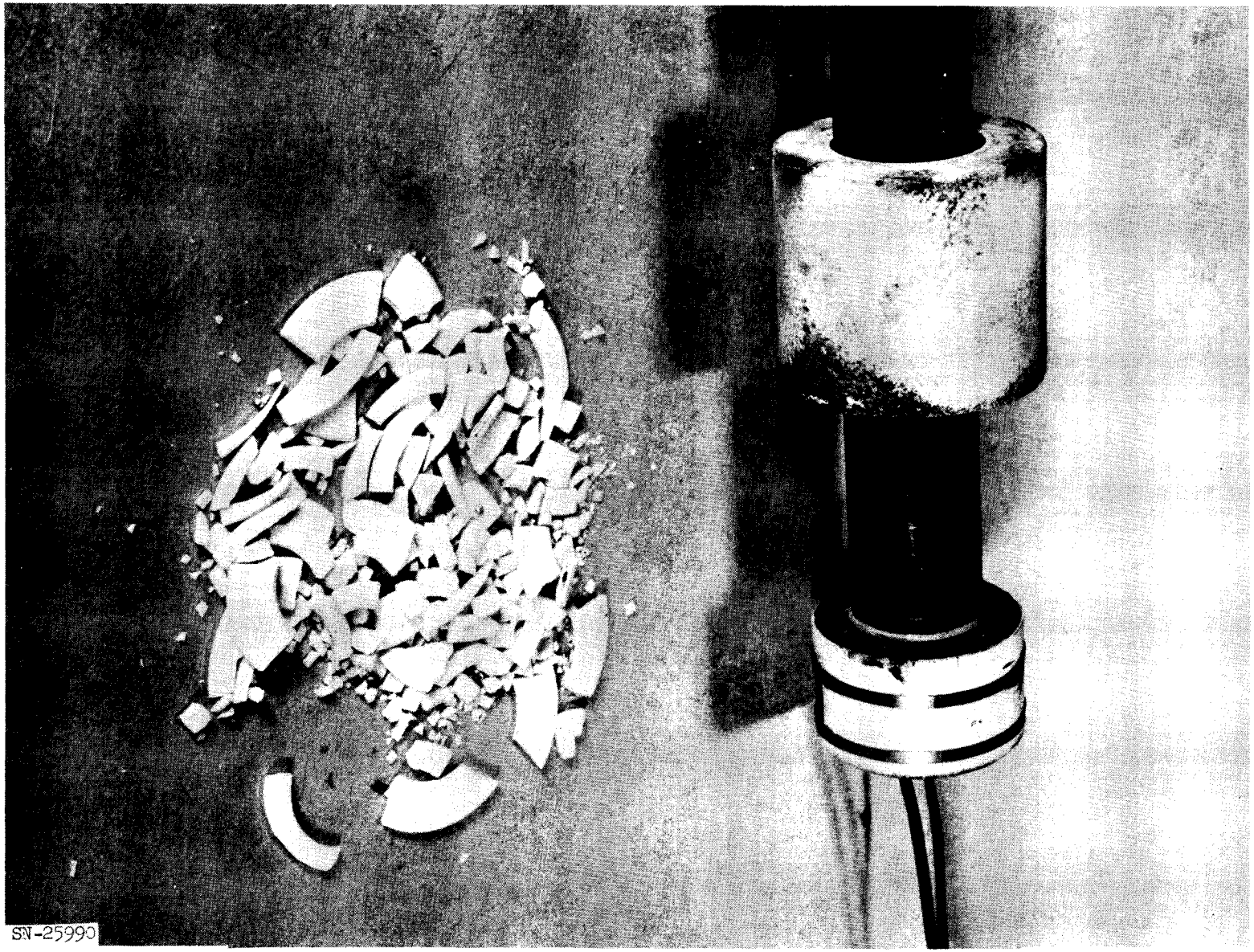

Fig. IV-50. Disintegration of zirconia washers.

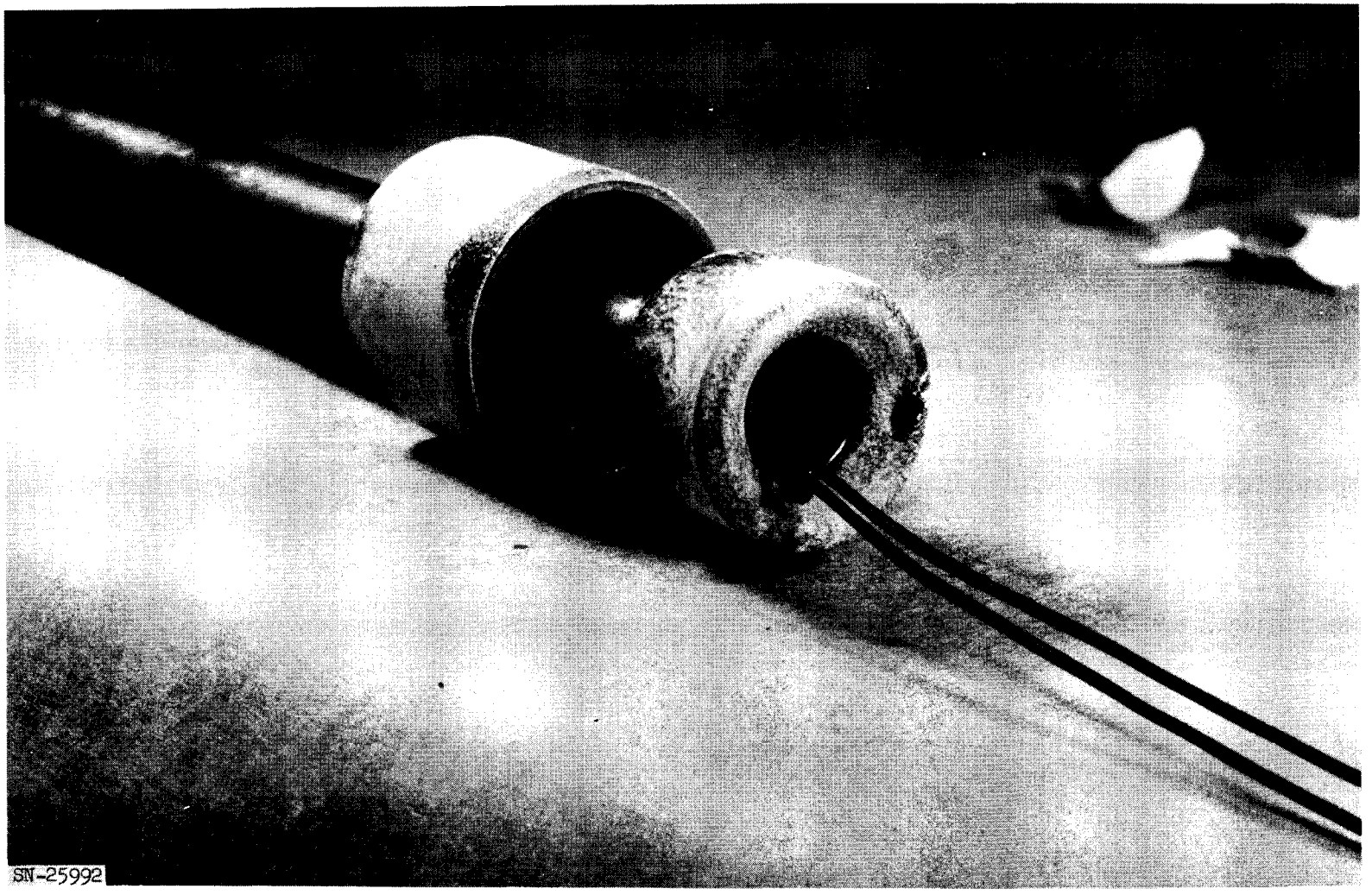

Fig. IV-51. Flame-sprayed ceramic coating on platinum cup after test.

observable at the rear lip, but these pits penetrate only a small way into the coating. Again, the coating is probably superfluous. The zirconia washers, which had already been replaced in the reactor design at the time of test, were thoroughly disintegrated, probably as a result of thermal shock (Fig. IV-50).

The base-plate coating survived in excellent shape (Fig. IV-52), except along the outer periphery. Here airflow between the cell tubes and the insulation wall produced a strong sandblast effect. This is believed due entirely to the loose fragments of insulation. There is no evidence of this type of damage in any other region. Considerable misalignment is obvious from discolorations on the baseplate. This resulted from the failure of the insulation support and the zirconia washers.

Noise levels were quite high. Measurements upstream and downstream of the cell showed that there was attenuation across the cell except at 1300 and 1700 cps cold. If there is any amplification at these points it is very low. The noise level averaged from 2.5 to 2500 cycles was as follows:

Run	Upstream noise (db)	Downstream noise (db)
1a	163.6	149.6
1b	165.2	158.6
1c	168.0	156.3

The difference in noise levels is almost constant throughout the spectrum with the exception of several poorly defined points where it decreases slightly, and the two points previously mentioned where there appears to be no decrease.

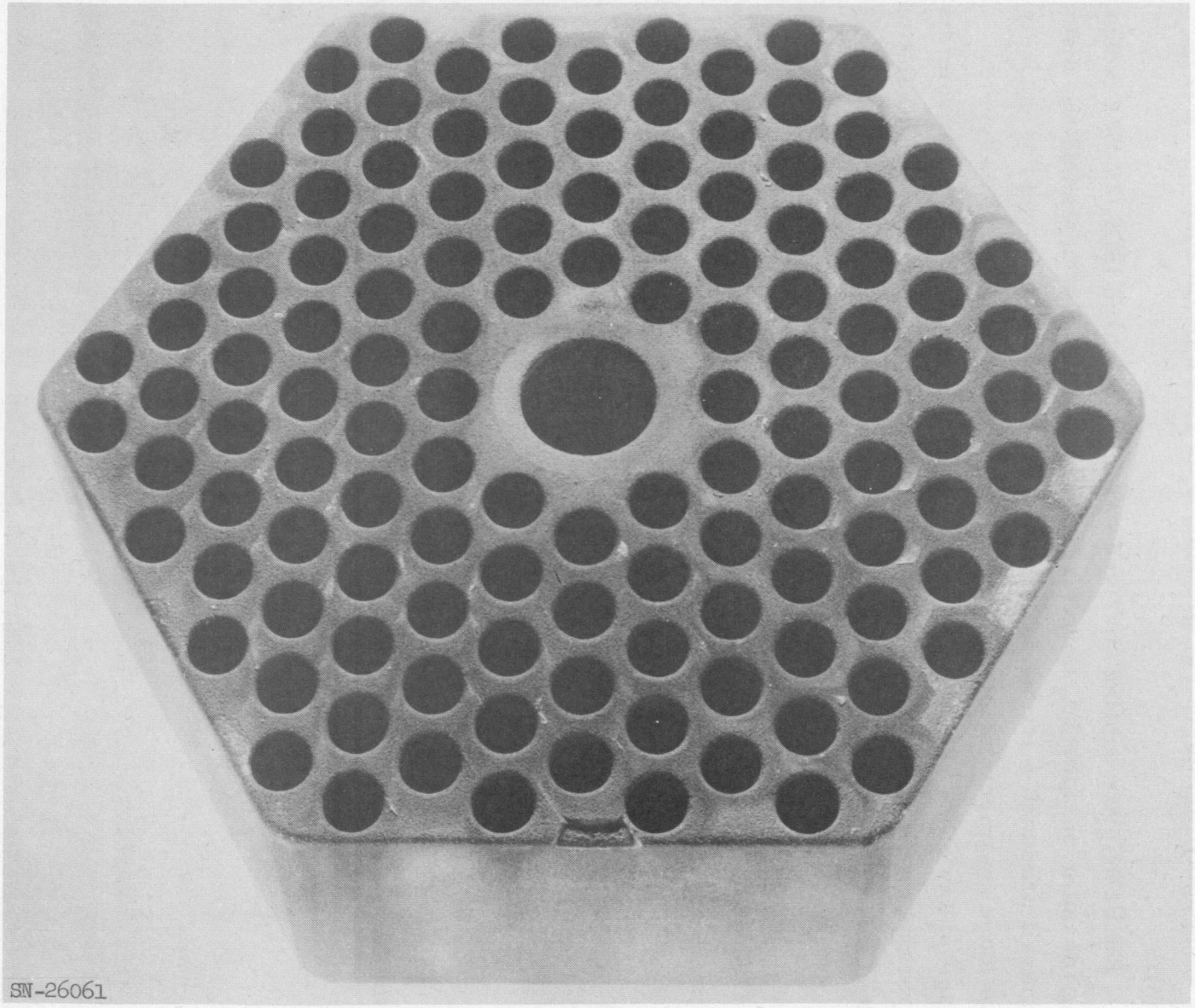

Fig. IV-52. Baseplate coating.

CHAPTER V. TORY III

SECTION I. INTRODUCTION

About two years ago LRL started serious efforts to select a design concept for the Tory II-C reactor. Initially, four different designs were being carried forward as possible contenders. About one year ago two of these initial concepts were eliminated, and the remaining two undertaken more intensively. Then, about six months ago the present II-C design was picked and our major effort was directed toward it. However, we carried the remaining "dome" reactor along on a "retro-fit" basis, largely because of concern over the base-plates needed in the "first-choice" design. About two months ago, it was decided that that worry was minor and the "dome" design was removed from consideration as a retro-fit possibility. However, for possible future applications requiring a life longer than ten hours, and/or an exhaust gas temperature greater than presently chosen, it was clear that the dome-type reactor might have something to offer.

In order to reflect the fact that the dome design is no longer being followed as a contender for the Tory II-C job, its designation has been changed from Tory II-C-2 to Tory III. It is important to note that Tory III is not yet, and may never become, a reactor construction program. It is a designation, used for convenience, to indicate one particular area of R & D which may bear fruit in the future.

SECTION II. ENGINEERING

SILICON NITRIDE

The mechanical and thermal properties of silicon nitride (Si_3N_4) as listed in the literature shows it to be a very interesting high-temperature material for Tory III. The Admiralty Materials Laboratory in England has developed a method of fabrication of the material as described in A. M. L. Report No. A/75 (S). However, the largest bodies made by A. M. L. to date are 5-in. -diameter cylinders 12-in. long. It was decided at LRL to determine the feasibility of making larger bodies using the A. M. L. method.

First attempts at LRL on small samples following A. M. L. 's procedure proved both the material and procedure to be promising. Both steel die and isostatic pressings were used in these first samples. However, A. M. L. 's

report gave test results which indicated material formed by the isostatic pressing method to have more desirable properties. A brief investigation of isostatic pressing of silicon powder at LRL revealed that a powder with a maximum particle size of 70 microns (200 mesh) could be pressed to shapes 14-in. in diameter and 10-in. high. However, a powder with a maximum size of 36 microns could not be pressed to a shape 3-in. in diameter and 2-1/2-in. high and have the piece remain intact. Each powder had more or less a normal particle size distribution curve and each had about the same particle shape when investigated under the microscope. Three bodies of the 14 in. × 10 in. size have been pressed to date using 20,000 psi, which is the maximum for the press used. Radiographs did not reveal any internal cracks or flaws.

Two of the large pressings were fired for 16 hours at 2100°F. This gave the partially fired, machineable material. However, both bodies had internal cracking, probably due to thermal shock. It is planned to fire the third pressing at a considerably lower heating and cooling rate in an effort to eliminate cracking. Cores of the fired bodies showed that nitriding had taken place throughout the bodies and appeared to be quite uniform. Even with the cracks, one body held together while being machined into a hexagonal shape with an array of holes.

SILICON CARBIDE

Flow Tests on SiC

Two sets of flow tests were run in the same contractor's facility used for Tory II-C columbium coating tests. Specimens used were 1-1/2-inch diameter by 1/2-inch thick with a seven-hole configuration as shown in Fig. V-1. Holes were 5/16-inch in diameter and total hole area was 0.537 square inch. Flow conditions for all tests were held as closely as possible to the following:

Temperature	2500°F
Flow rate	0.3 lb/sec
O_2 content	21 ± 1%

Hydrogen was used as a fuel, and oxygen addition after the burner was used to bring the oxygen content up to that of normal air.

In the first set of tests, three specimens were placed in a tandem arrangement in the flow for 5 hours. Weight losses were as follows:

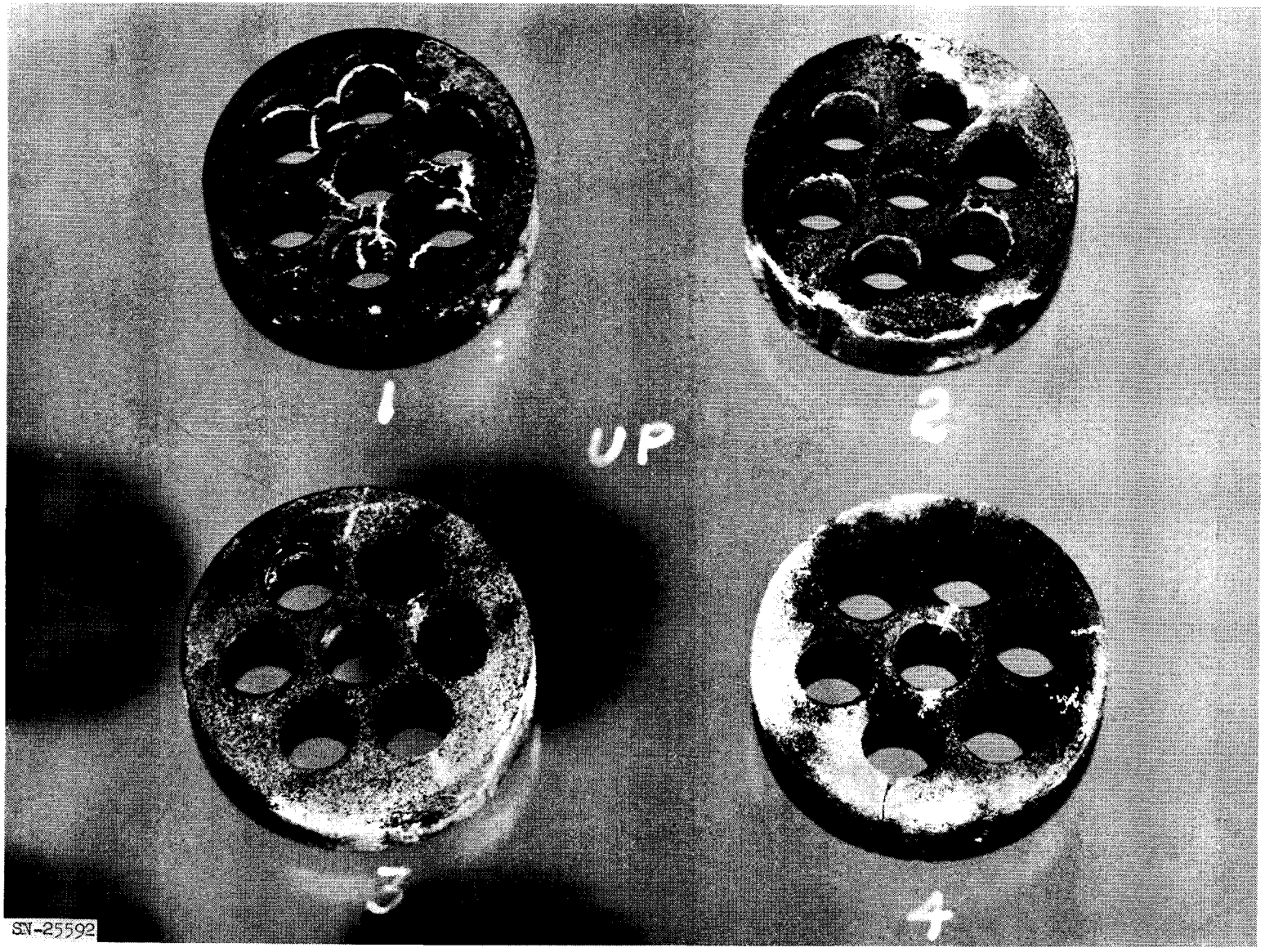

Fig. V-1. Seven-hole configuration SiC test specimens used in flow tests. Specimens had an as-fired finish (about 400 μ in.).

Specimen	Weight loss (%)	Average (%/hr)
1	0.857	0.161
2	0.918	0.184
3	0.782	0.156

No other damage was apparent to the three specimens and all dimensions were unaltered. The specimens used had an as-fired finish (about 400 μ in.) and it was initially surmised that the weight loss was due to loss of this rough finish in the flow.

Thermal shock tests were next run on three specimens, two of them from the flow test and one previously untested. Single specimens were brought to a stable temperature and the hydrogen supply was shut off abruptly. In all three cases, the rate of temperature decrease was identical; 2190°F/sec. This rate was constant from 2480°F to 1275°F with a much more gradual decrease from 1275°F to about 900°F.

The first test showed no visible damage to the specimen, although later Zyglo inspection showed some web cracking (see number 1 in Fig. V-1). Next, a previously unheated specimen was tested (number 4 in Fig. V-1) and cracked part way across, completely cracking two days later. The last test was on number 3 in Fig. V-1 and resulted in cracking about halfway across the diameter. Number 2 in Fig. V-1 was a flow-tested specimen that was not thermal shocked.

The second test series utilized specimens that had been ground to a 50 μ in. finish on all outside surfaces. Results of the flow test of 3 hours and 13 minutes were:

Specimen	Weight loss (%)	Average (%/hr)
1	0.500	0.155
2	0.570	0.177
3	0.710	0.221

These results indicated that surface finish had no effect on the weight loss. Silicon metal oozed out on all surfaces of the specimens in the form of small globules and the weight loss is believed due to this silicon being removed by the flow.

Four thermal shock tests were run at the rates indicated.

Specimen number	°F/sec	Results
4	871	Visible cracks in 3 webs.
2	795	Cracked across diameter.
3	793	Not visibly damaged. Cracks Zyglo indicated in webs.
1	772	Initially undamaged but cracked across diameter two days later.

Figure B-2 is a reproduction of a black light photograph of the specimens. Cracks are indicated by the Zyglo process.

Thermal Stresses in SiC

The thermal stress equipment described on page 59 of Pluto Quarterly Report No. 7 was used to test concentric tubular specimens 1-in. long by 1.25-in. diameter with a 0.25-in.-diameter hole in the center. Three specimens were stacked on end for each test. A temperature difference was generated by heating the center hole with a carbon element and holding the outer surface temperature constant with an array of carbon-rod elements spaced equally about the outside. Inside and outside thermocouples were initially used to record temperatures.

Two tests were made with thermocouples, but difficulties were encountered with short thermocouple life. For the third test, power across the inner carbon heating rod was measured and a heat balance between inner and outer surfaces was used to compute a temperature difference.

Results are listed below:

Test	T(°F) Inner surface	T(°F) Outer surface	ΔT (°F)	Calculated σ_{max} (tension) (psi)
1	2346	2018	328	13, 720
2	2452	2100	354	14, 800
3	--	2100	354	14, 800

No cracking or other damage was noted to the specimens, except that in the final test, the inner heating rod contacted the inside wall of one specimen, resulting in heavy arcing. This specimen was locally melted at the inner surface and cracked along a radius.

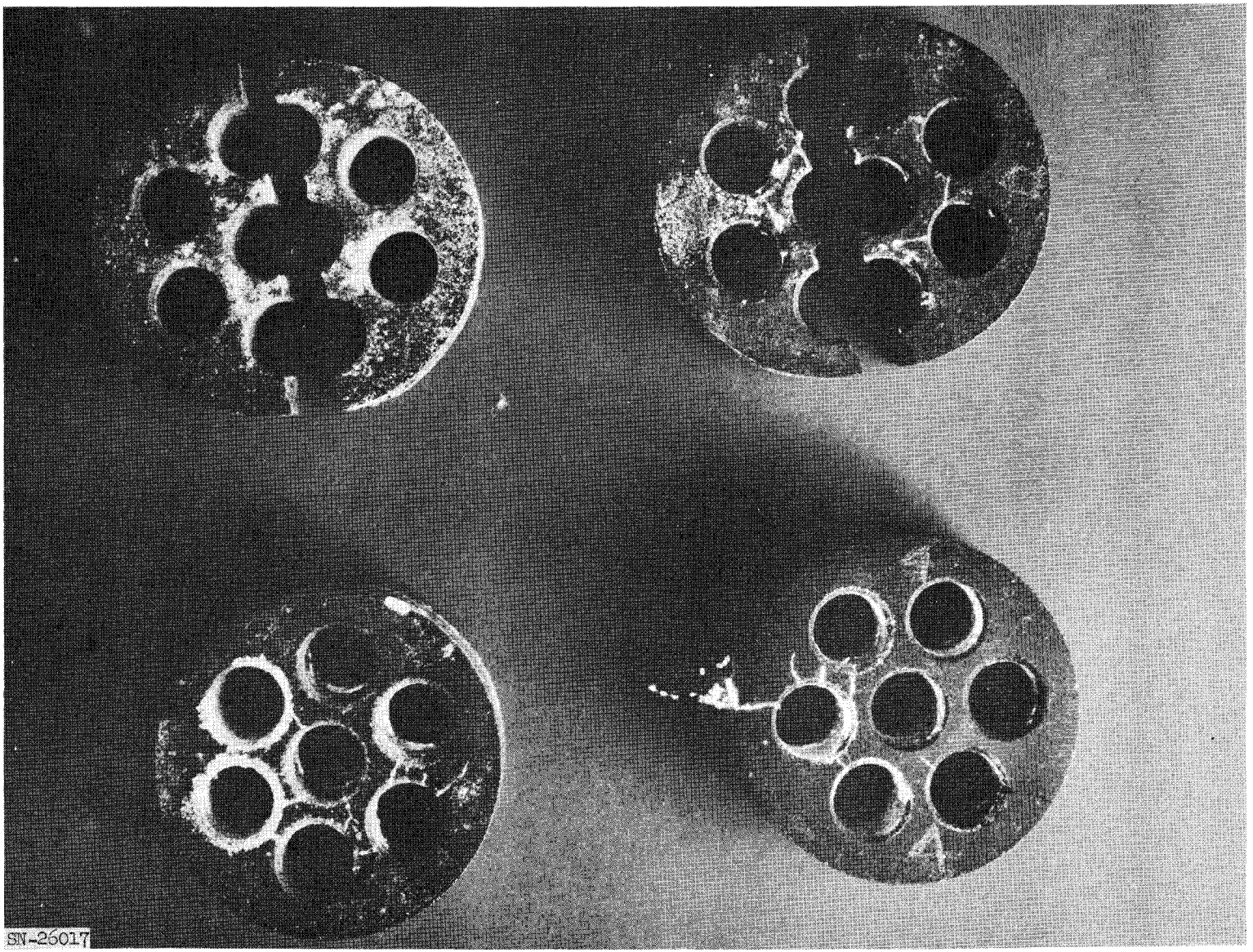

Fig. V-2. Seven-hole configuration SiC test specimens used in second series of flow tests. Specimens were ground to 50-μ in. finish on all outside surfaces prior to test.

TORY III AXIAL SUPPORT STRUCTURE PHOTOELASTIC STRESS ANALYSIS OF VARIOUS "DOME" GEOMETRIES

Five photoelastic models, representing two basic dome geometries in three variations each, were investigated under uniformly distributed loading. "Frozen stress" techniques were used to determine boundary stresses for each configuration. Deflections normal to the plan of loading were measured directly.

The loading apparatus is shown in Fig. V-3. Figure V-4 shows a typical model before loading. The applied load was distributed by means of a can filled with lead shot and a silicone-rubber-foam pad. The "stress freezing," sectioning, and analysis procedures employed are standard for three-dimensional photoelastic stress analysis.

The two basic dome configurations (Fig. V-5) chosen for analysis represent the extremes of the range of present interest. The 90° included seat angle (configurations 1, 3, 5, Figs. V-6, V-7, V-8) is near a maximum for which thin-shell theory predicts "all-compressive" stresses. The 60° included seat angle (configurations 2 and 4, Figs. V-9, V-10) is the minimum consistent with "free" motion upon thermal expansion against seat materials with presently attainable friction coefficients. The monolithic versions (configurations 1 and 2, Figs. V-6, V-7) were incorporated as reference cases. The two basic segmentation schemes ["pie" configurations 2 and 4 (Figs. V-9, V-10) plus "keystone" configuration 5, Fig. V-8] were considered for purposes of comparison as typical of the variations possible. The boundary stress values determined for the various configurations are shown plotted on the appropriate accompanying figures. Determination of internal stress trajectories requires the more elaborate graphical integration. Shear difference methods were not attempted since the primary purpose of this first work was to establish fundamental relationships and the applicability of the method. The results presented generally confirm that, for the range of configurations considered, boundary stresses resulting from the loads applied are generally compressive in kind, except where the geometry of the model differs significantly from a true spherical cap. In the application of these geometries to the reactor designs considered, the presence of radial preload forces, along with the removal of extraneous material, can be expected to reduce or eliminate regions subject to tensile stresses. The methods attributed to G. Horvay[1] for

[1] Problems of Mechanical Analysis in Reactor Technology, G. Horvay Reprint 355, Am. Inst. of Chem. Eng. (1955).

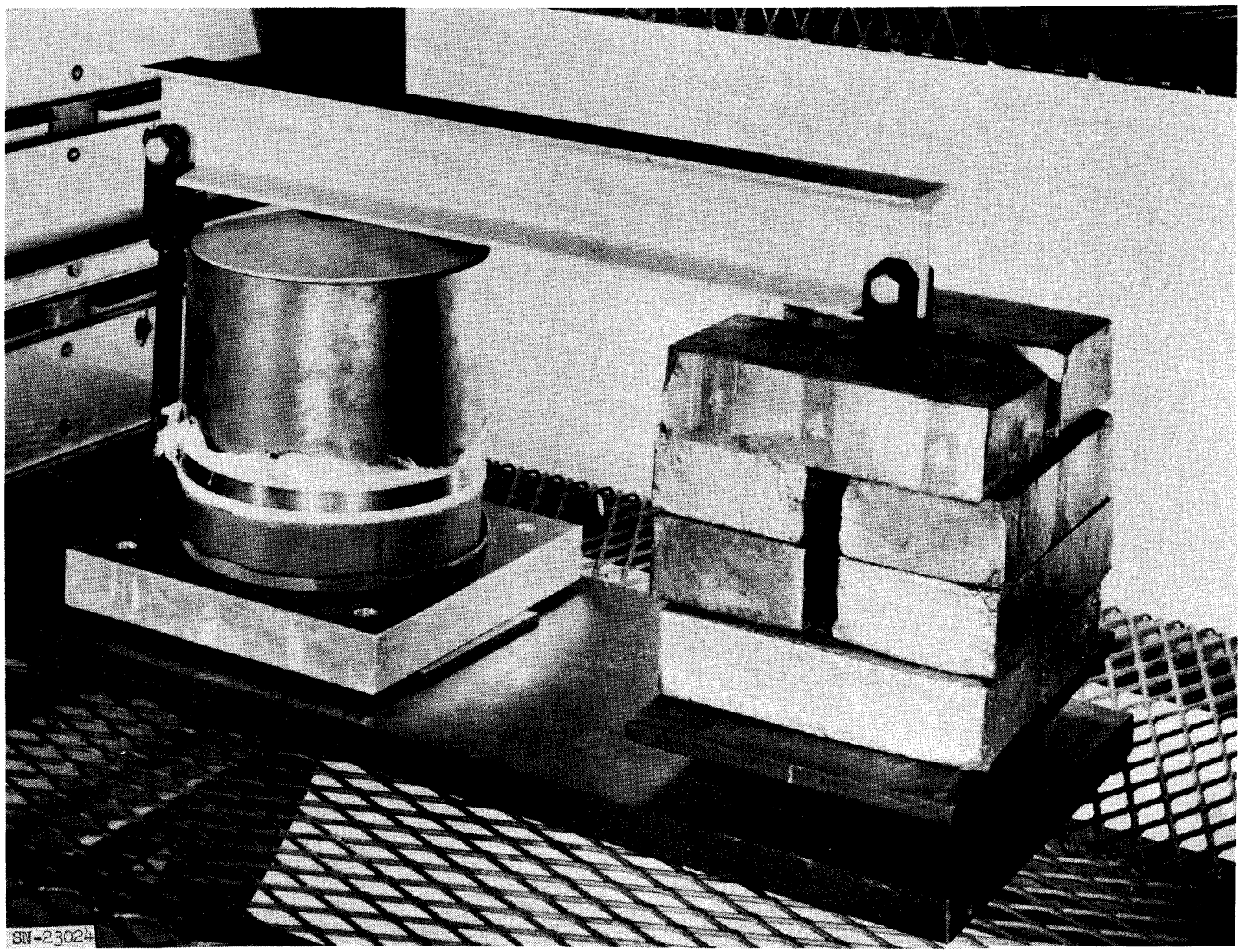

Fig. V-3. Loading apparatus with model in place.

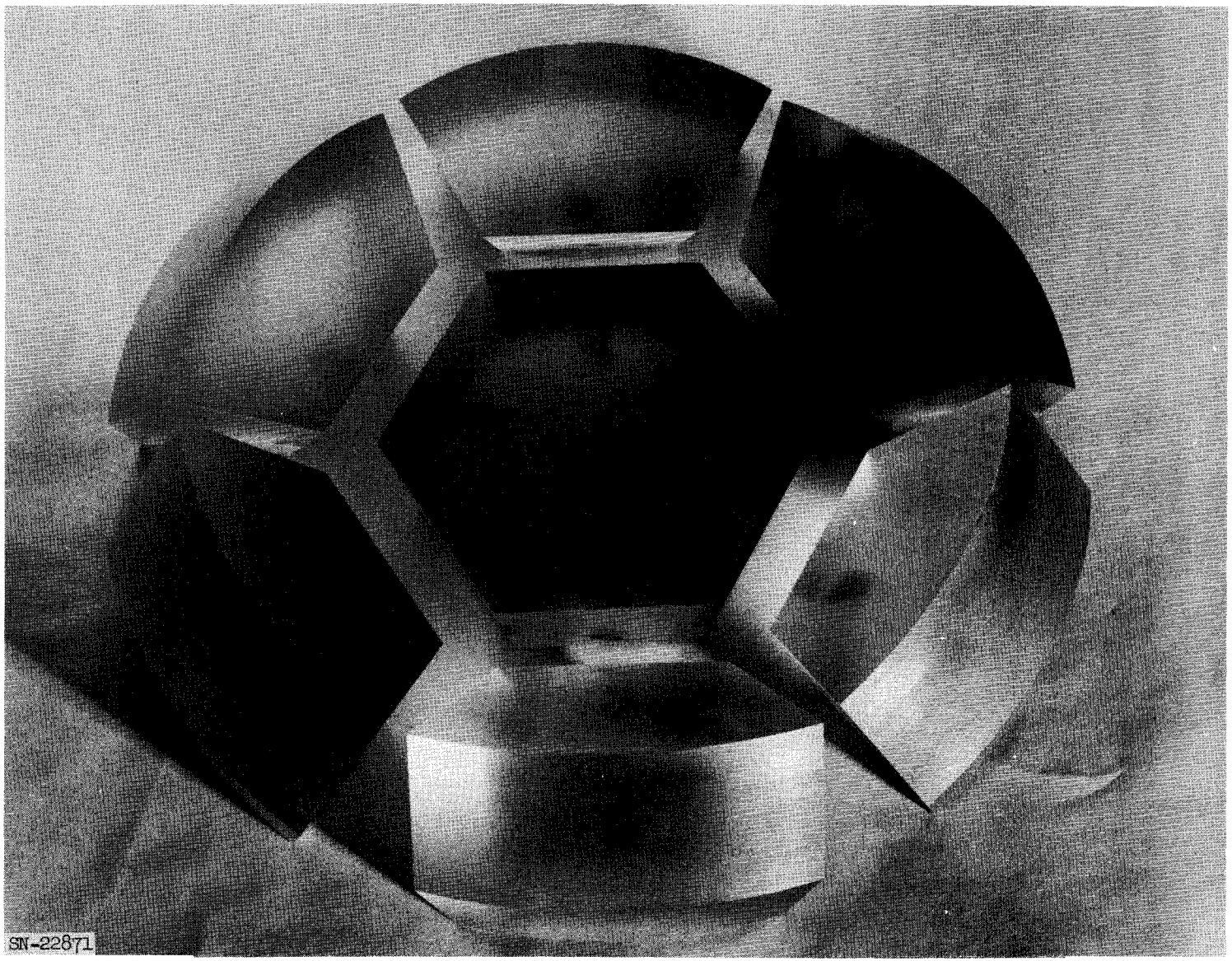

Fig. V-4. Photoelastic stress model, configuration No. 5.

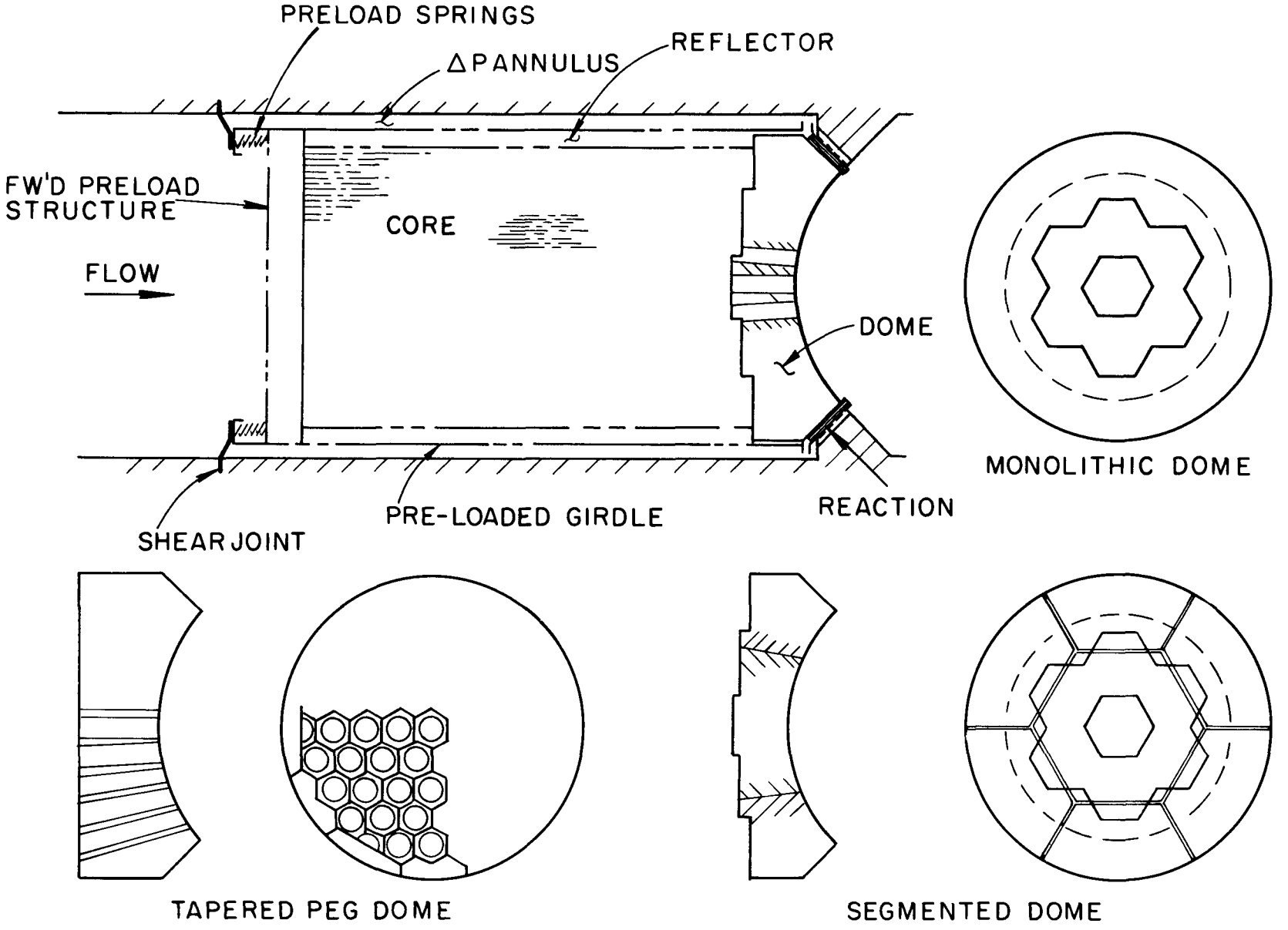

Fig. V-5. General configuration of Tory III rear (dome) supported reactor.

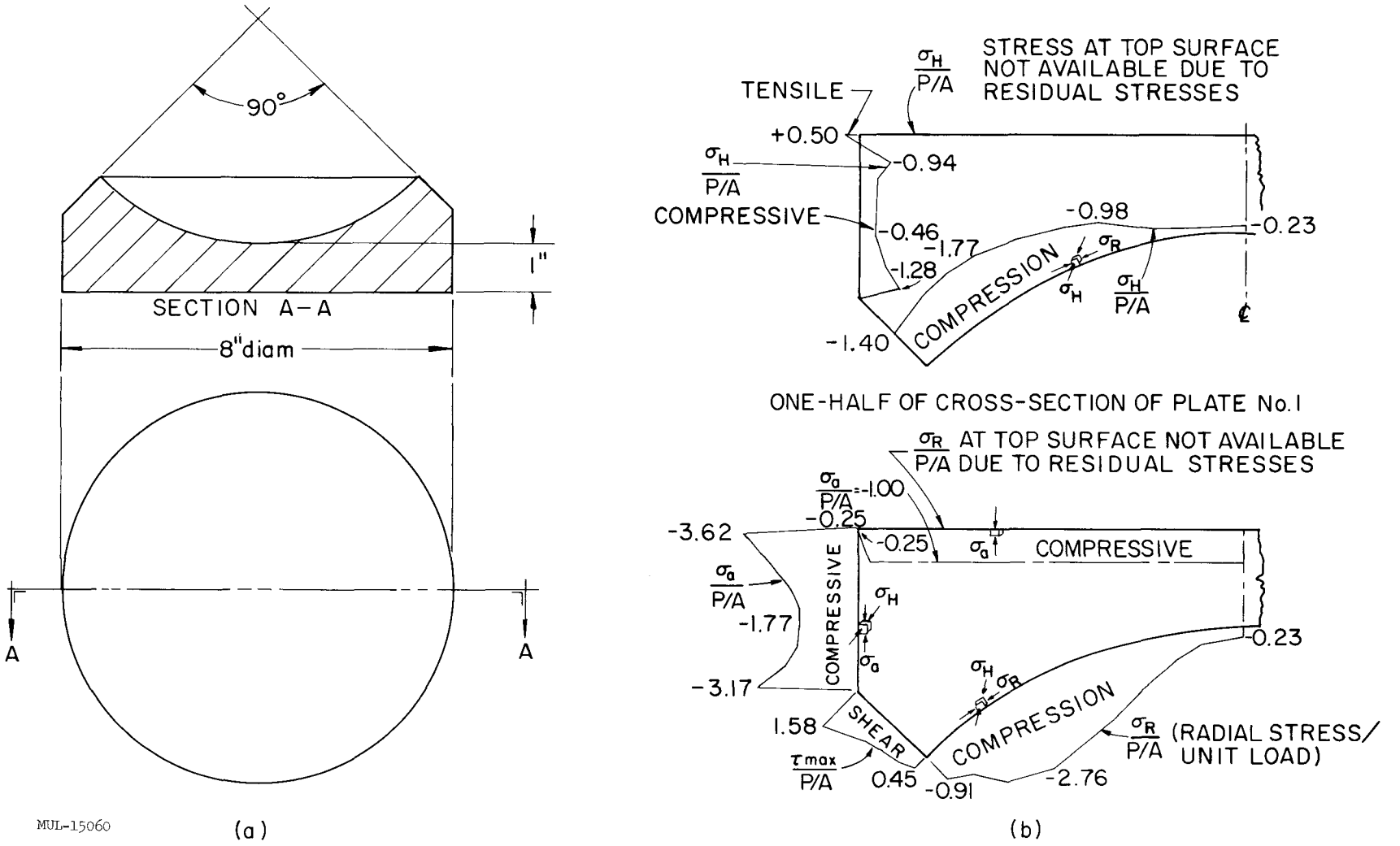

Fig. V-6. Dome photoelastic study. (a) Configuration No. 1. (b) "Frozen" photoelastic stress study, 90° dome (single piece), 8-in. diam, 1-in. minimum thickness; all stresses are plotted at 3.00 per inch scale from the surface where $\frac{\sigma}{P/A}$ is the ratio of stress (psi) to loading (psi).

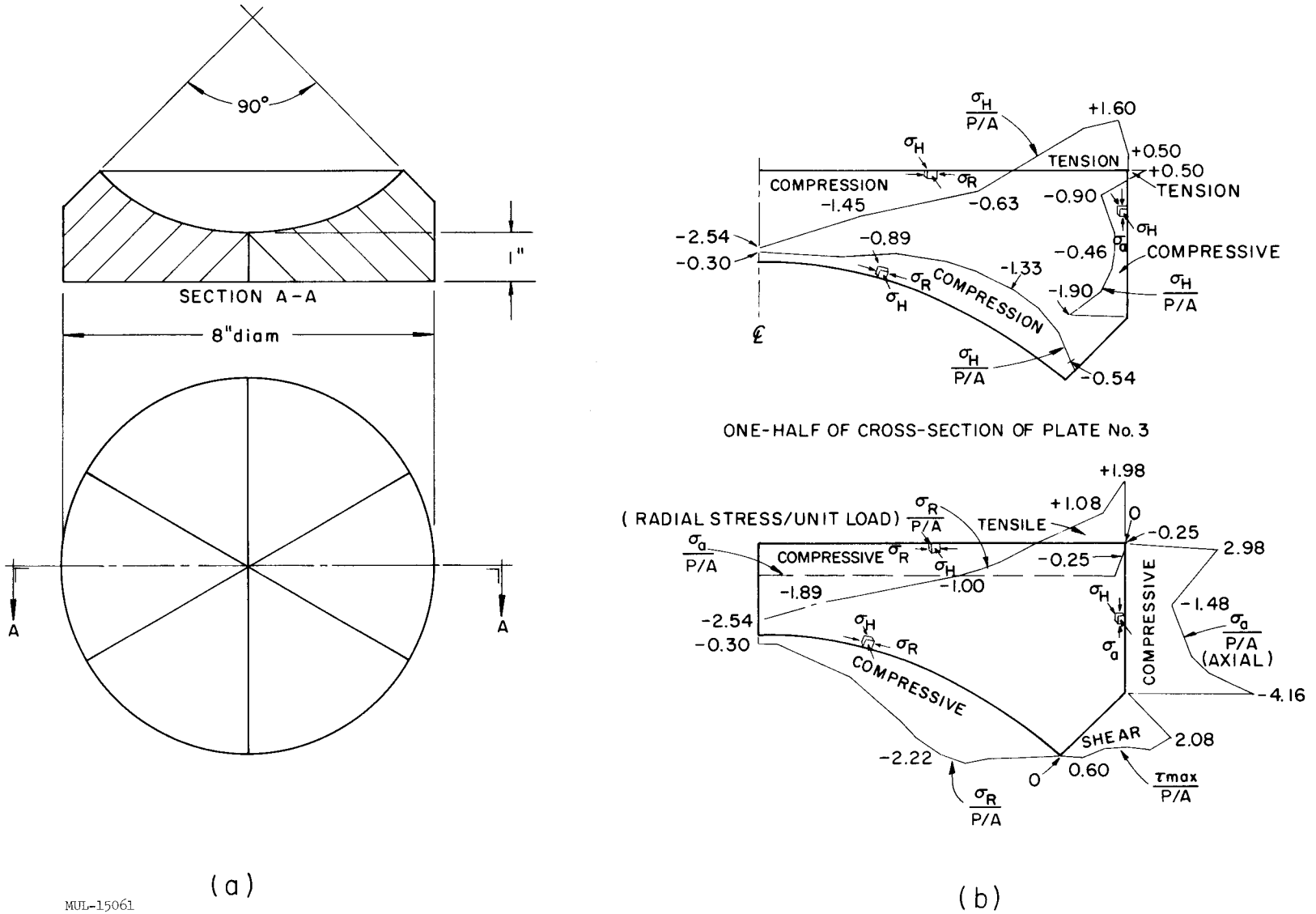

Fig. V-7. Dome photoelastic study. (a) Configuration No. 3. (b) "Frozen" photoelastic stress study, 90° dome, 6 "pie" segments, 8-in. diam, 1-in. minimum thickness; all stresses are plotted at 3.00 per inch scale from the surface; the stresses are from Dome 3b (through the middle of the pie section).

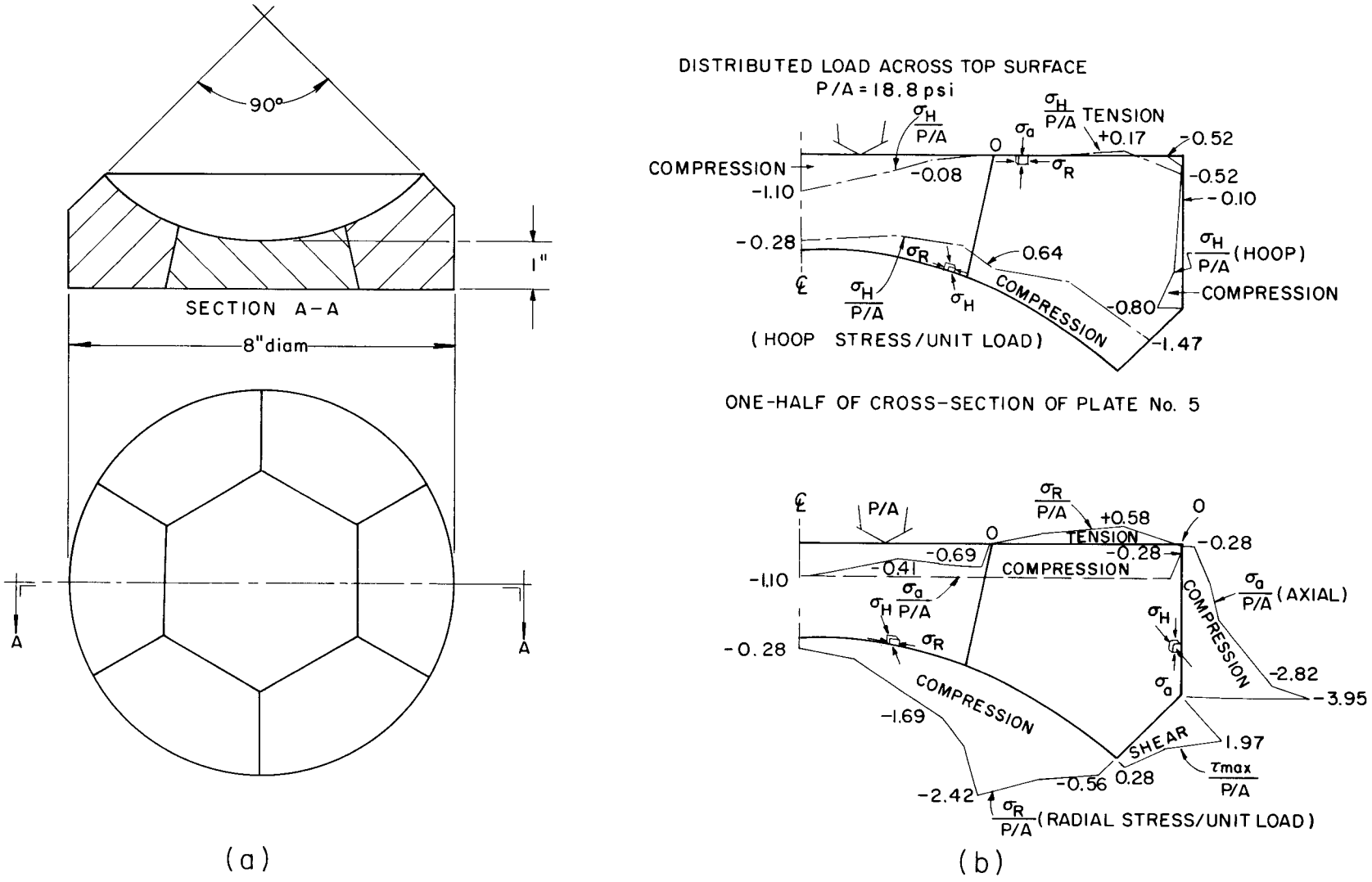

Fig. V-8. Dome photoelastic study. (a) Configuration No. 5. (b) "Frozen" photoelastic stress study, 90° dome, 7 segments (6 wedges plus central "keystone"), 8-in. diam, 1-in. minimum thickness; all stresses are plotted at 3.00 per inch scale from the surface; the stresses are from a slice through the middle of a pie section.

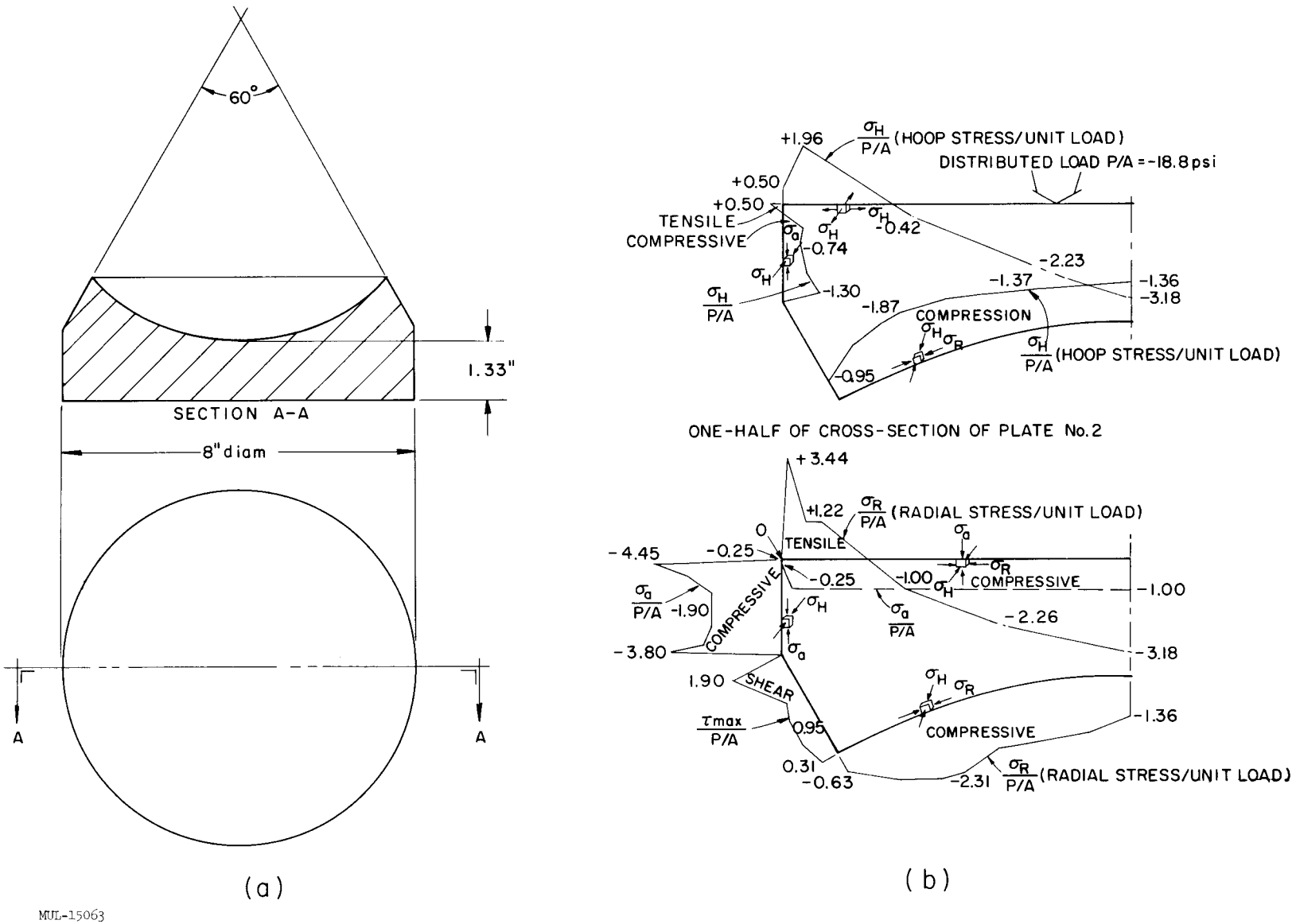

Fig. V-9. Dome photoelastic study. (a) Configuration No. 2. (b) "Frozen" photoelastic stress study, 60°dome (single piece), 8-in. diam, 1.33-in. minimum thickness; all stresses plotted at 3.00 per inch scale from the surface.

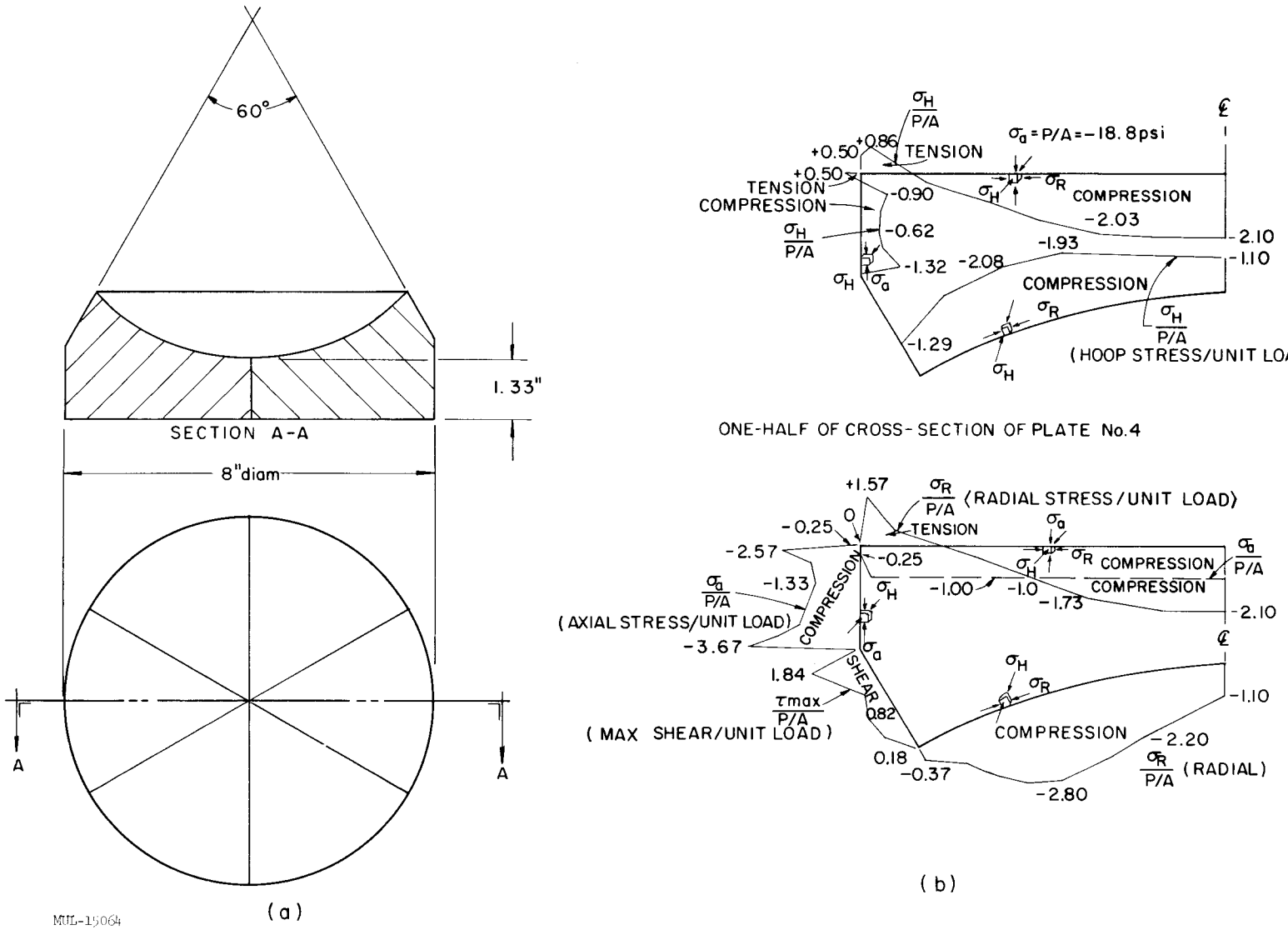

Fig. V-10. Dome photoelastic study. (a) Configuration No. 4. (b) "Frozen" photoelastic stress study, 60°dome, 6 "pie" segments, 8-in. diam, 1.33-in. minimum thickness; all stresses are plotted at 3.00 per inch scale from the surface; the stresses are from a slice through the middle of a pie section.

determining maximum ligament stresses in perforated bodies have been used to predict the apparent stresses of a perforated reactor structure. Such results seem to correlate well with fracture studies on small perforated silicon carbide domes reported previously. The result, therefore, seems to be that the magnitude of the maximum stresses in a reactor support dome can be predicted to be from 12 to 15 times the applied pressure drop loading.

FABRICATION DEVELOPMENT OF LARGE SHAPES OF SILICON CARBIDE

Green machining of the last of 2 center segments and 12 outer segments of a 3-foot-diameter dome assembly was completed at LRL. This number of twice the parts required for one assembly was assumed to be necessary to account for undetermined rejection.

To date, one center segment is fired and final machined, and 7 outer segments fired, with 3 of the outer segments being essentially completely machined. All firing and finish machining (diamond grinding) was done at the contractor's plant.

To date, 3 pieces approximately the size of those required for a 54-in. dome have been successfully fabricated. One is shown in Fig. V-11.

Recent theoretical studies have indicated that previous "green" mixes of the "KT" silicon-carbide have had a density which is sufficiently high as to induce cracking during firing. Reducing the green density has permitted the conclusion that pieces can be fired consistently without inducing cracks during the firing process.

/fj

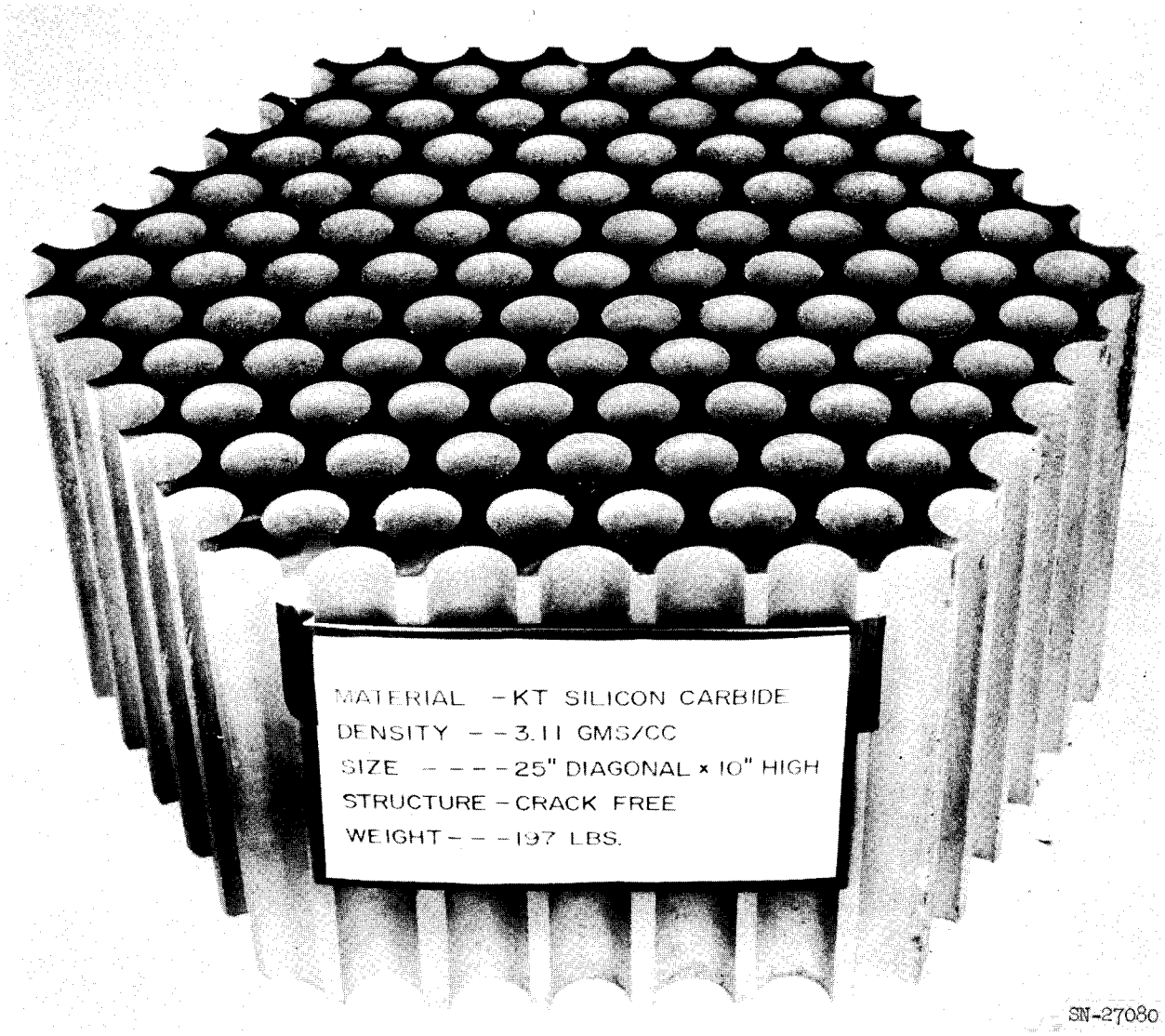

Fig. V-11. Silicon carbide segment for 54-in. dome.

LEGAL NOTICE

This report was prepared as an account of Government sponsored work. Neither the United States, nor the Commission, nor any person acting on behalf of the Commission:

A. Makes any warranty or representation, expressed or implied, with respect to the accuracy, completeness, or usefulness of the information contained in this report, or that the use of any information, apparatus, method, or process disclosed in this report may not infringe privately owned rights; or

B. Assumes any liabilities with respect to the use of, or for damages resulting from the use of any information, apparatus, method or process disclosed in this report.

As used in the above, "person acting on behalf of the Commission" includes any employee or contractor of the commission, or employee of such contractor, to the extent that such employee or contractor of the Commission, or employee of such contractor prepares, disseminates, or provides access to, any information pursuant to his employment or contract with the Commission, or his employment with such contractor.